Cranfield University

Johannes W. G. Treiber

Performance of tufted carbon fibre/epoxy composites

School of Applied Sciences

PhD Thesis

Academic Year 2010-2011

Supervisor: Professor Ivana K. Partridge

March 2011

Abstract

The thesis presents a detailed analysis of the effects of one-sided access z-direction reinforcement, ‘tufting’, on the morphology and mechanical performance of the resulting MVR-444 epoxy matrix/carbon fibre fabric composites. The dry fabric architectures used are pseudo-UD, twill woven fabric and non-crimped fabric (NCF). They are tufted with a range of commercial tufting threads, using KSL KL150 tufting head mounted on a 6-axis robot arm. The main focus is on the use of a twisted carbon fibre thread, at areal tufting densities of 0.5% and 2%. The composite plates are prepared via Resin-Transfer-Moulding (RTM) route, making it possible to control the plate thicknesses.

The morphological features characteristic of tufted, cured composites are described and categorised. The global and local fibre volume fractions are measured and simple models proposed that connect local increase with local fibre deviation and presence of resin rich surface loop layers. It is shown that the balance of in-plane and out-of-plane properties in tufted composites is highly dependent on the tufting parameters, but also on the fabric architecture, with the NCF option seeming the most attractive. Overall, the stiffness of tufted materials is not affected and the drop in in-plane strength of any realistic geometry combinations is below 20%. ‘Thread-less’ tufting experiments prove that the drop is not caused by fibre breakage from the passage of the needle alone.

Digital image correlation (DIC) techniques is used to map out the strain field distributions during mechanical testing, increasing the accuracy of crack tip location in Mode II delamination cracking studies and confirming the mode mixity changes during deformation of tufted structures. Single-tuft experiments provide the experimental data that are required for the development and validation of analytical models. A finite element unit cell model is developed to predict in-plane elastic and failure behaviour of tufted UD and NCF composites incorporating the critical meso-structural features of fibre deviation and increased fibre volume fraction.

The thesis also contains an overview of the tufting technology and some detailed information on recent manufacturing developments that were required to obtain the controlled quality specimens used in the study. A demonstration structural element was produced, in the form of a tufted omega-stiffener. A standard pull-off test demonstrates the superior load carrying and energy absorbing capacity of this strengthened structure.

Details of robot programming, additional single tuft bridging results, test fixture design, derivation of the analytical bridging model and additional publications are given in appendices to the main body of the thesis.

to Hannah

for her patience, support, and love.

Acknowledgements

I wish to express my deepest gratitude to my supervisor Professor Ivana Partridge for her continuous support, advice and guidance through this work. You gave me the great opportunity to work for you at Cranfield University, but also showed me when it is time to stop.

I am most grateful to Dr. Denis Cartié for bringing this project on its way and being a friend as much as a supervisor. You taught me to set the highest standards on experimental work.

I would like to thank Dr. Giuseppe Dell'Anno and Dr. Alex Skordos for the many discussions and technical help on both experiments and numerical challenges. To Jim Hurley for all your assistance in the lab, the many last minute jobs which kept me going and detailed technical discussions.

To my friends, Andrea, Beth, Christian and Mehdi, who fought alongside on their PhD during the last three years.

And to the many colleagues and friends, I have made during the time in Cranfield, in particular Ben, David, Francesca, Gary, James, Mar, Marco, Sharon McGuire, Silvia and Usama who helped me during the time of my PhD. A special thank you also to Mathieu for his dedication and assistance with experimental work.

To Hannah, for everything.

Table of contents

List of figures

List of tables

Acronyms

CBT – Corrected beam theory

CBTE – Corrected beam theory with effective crack length

CTE – Coefficient of thermal expansion

DCB – Double cantilever beam

DIC – Digital image correlation

DMA – Dynamic mechanical analysis

DSC – Differential scanning calorimetry

ECM – Experimental compliance method

ELS – End loaded split

ENF – End notch flexure

ILSS – Inter-laminar shear strength

NCF – Non-crimped fabric

PAN – Poly-acrylo-nitrile

PTFE – Polytetrafluoroethylene

RT – Room temperature

RTM – Resin transfer moulding

RVE – Representative volume element

SBCF – Stretch-broken carbon fibre

SENB – Single-edge notched bending

TMA – Thermo-mechanical analysis

TTR – Through-thickness reinforcement

UC – Unit cell

UD – Unidirectional

Nomenclature

Materials, manufacturing and in-plane performance:

A_t	infused tuft cross-section area (mm^2)
$A_{t,dry}$	dry fibre tuft cross-section area (mm^2)
L	resin rich pocket length (mm)
$m_{f,A}$	fibre mass in air (g)
$m_{f,IL}$	fibre mass immersed in liquid (g)
n	number of fabric layers (-)
s_x	tuft spacing along the tufting row (mm)
s_y	spacing between tuft rows (mm)
t	laminate thickness (mm)
t_l	loop layer thickness (mm)
t_{th}	thread layer thickness (mm)
$t_{th,max}$	max. thread layer thickness at point of tufting thread (mm)
T_{th}	linear density thread (g/km)
V_f	fibre volume fraction (-)
$V_{f,2D}$	2D equivalent fabric fibre volume fraction (-)
w	resin rich pocket width (mm)
w_{dev}	fabric fibre deviation width (mm)
w_{min}	minimal resin rich channel width (mm)
φ_{dev}	in-plane fabric fibre deviation angle (°)
φ_{th}	max. out-of-plane fabric crimp angle at surface thread (°)
ρ_A	mass per unit area of dry fabric (fabric areal weight) (g/cm^2)
ρ_f	fibre density (g/cm^3)
ρ_{IL}	density of immersion liquid (g/cm^3)
ρ_t	tuft areal density (%)

In-plane modelling:

E	axial modulus (MPa)
f_e	stress exposure (-)
G	shear modulus (MPa)
P	force vector at unit cell boundary surface for [x,y,z] (N)
R	material strengths (MPa)
u	nodal displacement vector for [x,y,z] (mm)
V_f	local fabric/thread fibre volume fraction (-)
γ	shear strain (engineering strain) (-)
ε	normal strain (-)
ν	Poisson's ratio (-)
σ	normal stress (MPa)
τ	shear stress
φ	in-plane fibre deviation angle (°)
θ_{fp}	angle of fibre parallel fracture plane (°)

Indices:

x, y, z	global unit cell coordinate system
1,2,3	ply coordinate system - aligned, transverse and normal to in-plane ply fibre orientation
$n/n1/nt$	normal, parallel and transverse direction relative to fibre orientation in action plane
r, f	resin matrix, fibre constituents
rp	resin pocket
t	tension (stress direction)
$\perp, \parallel$	orthogonal and parallel stressing index to fibre orientation in UD ply

Superscripts:

c, t	compression, tension

Delamination testing:

a	crack length (mm)
a_c	calculated effective crack length (mm)
a_0	initial pre-crack length (mm)
B	specimen width (mm)
C	beam compliance (N/mm)
$E_{f,i}$	flexural stiffness of uncracked beam/beam halves (i=a,b) (N/mm^2)
$E_f{}^*$	effective flexural stiffness (N/mm^2)
F	correction factor for large beam deformation (-)
$G_{I/II}$	strain energy release rate for mode I/II delamination (J/m^2)
$G_{Ic/IIc}$	critical strain energy release rate for mode I/II delamination (J/m^2)
h	half beam thickness (mm)
L	specimen length (mm)
N	correction factor for off-set in load line (-)
P	applied load (N)
x_t	distance between load line and first tuft row (mm)
δ	displacement at load line (mm)
Δ_{clamp}	correction factor for root rotation in ELS fixture (mm)
ρ_t	tuft areal density (%)

Indices:

t	tufted section
r	untufted section
ini	initiation values
$prop$	propagation values

Bridging behaviour of single Z-reinforcements:

A_t	infused tuft cross-section area (mm^2)
$A_{t,dry}$	dry tuft cross-section area (mm^2)
A_{th}	infused surface thread cross-section area (mm^2)

$A_{th,dry}$	dry thread cross-section area (mm^2)
D_t	ploughing width of tuft (mm)
D_{th}	ploughing width of surface thread (mm)
E_t	tensile Young's modulus of infused tuft (N/mm^2)
h	composite half thickness (mm)
L	resin pocket length (mm)
l_s	length of debonded slip zone from delamination plane (mm)
P_n	resistance per unit length of surrounding composite against ploughing (N/mm)
s_t	tuft circumference (mm)
s_{th}	surface thread circumference (mm)
u_t	total crack opening displacement at Z-reinforcement (mm)
U	dissipated energy by single tuft bridging in pull-out (Nmm)
v_t	total crack shear displacement at Z-reinforcement (mm)
V	dissipated energy by single tuft bridging in shear (Nmm)
w	resin pocket width (mm)
z_0	length of deflected tuft Z-reinforcement from delamination plane (mm)

$\boldsymbol{F} = [F_1, F_3]$	bridging force vector of Z-reinforcement parallel and transverse to delamination plane (shear/opening) (N)
$\boldsymbol{u} = [u_1, u_3]$	displacement vector of beam half parallel and transverse to delamination plane (shear/opening) (mm)
$\boldsymbol{T} = [T_1, T_3]$	bridging traction vector of Z-reinforcement parallel and transverse to delamination plane (shear/opening) (N/mm^2)

ε	axial tensile strain of Z-reinforcement (mm/mm)
$\xi(z), \zeta(z)$	displacements along Z-reinforcement parallel and transverse to delamination plane (mm)
φ	initial orientation of Z-reinforcement relative to composite z-axis (°)
$\theta(z)$	local deflection from initial orientation of Z-reinforcement (°)
$\sigma_{t/n}$	axial tensile and normal compressive stress in Z-reinforcement (N/mm^2)
σ_c	compressive strength of surrounding laminate (N/mm^2)
$\tau_{i/e}$	initial/enhanced interfacial shear friction stress in straight and deflected zone of the Z-reinforcement (N/mm^2)

Publications

Edited versions of the following chapters have been submitted for publication:

Chapter 5 Johannes W.G. Treiber, Ivana K. Partridge, Characterising tufted carbon fabric/epoxy composites: I. Morphology, *Composites Part A: Applied Science and Manufacturing*, submitted.

Chapter 6 Johannes W.G. Treiber, Ivana K. Partridge, Characterising tufted carbon fabric/epoxy composites: II. In-plane tension, compression and shear, *Composites Part A: Applied Science and Manufacturing*, submitted.

Chapter 8 Johannes W.G. Treiber, Denis D.R. Cartié, Ivana K. Partridge, Delamination behaviour of tufted non-crimped carbon fibre fabric/epoxy composites, *Engineering Fracture Mechanics*, submitted.

Chapter 9 has been prepared as draft with the intent of submission for publication:

Chapter 9 Johannes W.G. Treiber, Ivana K. Partridge, Crack bridging laws of single tufts and Z-pins in carbon fabric/epoxy composites, *Composites Part A: Applied Science and Manufacturing*, Draft.

Chapter 1 Introduction

Over the last two decades an increasing number of studies have focused on the through-the-thickness reinforcement of dry fibre composite preforms prior to injection with liquid resin. While initially adopted from textile industry to ease handling of the otherwise relatively unstable preforms the potential of stitching to create a structural Z-directional reinforcement which inhibits delamination propagation as critical failure mode of conventional two dimensional composites was identified in the 1990s, leading to intensive studies on the out-of-plane property enhancement. With increasing size and volume of the composite structures, automation and subsequent modification of the conventional stitching towards one-sided reinforcement techniques was driven by aerospace manufacturers, resulting in the development of tufting within the last decade. The modified stitching technique, originally a method for carpet making, requires only single-sided access and inserts open thread loops into the composite preform without interlocking mechanism, by using the natural friction between the fabric and the tufting thread.

While aiming for improvement of out-of-plane properties of the composite the structural disturbance of the composite due to repeated insertion of a Z-reinforcement entity comes at the potential cost of changed in-plane mechanical properties. Insufficient documentation of the meso-structural changes associated with in- and out-of-plane mechanical property changes in stitched and Z-pinned composites have been pointed out in several reviews [1-3].

This thesis describes advances in the manufacturing and mechanical property characterisation of tufted carbon fabric/epoxy composites, with a focus on the relationship between tuft-induced meso-structural features and the failure modes under in- and out-of-plane loading. The aim of this study was to develop a material database to extend and complement the limited studies available on one-sided Z-reinforcement technologies. Development of suitable modelling tools for the prediction of the mechanical performance and failure mechanisms of tufted composites was also seen as a priority.

The current state of development of manufacturing technologies for Z-reinforcement of dry and pre-impregnated composite preforms with discrete or continuous through-the-thickness reinforcements is presented in Chapter 2, as an update on existing reviews and with focus on textile one-sided through-the-thickness insertion methods.

A detailed summary of materials chosen for this study is given in Chapter 3. Methodology and results of additional characterisation tests on the material constituents are included for completeness.

Chapter 4 to Chapter 9 build the scientific core of this study, of which Chapter 5, Chapter 6, Chapter 8 and Chapter 9 are edited versions of papers submitted for publication. As such, each chapter provides an introduction of the relevant scientific background, as well as a separate description of the manufacturing route of required test samples, discussion of the results and conclusions.

Chapter 4 presents the essential advances in the automated manufacturing process of tufting as developed and applied in this study. Identified and optimised critical parameters of successful tufting of dry carbon fabric preforms are detailed. The second part of the chapter gives a summary of the resin injection applied via vacuum assisted resin-transfer moulding, with equipment used and relevant process parameters.

Detailed meso-structural characterisation of various tufted carbon fabric composites, and corresponding changes to the in-plane tensile, compressive and shear mechanical performance are the subject of Chapter 5 and Chapter 6.

A parametric numerical model, based on a single tuft unit cell, is developed in Chapter 7. The model is shown capable of predicting the in-plane mechanical behaviour of tufted composites in relation to their identified unique morphological features.

The content of Chapter 8 complements previous chapters by establishing the potential of the tufting technique to improve the out-of-plane performance (delamination cracking resistance) of the same tufted composites, under mode I and mode II loadings.

Single tuft bridging experiments and their results are described in Chapter 9.

The overall discussion in Chapter 10 brings together the scientific advancements of this study to provide a broader picture of the balance of out-of-plane property enhancement with the inevitable knock-downs in the in-plane behaviour of this new class of composite.

Supplementary information is contained in a number of Appendices at the end of the thesis.

Chapter 2 Overview of manufacturing technologies for Z-reinforced composites

The following chapter gives an overview of published literature on manufacturing of through-the-thickness reinforced composites. Further relevant literature on in- and out-of-plane mechanical characterisation and performance, as well as analytical and numerical modelling approaches to predict the behaviour of Z-reinforced composites is presented at the beginning of each corresponding chapter of this work.

2.1 Introduction

A growing number of Z-reinforcement methods are available for both dry and pre-impregnated laminates which are integrated at different steps in the manufacturing process of fibre reinforced polymers. In general, it has to be distinguished between integral techniques, such as 3D knitting, 3D weaving or braiding, and insertion of the Z-reinforcement in a separate manufacturing step after the initial perform layup, such as structural stitching, Z-pinning or Z-anchoring. While the former are developed for the manufacture of large scale continuously 3D reinforced laminates showing their cost benefits mainly at higher production volume, the later are ideally suited for the localised Z-reinforcement of sections in the composite with high out-of-plane stress state [4]. As numerous reviews have described the insertion methods of the Z-reinforcements [5-10], in the following section only a short introduction will be given in the manufacturing of Z-reinforced composites with focus on its area of application and limitations.

2.2 3D weaving, braiding and knitting

Figure 2.1 shows the typical 3D fibre arrangements for knitted, braided and 3D woven laminates. In 3D weaving relatively straight warp and weft tows, which are limited in general to a 0°/90° orientation, are interlocked by less tensioned binder yarns, which can be inserted at variable angle through the thickness [8; 11]. In contrast to 3D weaving the overlapping tows of a braided preform can vary in braiding angle creating intricate closed or open preform shapes [4]. The curved fibre architecture of the fibre loops in

knitted composites makes the 3D preforms highly conformable and thus suitable for the manufacturing of complex shapes which require high drapability.

In order to control the complex fibre paths of the interlocking tows in all three manufacturing processes expensive and bulky machinery is required which currently is limited in the producible cross-section of the 3D preforms and which requires large part numbers to balance the investment costs.

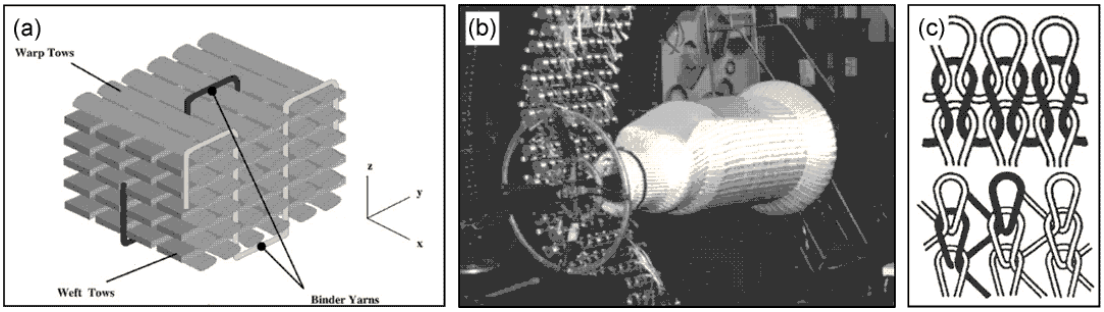

Figure 2.1 – Fibre arrangement for a) 3D woven [8; 11]**, b) 3D braided** [4]**, and c) knitted** [11; 12] **fabrics**

Yang et al. showed that the replacement of conventional T-stiffeners by 3D braided preforms reduces highly the strain concentration at the flange/web junction region which is normally filled by a noodle [13]. In general the integration of through-the-thickness tows improves the impact damage tolerance [14; 15] and increases the inter-laminar toughness of the integral 3D preforms, with the magnitude depending on type and density of the woven Z-binder [16]. However, fibre undulation within the load bearing fibre tows, which is required to accommodate the Z-reinforcing tows, abrasion damage by the weaving equipment [17] and low fibre volume fractions of less than 40% [18] appear to be the main source for reported reductions of in-plane stiffness and strength by up to 40% and 50% respectively compared to conventional 2D composites [3; 4; 10; 14].

Both 3D woven and braided parts find already application in a large number of aerospace structures, such as J-, C- or T-shaped stiffeners for multi-rib stiffened panels, components for Scramjet and rocket engines or rotor and stator blades [4]. By replacing the conventional stiffeners with 3D braided components in the Joint Strike fighter programme Lockheed Martin could eliminated up to 95% of conventional fasteners resulting in significant savings in weight and labour costs [4].

2.3 Z-pinning

Z-pins (also known under the brand-name Z-fibres™ of the original supplier Aztec Inc., now Albany International) are a through-the-thickness reinforcement designed for the insertion into uncured, pre-impregnated laminates (prepreg). Rigid Z-reinforcement rods of typically 0.1 – 1.0 mm diameter are supplied in a dual-density foam which ensures the equally spaced square pin arrangement and provides lateral support to the pins during the insertion process [5]. Initially, Z-pins were inserted into the laminate during resin cure in the autoclave using a metal caul plate and the typical vacuum bagging which applied pressure on the Z-pin preform and forced the rods into the laminate [19] (see Figure 2.2). However, insufficient control on the pin alignment and high tooling effort led to development of the ultrasonic insertion process, where the rigid pins are pushed into the laminate using either a hand-held or gantry based ultrasonically actuated horn with solid metal contact surface [20; 21]. The generated pressure waves in the horn push the pins into the laminate while moderately heating the surrounding resin which facilitates the process.

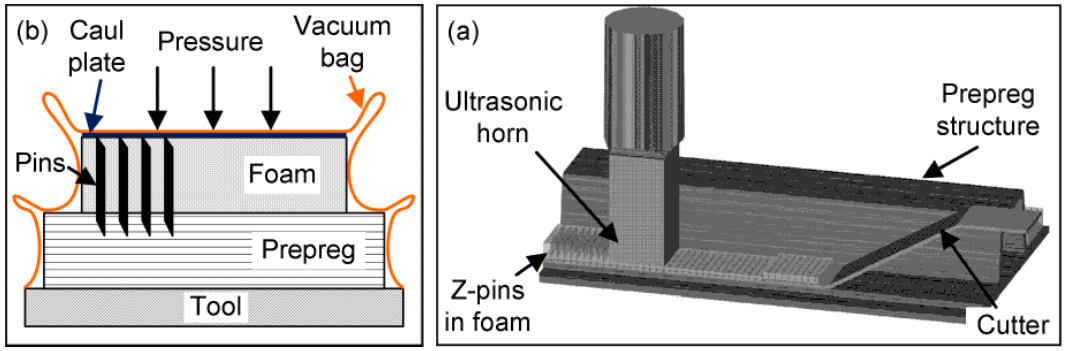

Figure 2.2 – Z-pinning technologies: (a) Insertion in autoclave – adapted from [19]**, (b) Hand-held ultrasonic horn** [5]

Each cured Z-pin is cut with 45° chamfer from a continuous rodstock, which is typically pultruded from T300 carbon fibre tows, impregnated with bismaleimide resin (BMI). The chamfer [22] is supposed to spread the fibres in the laminate during insertion to minimise fabric damage. Other high strength materials, such as titanium or stainless steel, and epoxy resin as matrix, have also been reported for Z-pins [19].

The used areal Z-pin densities, defined as the ratio of cured Z-pin cross-section area to product of Z-pin spacing along and parallel to the Z-pin rows, are most commonly in the range of 0.5% to 4% [5; 7; 19; 22-28]. In the majority of studies only orthogonal

insertion of the Z-pin to the laminate surface was investigate with the exception of Cartié et al [29] and Rugg et al. [30].

Collapsed foam and protruding Z-pin ends on the laminate surface are normally removed with a shear cutting tool or by abrasion [22; 31]. The required large number of manual process steps causes significant variability in the insertion angle and quality of the Z-pinning [22]. Currently, the use of Z-pins is mainly limited to military aerospace and Formula 1 [32] structures which are likely to fail in delamination. By replacing 4600 conventional fasteners with 0.28mm diameter Z-pins (0.6 pins/mm^2) to attach hat stiffeners onto the inlet duct of the F18 E/F fighter jet, substantial weight and cost savings of up to $83000 could be achieved [33]. Further efforts are made to reduce the cost intensive manual insertion process by automated Z-pinning equipment [34].

Besides the conventional Z-pinning of pre-impregnated laminates, Aztec Inc. developed two Z-reinforcement techniques for composite skin / foam core sandwich structures, also known as X-Core and K-Cor [20]. In the first step, partially cured Z-pins are inserted orthogonally or with angle into a closed cell foam core. Subsequently, the protruding pin ends are either flattened onto the foam surface in a thermal press (K-Cor) or left to protrude through the applied laminate skin (X-Cor) prior to cure of the final assembly [35]. By reinforcing the foam and foam/skin interface with stiff carbon rods high improvements on the out-of-plane and shear stiffness of the sandwich structure have been reported [36; 37].

2.4 Stitching

In the 1980s initially the textile sewing technique stitching was applied to pre-impregnated laminates in an attempt to increase the damage tolerance and fracture mechanical properties of the composite [38; 39]. Driven by the need for high manufacturing quality and reproducibility in aerospace industry and by advances in the resin transfer process Boeing Corporation and NASA Langley Research Centre for Aerospace Structures developed an automated structural stitching process in the joint Advanced Composite Technology (ACT) program to join dry fabric stringers to wing skin preforms of up to 12 m length and 38 mm thickness at 3200 stitches per minute [40] (see Figure 2.3).

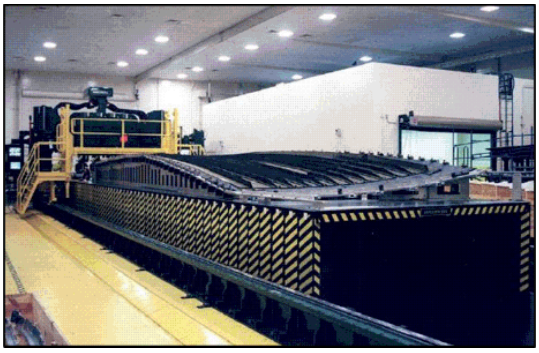

Figure 2.3 – Computer controlled Advanced Stitching Machine (ASM), developed by NASA and Boeing [41]

While non-structural stitching aims mainly for improved handling of the dry fibre preform by joining a limited number of plies with thin thermoplastic threads at low density [10; 42] high tensile strengths yarns from glass, carbon or aramid [2; 38] are inserted in the structural stitching process through the total laminate thickness to improve its interlaminar fracture toughness in mode I and mode II, stitched joint strength [43] and impact damage tolerance. In the majority of structurally stitched composites threads of linear weight between 16 and 400 g/km [44; 45] have been inserted orthogonally into the composite at 2 mm to 20 mm spacing, resulting in an areal Z-reinforcement fraction of 0.5% to 10% [3]. Very limited number of studies investigated the effect of angled stitch insertion [46].

In conventional lock stitching two threads (needle and bobbin thread) are interlocked within the laminate. The modified lock and chain stitch evolved from the basic lock stitch pattern in order to reduce the fabric disruption by the presence of the thread knot [6; 47]. While in chain stitching loops of a single thread are interlocking on the surface, the knot position of two joined threads in the modified lock stitching is simply shifted to the laminate surface by varying the tension between needle and bobbin threads.

As summarised by Klopp et al. [48], the mechanical performance of stitched composites highly depends on a large number of process parameter, which are: thread tension, fabric compaction by the stitching equipment, fabric compaction by stitching yarn, type of stitching needles, stitching thread (size, stiffness, strength), textile preform (fabric thickness, draping) and stitching process parameters (speed, stitching pattern). While stitching improves the handling of dry fabric preforms, it potentially affects further manufacturing steps such as preform drapability [41] and resin impregnation [49; 50]. To increase the versatility of stitching as localised Z-reinforcement technique current

stitching machines are no longer as immobile as NASA's original ASM, but are part of a complete production line with interchangeable small stitching heads mounted onto multi-joint robot arms (see Figure 2.4).

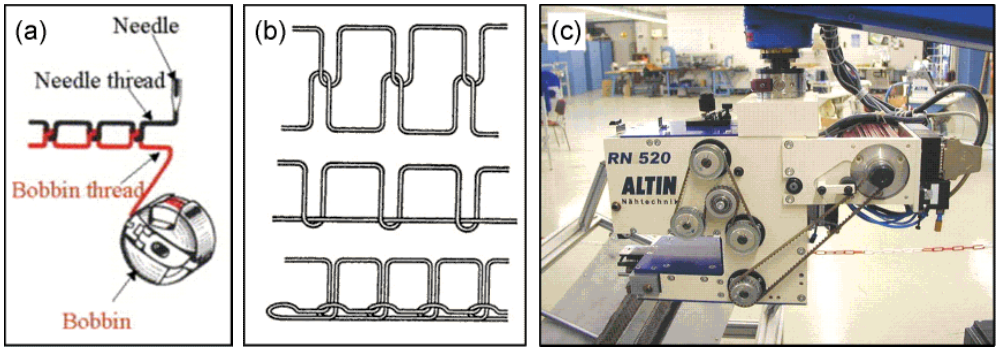

Figure 2.4 – Conventional stitching: a) principle of lock stitching [51]**, b) typical lock, modified lock and chain stitching (from top to bottom)** [47]**, c) robot-mounted double lock stitching head** [9]

Mouritz et al and Bannister give an extensive overview of typical applications of stitching, braiding and 3D weaving of structural composites which are made from dry fibre preforms and infused with resin after formation of the 3D reinforced preform [4; 8]. Zhao et al found structural stitching of composites with thermoplastic polypropylene matrix to improve its impact toughness and in-plane strength [52; 53]. By through-thickness reinforcement of dry laminate skin to foam core sandwich structures Potluri et al found the out-of-plane stiffness and energy absorption under impact of the sandwich structure to improve [52-54].

2.4.1 Single-sided stitching

In order to overcome restrictions in application of the conventional stitching methods due to part dimensions and required location for reinforcement several one-sided stitching methods have been developed. The two-needle ITA (institute of textiles, university RWTH Aachen) and one-sided (OSS®) stitching, curved needle blind stitching and single needle tufting are all integrated in small-size mechanical units which can be attached to multi-joint robot arms to ensure precision, versatility and application of the single-sided stitching into an automated manufacturing processes. Table 2.1 gives an overview of the typical maximum speed, depth and spacing of the different types of single-sided stitching.

Table 2.1 - Typical process parameters of single-sided stitching and tufting

		ITA [55]	OSS [56]	Blind [57]	Tufting [57]
Speed	min^{-1}	2 x 700	500	500	500
Max. laminate thickness	mm	5 (– 8)	20	10	40
Stitch spacing	mm	3 - 7	2 - 10	5 - 10	2 - 10

The one-sided sewing technique in Figure 2.5 a, developed by the institute for textiles (ITA) of the university RWTH Aachen, interlocks two threads in a chain stitch pattern by two 45° inclined needles, as shown in the schematic of Figure 2.5 b [48]. Each needle assumes the task of both inserting a thread loop and catching alternately the thread loop of the other stitching needle with stitch interlock on the opposing preform surface. While increasing deflection of the inclined needles within the fabric preform limits the technology to laminates of maximal 8 mm thickness, the current design allows for a relatively high speed of up to 1400 stitches per minute [55].

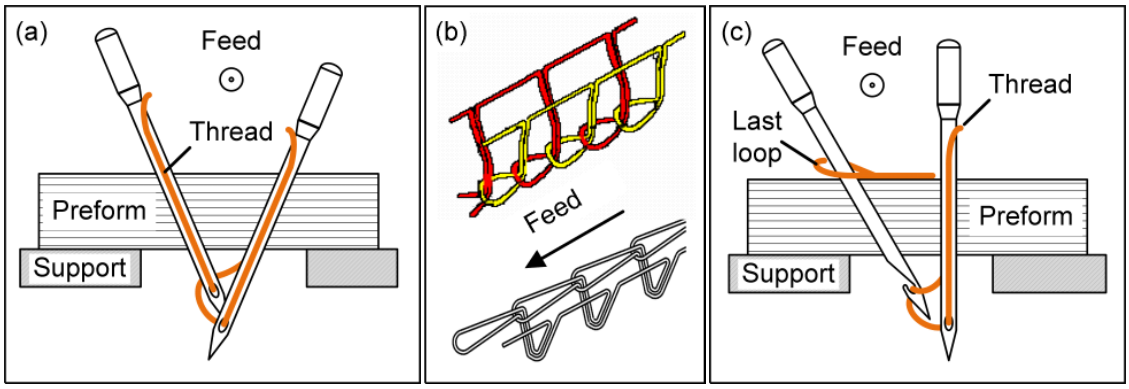

Figure 2.5 – a) ITA one-sided sewing principle – adapted from [48]**, b) typical thread path of ITA (top) and OSS (bottom)** [55; 56]**, c) one-sided stitching principle – adapted from** [58]

The one-sided stitching (OSS®) technique of Figure 2.5 c, initially developed by Altin Nähtechnik GmbH, is based on a modified chain stitching pattern of a single thread which is introduced into the dry laminate preform by two needles. The vertical needle inserts the thread loop which is caught and retracted by a 45° inclined hook needle and interlocked with the previous thread loop on the composite surface (see Figure 2.5 c). The specific design and independence between feed rate and needle mechanism allow for variable stitch spacing and close stitching to structural components such as stringers on the fabric preform [56].

In the blind stitching technique of Keilmann Sondermaschinenbau GmbH (KSL) dry fabric layers are joined by a curved needle of 50 mm radius which inserts a single thread loop in a curved trajectory with needle entry and exit on the same preform surface. The loop end is caught by a separate hook mechanism and interlocked with the previous thread loop in a modified chain stitch pattern on the preform surface (see Figure 2.6 a) [57].

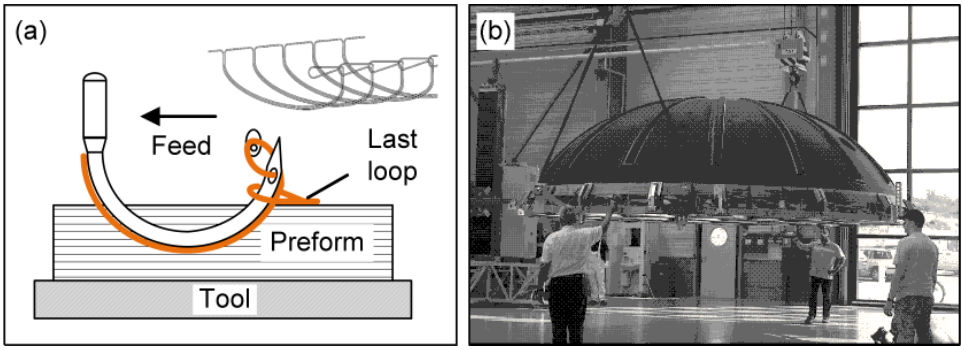

Figure 2.6 – a) Blind stitching principle – adapted from [59]**, b) application on rear pressure bulkhead of commercial airplane A380** [60]

In the single-sided tufting process, developed by the German Aerospace Centre (DRL) in corporation with the industrial partners EADS and Keilmann Sondermaschinenbau GmbH (KSL) (see Figure 2.7 a and c), a specially designed needle with inclined needle eye enables the insertion of thread loops into the dry preform without the conventional interlocking between thread loops. The thread loops remain within the dry preform by friction between thread and the surrounding fabric layers. Hence, tufted preforms require careful handling prior to infusion with resin.

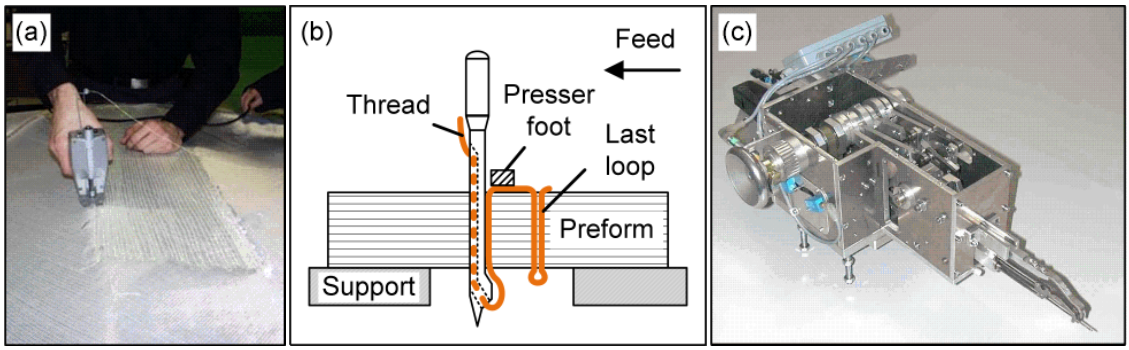

Figure 2.7 – a) Original tufting trials at DLR with modified jig saw [57]**, b) tufting schematic, c) early tufting head design for use with CNC machine** [61]

Depending on the needle penetration depth, tuft loops either protrude from the preform surface or end as blind stitch within the laminate. A foot element secures the already

inserted loops from pull-out during subsequent needle penetration (see Figure 2.7 b) [56]. In comparison to the other single-sided stitching techniques the simple tufting mechanism and compact tufting head design allow maximum variability in stitch spacing, seam radius, insertion angle (45° - 135°) and preform thickness (see Table 2.1).

Both the one-sided stitching and sewing techniques require a support structure with free space under the penetrating needles. In contrast, blind stitching and tufting have the potential to be applied to preforms which are already placed in a rigid mould tool as a full penetration of the fabric preform is not necessary for the stitch formation [58].

While the application of the two-needle stitching techniques has been primarily subject of scientific research [62-65], blind stitching is already used on industrial scale to join several non-crimped fabric layers into dry preforms of up to eight metre width for manufacturing of the rear pressure bulkhead for the commercial passenger aircraft A380, from Airbus (see Figure 2.6 b) [60]. Furthermore, the research project AutoPreform analysed the requirements to integrate blind stitching into the automated manufacturing process of an automotive roof structure [66].

On industrial level, tufting is successfully used in the production of automotive crash structures to join I-stiffeners to a braided oval crash tube in order to enhance its energy dissipation during impact [67]. Furthermore, Laourine used tufting on a complex three-dimensional composite structure of an undercarriage demonstrator where ITA one-sided sewing could not be applied due to spatial restrictions [65]. In aerospace research, tufting has been applied on demonstrator level to attach T- and J-stiffeners to composite skins, resulting in threefold increase in maximum load bearing capability before failure, although tufting performed worse than other single-sided stitching techniques [57; 68; 69]. Stickler et al. used the unique feature of partial tuft insertion to connect a novel T-shaped composite butt joint [70-74].

Henao et al. investigated experimentally and numerically the joining of skin to foam sandwich structures by tufting with glass and carbon threads. Tufting yielded significant increase in energy absorption and strength of up to 110% during edgewise compression and flexural bending of the Z-reinforced sandwich structure [75].

While the majority of research projects focus on the Z-reinforcement of relatively thin composite structures, Havar used tufting to Z-reinforce carbon fibre composite hinges of up to 56 mm thickness. Especially for out-of-plane loading, significant improvement in

static strength could be observed and repeated by numerical simulation for different designs of the force introducing loops which are used for the actuation of miniature trailing edge devices [65; 76].

Several projects in the author's laboratory at Cranfield University involved the structural application of tufting for reinforcement of T-, Pi- and omega stiffener-to-skin joints with thin laminate thickness [77-81].

Chapter 3 Material characterisation

The following chapter details the selected materials for the manufacturing of tufted composite specimens and structures in this work.

Basic material properties are summarised as required for the study. Where required, standardised tests were performed to complement and verify the manufacturers' data. In case of discrepancy between the measured and stated material properties, the experimentally determined properties were used as the preferred set for following analyses.

For safe storage, handling and disposal of all materials it is referred to the manufacturers' safety data sheets and existing operation procedures.

3.1 Fibres and fabrics

3.1.1 Reinforcement fibres

Table 3.1 summarises the basic properties of filaments, as stated by the manufacturers, which are included in dry fabrics and tufting threads of this work. The aligned ultra-long carbon filaments are processed as bundles (tows), consisting of 1000 (1k) to 24000 (24k) filaments each. The tow size of glass and aramid filaments is not standardised and is varied by the manufacturer depending on the area of application.

Table 3.1 – Reinforcement fibres - properties

Fibre type		HTA 40	HTS 40	Grafil 34-700	Kevlar® 29	EC9 68 Z28
Material	-	PAN-carbon	PAN-carbon	PAN-carbon	Para-aramid	E-glass
Manufacturer	-	Toho Tenax	Toho Tenax	Grafil	DuPont®	Saint Gobain
Filament diameter	µm	7	7	7	12	9
Density	g/cm^3	1.76	1.77	1.80	1.44	2.6
Tensile modulus	GPa	238	240	234	70.5	73
Tensile tow strength	MPa	3950	4300	4830	2920	2400
Elongation at break	%	1.7	1.8	2.0	3.6	4.5
Thermal expansion	$10^{-6}/°C$	-0.1	-0.1	0.5	-1.2	5.3

HTA, HTS and Grafil carbon filaments are aerospace qualified high and higher strength fibres with high strength- and stiffness-to-density ratio and minimal thermal expansion. Aramid fibres exhibit the lowest density of the given fibre types with maximum elongation, but are disadvantageous in processing and sensitive to degradation under ultraviolet radiation and moisture absorption.

Standardised density measurements were performed to confirm the filament density for the two types of carbon fibre which are processed in the fabrics of section 3.1.2, using the liquid-displacement method according to BS ISO 10119:2002. Single carbon fibre tows were extracted at different positions from each fabric.

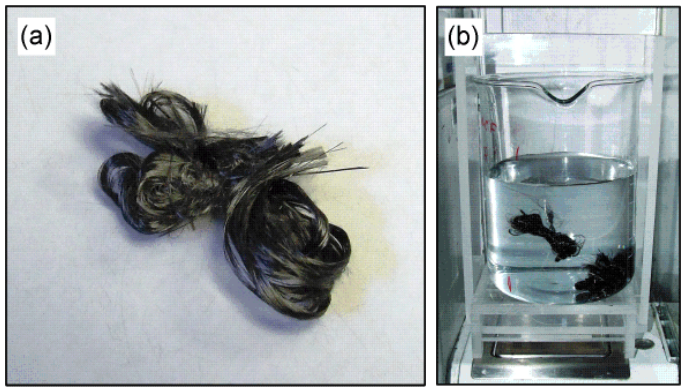

Figure 3.1 – Fibre density measurement: (a) dry fibre sample, (b) sample immersed in distilled water on Mettler AT 460 DeltaRange precision scale

Prior to weighing, the samples were immersed and washed repeatedly in acetone to remove any fibre seizing and were dried for one hour at 70°C. Three samples of 0.5 to 1.5 grams were cut from each tow bundle and bound into loose knots. Distilled water of known density was used as immersion liquid. To avoid additional buoyancy by entrapped air bubbles in the filament samples, each immersed sample was degassed twice for 10 minutes in a vacuum chamber at 20 mbar, followed by ultrasonic agitation for 1 minute. Table 3.2 summarises the measured densities, calculated from the difference between dry and immersed specimen weight, which was measured to 0.1 mg precision on a Mettler AT 460 Deltarange precision scale.

Table 3.2 – Measured filament densities (Std.dev. in brackets)

Average property		HTS 40	Grafil 34-700
Density	g/cm^3	1.769 (±0.004)	1.786 (±0.007)

The density for HTS 40 filaments, as stated by the manufacturer, was confirmed by the experiment. Due to a significant deviation of density for the Grafil 34-700 filaments,

fibre volume fraction calculations for the infused composite panels in this work were based on the measured density of 1.786 g/cm^3 instead of the manufacturer's value of 1.8 g/cm^3.

3.1.2 Fabric types

In order to investigate the influence of tufting on a broad range of aerospace grade carbon fabrics, four types of dry fabric were chosen, as detailed in Table 3.3. Several procedures exist to infuse dry fibre preform with liquid resin to manufacture fibre reinforced parts, such as resin film infusion, resin vacuum infusion or resin transfer moulding. In this work vacuum assisted resin transfer moulding was chosen as manufacturing route, as explained in detail in chapter 4.2.

Table 3.3 – Fabric properties

Fabric type		Uni-weave	2x2 Twill	Biaxial NCF 0°/90°, ±45°	Biaxial NCF ±45°
Specification	-	R300/10C	RE650C	MC90-41270 MC90-31270	CBX 440
Manufacturer	-	OCV™	OCV™	Sigmatex	OCV™
Areal weight	g/m^2	310	650	1010	440
Weight ratio (warp/weft/stitch)	%	97/3/-	50/50/-	49/49/1	49/49/1
Fibre type (warp/weft)	-	Grafil 34-700/ Hotmelt[1]	Grafil 34-700	HTS40	HTS40
Fibre type (stitch)	-	-	-	Polyester	Polyester
Stitch pattern	-	-	-	hybrid/chain	chain
Filaments per tow	-	12000	12000	24000	12000

A uni-weave fabric with thermoplastic weft yarn was preferred over unidirectional tapes for manufacturing of unidirectional test specimens due to its loose weave style which is preferred for tufting. The thermoplastic hotmelt weft yarn is intended to improve handling and stability of the uni-weave fabric and can be activated at temperatures above 70°C, as confirmed by a DSC test on hotmelt samples. However, void creation was observed during high temperature post-cure of infused panels due to the insolubility of the thermoplastic into the surrounding epoxy matrix. Such voids have the potential to reduce in-plane mechanical performance of the unidirectional composite and to act as crack initiators.

[1] Hotmelt weft yarn composed of glass filaments and polyamide based binder

The biaxial non-crimp fabrics (NCF) of different areal weight allow easy lay-up with high fabric stability and minimal crimp, only caused by the non-structural thermoplastic stitching threads. The heavy weight non-crimp fabric, supplied by Sigmatex, was chosen in 0°/90° and ±45° configuration to avoid asymmetry effects in the fabric layup due to varying direction of the non-structural stitching seams.

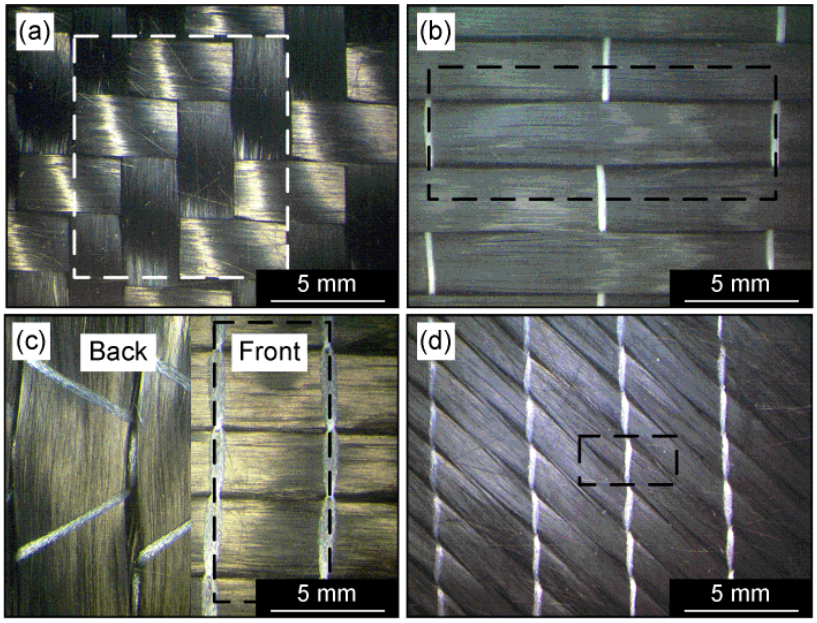

Figure 3.2 – Dry fabrics: (a) twill , (b) uni-weave, (c) 0°/90° Sigmatex NCF (top and bottom view), (d) ±45° OCV NCF – typical fabric unit cells marked by dashed line

The woven fabric with twill weave pattern was chosen to investigate the influence of initial fabric crimp, caused by the weave style, against possible crimp effects caused by tufting. Dell'Anno found that such fabric weave might mask the effect of tuft insertion on the in-plane performance of the laminate [82].

Figure 3.2 illustrates the four types of dry fabric with its typical fabric unit cells. The tricot stitching pattern on the back of the 0°/90° non-crimp fabric causes repetitive warp in the dry weft carbon tows which persisted even in the infused panels. To enable a clear distinction between the effects of fibre waviness caused by tufting and by non-structural stitching, the front layer made of straight warp tows was always chosen as the load-bearing 0° layer.

Table 3.4 summarises the typical width and length of unit cells, the tow width in warp and weft direction and the width of the stitching yarn for each fabric. The fabric unit cell is important for the selection of test specimen dimensions [83] as local variations in

the mechanical response could affect the measured response by choosing too small sample sizes.

Table 3.4 –Measured fabric unit cell dimensions (Std.dev. in brackets)

Aver. (St.dev.)		Uni-weave	2x2 Twill	Sigmatex NCF 0°/90°	Sigmatex NCF ±45°	OCV NCF ±45°
Unit cell width	mm	5.7 (0.0)	9.9 (0.1)	5.2 (0.2)	3.1 (0.1)	2.1 (0.1)
Unit cell length	mm	15.4 (0.1)	10.9 (0.1)	13.7 (0.3)	5.9 (0.1)	4.3 (0.1)
Warp tow width	mm	2.7 (0.1)	2.6 (0.1)	3.4 (0.3)	2.4 (0.2)	1.3 (0.1)
Weft tow width	mm	-	2.6 (0.1)	5.2 (0.2)	2.4 (0.2)	1.3 (0.1)
Stitch yarn width	mm	0.3 (0.2)	-	0.5 (0.1)	0.6 (0.1)	0.3 (0.1)

The theoretical fibre volume fraction of each fibre reinforced panel was determined based on the number of dry fabric layers n, the dry carbon fabric weight per unit area $\rho_{A,f}$, the density of the carbon fibre ρ_f and the final panel thickness t, as described in equation 3-1.

$$V_f(\%) = \frac{n \cdot \rho_{A,f}}{\rho_f \cdot t} \qquad \textbf{3-1}$$

The combined areal weight of carbon fibre tows $\rho_{A,f}$ and non-structural stitching yarn $\rho_{A,s}$ results the total weight per unit area $\rho_{A,total}$ for each type of dry carbon fabric. The total weight per unit area was verified for each selected fabric by measuring the weight of at least three samples, each with a minimum area of 200 mm by 200 mm, following BS ISO 3374:2000. The measured areal weight values are within the manufacturers' tolerances. Hence, the values, as stated by the manufacturers, were used for further design and dimensioning of test panels.

3.2 Tufting threads

During the tufting operation, which is explained in detail in chapter 4.1, the tufting thread has to withstand high mechanical wear caused by the sharp bending radius in the needle eye and friction along the surrounding dry fabric. Dell'Anno [82] found that the ideal tufting thread features several yarns which are twisted together with high twist exceeding 260 turns per meter. The twist compacts the yarns and forms it into a uniform, quasi-circular cross-section which reduces snagging of the thread in needle eye and thread feeding mechanisms at high manufacturing rate [47]. Other critical parame-

ters for the thread selection are compatibility with the selected resin system, impregnation behaviour and suitability for the automated manufacturing process [44]. The tufting thread has to fit through the currently available tufting needles, which have a needle eye diameter of 0.68 mm to 1.0 mm. Based on these limitations, four different threads were selected for tufting in this work, as summarised in Table 3.5.

The carbon (2k filaments), aramid and glass threads feature a comparable dry cross-section to enable a direct comparison of performance of the different thread materials, which are common for the structural stitching process in aerospace applications [38; 45]. Additionally, a stretch-broken carbon fibre thread (SBCF) of smaller diameter (1.2k filaments) was chosen to investigate the influence of thread size. Figure 3.3 a) illustrates the selected dry threads in this work.

Table 3.5 – Types of tufting threads

Thread type		Carbon	Carbon SBCF	Aramid	Glass
Thread specification	-	Tenax® Carbon	Nm25/2 Carbon	Kevlar® Tkt 30	EC9 68x3 S260
Fibre	-	HTA40	HTA40	Kevlar® 29	EC9 68 Z28
Manufacturer	-	Schappe Techniques®	Schappe Techniques®	Somac Threads	Saint Gobain Vetrotex
Linear weight	g/km	140	80	92	204
Filament count	-	2 x 1000	2 x 590	4 x 134	3 x 411
Dry cross-section area	mm^2	0.077	0.045	0.065	0.078

Tufting trials with a thread blend of carbon and polyamide, consisting of a single carbon yarn (1k tow) twisted together with a single polyamide yarn (68% carbon : 32% polyamide 12), supplied by Schappe Techniques®, were successful. However, from further use of the material combination was refrained due to reduced performance of the thread under tension caused by the unsymmetrical spinning of the two yarn materials.

3.2.1 Verification of thread properties

As the study on stitching by Morales [47] showed, the strength of dry carbon, glass and aramid threads reduces significantly with twist, which is most pronounced for carbon threads with a drop in strength of 56% for a twist count of 350 twists per meter. Limited information on the mechanical parameters of the selected thread types of this study, partially due to on-going thread development [45], required a number of characterisation tests which were performed on dry and infused thread rodstock to determine its

potential mechanical performance. A summary of the thread characterisation results is given in Table 3.6.

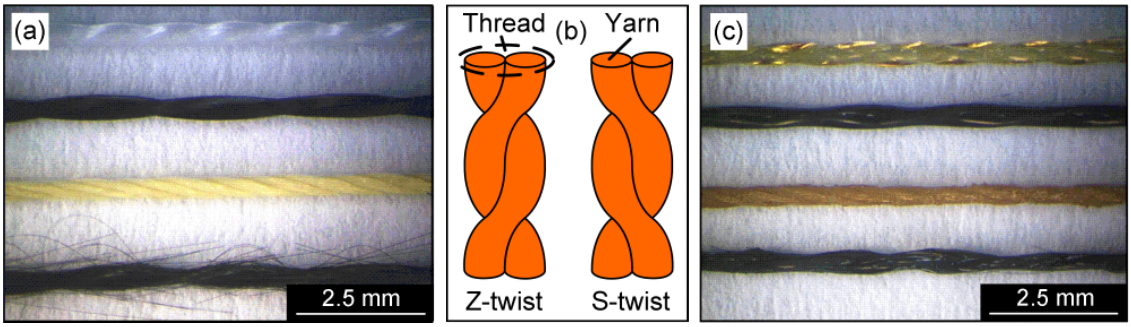

Figure 3.3 – a) Dry thread and c) resin infused thread rodstock of glass, carbon, aramid and stretch broken carbon (from top to bottom); (b) thread morphology

At least five dry thread samples of one meter length (±1 mm) were cut from each bobbin to measure thread twist and dry thread diameter according to BS EN ISO 1890 and DIN 53811 respectively. Prior to cutting, thread ends were secured with tape to inhibit unwinding of the twisted yarns. Each sample was cut and tested under a pretension of 0.25 cN/tex. A travelling optical microscope was used to measure the dry diameter at 8 arbitrary locations along each thread. The low number of yarns in the carbon thread causes significant variation in thread diameter, depending on the location and angle of view on the twist pattern (see Figure 3.3 a)). The twist direction, i.e. S- or Z-twist as defined in Figure 3.3 b), and number of turns per meter were determined for each type of thread and its yarn components by a manual winding tool.

The linear weight of each thread type was confirmed by measuring the weight of at least three thread samples of five meter length on the precision scale Mettler AT 460 Delta-Range (to 0.1 mg). Prior to weighing, sizing on the fibres was removed by soaking the samples in the solvent methyl-ethyl-ketone (MEK) for 48 hours. Subsequently, each sample was dried at 105°C for two hours and conditioned in standard atmosphere.

The tensile strength and modulus of the dry thread was determined by loading at least ten thread samples on the universal test machine Zwick Z010 with 2kN load cell at a constant cross-head speed of 5 mm per minute, according to BS ISO 3341:2000. Rope grips, as illustrated in Figure 3.4 a), ensured thread failure within the 300 mm gauge length. The true strain was measured with the laser extensometer EIR LE-05. The tensile dry modulus was calculated from the stress to strain ratio between 0.1% and 0.6% tensile strain.

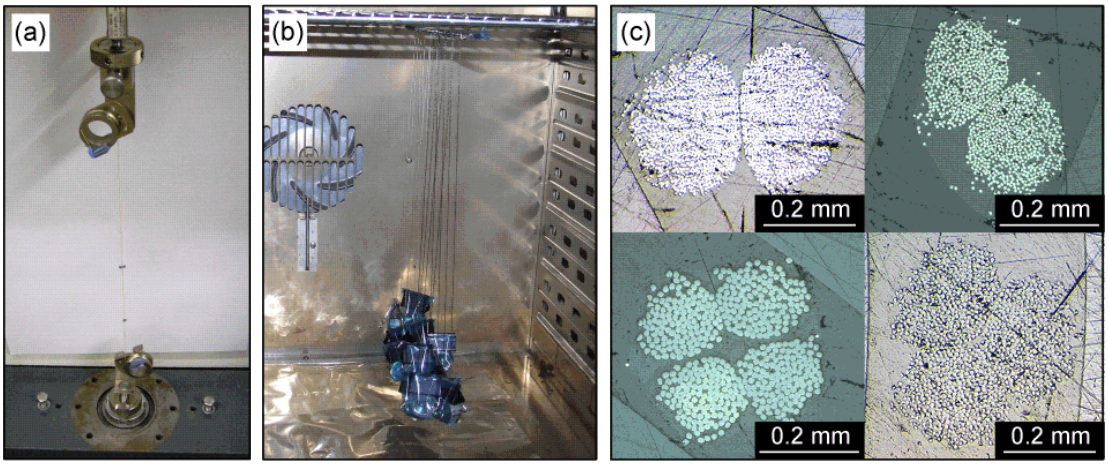

Figure 3.4 – Thread characterisation: a) dry thread tensile test, b) curing of infused thread under pretension, c) thread rodstock cross-section: carbon (top left), carbon stretch (top right), aramid (bottom left), glass (bottom right)

In order to measure the impregnated thread strength and modulus, at least six samples of 250 mm long thread rodstock for each thread type were manufactured by immersing dry thread samples in 30g of MVR 444 epoxy resin at 80°C for 30 minutes, following the recommended process of BS EN ISO 10618:2004. To improve wetting, the immersion process was halted after 15 minutes to degas the resin in a vacuum chamber at 10 mbar pressure for 10 minutes. After complete impregnation, each sample was manually cleaned from excess resin before suspending and curing it in a circulation oven according to the cure cycle of Figure 3.6. Each rodstock was pre-tensioned with 0.25 cN/tex during cure by attaching metal weights (see Figure 3.4 b)). The described manufacturing procedure ensured a resin droplet free impregnation with the resin weight content between 19% and 27%.

To avoid local failure within the grips under tension, each sample was tabbed with eight layers of 50 mm x 25 mm textile Hexply® 913 glass prepreg, supplied by Hexcel®, prior to testing. Tensile tests were performed with a constant cross-head speed of 1.0 mm per minute on the universal test machine Instron 5500R with 5kN load cell. Strain was measured by the aforementioned laser extensometer. Infused tensile strength and modulus are calculated as ratio of load divided by the dry cross-section of the thread, according to the test standard. The tensile modulus is determined between 0.1% and 0.6% tensile strain.

The diameter, count of filaments and linear weight for glass, carbon and aramid thread lie within the manufacturers' tolerances. The high twist of each thread, even if preferred

for the tufting process, causes significant reduction of its dry material strength and modulus compared to the filament data of Table 3.1, confirming the observations by Morales [47]. Aramid performs best with only 25% and 31% drop in modulus and strength respectively, indicating a low susceptibility to failure caused by local twist and helical orientation of the filaments. This attribute makes it an ideal thread material for the tufting process. Both carbon and glass threads show high reduction in the dry tensile strength of up to 55%. However, resin impregnation of the threads resulted in only small reduction of strength and modulus compared to the dry filament properties of up to 5% to 15% due to better load distribution between the yarn filaments. Hence, for the selection of the ideal thread material both dry properties for the manufacturing process and infused properties for the mechanical performance in the tufted material have to be investigated.

Table 3.6 – Measured properties of tufting threads (Std.dev. in brackets)

Average property (St. dev)		Carbon	Carbon SBCF	Aramid	Glass
Filament diameter	µm	7.2 (0.4)	7.2 (0.4)	13.8 (1.1)	9.4 (0.9)
Filament count	-	1974 (10)	1071 (16)	536 (2)	1194 (6)
Thread diameter (dry)	mm	0.42 (0.11)	0.33 (0.09)	0.40 (0.03)	0.47 (0.01)
Twist thread (S-/Z-direction)	m^{-1}	S 190 (11)	S 210 (12)	Z 315 (6)	S 253 (3)
Twist yarns (S-/Z-direction)	m^{-1}	Z 237 (3)	Z 316 (20)	S 445 (10)	Z 287 (1)
Linear weight (dry)	g/km	136 (0.5)	80.5 (0.3)	94.3 (0.1)	205 (0.3)
Tensile modulus (dry)	GPa	195 (9)	163 (15)	53 (6)	53 (4)
Tensile strength (dry)	MPa	1848 (81)	1776 (117)	2018 (83)	1319 (45)
Ultimate strain (dry)	%	0.9 (0.05)	1.1 (0.1)	2.9 (0.2)	2.1 (0.3)
Impregnated cross-section area	mm^2	0.121 (0.006)	0.062 (0.003)	0.096 (0.001)	0.130 (0.005)
Tensile modulus (impregnated)	GPa	199 (10)	200 (22)	72 (5)	70 (2)
Tensile strength (impregnated)	MPa	3544 (72)	3721 (359)	2409 (54)	2382 (39)
Ultimate strain (impregnated)	%	1.7 (0.1)	1.7 (0.1)	2.8 (0.1)	3.6 (0.1)
Resin weight content	%	27	19	27	23

3.3 Z-pin rodstock

In this study, 0.51 mm diameter Z-pins (Batch #71265) are used, manufactured from 3k T300 carbon fibre tows and bismaleimide resin, provided by Albany International. For commercially available Z-pin rodstock the selected pin diameter is closest to the selected carbon and glass tufting threads, featuring a dry cross-sectional area of 0.113 mm^2. Single Z-pins were extracted from the support foam for the process of manual insertion into dry fabric (see Chapter 9).

Table 3.7 – Measured Z-pin cross-section parameters (Std.dev. in brackets)

Average property (St. dev)		0.51 mm Z-pin
Impregnated diameter	mm	0.53 (0.02)
Impregnated cross-section area	mm^2	0.221 (0.026)
Calculated fibre volume content	%	51.6 (0.2)
Tensile strength	MPa	3099 (460)
Tensile modulus	GPa	217 (19)
Tensile strain at failure	%	1.3 (0.2)

For mechanical characterisation, micrographs of the cross-section of six Z-pins were taken to confirm its shape and infused cross-sectional area. Furthermore, tensile tests were performed on at least five rodstock specimens of 250 mm length following the same procedure as for the impregnated tufting thread. Table 3.7 summarises the measured average diameter, cross-sectional area, calculated fibre volume content and mechanical properties of the analysed Z-pins. The fibre volume fraction is based on the ratio of theoretical dry fibre to infused rodstock cross-sectional area. Tensile modulus and strength were normalised against the dry fibre cross-sectional area.

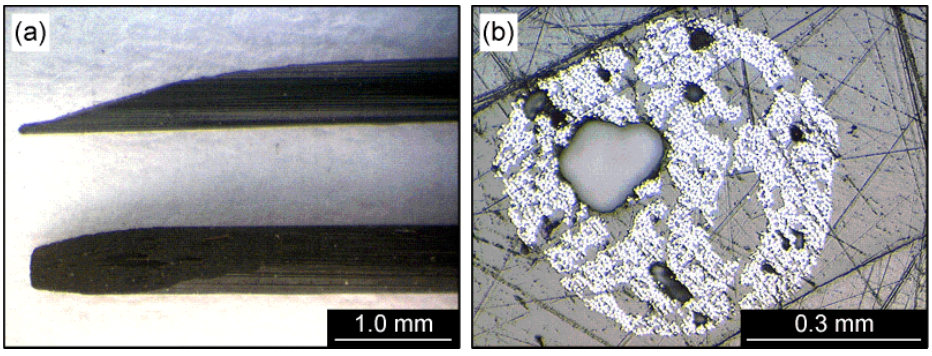

Figure 3.5 – T300/BMI 0.51mm diameter Z-pin: a) Rodstock with chamfer, b) Cross-section with voids

Due to the high processing temperature of the BMI resin, the cured Z-pin is not changing shape during cure of the hosting epoxy resin composite. Hence, the local fibre volume fraction and circumference of the rodstock should not be changed by the surrounding composite. Micrographs of the Z-pin cross-section revealed large voids and dry sections in all analysed rodstock samples, indicating insufficient wetting of the rodstock with BMI resin prior to pultrusion, as illustrated in Figure 3.5 b). While showing only small reduction in tensile modulus and strength under axial tension such voids potentially reduce the bending and shear performance of the pin.

3.4 Resin

All dry fabrics were infused via the resin transfer moulding process with the aerospace grade, single component epoxy resin MVR 444, supplied by Advanced Composites Group. The un-toughened epoxy resin was chosen due to its low infusion temperature of only 70°C, high performance before and after hot/wet conditioning, low viscosity at higher temperatures and a pot life of 5 hours at 70°C. Table 3.8 summarises the neat resin properties for MVR 444, as stated by the manufacturer.

Table 3.8 – Neat resin properties

Resin		ACG MVR 444
Cured resin density	g/cm^3	1.14
Glass transition temperature (T_g)	°C	DMA 190
Compression modulus	GPa	2.2
Compression yield strength	MPa	146
Compression yield strain	%	13.5
Tensile modulus	GPa	3.1
Tensile strength	MPa	77.6
Tensile strain	%	4.0
Poisson's ratio	-	0.35
Fracture toughness G_c	J/m^2	300
Initial viscosity at 80°C	mPa·s	105

As resin and hardener are already premixed the resin system has to be stored at -18°C to achieve a storage life of 12 months. Care has to be taken while defrosting the resin to avoid contamination with condensing water. MVR 444 can be cured at temperatures as low as 90°C. The detailed resin injection parameters for the manufacturing of tufted

composite panels via resin transfer moulding for this work are summarised in chapter 4.2.2.

3.4.1 Verification of neat resin properties

As glass transition temperature and related material properties of neat resin depend on the chosen cure cycle a set of mechanical and thermo-analytical characterisation test were performed on neat resin samples which were manufactured by resin transfer moulding according to the procedure of chapter 4.2.2.

Three samples of five milligrams uncured epoxy resin were cured following the defined curing cycle according to Figure 3.6 in a TA Instruments Q200 differential scanning calorimeter (DSC) to monitor the state of cure. Directly after completion of each cycle, a modulated DSC analysis was performed between 150°C and 210°C with a ramp rate of 1°C per minute to determine the as-cured glass transition temperature of the neat resin, according to BS EN ISO 11357:2009. Additionally, three dried samples of cured resin were tested in a TA Q800 dynamic mechanical analyser (DMA) between 150°C and 250°C with a ramp rate of 1°C per minute and oscillation frequency of 1 Hz, following the draft version of BS ISO 6721-11. Each resin sample was cut to the size of 17 mm x 4 mm x 1.8 mm for single cantilever test setup. The tangent intercept, also known as the onset temperature, of the drop in storage modulus was determined.

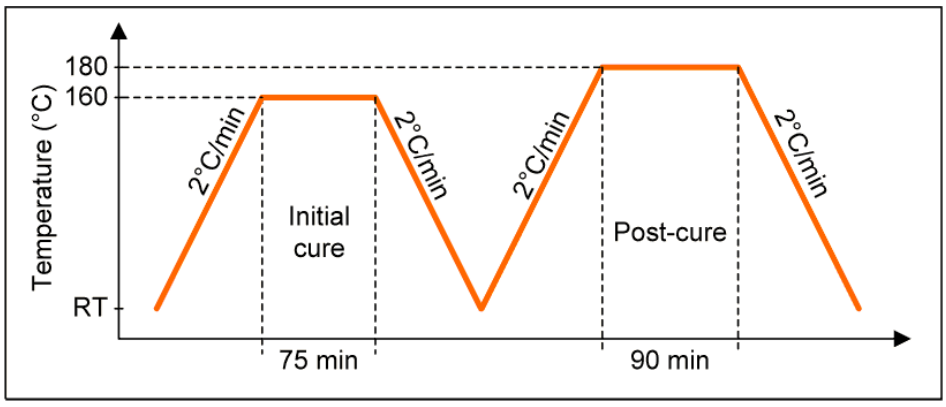

Figure 3.6 – Cure cycle for neat MVR 444 epoxy resin

Furthermore, the following standardised mechanical tests were performed to verify and complete the neat resin properties for the selected cure cycle: compression, flexure, single-edge notched bending and thermo-mechanical analysis.

All resin samples for mechanical testing were cut with a dry diamond blade saw from a 4 mm thick resin plaque which was manufactured via RTM following the selected cure cycle. Due to the use of rigid tooling the specimens were void free with smooth surface finish. Prior to testing, the cutting edges of each coupon were polished to final tolerances on a plate polishing machine with 400 grit silicon carbide abrasive paper. All specimens were conditioned for at least 48h in the standard test atmosphere prior to testing. Compression, flexure and single-edge notched bending tests were performed on a universal test machine Instron 5500R with 5kN load cell.

The density of three cured resin samples with the dimensions of 10 mm x 20 mm x 4 mm was determined by immersion method in distilled water following BS EN ISO 1183-1:2004.

Compression tests were performed in a compression cage on six resin samples with a cross-head speed of 1.0 mm per minute. Coupons were cut and polished to the dimensions of 4 mm x 10 mm x 10 mm, according to BS EN ISO 604:2003. To ensure parallelism of the loaded sample surfaces each sample was cut from a continuous resin beam with a Buehler Isomet slow speed diamond blade saw. The digital image correlation system Vic2D, supplied by Limess Messtechnik & Software GmbH, enabled the measurement of the full strain field on the resin samples and the determination of compression modulus and Poisson's ratio.

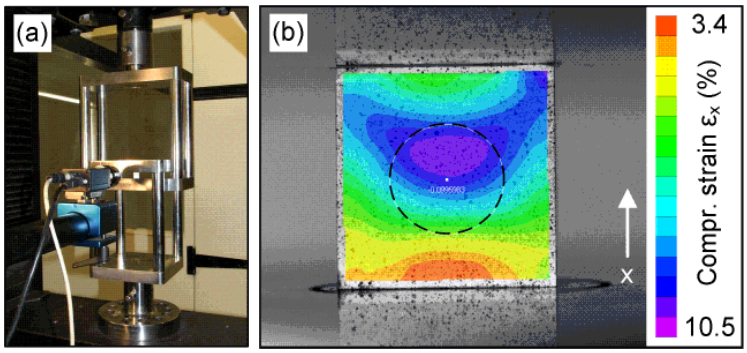

Figure 3.7 – Resin compression test: (a) compression cage with DIC strain measurement unit, (b) typical compression strain field of a resin sample at yield point

Figure 3.7 illustrates the compression setup and the typical strain field on a compression specimen at yield point. The dashed line circle frames the selected area of interest to extract the averaged compressive strain of the sample, excluding edge effects. The compressive modulus was determined between 0.5% and 1.0% strain to avoid initial non-

linear effects in the stress-strain curve. Figure 3.8 illustrates the measured axial stress-strain curve for a sample of MVR 444 epoxy resin in compression and flexure.

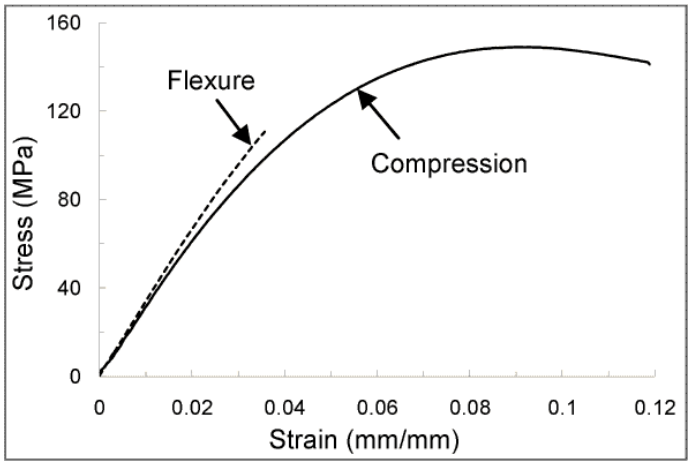

Figure 3.8 – Stress-strain curve for compression and flexure of MVR 444 epoxy resin

Flexural 3-point bending tests were performed on eight 80 mm x 10 mm x 4 mm specimens with a constant cross-head speed of 2.0 mm per minute to determine flexural modulus and strength, according to BS EN ISO 178:2003. The maximum specimen deflection was measured using the laser extensometer EIR LE-05. The flexural modulus was calculated in the interval between 0.05% and 0.25% flexural strain.

The coefficient of thermal expansion (CTE) of the cured neat resin, as required for numerical material modelling, was measured on three samples by thermo-mechanical analysis (TMA) in the range of 20°C to 190°C with a thermal ramp of 5°C per minute, according to BS EN ISO 11359:1999.

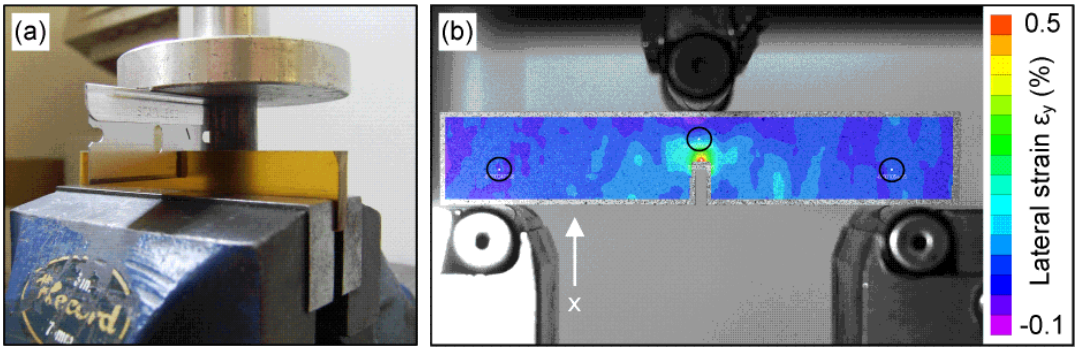

Figure 3.9 – Single-edge notched bending test: (a) pre-cracking of notched specimen, (b) lateral strain field before crack propagation

Seven samples of 80 mm x 15 mm x 4 mm were cut and polished for single-edge notched bending to determine the resin fracture toughness. The preparation of pre-

cracked single-edge notched specimens in accordance to BS ISO 13586:2000 requires skill to achieve a sharp, instantly propagated crack with a length within the limits of 0.45 to 0.55 times the specimen width [84]. In order to create a sharp pre-crack from a pre-manufactured notch, samples were clamped into a vice at 0.45 times the specimen width. A tapping device consisting of a guided aluminium weight of 96 grams was dropped three to five times onto a fresh razor blade to propagate a sharp crack from the manufactured round notch of 6.1 mm length into the given limits (see Figure 3.9 a)). Three-point bending tests were performed with a test span of 60 mm and cross-head speed of 1 mm per minute to determine the resin fracture toughness. The use of a 2D digital image correlation system enabled recording of the true deflection between the loading pins (measurement circles in Figure 3.9 b)). Hence, compliance calibration of the test setup becomes redundant.

Table 3.9 summarises the measured mechanical properties of the neat resin.

Table 3.9 – Measured resin properties (Std.dev in brackets)

Average property (St. dev)		ACG MVR 444
Cured dry resin density	g/cm^3	1.157 (0.001)
Glass transition temperature (T_g)	°C	DSC 209 (0.1) DMA 199 (2.2)
Compression modulus	GPa	3.2 (0.02)
Compression yield strength	MPa	149 (0.7)
Compression yield strain	%	9.0 (0.2)
Poisson's ratio	-	0.34 (0.02)
Flexural modulus	GPa	3.4 (0.05)
Flexural strength	MPa	121 (14)
Flexural strain	%	4.1 (0.6)
Fracture toughness G_c	J/m^2	100 (19)
Thermal expansion (at RT)	10^{-6}/°C	62.1 (1.2)

The measured density of 1.157 g/cm^3 for the cured resin is significantly higher than the manufacturer's data. Hence, measured values were used for later fibre volume calculations. While the compressive strength of the cured epoxy resin confirms the manufacturer's data, significant reduction in yield strain along with an increase in compressive modulus were observed, which was confirmed by the flexural test data.

As the digital image correlation system was limited to a data acquisition rate of 5 frames per second, the test speed in the SENB test was chosen to 1 mm per minute to obtain at least 60 data points per test. Initial test at the suggested 10 mm per minute showed no significant difference. Hence, the three times lower fracture toughness of only 100 J/m^2, compared to the manufacturer's data, can only be attributed to the high resin cure temperature. The selected cure cycle at 160°C results the maximum achievable mechanical performance of the resin in compression and flexure. However, the reduction in fracture toughness, along with the increase in glass transition temperature indicate a very brittle nature of the resin for the chosen cure temperature.

3.5 Ancillary adhesives

The aerospace qualified two component epoxy adhesive Araldite® 420 A/B, supplied by Huntsman Advanced Materials, was used to bond tabs and composite reinforcement strips to the composite test specimens if high shear strength was required. All bonding surfaces were abraded with 400 grit sandpaper and degreased with acetone. Resin component A (yellow) and hardener component B (blue) were mixed in a ratio of 100:40 by weight, applied and cured for 4 hours at 50°C to achieve the full shear strength of 37 MPa, as stated by the manufacturer. To achieve a uniform thickness of the adhesive layer, the tabs and composite specimens were clamped together with spring clips, which applied a force of 35N onto the tabs. Tabs and reinforcement strips could be debonded easily from the test specimens with a metal blade after testing by heating the samples to 150°C for 10 to 20 minutes.

For lower load applications and bonding of composite specimens onto jig components, as required for delamination and pull-off tests, the cyano-acrylate based adhesive Loctite® Precision was used, supplied by Henkel. Manual pressure and a cure time of 60 to 90 seconds are sufficient to achieve typical shear strength of 18 MPa and a tensile strength of 26 MPa according to the manufacturer. Specimens were pre-treated in the same way as for the epoxy adhesive Araldite® 420. To avoid damage to the specimens while debonding them from the metal jig components, the debonding was facilitated by dissolving the cyano-acrylate with acetone.

Chapter 4 Advances in manufacturing methodologies

The following chapter summarises the basic parameters and processes to manufacture the tufted carbon fibre/epoxy composites of this study. Advances in the automated Z-reinforcement technique of tufting of dry carbon fibre fabrics are described in the first section of this chapter along with critical parameters for successful tufting. Section 4.2 summarises the resin injection equipment and injection parameters which are used for the manufacturing of all tufted composites of this study.

4.1 Automated tufting

The initial setup and process of automated tufting at Cranfield University has been presented in previous publications by Dell'Anno [82; 85]. This section details development and improvements in the tufting process, which were made in the course of this work, along with identified critical parameters for high quality tufting. A summary of required auxiliary materials and equipment for the tufting process is given.

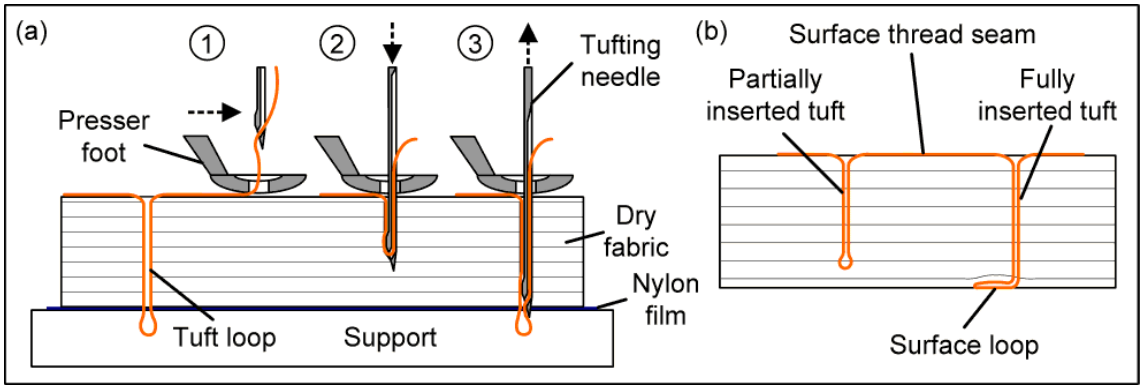

Figure 4.1 – Tufting schematic: a) tuft insertion steps, b) tufted composite with partially and fully inserted tuft

4.1.1 Tufting process and equipment

In contrast to conventional stitching techniques, the tufting process requires only single-sided access to the dry fabric preform. As shown in the tufting schematic of Figure 4.1 a), through-the-thickness reinforcing thread loops are inserted along a continuous thread seam into the dry fabric layup by a specially designed tufting needle. After moving to the designated tuft location (step 1), the needle penetrates the fabric inserting a dry

thread loop at relatively low tension (step 2). While the needle is retracting (step 3) the dry thread loop is retained in the preform by friction of the surrounding fabric layers. Depending on the chosen needle insertion depth partial or full through-the-thickness reinforcement can be aimed for. In case of full penetration, a free loop end is typically left to protrude from preform back surface to ensure consistent tuft insertion quality. The free loop end is bent onto the composite surface during mould closure and secured by injected and cured resin (Figure 4.1 b).

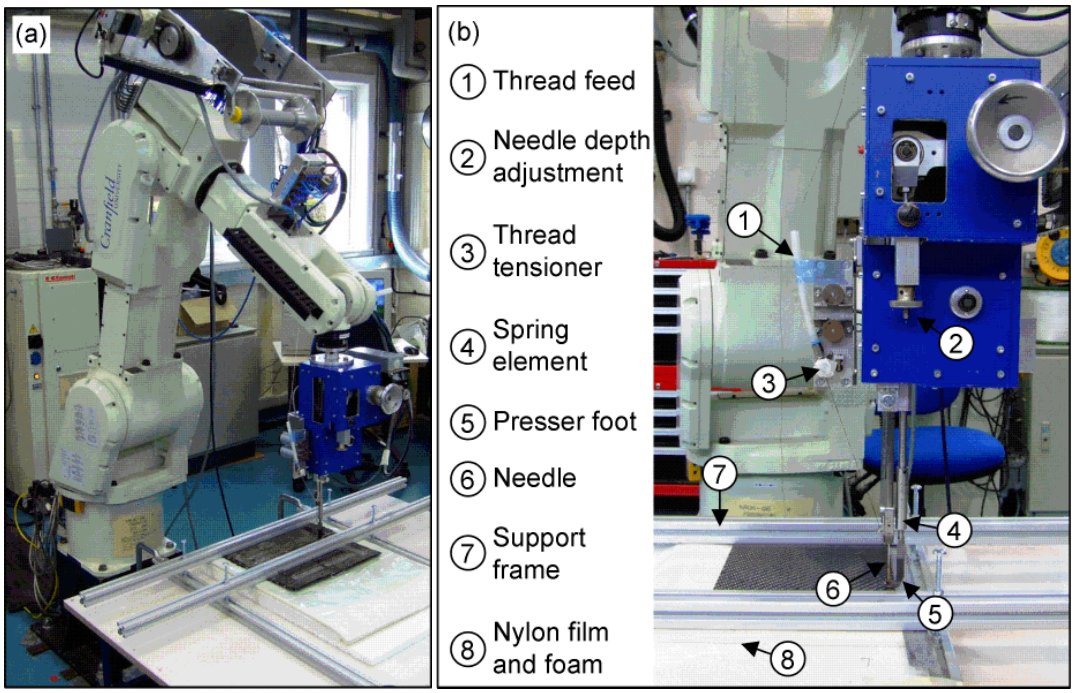

Figure 4.2 – Automated tufting setup: a) Kawasaki FN 20 robot arm with tufting head, (b) KSL KL150 tufting head and fabric support frame

In order to meet high manufacturing output and tolerances, as expected for manufacturing of structural composites in aerospace industry, a robot controlled automated tufting process is used, as illustrated in Figure 4.2. The setup comprises a commercial tufting head KSL KL 150 which is mounted onto a Kawasaki FS 20N six-axis robot arm. A table of 0.9 m x 1.2 m area, which is aligned and levelled with the robot coordinate system, supports the fabric preforms during tufting.

Similar to conventional sewing machines, both needle and presser foot are actuated synchronously by a mechanical extender mechanism, featuring a fixed stroke of 60.5 mm and 11 mm respectively. To enable the continuous movement of the tufting head without disruption of the fabric by lateral movement of the tufting needle, an additional oscillation mechanism keeps the needle and presser foot in a quasi-static position while

the needle is penetrating and extracting from the preform. Only after the needle tip has cleared the preform surface, needle and presser foot are shifted to the next tuft location. The fixed oscillating movement of this mechanism in the tufting head limits the tuft spacing to between 2 mm and 10 mm. For larger spacing the drive has to be actuated separately at each individual tuft location. The driving servomotor enables a maximum tufting speed of 500 tufts per minute.

Pneumatically actuated scissors for cutting of the tufting thread after the tufting operation were substituted by manual cutting. The required lifting of the tufting head of 120 mm from the preform surface for access of the automated cutting mechanism to the tufting thread resulted in unacceptable pull-out of a few final tufts.

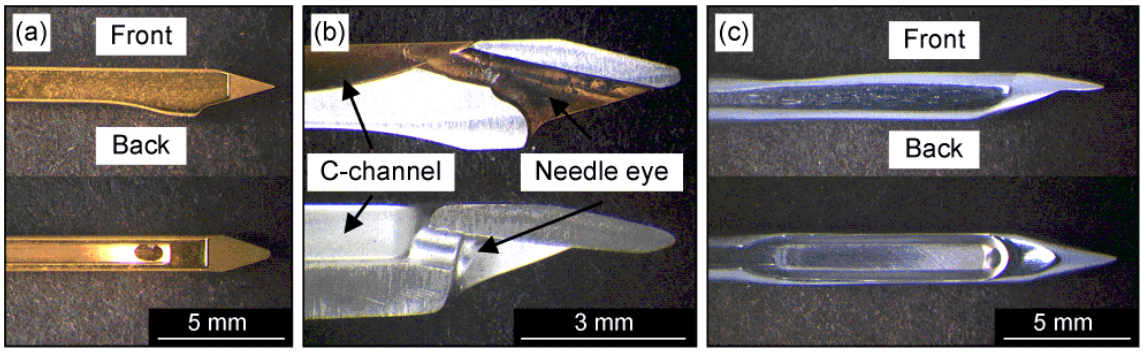

Figure 4.3 - Types of tufting needle: a) KSL square tufting needle, b) needle tip section of square (top) and EP12 needle (bottom), c) KSL EP12 Nm230

A key element of successful tuft insertion is the tufting needle. Currently, two types of needle are available, as illustrated in Figure 4.3, both supplied only by the tufting head manufacturer. The needle types differ by outer dimensions and cross-sectional shape, as summarised in Table 4.1. In contrast to conventional sewing needles, the eye of the tufting needle is highly inclined. This ensures needle retraction along the feeding side of the thread loop. During tufting, the reinforcement thread is fed with minimal friction through a C-shaped channel in the needle front to the needle eye. Behind the needle eye, a small bulge forces the thread against the surrounding fabric, enhancing the frictional contact between thread and surrounding fabric layup. This ensures the formation and retention of the thread loops in the preform and minimises flexural damage of the tufting thread as the bending radius at the needle eye is increased.

The needle eye diameter and C-channel depth limit the maximum thickness of the tufting thread. For tufting of the selected threads of chapter 3.2, square and round needles with a needle eye diameter of 0.68 mm were used. Although the square needle features

an eye diameter of 0.68 mm, the C-channel was found to narrow to only 0.44 mm close to the needle eye, further limiting the thread dimensions (see Figure 4.3 b).

Table 4.1 – Dimensions of tufting needles

Needle type		Square needle	EP12 Nm230	EP11 Nm230
Cross-section	-	square	round	round
Max. width	mm	1.47	2.3	2.3
Max. depth	mm	1.85	2.3	2.3
Eye diameter	mm	0.68	0.68	1.00
Tip/Eye offset	mm	2.8	4.0	4.0
Needle length	mm	90	93	93

In the current tufting setup the thread is fed directly from a bobbin to the tufting needle without an active feeder mechanism. Thread tension is controlled by a spring-loaded tensioner, see Figure 4.4 a). An additionally installed tensioner of counter-rotating metal wheels was found to be unsuitable for the carbon thread used as its high rotational speed results in thread damage.

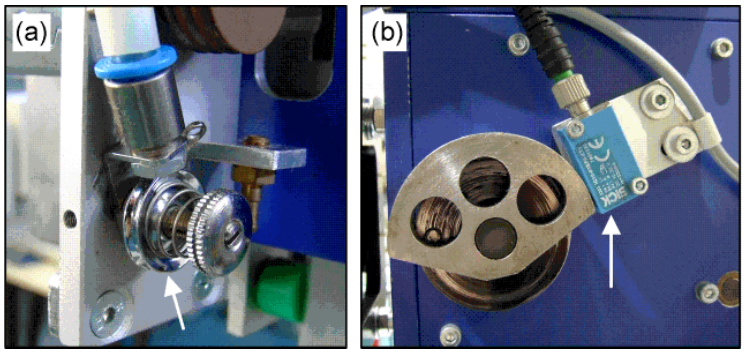

Figure 4.4 – Tufting head control elements: a) spring-loaded thread tensioner, b) Needle position sensor (recognises only reversal points)

Given the current needle design, the maximum practical thickness of dry preforms for tufting is limited to 40 mm. The penetration depth can be varied by adjusting the height of the needle rod in relation to the presser foot. For general tufting of the full preform thickness local clearance under the fabric layup is required for the needle to penetrate through the preform. Several options of support have been considered in this study, as discussed in detail in section 4.1.3.3.

The stroke position of the needle is controlled by a proximity switch at the extender, the only feedback sensor of the current tufting head. This sensor is only able to determine if the needle is at the upper or lower pivot point, see Figure 4.4 b). The missing continu-

ous feedback of the current needle position during the tufting process limits the control on the tufting accuracy within each tufting row as rotational delays and subsequent shift in the insertion pattern are not identified by the robot control.

The presser foot for the current tufting head consists of two functional components, the spring unit and actual foot element, see Figure 4.5 a). The foot element is designed to either allow sliding over the preform surface, characterised by the wide, curved base plate (left), or to guide the needle with contact to the fabric (right) only at needle penetration. In this study, the sliding foot element of Figure 4.5 b) was used as it enhances the quality of tuft insertion. The spring unit compresses during needle penetration and extraction, increasing the pressure of the foot base onto the preform, while releasing pressure when sliding to the next tuft insertion point. While in contact with the preform the spring-loaded presser foot fulfils two tasks. Firstly, the foot compresses the preform close to its net-shape thickness. This is essential as too low fabric compaction during the tufting process was found to result in crimping of the through-the-thickness reinforcement when compressed within the mould tool for resin injection. Secondly, the foot element inhibits unwanted extraction of previous tuft loops during insertion of the next tufting loop by clamping the connecting thread seam against the fabric preform.

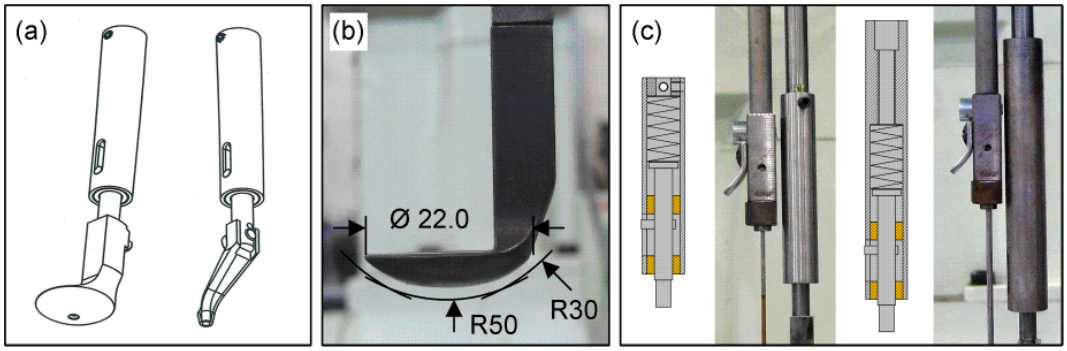

Figure 4.5 – Spring loaded foot element: a) KSL compression and needle guidance foot, b) basic dimension of fabric compression foot, c) original and modified spring element

Due to insufficient stability and alignment of the spring unit and actuation rod of the original presser foot assembly (see left - Figure 4.5 c)) the author redesigned and installed a new spring unit. In the new design, see Figure 4.5 c), the actuation rod and spring unit are connected by a threaded and form-locked joint. This increases the stability of the joint against bending moments, introduced by frictional sliding of the foot element along the fabric preform.

4.1.2 Tuft arrangement and density definition

For automated tufting a program was adapted and extended by the author from the original work of Dell'Anno [82]. The program code was written in the AS language code, a simple programming language to control and monitor the Kawasaki robot arm and attachments. User interface for programming and execution was KCWin software on a desktop PC. In the program four options can be accessed for tufting of the following arrangements: single row tufting in x- and y-direction of the robot coordinate system, tufting of rectangular areas and angled tufting of a single tuft row. Figure 4.6 illustrates the different tufting arrangements and motion paths of the robot arm in relation to the robot coordinate system. The full program code can be found in appendix A.

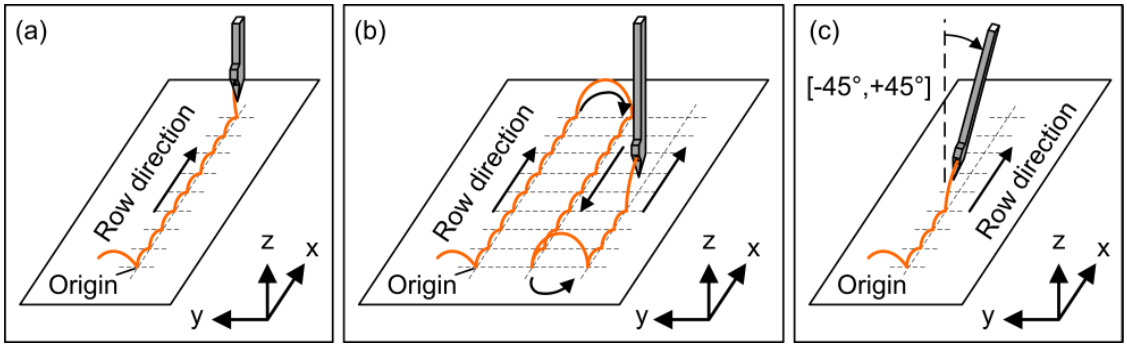

Figure 4.6 – Motion path of robot controlled tufting program: a) single row tufting along robot x-axis, b) tufting of rectangular area and c) angled insertion of single tuft row

Automated tufting was executed using transformation locations, i.e. Cartesian coordinates, with linear interpolated movement between automatically determined turning points. The use of coordinate based motion control was selected to ensure high accuracy between tufting rows and to avoid compound errors in continuous tufting of large areas with multiple tufting rows.

Each tuft arrangement is defined by a set of the following parameters: length and width of the tufting area, tuft pitch s_x, i.e. distance between two adjacent tufts in the same tuft row, tuft spacing s_y, i.e. the distance between two neighbouring tuft rows, and speed as percentage of the maximum rate of 500 tufts per minute. Set parameters and instructions are displayed on-screen to the operator by print commands, allowing even inexperienced users to quickly set up and execute the tufting process.

In the subroutine for tufting of rectangular areas, square and triangular patterns were incorporated, as illustrated in Figure 4.7, differing by the relative alignment of tufts be-

tween adjacent tuft rows. From length, width, tuft pitch and row spacing the program derives automatically the maximum number of tufts which can be accommodated in the given area. Subsequently, the Cartesian coordinates of start and end points of adjacent tuft rows are determined. Both row length and tufting width are rounded off to the closest multiple of tuft pitch and row spacing to finish each row on a fully inserted tuft.

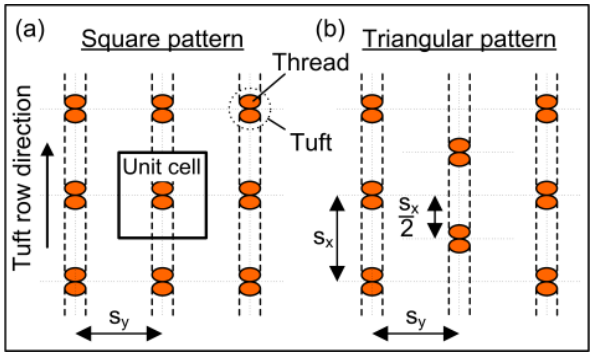

Figure 4.7 – Square (a) and triangular (b) tufting pattern with typical unit cell for areal tuft density definition

In contrast to a fully cured Z-pin, which maintains its fixed diameter during insertion, consolidation and cure, dry tufting thread interacts with the surrounding fabric layup, as discussed in detail in Chapter 5. Hence, an areal tuft density definition based on infused thread diameter, as conventionally used for Z-pinned composites, is not necessarily the best choice. For this study an areal tuft density ρ_t has been defined taking only the dry fibre cross-sectional area of the structural effective vertical segment of the tuft into account. Equation 4-1 describes the areal density, defined by the ratio of dry fibre cross-sectional area of the tuft versus the functional unit cell area of tuft pitch and spacing (see Figure 4.7). The dry tuft cross-section area $A_{t,dry}$ is twice the dry thread cross-section $A_{th,dry}$ which can be derived from the filament diameter d_f and number of filaments per thread n_f or the ratio of linear weight T_{th} to density ρ_f of the dry thread, as shown in equation 4-2.

$$\rho_t(\%) = \frac{2 \cdot A_{th,dry}}{s_x \cdot s_y} \qquad \textbf{4-1}$$

$$A_{th,dry}(mm^2) = n_f \cdot \left(\frac{d_f}{2}\right)^2 \cdot \pi = \frac{T_{th}}{\rho_f} \qquad \textbf{4-2}$$

4.1.3 Tufting process characteristics

In general, the aim of an automated tufting process has to be the insertion of Z-reinforcing thread loops at high spatial accuracy, insertion quality and rate with minimal disturbance of the original fabric preform and minimal reduction of the Z-reinforcing potential of the tufts. Initial observations on the manufacturing process of automated tufting by Dell'Anno [82] have suggested that the successful insertion of dry tuft loops into thin carbon fabric preforms up to 3.5 mm thickness is influenced primarily by the process parameters of thread, fabric and support material. Free thread loops of limited structural functionality on the preform surface were found to be useful for quality analysis but to have a potentially negative effect on the in-plane mechanical performance due to their typical length (above 5 mm) and potential accumulation in volume for close tuft spacing. Hence, in this section a wider range of material and process characteristics is analysed with emphasis on identification, characterisation and possible optimisation of the effect on the loop formation with application to fabric preforms of 2 to 20 mm thickness. The effects of tufts on the morphology and mechanical performance of resin infused and cured composites are examined in detail in Chapter 5 and Chapter 6.

4.1.3.1 Fabric and thread material

Figure 4.8 a) to c) shows the typical surface thread seams and individual free tufting thread loops, which are created on the preform surface opposite the insertion side, for UD and twill woven carbon fabrics.

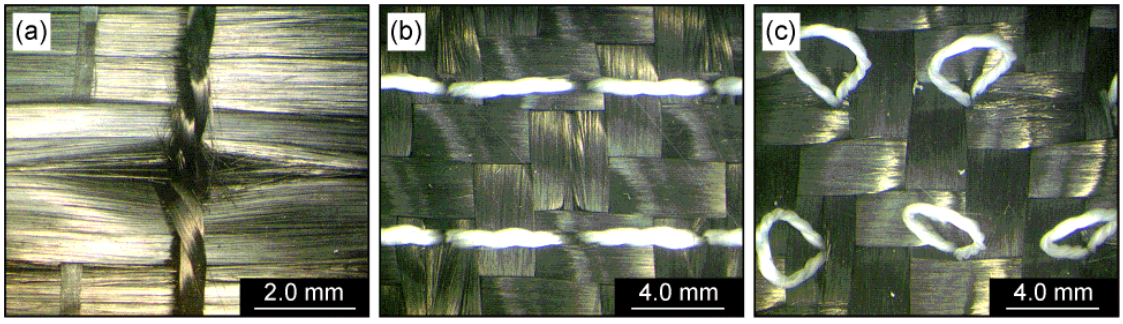

Figure 4.8 – Tufted dry preforms: a) fabric deviation around carbon tuft in UD, b) 5.6 mm spaced square arrangement of glass tuft in twill woven fabric (thread seam side), c) equivalent loop side

Similar to conventionally stitched preforms [44], the inserted tufting thread spreads the individual dry fabric plies creating fibre free zones parallel to the fibre orientation of the fabric (see Figure 4.8 a).

All three chosen thread materials, i.e. carbon, glass and aramid, showed to be suitable for the tufting process, although most consistent loop formation was achieved with the glass and aramid threads. The brittle nature of the carbon filaments makes the carbon thread susceptible to local splitting under high curvature in the needle eye especially if used in closely packed fabric preforms. Carbon thread damage was found at the non-critical surface loops (see Figure 4.9 a), but also at the entry point of the needle (see Figure 4.9 b). The latter, which often led to complete failure of the tufting thread, has potentially detrimental effects on the mechanical bridging performance of the tuft and must be avoided. In the selection of the thread material a compromise must be found between suitability for the manufacturing process and mechanical performance in the cured composite.

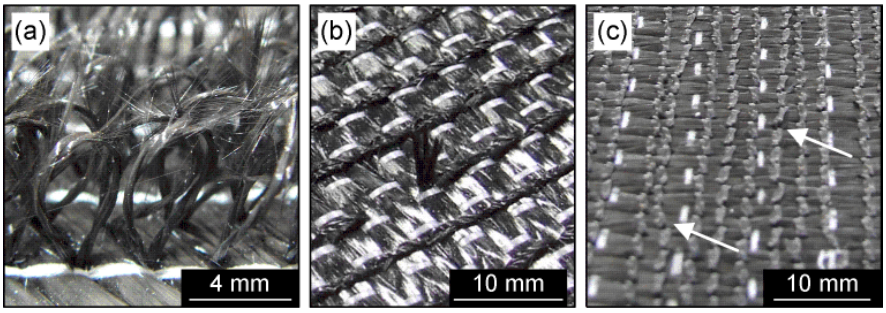

Figure 4.9 – Tufting defects: a) carbon thread splitting, b) thread rupture at needle entry point, c) tufting seam deviation in UD layup

Both dry non-crimped and woven carbon fabrics without binder in biaxial layup appear to be perfectly suitable for tufting of preforms between 3 mm and 10 mm thickness with little effort of needle penetration and negligible damage to the tufting thread. The biaxial fabric geometry creates sufficient frictional contact with the tufting thread to ensure uniform loop formation. Only in the case of quasi-isotropic layup of a large number of non-crimped fabric plies the interaction of non-structural stitching seams with the penetrating needle appeared to cause extensive compaction of underlying fabric layers leading to possible stoppage. In trials on 32 layers of biaxial (0°/90°) NCF (OCV Technical Fabrics) in quasi-isotropic layup with an areal weight of 440 g/m^2 the problem could be avoided by reducing the stiffness of the underlying support material. Resulting fabric distortion, however, has potential implications on the final preform geometry, as discussed in section 4.1.3.3.

A similar effect was observed on preforms which were assembled and stabilised with activated epoxy powder binder, thermoplastic binder yarn or veil. Activation of the hotmelt weft yarn in 14 layers of carbon fibre uni-weave fabric (OCV Technical Fab-

rics) for a unidirectional composite of only 4 mm thickness caused repeated carbon thread failure and arrest of the penetrating needle due to the inhibition of fibre spreading by the binder. Furthermore, the tufting needle was observed to deviate from the insertion path, caused by contact with and deflection from the binder yarns (see Figure 4.9 c).

The presence of non-activated E01-type epoxy binder (2.5% by weight), as used for preform stabilisation in a study on tufted Pi-stiffener-to-skin joints to which the author contributed the tufting process [81], was found to enhance the friction between thread and surrounding layup, resulting in uniform loop formation even for thin composites. However, accumulation of binder at the heating needle tip can close-up the needle eye and cause unacceptable thread damage. Hence, the presence of binder, especially for thick composite layup, should be avoided in the zone of tufting despite consequential need for increased support of the dry preform structure.

4.1.3.2 Mechanical tufting parameters

In contrast to conventional stitching with interlocking threads [51], the application of tension to the tufting thread during thread insertion was found to affect primarily the loop formation process and only conditionally the final preform geometry as thread tension is only retained along the free thread loops during insertion. An increase in thread tension up to 70 cN, a typical value for conventional stitching [86], resulted only in high variability of final loop length. Tufting without thread pretension led to insufficient tensioning of the surface seams (see Figure 4.10 a). For carbon fabric preforms of this study the best insertion quality was achieved for a thread tension of 12 cN.

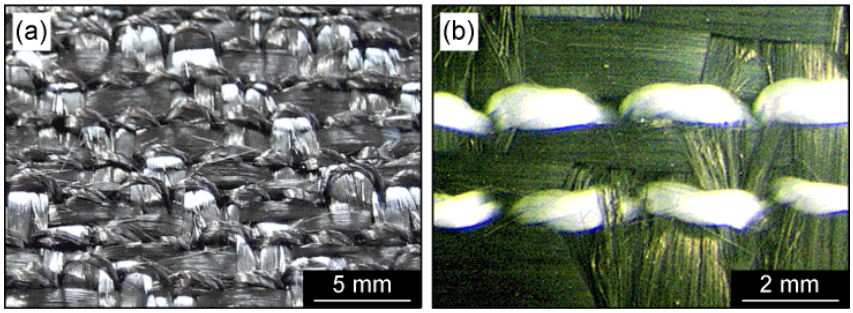

Figure 4.10 – Effect of mechanical process parameters on loop formation: a) insufficient tensioning of tufting seams b) needle induced fabric damage in dry carbon fibre woven fabric

The described features of C-channel and inclined needle eye in the currently available tufting needles are essential for the tufting loop formation. However, other features such

as the diameter and sharp edges on the square needle appear to cause significant fabric disruption and damage by breaking bundles of filaments along the penetration path (see Figure 4.10 b). A change from square to round needle reduced the visible damage to the preform at the cost of larger needle diameter. Both unsupported needle length and stroke of the insertion mechanism of 60 mm length are designed to allow tufting of a greater range of preform thicknesses, but were found to increase the spatial variation of inserted tufts due to increased needle deflection. For future design a thinner and shorted needle is suggested to minimise fabric disruption and stability during the insertion of tufts into thin preforms.

The primary control mechanism for the insertion depth of tuft loops into dry fabric preforms was found to be the needle penetration depth.

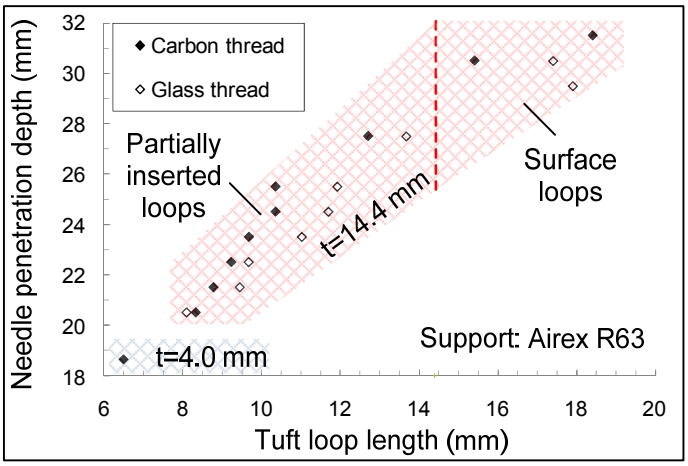

Figure 4.11 – Dry tuft loop length versus needle penetration depth depending on preform thickness and thread material

Figure 4.11 shows the typical tuft loop lengths for various needle penetration depths, measured between the thread seam surface and the reversal point of the tuft loops either on the opposing preform surface or within the preform (partially inserted). Both glass and carbon tufts were inserted into biaxial NCF preforms of 4 mm (9 layers, 440 g/m^2) and 14.5 mm (32 layers, 440 g/m^2) thickness at 5.6 mm spacing with an aerospace certified closed-cell foam as support material (full specification in Table 4.2).

There appears to be a linear dependence between needle penetration depth and resulting tuft loop length, with only limited effect of the preform thickness on the loop lengths. For a fixed needle depth glass thread tufts were typically 1.0 to 1.5 mm longer than carbon thread tufts. Main cause for the difference is assumed to be the less uniform and

compliant surface and higher flexural stiffness of the two-stranded carbon thread which affect interaction of the thread with the surrounding fabric preform.

Mechanical restrictions in the current tufting head design limited the needle penetration depth to a minimum of 18 mm, measured between the fully compressed presser foot and the tufting needle tip in the lowest needle position. As a consequence, UD, NCF and woven fabric preforms with 4 mm thickness, as used primarily for the in-plane characterisation of this study, featured free surface tuft loops of at least 3 mm heights. By comparing the needle depth to the resulting loop length it becomes apparent that the needle has to advance between 12 to 14 mm further into the preform than the intended final loop length. The offset can be attributed partially to the distance between needle tip and needle eye (see Table 4.1). However, the main source of the offset appears to be extraction of the already inserted tuft loops at insertion of following tufts. Based on this observation, tufting of preform structures directly on rigid mould tooling, as suggested by [9; 87] and apparently derived by potential industrial users, appears to be feasible only on thick fabric preforms or sandwich structures which require partial tuft insertion and exceed the intended loop length plus necessary offset in thickness.

The bulk factor of untufted and tufted fabric preforms, i.e. the relative change in preform thickness under an applied level of surface pressure, potentially affects both the straightness of the inserted Z-reinforcement and the resin injection process. In contrast to lock and chain stitching, in which the preform compaction can be controlled by the thread tension, the tufting foot is the only means to compress the dry fabric preform close to net thickness during tufting. In the current setup, a spring loaded foot element with a pretension of 10.9 N and spring stiffness of 0.75 N/mm was employed. As only half of the curved foot base is typically in contact with the preform surface (see Figure 4.5) a maximum compaction pressure of 0.18 MPa can be achieved with the current assembly.

Figure 4.12 a) shows the relationship between fibre volume fraction and applied pressure of the typical untufted UD, NCF and woven fabric preforms of 4 mm thickness, as used for the in-plane characterisation of this study. At least three samples of each preform were compressed over an area of 50 x 50 mm^2 at a constant cross-head speed of 0.5 mm per minute. The fabric fibre volume fraction of the compressed dry preform was determined based on the number and weight of the fabric layers and the measured preform thicknesses. It becomes apparent that the applied tufting foot pressure is sufficient to compact the dry fabric preforms during tufting to a thickness which equals fibre vol-

ume fractions of 56% to 59%. Such values are within the typical range of the final cured composite. Subsequently, local thread crimp due to fabric compaction in the mould is limited only to the outer surface layers which are able to relax after the tufting process.

Additional compression tests on 32 layers of biaxial (0°/90°) NCF with an areal weight of 440 g/m^2 , which were performed by the author in cooperation with a student to investigate the performance of a tufted omega stiffener-to-skin joint [88], revealed that the presence of both 0.5% carbon and glass tufts equally raises the required consolidation pressure of the Z-reinforced preform by up to 40% to achieve the same thickness as the untufted preform for a typical 2D equivalent fabric fibre volume faction of 55% (see Figure 4.12 b). This is in agreement with compression results on conventional stitched dry fabric preforms by Mitschang et al [51; 89]. While the thread material appears to have a negligible effect on the consolidation behaviour the local fibre spreading is assumed to be the main contributor to the enhanced bulk factor. Depending on the resin infusion process the increased bulk factor of the tufted fabric can either require a higher closure force of the mould (for rigid mould tooling) or increase the net thickness of the composite (for flexible tooling and vacuum infusion root).

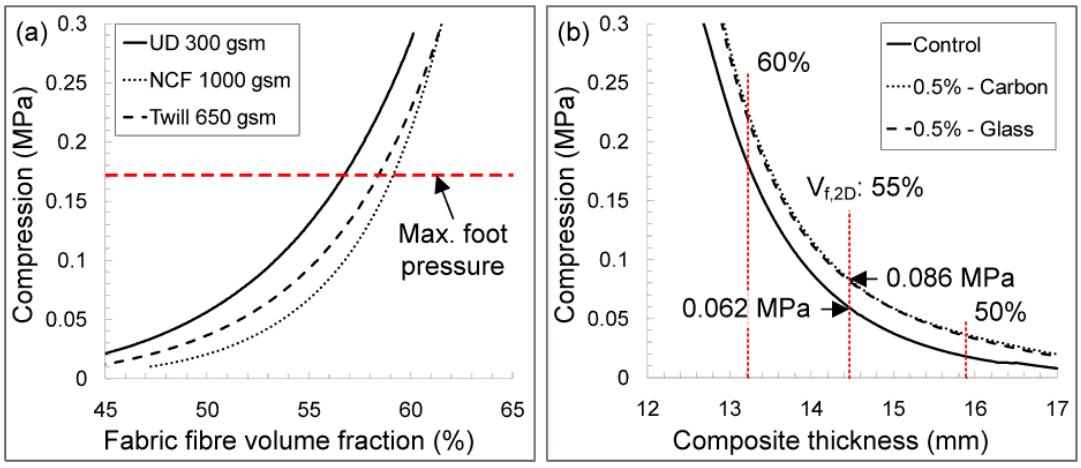

Figure 4.12 – Compaction versus dry fabric volume fraction plot: a) untufted UD, 0°/90° NCF and twill fabric, b) 0.5% glass and carbon tufting in 0°/90° NCF

Variation of the tufting speed from 100 to maximum 500 tufts per minute has been used successfully during tufting of both carbon and glass threads with little effect on the insertion quality. Hence, a general speed of 400 tufts per minute was adopted for the tufting of all in- and out-of-plane fabric preforms.

Despite all measures introduced to increase the accuracy of tuft insertion it was found that the coordination between forward motion of the robot arm and the rotational speed

of the current tufting head caused an offset of up to one percent in target number of tufts for a given tuft row length. Hence, variation in the insertion pattern, especially for small tuft spacing, could not be avoided (see Chapter 5 and Chapter 6 for consequences on meso-structure and mechanical properties respectively).

4.1.3.3 Fabric fixation and support

The necessary fabric compaction and sliding of the foot element over the surface of dry fabric preforms, especially if featuring significant bulk factor, were found to disrupt the global fabric layup by fabric distortion and dilution due to lateral spreading of un-stabilised fabric layers. Hence, in the course of this project a frame system was designed and installed on the tufting table to secure the dry fabric preforms. Besides inhibiting fibre distortion the clamping of the dry preform showed to be essential for successful tufting if the tufted area was unsupported (see below). Additional tufting seams bordering the area of tufting were found to reduce the splicing, global warp and lateral dilution effects to the dry fabric preform.

The support under the fabric preform has to withstand the applied pressure of presser foot and penetrating needle and has to allow the needle to travel beyond the back face of the preform. In literature, several support structures and materials have been considered, including metal support with local grooves along the tuft path [58], closed-cell silicone foam or rubber layers [85; 87] or a substrate consisting of closely spaced standing plastic tubes similar to a brush [90].

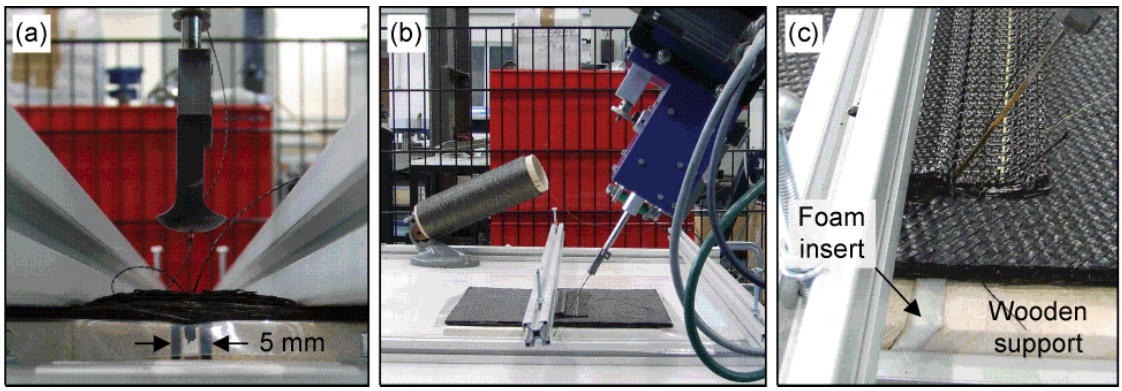

Figure 4.13 – Support for a) orthogonal and b) angled (45°) tufting of 3D woven Pi-stiffener to 5 harness woven skin , c) details of angled support

For the tufting of single Z-reinforcing seams, as used in the structural joint of Pi-stiffener to thin skin [81], the author successfully employed a stiff wooden support with 5 mm wide and 25 mm deep slot to accept the penetrating tufting needle (see Figure

4.13 a). The only limitation to this approach was the necessary mounting and fixation of the fabric against distortion into the unsupported slot.

For angled tufting at 45° to the preform surface in the same project (see Figure 4.13 b), the tufting foot could not be used to achieve fabric compaction due to its insufficient flexural stiffness and shape of the foot base. The subsequent loss in clamping of the surface thread against the preform surface resulted in unacceptable variability of the loop formation process. A possible solution was the insertion of a friction enhancing silicone foam into the slot (properties see below), as shown in Figure 4.13 c).

When tufting complete areas of up to 0.9 m x 0.6 m, as was the case for the preforms of the present study, the approach of slotted support structure was found to be inconvenient for tufting at variable spacing. Hence, several closed-cell foam materials were considered (Table 4.2) for placement under the fabric preform. A nylon film was placed between foam and preform to inhibit contamination of the fabric with foam particles and to facilitate distortion free separation of preform and foam after the tufting process.

Table 4.2 – Foam types for tufting

Foam type		Sil 16	Airex® R63.50	Polystyrene EPS 70
Material	-	Silicone	Thermoplastic	Polystyrene
Manufacturer	-	Samco®	Alcan Airex®	Jablite®
Density	kg/m^3	250	60	15

Both silicone and polystyrene foams proved to enhance significantly the uniformity of the inserted tuft loops and the loop length by up to 3 mm. However, micrographs of infused and cured composite revealed the presence of silicone particles with a diameter of up to 0.5 mm within the fibre-free zone around the tuft. The incompatibility of silicone with epoxy matrix resins could lead to unacceptable formation of voids which act as potential initiation points for micro-cracks. Best compromise between stiffness, sufficiently low resistance to the penetrating needle and enhancement of the frictional contact to the tufting thread was found for a closed-cell thermoplastic foam (Airex R63.50) which is typically used as reinforcing sandwich foam in aerospace applications, thus ensuring the compatibility to the epoxy matrix. The damage tolerant properties of the foam allowed repeated use of up to three tufting cycles, thereby reducing the amount of necessary auxiliary materials for the tufting process.

4.2 Resin transfer moulding (RTM)

Vacuum assisted resin transfer moulding (RTM) with rigid tooling was chosen as manufacturing route for all carbon fibre composite panels and structures in this study. The selection of RTM over other techniques, such as resin infusion, was made due to better control on resin injection parameters, i.e. vacuum and pressure level, fibre volume fraction, void content and dimensions of the final product, due to the use of rigid aluminium or steel tooling and combination of injection pressure and vacuum. As identified by Mouritz and Cox [3], the dimensional control of the Z-reinforced composite is essential for a clear characterisation and differentiation of the effects of Z-reinforcement on the mechanical in-plane properties of the composite.

4.2.1 RTM equipment

Two rigid mould tools with internal cartridge-heating elements were used for the injection of tufted composite panels, as shown in Figure 4.14 b) and c). The aluminium tool in Figure 4.14 b) with a fixed cavity size of 340 x 900 mm^2 was used for the manufacturing of in-plane test specimens of Chapter 6. The large cavity size allowed injection of composites panels which included both control and tufted areas of different tuft density, ensuring an identical production procedure for the different types of samples. The steel mould of Figure 4.14 c) had an internal cavity size of 200 x 200 mm^2 and was used for the manufacturing of out-of-plane test specimens of Chapter 8 and Chapter 9. In both moulds the cavity thickness could be controlled by metal shims of variable thickness which were sealed against mould top and bottom with silicone seals.

In order to minimise resin injection time and potential formation of uninfused patches due to variable permeability of untufted and tufted sections, resin inlet and outlet ports in the large aluminium mould were arranged to allow the resin to permeate from the preform edges towards the preform centre. In contrast, the fixed position of inlet and outlet ports in the smaller steel mould allowed only the injection along a linear flow front. To avoid air entrapment the mould was inclined towards the outlet port at 10°.

Before resin injection, each tool was released with at least two layers of release system. For the existing aluminium tool a conventional solvent based release system Chem-Lease® PMR 90 (ChemTrend) was used. For the newly procured steel tool a water-based aerospace release system Waterworks (Zyvax) was selected in order to meet the introduced environmental policy ISO 14001 at Cranfield University by reducing the use

and necessary disposal of hazardous material. The new type of water-based release agent is free of solvents, but requires laborious surface preparation and time-consuming preconditioning and build-up of the release layers.

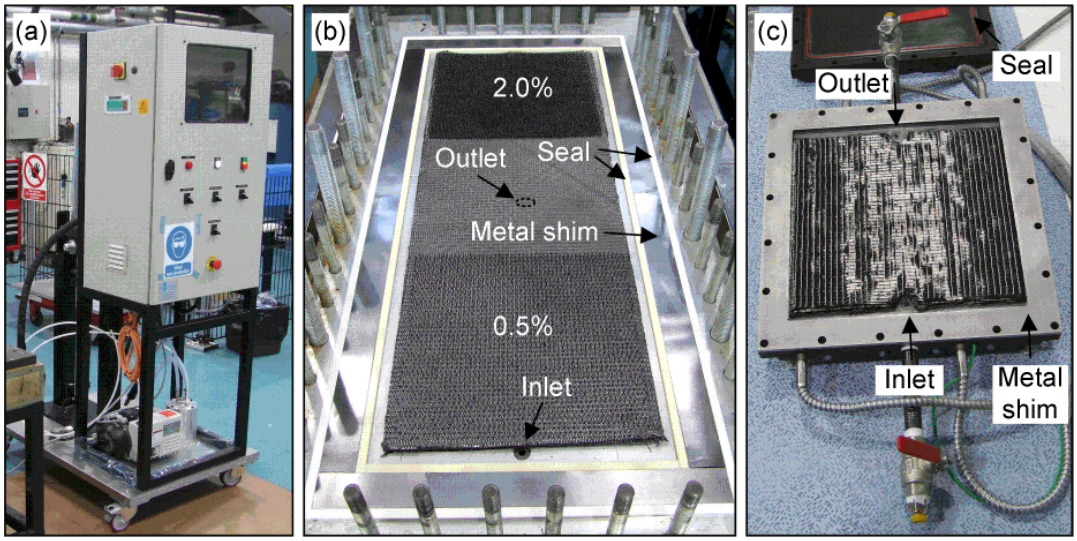

Figure 4.14 – RTM equipment: a) Isojet 3l piston RTM unit, b) 900 x 340 mm^2 heated RTM aluminium tool, c) 200 x 200 mm^2 heated RTM steel tool

Resin injection was carried out with a newly commissioned computer controlled injection unit Isojet Piston 3l (Isojet) for single-component resins, as shown in Figure 4.14 a). The integral unit of heated, screw-driven injection piston and vacuum pump allows both flow rate and pressure controlled resin injection with monitoring of all process parameters including resin temperature, injection pressure, vacuum level, flow rate, resin volume and mould temperature. Due to the nature of the selected single component epoxy resin the injection unit required cleaning at elevated temperature (~45°C) to reduce sufficiently the viscosity of the epoxy resin for easy removal. The use of a solvent-free universal cleaning agent based on a diluted surfactant RST-5™ in water showed to be beneficial, as volatiles and hazardous waste were reduced. Instead of dissolving into conventional organic solvent, the resin is removed mechanically by forming dispersion with the cleaning agent. By boiling the dispersion for at least 4 hours the agglomerated resin can be filtered from the agent and thermally processed for disposal as cured resin waste. After filtering, the cleaning agent remains a non-hazardous material which can be reused multiple times.

4.2.2 Resin injection and cure

After placing the untufted or tufted fabric layup into the fixed mould cavity the dry preforms were injected with the aerospace grade epoxy resin MVR 444 (Advanced Composites Group). A summary of the measured resin properties for the chosen cure cycle is given in chapter 3.4.1.

To achieve the highest performance in strength and modulus, the resin was processed and cured following the suggested cure cycle of the manufacturer. Initial heating of the resin to injection temperature of 70°C was executed in a circulating oven. After transferred into the injection unit, the resin was degassed in the piston for 15 min at vacuum level of -98 kPa to avoid the formation of voids during the vacuum assisted resin injection. Resin injection into the dry preform was executed at 70°C and a positive pressure of 150 kPa (±1 kPa), assisted by vacuum of -99 kPa which was applied on the resin outlet of the mould. After completion of the injection step the mould temperature was increase to 160°C at a rate of 2°C/min to initiate resin cure of 75 minutes length. Pressurisation of the mould at positive pressure of 400 kPa for 50 minutes during cure minimised the void formation within the composite parts. Upon completion of the resin cure in the rigid mould tool panels were post-cured free-standing in an oven for 90 minutes at 180°C. Heating and cooling rates of 2°C per minute were monitored carefully to avoid thermal stresses in the cured parts. The pressure controlled injection process lasted typically between 5 and 15 minutes for both small and large mould tool with a required resin mass between 0.25 kg and 1.1 kg depending on cavity size, preform dimensions and fibre volume fraction.

4.2.3 Quality control

Each panel was inspected after resin injection and cure using ultrasonic and metallographic sectioning techniques to ensure full resin impregnation. Sectioning showed that the used carbon and glass thread tufts impregnated perfectly. However, some aramid tufts featured insufficient internal wet-out which appears to be caused by the close fibre packing and high twist of the aramid thread.

Pressurisation of the resin at 400 kPa during cure ensured that the void volume in the resin matrix was negligible, as measured by acid digestion (see following chapter). However, micro-cracking in close vicinity to the tufts was observed for biaxial NCF and twill woven fabric layup, which appears to be caused by thermal cure stresses due to

mismatch of thermal expansion between the fibre free resin pockets, the compacted fabric plies and the Z-reinforcing tufting thread. Further effects of the observed micro-cracks are addressed in the following chapters.

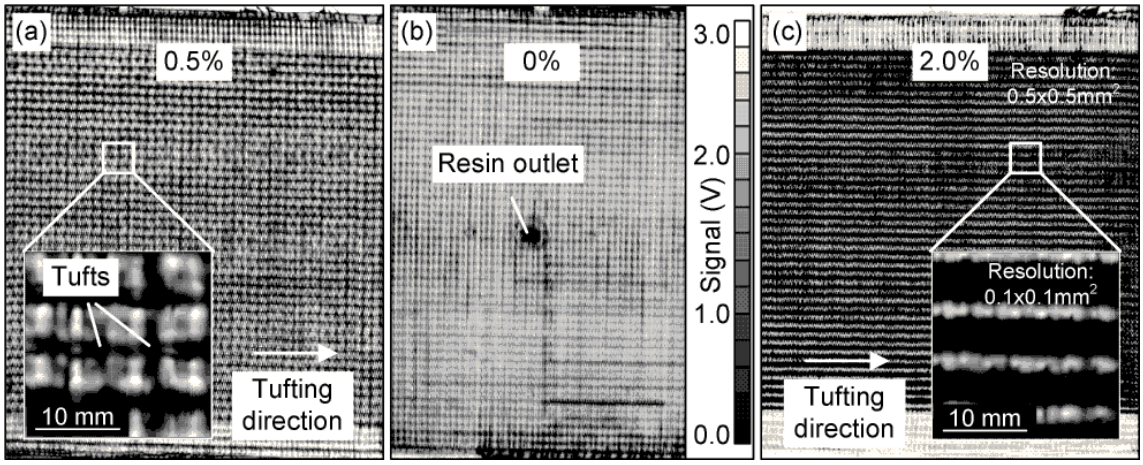

Figure 4.15 – Typical signal attenuation in amplitude C-scan of a) 0.5% carbon tufted, b) untufted and c) 2.0% carbon tufted NCF

Figure 4.15 a) to c) show the ultrasonic amplitude scans of untufted, 0.5% and 2% carbon tufted non-crimped fabric composites, using a 5 MHz phased array probe (Olympus Omniscan MX PA64). With increasing areal density the presence of tufts increased significantly the signal attenuation by up to 12 dB. Detail scans revealed the maximum attenuation to coincide with the position of the surface thread seams. Both thermally induced micro-cracks and unavoidable morphologic changes in the laminate, i.e. formation of resin rich pockets and fabric crimp around tuft and surface thread seams, appear to contribute to the signal attenuation. Hence, careful calibration of the ultrasonic scanning as typical instrument of quality control is required to distinguish between unavoidable morphologic changes and unacceptable infusion defects.

Chapter 5 Morphology of tufted composites

The study reported in this and the subsequent chapter aims to identify and quantify the effects of meso-structural fabric defects, introduced by the insertion of carbon thread tufts, on the in-plane mechanical properties of cured carbon fabric/epoxy composites. Resin transfer moulding (RTM) is chosen as the manufacturing route, as it ensures controlled high quality laminate infusion and comparable final laminate thicknesses irrespective of the areal density of tufting.

5.1 Introduction

Stitching and Z-pinning have been shown capable of conferring significant improvements to the mode I and mode II delamination crack resistance [27; 91-93] and overall out-of-plane damage tolerance [19; 94] of polymer matrix composite coupons containing such localised through-the-thickness reinforcement (TTR). The one-sided Z-Fiber® (Z-pinning) process is practically limited to the insertion of thin cured carbon/bismaleimide or titanium rods into uncured prepreg lay-up and is generally unsuitable for the reinforcement of composites made via the dry preform/liquid resin infusion processes. The process of structural lock stitching is suited to the through thickness modification of dry preforms, but requires double sided access. The technique of tufting, which is the topic of the present paper, has therefore been developed in recent years, to provide a suitable TTR alternative for the growing number of combinations of dry preforms, resins and processes entering the market. In this method a vertical thread loop is inserted into the dry preform from only one side, using a specially designed single needle. Dry thread loops are retained within the laminate by friction of the surrounding material while the needle retracts from the preform [85]. Significant improvements in the out-of-plane properties of tufted composites have been reported [85; 95], but there remains an uncertainty regarding the extent of the knock-down in their in-plane mechanical properties. While Dell'Anno et al [85] report a 10% drop in the tensile strength for a 5 harness woven composite tufted with 3 mm spaced glass thread, Koissin et al [96; 97] observe an increase in tensile strength by up to 17% for 5 mm spaced Kevlar tufted non-crimped and woven laminates with quasi-isotropic layup, with no change in the tensile modulus.

In recent reviews of studies on conventionally stitched polymer matrix composites Mouritz and Cox [1-3] point out that the characterisation of changes to the laminate meso-structure from the insertion of stitches is essential to understand the changes in macro-mechanical performance and to identify the associated failure mechanisms. Furthermore, close control of the laminate thickness is required in order to distinguish between effects due to the presence of the Z-reinforcement and any 'dilution' effect due simply to increased laminate thickness consequent on the greater bulk of the stitched material.

While extensive work has been conducted on the morphology characterisation of conventionally stitched [44; 86; 89; 90; 98; 99] and Z-pinned laminates [7; 22; 23; 26; 100-102], to date only very few studies have focused on structural characteristics of tufted composites [96; 97; 103]. In Z-pinned laminates, filament damage, in-plane fibre spreading around the inserted solid pin, and reduction of the global fibre volume fraction by increase in laminate thickness have been identified as main contributing factors to the consistently reported reductions of in-plane mechanical properties [7]. Chang et al [22] and Steeves and Fleck [26] found the maximum fibre distortion angles to reach between 4° and 14° in unidirectional carbon/epoxy laminates with 0.28 mm Z-pins at 3.5 mm and 1.75 mm spacing. This fibre waviness, coupled with some limited fibre damage from the actual Z-pin insertion, are considered as the cause of the observed 27% and 30% reduction in the uniaxial tensile and compressive strengths of the laminates respectively.

The insertion of a dry formable stitching thread into a dry fibrous preform and subsequent fabric compaction in the following manufacturing steps result in rather more complex changes in morphology; the fibre arrangement within the stitch itself is found to depend on laminate and thread material, layup, as well as on the detail of the further manufacturing processes [98]. Dry stitched preforms can be analysed fairly simply by photographic inspection but the structural analysis of infused and cured composites requires labour intensive sectioning and microscopy or the application of more sophisticated techniques such as X-ray micro-tomography [104]. In an early study on structurally stitched biaxial carbon fabric, Farley and Dickinson [105] identified the typical defects in stitched composites to be as follows: misalignment of the initially straight in-plane fabric tows around the stitch, fibre-free resin filled zones and channels between stitching yarn and deviated fabric, out-of-plane fabric crimp around surface thread seams, and breakage of in-plane fibres. The in-plane fibre misalignment was identified

as the main cause for the reported reductions in the in-plane strength and has been measured repeatedly, with deviation angles varying from 2.5° to 10° depending on fabric type and thread insertion parameters [90; 100; 101]. Quantification of the effects of other defects such as out-of-plane crimp and fibre breakage is very rare. Change in local fibre volume fraction from the compaction by the stitching yarn relies mostly on estimation of the averaged local fibre volume increase by taking the resin pocket volume into account [97; 98; 104]. Only Koissin et al. investigated the local fabric compaction in close vicinity to tufts, finding a local increase of up to 16% [96; 103].

Resin micro-cracking is a reported defect for both stitched and Z-pinned composites, as a result of residual stresses due to mismatch in coefficient of thermal expansion between Z-reinforcement and the surrounding composite material [104; 106; 107]. It can be postulated extensive micro-cracking may lead to the degradation of the hot-wet and fatigue performance of such laminates. To date only Sweeting et al have simulated the thermo-mechanical behaviour of Z-pinned laminates to investigate the influence of cure temperature and Z-reinforcement materials [107], identifying the cure temperature as critical cause for the micro-cracking.

5.2 Materials and manufacturing

Unidirectional $[0]_{10}$ preforms were prepared by assembling ten layers of uni-weave carbon fabric (OCV Technical Fabrics™, 310 g/m^2, 97% 12k Grafil 34-700), stabilised with a hot-melt weft yarn (3 wt% loading) to ease preform handling. A biaxial symmetrical $[(0/90)_s]_2$ preform was also made, from four layers of (0°/90°) carbon fibre non-crimped fabric (Sigmatex®, 1010 g/m^2, equal warp to weft content, 24k Tenax HTS). Each 0°/90° NCF layer was non-structurally stitched with a polyester binding yarn (8 g/km), in tricot/chain pattern parallel to the 0° of the fabric plies. Both of these dry preforms were then structurally tufted in our laboratory, with a high twist carbon fibre thread (Schappe Techniques®, 136 g/km, 2x1k Tenax HTA yarns). The tufting was carried out using an automated KSL KL 150 one-side tufting head, mounted onto a Kawasaki FN 20 six axes robot arm. Each panel was divided into three sections; one left untufted for control samples and the other two tufted with 5.6 mm x 5.6 mm and 2.8 mm x 2.8 mm square tufting pattern. The resulting areal tuft densities, 0.5% and 2% respectively, were determined from Eq. 5-1:

$$\rho_t(\%) = \frac{2 \cdot A_{th,dry}}{s_x \cdot s_y} \cdot 100 = \frac{2 \cdot T_{th}}{s_x \cdot s_y \cdot \rho_{f,th}} \cdot 100 \qquad \textbf{5-1}$$

where ρ_t is the areal tuft density (%), s_x the spacing along and s_y the distance between neighbouring tuft rows (mm), $A_{th,dry}$ the dry thread cross-section (mm^2), T_{th} the linear thread density (g/km) and $\rho_{f,th}$ the thread filament density (g/mm^3).

The loops were inserted vertically in a continuous seam at a rate of 400 tufts/minute under a constant thread tension of 12 cN, using a single hollow needle with square cross section of 1.5 x 1.8 mm^2. The tufting seams were aligned orthogonally to the ply orientation on the upper surface of the stack. A more detailed description of the automated tufting process can be found in [85].

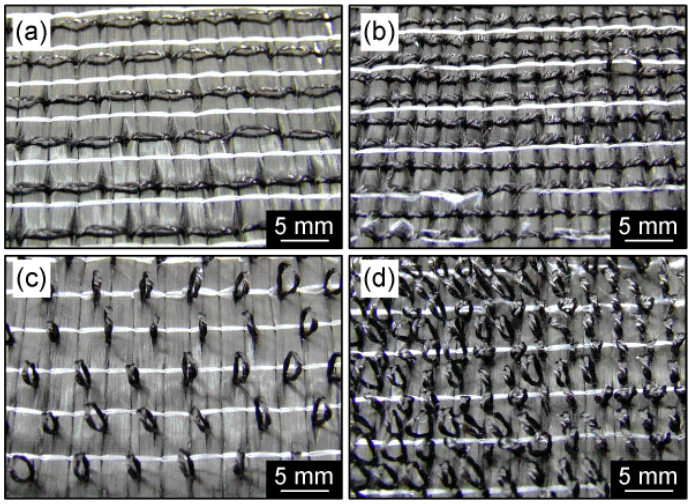

Figure 5.1 - Carbon tufted dry NCF preform with 0.5% (left) and 2.0% (right) areal tuft density: a) and b) tufting seams on thread side, c) and d) free carbon thread loops on loop side

Free loop ends, which protrude from the back of the dry stack (hereafter called "loop-side" as opposed to the "thread-side"), are bent over and become locked into a resin rich layer on the laminate surface during subsequent resin injection and cure. The free loop height was kept between 3 and 6 mm. Trials with shorter loop heights resulted in unsatisfactory variations in the loop formation as the holding force exerted by the surrounding fabric is quite low in the relatively thin composites. A 25mm thick Airex® R63 foam layer was placed underneath the preform to ensure sufficient compaction by the presser foot, full penetration of the tufting needle and uniform creation of free thread loops. A thin nylon film was placed between the foam and the carbon preform to avoid contamination of the latter, and to ease removal of the foam layer after tufting. Figure 5.1 illus-

trates the thread- and loop-sides of the tufted NCF preform for 0.5% and 2.0% areal tuft densities.

The tufted preforms were injected with the epoxy resin MVR 444 (Advanced Composites Group) in a rectangular aluminium mould tool using Isojet 3L RTM injection unit. The resin flow was regulated by keeping a constant injection pressure of 1 bar (± 0.01) and vacuum level of 10 mbar (± 5). After successful injection at 70°C, the resin was cured in the mould at 160°C for 75 minutes under 4 bar pressure, followed by freestanding postcure in an oven at 180°C for 90 minutes. Heating and cooling ramps were controlled at 2°C per minute.

Table 5.1 - Measured loop lengths for 0.5% and 2.0% tufted UD and NCF laminate

		Composite		Infused surface loop	
Fabric	ρ_t (%)	Thickness (mm)	$V_{f,2D}$ (%)	Length (mm)	Width (mm)
UD	0.0	3.09	54.4	-	-
	0.5	3.06	54.9	4.8 (0.5)	3.6 (0.6)
	2.0	3.17	53.0	4.9 (0.4)	2.9 (0.5)
NCF	0.0	4.26	53.1	-	-
	0.5	4.22	53.6	4.9 (0.5)	3.6 (0.4)
	2.0	4.29	52.7	3.6 (0.5)	2.6 (0.3)

Table 5.1 summarises the measured thicknesses of the cured laminates, average widths and lengths of the infused elliptical loop ends on the laminate surface and the theoretical in-plane fabric fibre volume fractions. Corresponding standard deviations are given in brackets. For comparison of meso-structural detail between the different laminates, the aim was to achieve equal fabric fibre packing and average loop lengths in all cases. While the thickness within each section varied by less than 0.02 mm, a small but consistent increase was noted for the 2% areal density tufted composite sections. The fact that this has happened even with rigid mould tooling, indicates the cause to be the increased preform bulk, from the addition of the tufting thread. The fabric fibre volume fraction $V_{f,2D}$ is derived from the number of plies, the measured areal weight and the density of in-plane filaments.

The cured panels were scanned ultrasonically with a phased array probe (Olympus Omniscan MX PA64). The presence of tufts increases the attenuation of the ultrasonic signal which can be attributed to the presence of resin rich regions around them. Optical

micrographs were taken of polished in- and out-of-plane sections, which verified complete resin wet-out of the tufting threads and very low void content in all control panels.

5.3 Morphology characterisation

The robot was set up to deliver a square tuft arrangement. However, it needs to be recognised that the final local tuft pattern within each ply will depend on the orientation between tufting rows and ply fibre direction, as well as on the precision of the automated thread insertion. Slight imperfections in the robot control of the needle movement during the initial acceleration phase of each tuft row caused some individual rows to shift, resulting in a quasi-triangular tuft arrangement for a small number of tuft rows. Any such shift potentially affects the meso-structure of the tufted laminate (see Figure 5.1 a).

Square samples with an edge length of 25mm, taken at different locations in the tufted regions, were sectioned and polished metallographically to identify and quantify the tuft induced repetitive fabric defects. Within each sample, the coordinate system is defined as follows: the x-axis is parallel to the orientation of the undeviated 0° plies, the y-axis is normal to the fibre direction in the fabric plane and the z-axis is orthogonal to the fabric plane. In order to extract a full 3D morphology by analysing 2D sections of the composite , half the samples were repeatedly sectioned at one quarter, one half and three quarter of the plate thickness (along the x-y plane); the other half were sectioned along the x-z plane (orthogonal to the tuft row direction) through and between subsequent tufts. Micrographs of 25 to 50 individual tufts were processed with the imaging software AcQuis 4.0.1 to measure the dimensions of the repetitive defects around the tufts. As the fabric defects potentially depend on the local tuft arrangement, samples of both square and triangular tuft patterns were analysed. The latter were taken from plate sections where the offset between at least three adjacent tufting rows was sufficient to provide a quasi-triangular tuft pattern.

Total fibre volume fraction values were determined on at least three samples from their measured densities and confirmed by acid digestion of the same samples (BS EN 2564:1998). The required density values for the epoxy resin (1.157 g/cm^3), HTS 40 (1.769 g/cm^3) and Grafil 37-700 filaments (1.786 g/cm^3) were determined separately by the standard immersion method (BS EN ISO 1183:2004 and BS ISO 10119:2002).

5.4 Results and discussion

Figure 5.2 shows a schematic of the tuft within the composite, with the selected planes for sectioning and typical fabric disruptions around the tuft.

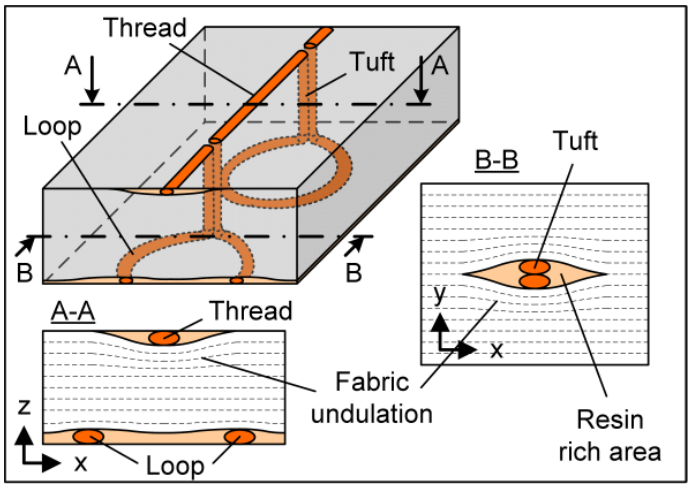

Figure 5.2 - Schematic of tufted UD sample with the planes of sectioning

5.4.1 In-plane defects (plane x-y)

5.4.1.1 Tow misalignment and resin rich pockets

As illustrated in Figure 5.3, fabric fibre misalignment is the most prominent in-plane laminate disruption which is caused by the insertion of the tufts. In order to accommodate the tufting thread, the initially straight fibres within each ply have to spread around the impelled needle, creating a lasting fibre free-zone which subsequently gets filled with resin during the injection step. The resin pockets have a rhombic shape with elongation oriented along the local ply direction.

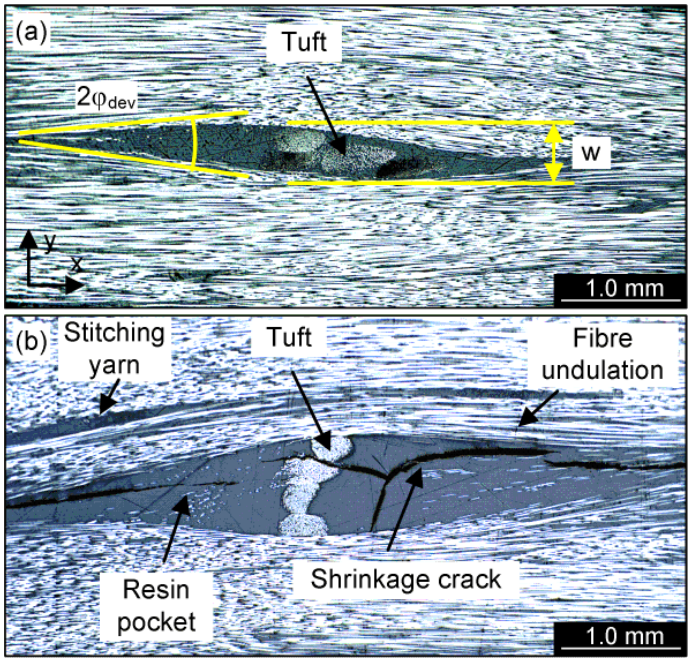

Figure 5.3 - In-plane section of 0.5% tufted a) UD and b) NCF cured composite, showing typical fabric disruptions

The fabric deviates most from the initial ply direction at the flanks of the resin rich pocket, identified as the maximum fibre deviation angle φ_{dev}. With increasing lateral distance from the resin pocket the undulated fibres straighten and align with the global ply orientation until no further differentiation is possible. The area of misaligned fibres can be determined by the fibre free pocket length L and maximum lateral width w_{dev} of undulated fibres, measured orthogonal to the ply orientation around the tuft. As both uni-weave and non-structurally stitched fabrics exhibit natural fibre waviness, visual determination of maximum undulation width is subject to a certain degree of uncertainty.

Table 5.2 summarises the average dimensions of the in-plane imperfections. The internal fibre volume fraction within the infused tuft is calculated by the ratio of measured infused cross-section A_t to theoretical dry tuft fibre area. Pocket width w values were up to 53% higher for the fibre free zones of the non-crimped fabric compared to those in the unidirectional samples (see Figure 5.3). While the uniform orientation of the unidirectional plies allows the tuft yarns to spread and fill the resin rich zones, crossing plies of the NCF laminate compact the tuft into a quasi-circular shape of increased lateral diameter and higher internal fibre packing, forcing the fabric wider apart. Additionally, it is assumed that friction between the orthogonal fabric plies of NCF at mould closure

limits the redistribution of the misaligned fibres, which have to spread significantly further in this dry preform to allow the penetration of the large diameter needle.

Table 5.2 - Measured dimensions of in-plane fabric defects around tufts in triangular and square arrangement (Std.dev. in brackets)

			Resin pocket dimensions			Fabric deviation		Tuft
Fabric	ρ_t	Pattern	Max. width w	Min. width w_{min}	Length L	Width w_{dev}	Angle φ_{dev}	$V_{f,t}$
	(%)		(mm)	(mm)	(mm)	(mm)	(°)	(%)
UD	0.5	Squ.	0.48 (0.06)	0.16 (0.04)	-	2.8 (0.2)	4.6 (0.7)	49.4 (5.8)
	0.5	Tri.	0.43 (0.07)	-	5.31 (0.4)	2.6 (0.3)	4.7 (0.4)	51.3 (5.9)
	2.0	Squ.	0.29 (0.04)	0.21 (0.04)	-	1.5 (0.2)	3.4 (0.7)	53.7 (4.1)
	2.0	Tri.	0.30 (0.04)	-	3.20 (0.2)	-	6.3 (0.9)	52.6 (6.0)
NCF	0.5	Squ.	0.73 (0.06)	0.32 (0.04)	-	3.9 (0.3)	7.3 (1.1)	61.0 (6.5)
	0.5	Tri.	0.60 (0.04)	-	4.99 (0.5)	3.6 (0.3)	7.6 (1.3)	62.6 (3.2)
	2.0	Squ.	0.61 (0.05)	0.39 (0.04)	-	1.9 (0.2)	3.9 (0.9)	55.9 (5.5)
	2.0	Tri.	0.52 (0.04)	-	3.61 (0.3)	-	8.9 (0.8)	63.6 (4.2)

Fibre free zones around the non-structural stitching between single NCF layers have widths an order of magnitude smaller than the structural tufting pockets (see Figure 5.3 b).

Variable spreading of the formable tufting yarns along the plies explains the similar pocket lengths in UD and NCF laminates, even if the pockets in biaxial layup are spread further apart. This differs from studies on Z-pinned composites, where a wider pocket width was directly related to longer fibre free pockets [25].

The lengths of the fibre free zones were found to reduce with increased tuft density in regions with triangular arrangement of tufts; as the tufts get closer together the fibre tows have to weave more tightly between them. In contrast, square tuft arrangement with 5.6 mm spacing is sufficient for the resin filled pockets to join into continuous channels in both types of fabric.

For both fabric types and tuft arrangements the maximum width of fibre free zones in direct vicinity of the tufts is reduced with reduced tuft spacing. However, in joined resin channels for square tuft arrangement closer spaced tufts restricted increasingly the closure of the resin rich channels with deviating fabric, leading to relatively wider channel width w_{min} at the centre point between adjacent tufts (see Figure 5.4 b).

Even for perfectly aligned tuft arrangement along the 0° fabric plies local bridging of the resin rich channels by single fibre tows could not be avoided due to natural fabric fibre waviness (see Figure 5.4 a) to c)). However, the volume of bridging fibres was found to be negligible.

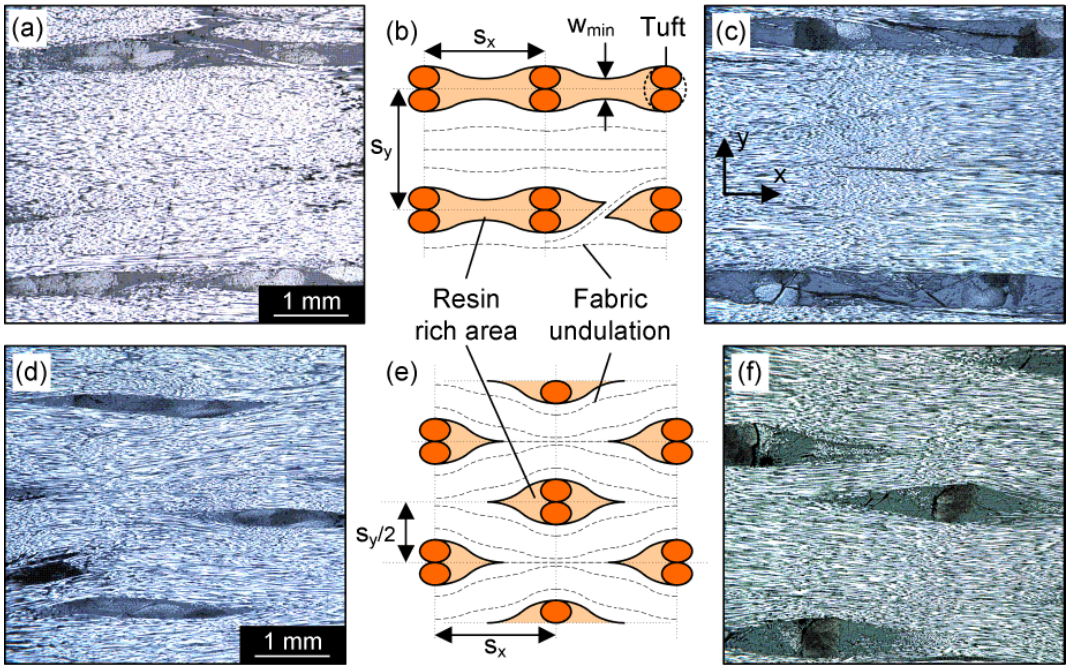

Figure 5.4 - Fibre free zones in unidirectional (left) and non-crimp fabric laminates (right) at 2% areal tuft density: a) – c) typical geometric features of resin rich channels in square arrangement, d) – e) separate resin pockets in triangular arrangement

Measurements at ¼, ½ and ¾ of the specimen thickness revealed no significant differences in pocket length and width as the tuft is inserted at very low tension. Hence, only averaged width and length values at the sample mid-plane are stated in Table 5.2. This observation differs from what is seen in conventionally stitched laminates, where thread tension is cause for significant local fibre nestling and creation of resin regions on the surface of the cured plate [99; 104].

The maximum angle of fibre misalignment appears to be directly related to the pocket length and width and can be estimated by the simple relation $\varphi_{dev} = arctan((w\text{-}w_{min})/L)$. At low tuft density, no significant difference was observed between angles in triangular and square pattern. With increasing density, the two tuft arrangements cause opposing effects on the fibre misalignment. If the tuft spacing is reduced from 5.6 mm to 2.8 mm in triangular arrangement the deviation angles increase for both UD and NCF case, from 4.6° and 7.3° to 6.3° and 8.9° respectively. In contrast, for 2% density square arranged

tufts the maximum angles reduce to only 3.4° and 3.9° in UD and NCF laminate respectively as the fabric plies straighten along the resin rich channels (see Figure 5.4). The observed misalignment angles around tufts at low density agree with previous study by Chang [7] for Z-pinned unidirectional prepreg, where a maximum deviation angle of 5.4° was observed for a comparable pocket width of 0.51 mm.

At higher tufting densities width of the area of misaligned filaments around the resin pocket increases linearly with increasing tuft spacing, keeping a constant ratio of deviated to straight fabric tows of 0.5 and 0.7 for UD and NCF fabrics respectively. Only at close spacing and triangular arrangement the total volume of fabric is forced to weave harmonically around the tufts (see Figure 5.4 d + f). From the difference between UD and NCF tufted composites it becomes apparent that the resin pocket width directly affects the total volume of misaligned fabric.

5.4.1.2 Fabric filament breakage (plane x-y)

The question of just how many of the fabric in-plane filaments get broken by penetration of the sewing needle into the dry preform [93], or the insertion of a Z-pin into uncured pre-preg [7] remains largely unanswered, other than the limited experimental data on the in-plane property knock-downs. In this study, visual inspection of single dry preform layers, which were tufted with and without thread, revealed a comparable, relatively low frequency of broken filaments. The specific design of the tufting needle, i.e. relatively blunt needle tip and sharp edges on the square needle shaft, seems to be the main source of the damage. In the infused composite, the broken filaments do not follow the undulation of the intact filaments, but protrude into the resin zones (see Figure 5.5). Accurate microscopic quantification of the total broken fibre content is clearly not feasible and accurate determination of the relevant mechanical property changes remains the sensible option for evaluation of this effect (see Chapter 6).

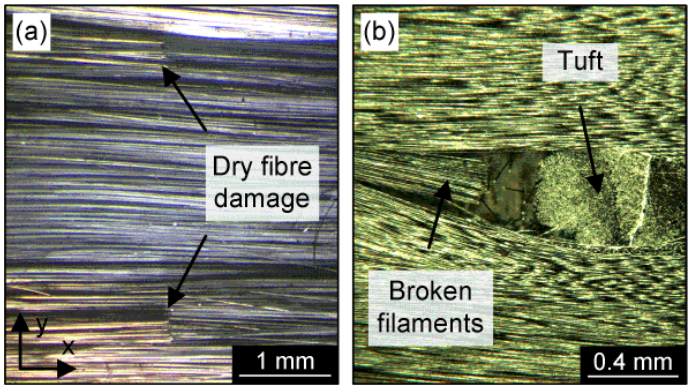

Figure 5.5 - Fabric damage and filament breakage in: a) tufted preform without thread, b) resin pocket of infused composite

5.4.1.3 Micro-cracking in resin-rich pockets

Local debonding of the tufts from the surrounding resin and splitting cracks between the tuft yarns were observed in the majority of the resin rich regions within the untested NCF composite for both 0.5% and 2.0% areal tuft densities, while fewer than 10% of the resin pockets in the unidirectional plates contained such features. As thermal stresses and thermal expansion coefficient mismatch are the most likely causes of this micro-cracking [107] the increased amount of cracking in the non-crimped fabric may be explained by restricted lateral shrinkage of the relatively large resin pockets in bidirectional laminate layup.

Most micro-cracks were found in close vicinity of the tuft and between the two tufting threads. Splitting between the tufting yarns appears to be caused by unequal straightness of the two threads. In closely spaced square tuft arrangement such cracks were also found to propagate along the joined resin rich channels (see Figure 5.4).

5.4.2 Out-of-plane defects (plane x-z and y-z)

Figure 5.6 illustrates the typical out-of-plane morphological features observed in unidirectional and non-crimp fabric tufted composites.

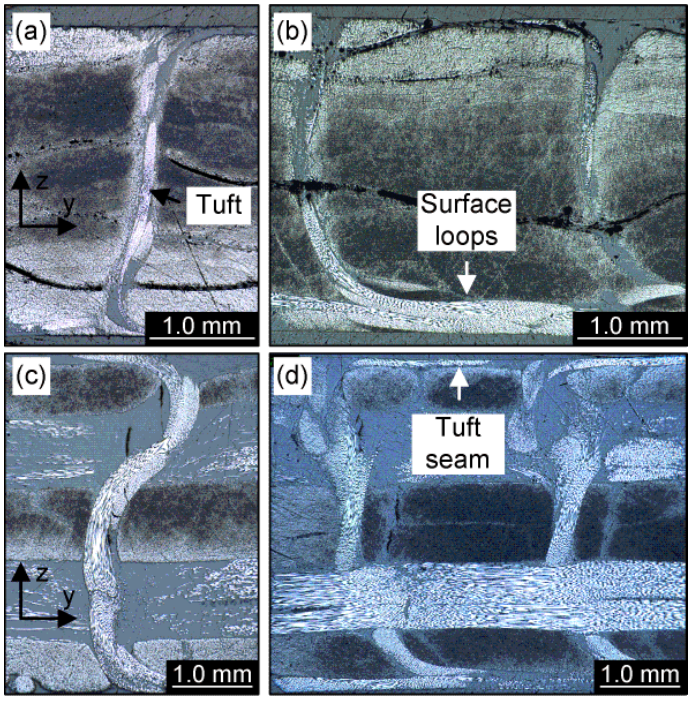

Figure 5.6 - Out-of-plane tuft features (y-z section) in 0.5% (left) and 2% (right) tufted composites: a) and b) unidirectional layup, c) and d) biaxial non-crimped fabric composite

5.4.2.1 Surface resin-rich layers

During mould closure the tufting seams indent into the preform surface, causing local out-of-plane fibre crimp in the (top-face) surface plies. This is a known effect, found also in conventionally stitched composites [108]. Individual resin rich regions are then created around each thread seam where fibres undulate away from the laminate surface (see Figure 5.7 a)). In contrast to the joined-up channels in the x-y plane, the local resin rich regions around the tuft seams remain separated even for tuft density of 2%; the single thread on the surface has half the cross-section of the through-the-thickness tuft.

For 5.6 mm spacing the tuft loop ends on the opposing (back-face) surface have been kept short enough to avoid overlapping. For 2.8 mm spacing they do overlap, in random orientations, leading to the creation of a resin rich layer of fairly uniform thickness.

In order to characterise the top-face (thread) and back-face (loop) layers, their average thicknesses, t_{th} and t_l respectively, were determined together with the maximum fibre deviation $t_{th,max}$ and crimp angle φ_{th} at the thread seam. Table 5.3 summarises the measured dimensions of these defects in 0.5% and 2% tufted UD and NCF composites.

The formation of the resin rich layers appears not to depend on the tufting pattern and thus all values are given as average for triangular and square arrangements. Furthermore, the measured thicknesses are similar for the tufted UD and NCF composites as both have similar global fabric fibre volume fractions and comparable free loop lengths.

Table 5.3 - Measured dimensions of out-of-plane fabric defects (Std.dev. in brackets)

Fabric	ρ_t (%)	Loop layer	Thread layer		
		av. t_l (mm)	max. $t_{th,max}$ (mm)	av. t_{th} (mm)	max. φ_{th} (°)
UD	0.5	0.16 (0.05)	0.18 (0.02)	0.08 (0.03)	2.8 (0.7)
	2.0	0.33 (0.05)	0.11 (0.01)	0.07 (0.01)	5.0 (1.0)
NCF	0.5	0.23 (0.06)	0.16 (0.02)	0.08 (0.02)	4.4 (0.8)
	2.0	0.30 (0.03)	0.14 (0.04)	0.09 (0.02)	6.5 (1.2)

In all cases the loop layer is significantly thicker than the thread layer, reaching up to 0.33 mm. This becomes most significant for thin panels, accounting for over 10% of the total thickness in the tufted UD composite.

In contrast to randomly oriented surface loops the repetitive indentation of thread seams into the top-face of the composite caused the outermost fabric plies to crimp at angles up to 6.5° from the surface plane. Surface crimp affected typically a zone of less than 0.5 mm from the composite surface (see Figure 5.7 a).

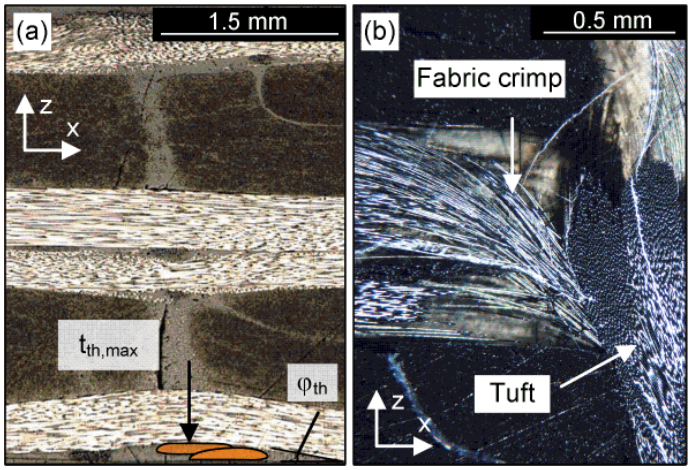

Figure 5.7 - Micrographs (x-z plane) of out-of-plane fibre crimp in 0.5% tufted NCF: a) surface crimp around tuft seam, b) internal crimp of broken filaments close to tuft (darkfield)

Additional crimped fibre bundles away from the laminate surface, as depicted in Figure 5.7 b) were identified as broken filaments, which were severed and undulated during

needle penetration. Similar to Z-pinned laminates [7], these crimped fibres were confined to the resin rich pockets in direct vicinity of the tufts.

5.4.2.2 Tuft kinking

A disadvantage of the tension-free tuft insertion is the potential misalignment of the vertical tuft as the preform is compacted during mould closure. By applying a local pressure of up to 0.18 MPa with the presser foot on the preform during the tufting process it could be ensured that the tuft remained straight during preform compaction. However, the outermost plies appear to have shifted to enable the relatively stiff free carbon tuft loops to bend onto the laminate surface. Hence, relatively large curvature of the otherwise straight vertical tuft was observed in the outermost plies (see Figure 5.6).

5.4.3 Determination of global and local fibre volume fractions

While the manufacturing with rigid mould tooling of constant cavity size aims to keep a constant fabric fibre volume fraction within the panels, the addition of tufts affects both the total and local fibre volume fraction of the laminate.

In general, the addition of tufting thread to the constant volume of fabric (2D equivalent) increases the total measurable fibre volume fraction within the tufted samples depending on the tuft spacing, the length of the structural through-the-thickness component of the tuft and the free loop length on the laminate surface.

By adding the infused surface loop circumference, which can be derived from the measured minimum and maximum extension of the elliptically shaped tuft loop, the surface thread length and the laminate thickness for each tuft unit cell the added thread volume fraction can be estimated according to equation 5-2:

$$V_{f,thread}(\%) = \frac{\left(2l_l + s_y + 2t\right) \cdot T}{s_x \cdot s_y \cdot t \cdot \rho_f} \cdot 100 \qquad \textbf{5-2}$$

where l_l is the surface loop height (mm), T is the linear thread weight (g/km) and ρ_f is the thread fibre density (g/cm^3).

The total fibre volume fraction $V_{f,tot}$ results from the sum of 2D equivalent fabric fibre volume and the contribution of the tufting thread for a given cavity thickness. Table 5.4

summarises the theoretical thread and the total fibre volume fractions, determined from density measurements and by acid digestion, for the different samples. The theoretical estimation of the thread fibre volume fraction is in close agreement with the measured differences in the total fibre volume content values between control samples and the samples at the two different tufting densities. Density and acid digestion methods give comparable total fibre volume fractions as long as the void content is small. In control and 0.5% tufted laminates the measured void content is negligible thanks to the RTM manufacturing route; however, in the 2% tufted NCF laminate the thermally induced micro-cracks in resin rich regions create up to 2% void volume. While the addition of tufting thread at 5.6 mm spacing increases the total fibre volume by up to 1.8%, close tuft spacing can cause an increase of 7%. For the relatively thin composites of this study and the chosen free loop lengths, the structurally important through-the-thickness segment of the tuft contributes only one third of the additional fibre volume, with the majority accounted for by thread seams and loops on the external surfaces.

Table 5.4 - Table: Comparison of calculated and measured total fibre volume fraction (Std.dev. in brackets)

Fabric	ρ_t (%)	Theoretical	Density measurement		Acid Digestion
		$V_{f,\text{thread}}$ (%)	Total $V_{f,tot}$ (%)	Total $V_{f,tot}$ (%)	V_{void} (%)
UD 90°	0.0	-	53.8 (0.4)	53.5	0.1
	0.5	1.68 (0.03)	55.5 (0.2)	55.4	0.4
	2.0	5.25 (0.29)	60.9 (0.7)	61.2	1.1
NCF	0.0	-	51.9 (1.2)	50.2	0.1
	0.5	1.38 (0.06)	53.9 (0.9)	56.1	0.8
	2.0	5.39 (0.24)	56.8 (0.2)	60.4	2.0

Locally, the insertion of tufts affects the fabric fibre packing within the plies in two ways: - the lateral in-plane fabric spreading around the Z-reinforcement and the fabric compression by the loop and thread layers on the external surfaces. In order to accommodate the tuft, the composite has to compress locally between neighbouring resin rich pockets and the resin rich surface layers as expansion in the thickness direction is restricted by the rigid mould tool. For square tuft arrangement, the local increase can be estimated with the simple equation 5-3:

$$V_{f,i}(\%) = V_{f,2D} \cdot \frac{t}{(t - t_{th} - t_l)} \cdot \frac{s_y}{s_y - w_i} \qquad \textbf{5-3}$$

where t_{th} is the resin-rich thread layer thickness (mm), t_l the resin-rich loop layer thickness (mm), and w_i the local width along the resin pocket (mm). Maximum compaction $V_{f,max}$ is reached for $w_i = w$ (maximum pocket width).

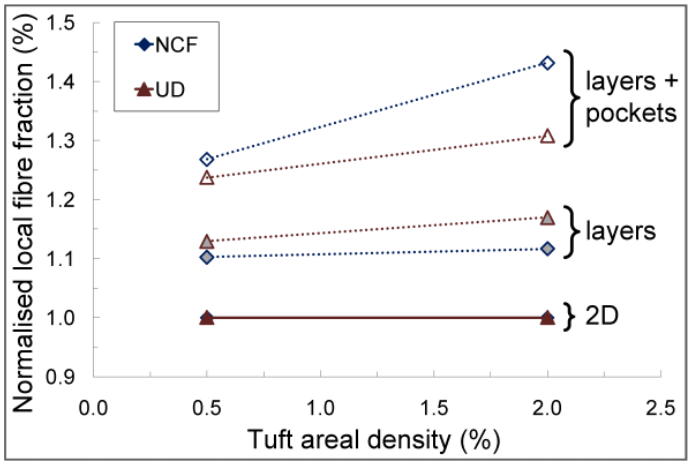

Figure 5.8 - Calculated contributions to local laminate compaction by resin rich pockets, surface loop and thread layers

Figure 5.8 illustrates the estimated relative contributions of pocket width and resin rich surface layers to the undisturbed fabric fibre volume fraction, normalised by the 2D equivalent fibre volume content of UD and NCF composites. The values are derived for square tuft arrangement from the measured maximum pocket widths, average loop layer and maximum thread layer thicknesses. It becomes clear that in thinner samples and samples with shorter pocket width the loop side layer causes the most significant increase in the local fibre volume fraction, from 55% up to 64% in the 2% tufted UD case. For the thicker NCF samples, the effect of resin rich surface layers is exceeded by the existence of wider resin filled pockets, with local fibre volume fraction (77%) approaching the theoretical packing limit for square fibre packing. Such increase in local fibre packing affects the geometry of the fabric imperfection as the highly compressed fabric plies exert an increased pressure on the tuft, surface loops and thread seams. This explains the previously noted reduction in maximum thread layer thickness and resin pocket width for increasing tuft density.

The validity of equation 5-3 was tested, by measuring the local fibre distribution between and away from two neighbouring tufts in square arrangement, for at least 5 locations, in 0.5% and 2% tufted UD and NCF composites. The ratio of filament to resin area was determined from the automated filament count in equally spaced 0.25 mm wide analysis cells along the fabric mid-plane between two tuft rows, which were taken

from contrast enhanced binary micro-sections according to [109]. As illustrated in Figure 5.9, close agreement was found for the theoretical and actual local fibre volume fractions.

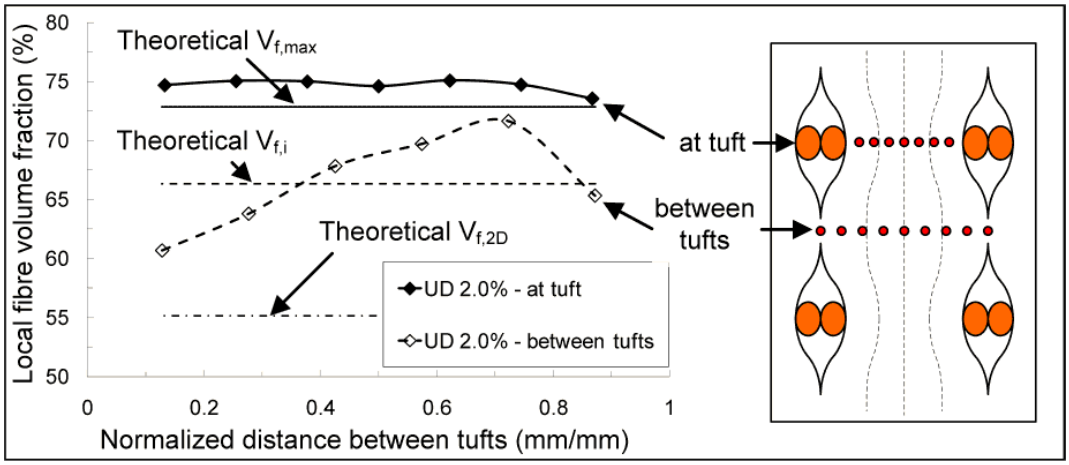

Figure 5.9 - Measured versus theoretical distribution of local fibre volume fraction in compacted plies of 2% tufted unidirectional composite

5.5 Conclusions

The major factors determining the details of the meso-structure of tufted cured composites, other than the initial preform structure, are the tuft spacing, the tuft array geometry and the free loop length. Under the manufacturing conditions in resin-transfer moulding, the detail of fabric layup determines the final cross-sectional shape of the infused and cured tuft by assisting (UD) or restricting (biaxial NCF) its spread within the surrounding resin rich zones. The measured increase in local fibre packing potentially affects the resin permeability of the preform in the clamped tool [50] and may enhance the formation of thermally induced micro-cracks.

Reduction in tuft spacing leads to smaller resin pockets, as the local fibre packing density increases between the tufts to accommodate the increasing volume of resin rich regions. However, its exact effect on in-plane fibre misalignment depends on the tuft arrangement, being significantly different for cases of tufts arranged in locally square or triangular patterns. This points to the need for high positional accuracy and reproducibility of the tufting process, in order to arrive at consistent sample morphologies and hence consistent mechanical properties.

Chapter 6 In-plane tension, compression and shear behaviour of tufted composites

6.1 Introduction

To date, the literature on Z-direction reinforced polymer matrix composites remains dominated by studies of their delamination resistance [27; 91; 92; 110-112] and by the development of associated models [113-118]. The attractiveness of stitching, Z-pinning [5; 7] and, more recently, tufting [85; 95] in terms of their ability to improve greatly the load-carrying capability/damage resistance of continuous fibre reinforced composite structures is now well established.

In a recent extensive review of studies of through-the-thickness reinforced polymer matrix composites Mouritz and Cox [3] point out the current need for better determination of the in-plane properties of such locally reinforced composites and for establishing of the relationships between their meso-structural characteristics and their mechanical properties. The basic question is whether sufficient improvement in the out-of-plane properties can be achieved without unacceptable detriment to the in-plane properties of through-the-thickness reinforced (TTR) composites. The work reported here aims to provide part of the answer for the specific case of tufted epoxy matrix carbon fibre composites, for a variety of fabric geometries.

6.2 Literature overview

The reader is referred to the above mentioned recent review by Mouritz and Cox [3] for comprehensive treatment, but some findings particularly relevant to the in-plane tensile, compressive and shear properties of traditionally stitched composites are summarised here, as a backdrop for the new data to be reported. All these findings relate to thermosetting composites obtained by traditional two-sided stitching of dry fabric preforms, followed by liquid resin infusion and cure. The stitching thread materials are typically aramid or carbon. There is very little reported work on the relatively simple case of stitched unidirectional fabric layup, as handling and stitching of the dry UD / pseudo-UD preforms has proved to be difficult [99].The majority of studies, irrespective of fab-

ric type, found stitching to have no effect on the elastic axial tensile stiffness [1-3; 119; 120], although a few report a tensile modulus reduction by up to 15% [94; 95; 121]. Kamiya [122] reported no reduction for areal density of stitching of 1.7%, but does observe a stiffness reduction of 10% when stitching densities are 3.4% and 5.1%. It must be pointed out that the latter two are very high areal densities of stitching, probably higher than would be of any practical use.

Both reduction and increase in the tensile strength of stitched composites have been reported, with the difference always below 20% of the value measured in the control, unstitched samples [85; 94-96; 119; 120; 123; 124]. The cases where an increase in strength was observed seem to involve stitching seams aligned with the test direction or the lay-up containing off-axis plies.

Stringer and Hiley found a small reduction (<10%) in the tensile strength of QI composites, stitched with Kevlar thread at 0.5% density, but report a 40% improvement in the compressive strength [93]. There is no obvious cause for this increase; indeed, given the probable mis-alignment of fabric tows around the stitching yarns it may be reasonable to expect a lowering of the resistance of the composite to uni-axial in-plane compression [125]. Indeed, Reeder showed in a linear bearing compression test of quasi-isotropic laminates that stitching reduces the compression strength by up to 20% due to local fibre misalignment in the load bearing 0° plies, if global buckling is avoided [101].

Surface kinking and bending due to loops in biaxial (0°/90°) stitched composites under compression in short block arrangement reduces the compressive strength by up to 35% [105; 108]. Beier et al reported no change in compressive modulus for 0.1% polyester stitched biaxial NCF, but a reduction in strength of 17% [86].

Relatively few studies report results on in-plane shear measurements in stitched composites. Given the matrix dominated response, and the role of stitching in limiting delamination, then the shear strength increase reported by Aymerich [124] in QI and (±30°/90°) fabrics stitched with Kevlar might be expected. However, recent comprehensive study by Hess and Himmel reports 15% reduction of shear modulus and a 9 – 22% reduction in shear strength in QI carbon NCF based materials. The reduction in properties is more severe when thicker thread and higher density of stitching are used [126]. There is similar polarity in results from ILSS tests on stitched composites [127, 128].

Whilst there has been a recent upsurge in industry activity in tufted composites, the publically available database on in-plane properties in such materials is extremely limited, and already showing signs of apparently opposing findings [85; 95-97].

It becomes clear that no definitive agreement on the effects of any kind of stitching, or tufting, on the properties of the final composites is likely to be achieved without a wider database, supported fully by meso-structural characterisation of the materials being tested. The first part of this study in Chapter 5 therefore involved a detailed morphology characterisation of tufted pseudo-UD and of a biaxial non-crimped fabric preform and its resulting composite. These materials, and additional tufted fabric types, are now characterised for their in-plane tension, compression and shear properties. Digital image correlation, ultrasonic scanning and conventional micrography are used before, during and after testing to determine the criticality of the identified structural imperfections on the in-plane damage evolution and failure mechanisms between control and tufted composites.

6.3 Materials and manufacturing

In order to explore the effect of tufting on a representative range of current carbon fibre fabric architectures, the samples for mechanical testing were prepared from the following preforms:

- $[0]_7$ and $[0]_{10}$ unidirectional stacking, assembled of uni-weave carbon fabric layers (OCV Technical Fabrics™, 310 g/m^2, 97% 12k Grafil 34-700), stabilised with 3% hot-melt weft yarns;

- $[(\pm 45)_s]_2$ biaxial NCF stacking, assembled from four carbon fibre (±45°) non-crimped fabric layers (Sigmatex®, 1010 g/m^2, equal warp to weft content 24k Tenax HTS), non-structurally stitched 45° to the ply orientation with polyester thread (8 g/km) in chain pattern;

- $[(0/90)_s]_2$ biaxial preform, from four layers of carbon fibre (0°/90°) non-crimped fabric (Sigmatex®, 1010 g/m^2, equal warp to weft content 24k Tenax HTS), non-structurally stitched with polyester binding yarn (8 g/km) in tricot/chain pattern parallel to the 0° of the fabric plies.

- $[(0/90)]_{3s}$ and $[(\pm 45)]_{3s}$ biaxial preforms of six 2x2 twill woven carbon fabric layers (OCV Technical Fabrics™, 650 g/m^2, equal warp to weft content 12k Grafil 34-700).

Each preform was divided into equal section of control, 0.5% and 2% tufted areas. High twist carbon fibre thread loops (Schappe Techniques®, 136 g/km, 2x1k Tenax HTA yarns) were inserted vertically through the full laminate thickness via the automated tufting process using a KSL KL 150 tufting head, mounted on a six-axes Kawasaki FN20 robot arm. Tufts in neighbouring rows were aligned to each other in square arrangement of 5.6 mm and 2.8 mm spacing, corresponding to 0.5% and 2% areal tuft density. Thread seams in the unidirectional and [0°/90°] preforms were aligned orthogonal to the 0° ply orientation. In the ±45° preforms tuft seams were inserted at 45° to the main ply orientations to avoid asymmetry effects. Injection of the preforms with the epoxy resin MVR 444 (Advanced Composites Group) and the subsequent cure were carried out as described in Chapter 5. Table 6.1 summarises the types of manufactured composite panels, its use for in-plane tension, compression or shear testing, and the widths and lengths of the infused elliptical loop ends on the laminate backside.

Table 6.1 - Measured loop lengths for 0.5 and 2.0% tufted UD, NCF and twill woven composite (Std.dev. in brackets)

Layup	Test	Tufting	Backside loop	
		ρ_t (%)	Length (mm)	Width (mm)
UD $[0]_7$	0° - T	0.5	5.2 (0.5)	3.7 (0.6)
		2.0	4.2 (0.5)	2.9 (0.5)
UD $[0]_{10}$	90° - T, 0° - C	0.5	4.8 (0.5)	3.6 (0.6)
		2.0	4.9 (0.4)	2.9 (0.5)
NCF [0/90]	0° - T/C	0.5	4.9 (0.5)	3.6 (0.4)
		2.0	3.6 (0.5)	2.6 (0.3)
NCF [±45]	±45° - Shear	0.5	5.0 (0.4)	3.7 (0.4)
		2.0	4.7 (0.3)	3.2 (0.4)
Twill [0/90]	0° - T/C	0.5	6.0 (0.7)	4.3 (0.6)
		2.0	5.5 (0.2)	3.1 (0.4)
Twill [±45]	±45° - Shear	0.5	3.5 (0.4)	2.4 (0.2)
		2.0	3.8 (0.4)	2.8 (0.4)

The thickness and according 2D equivalent in-plane fabric fibre volume fractions for different areal tuft densities ρ_t can be found in the result tables of each test. While the thickness measurements for each section within the panels varied by less than 0.002 mm, a small increase in thickness of up to 3% was measured for the 2% tufted laminates. This can be attributed to the increased fabric bulk factor due to addition of closely spaced tuft loops. The 2D equivalent fabric fibre volume fraction is derived from the

number and areal weight of assembled fabric layers for the given laminate thicknesses. As stated in the first part of this study, the addition of 5.6 mm and 2.8 mm spaced tufting thread loops of the given length in Table 6.1 to the global fabric volume increases the overall measurable fibre volume fraction by 1.8% and 7% respectively, of which over two third are contributed by the non-structural tuft segments of surface thread seams and loops and only one third by the structural through-the-thickness segment of the tuft.

6.3.1 Meso-structure

Figure 6.1 shows the in- and out-of-plane sections of the 2% tufted [0°/90°] twill woven composite. Although differing most from the preforms characterised in Part I of this study the same typical fabric defects around the tuft were noted: - in-plane fibre misalignment, resin rich zones (channels) and thermal micro-cracking around the tuft, out-of-plane fabric fibre crimp at the tufting seams, increase in local fibre packing and resin rich layers to accommodate loop ends and thread seams on the composite surface, with dimensions of comparable size as those found in the NCF based composites for a given tuft density. However, the range of defect sizes in the tufted twill fabric was significantly higher than that observed in NCF as the exact location of the tuft within the weave pattern affects the extent and maximum in-plane fibre misalignment, especially if the tuft is located at the cross-over of weft and warp tows. Furthermore, out-of-plane fabric weave increases at the intersections of warp and weft tows as the fabric is compacted by the resin rich layers on the surface. Indentation of the thread seams on the composite surface superposes onto the natural fabric waviness, leading to random reduction or amplification of the surface fabric weave.

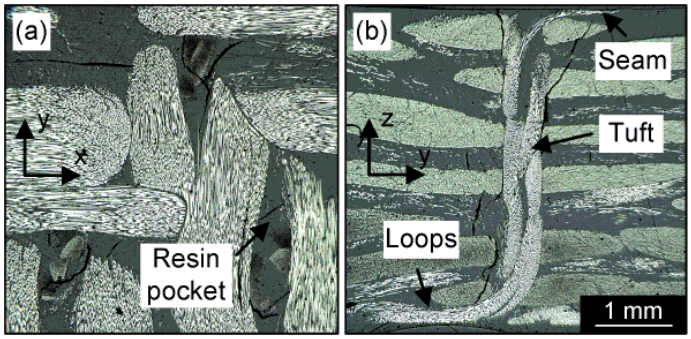

Figure 6.1 – Meso-structure of 2% tufted twill woven composite: a) in-plane and b) out-of-plane sections through tufts within resin rich pockets

While the alignment of the tufting seams with the transverse fibre direction results in a square tuft arrangement within the [0°/90°] laminates, the orientation with the bias fibre direction in the [±45°] laminates results in a triangular configuration.

6.4 Experimental

6.4.1 Sample preparation

Figure 6.2 illustrates the chosen specimen dimensions and tuft arrangements for the in-plane tension, compression and shear tests. Specimens were dry cut from the cured plates with a circular diamond coated blade. NCF and twill woven [0°/90°] samples were taken along the 0° direction of the laminate, orthogonal to the tufting seams. The thread seam direction coincided with the loading direction only in the case of the unidirectional transverse tension test (90°). Unidirectional samples were taken from the $[0]_7$ and $[0]_{10}$ laminates for tensile testing in longitudinal (0°) and transverse (90°) directions respectively. Samples for in-plane shear testing were cut from separately manufactured [±45°] layup with tufting seams orthogonal to the loading direction, aligned 45° to the ply fibre orientation.

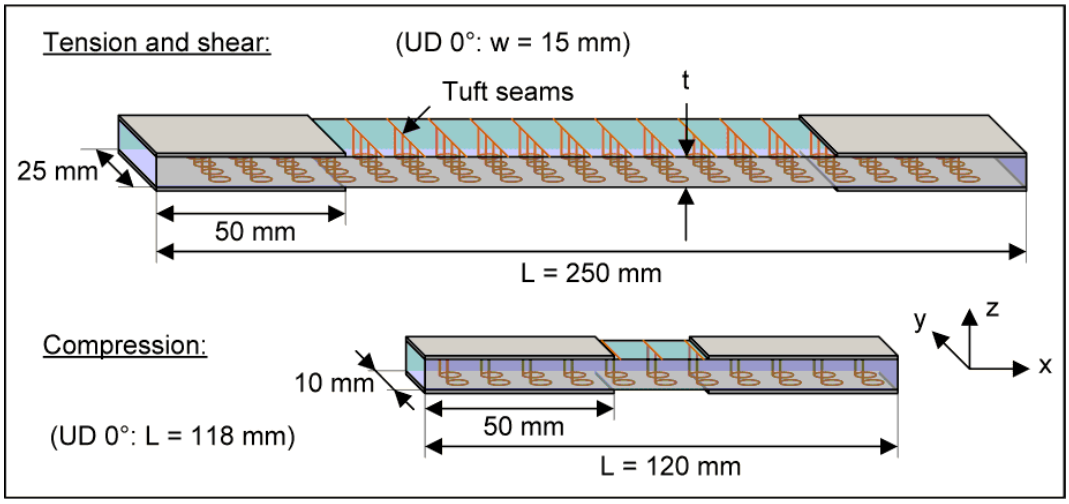

Figure 6.2 - Schematic of tuft arrangement within specimens for in-plane tension, compression and shear testing

Compression specimens were cut to a width of 10 mm. The gauge length to thickness ratio was kept small (6:1 for NCF and Twill, 4.5:1 for UD) to ensure minimal out-of-plane bending and to avoid invalid failure by global buckling within the unclamped gauge area.

To prevent invalid specimen failure in the clamps, 50 mm x 0.7 mm thick non-tapered aluminium tabs were adhesively bonded with Araldite 420 to both ends of all specimen types. The bond strength was compromised on the surfaces of UD control specimens, presumably by the presence of undissolved surface thermoplastic weft yarn. This led to some invalid failures in the uni-axial tensile tests. Additional, thinner (1.3 mm) control samples of $[0]_4$ layup were manufactured and tested to determine the longitudinal tensile strength of untufted UD material. Prior to testing, cut edges were polished to the final tolerances on a plate polishing machine with 400 grit silicon carbide paper and conditioned according to the individual test procedures.

A random black and white paint speckle pattern was applied to each specimen surface for full strain field imaging using the 3D digital image correlation (DIC) system Limess VIC3D. During testing the DIC system recorded a synchronised sequence of stereo pictures of the speckle pattern, the load and cross-head displacement. In a subsequent post-processing operation, the local strain distribution and globally averaged strain level were derived from the incremental displacement change of discrete paint dots within the pattern.

6.4.2 Tension test

All the mechanical tests were carried out on an Instron 5500R universal test machine with a 100 kN load cell. In-plane tensile tests were carried out at constant cross-head speed of 1.5 mm per minute, at 21°C (±2°C), according to BS EN ISO 527-4:1997. A stereo camera system of two 1.4 megapixel CCD cameras recorded the strain field within an 80 mm x 25 mm area at a rate of 2.5 Hz, with resolution of ~17 px/mm. A subset of 21 pixels and step size of 3 pixels were chosen for the correlation algorithm. To ensure equal strain levels on the opposing surfaces of the tufted coupons, strain was measured for half of the samples on the thread and for half on the loop surface. An additional tensile test on a single NCF control sample, equipped with both a conventional 25 mm long strain gauge and DIC surface strain mapping, confirmed identical average strain levels for both strain acquisition methods.

An additional NCF panel was prepared, specifically to check the effect of fabric fibre breakage on the tensile performance of tufted laminates. While half of the panel was left for control samples the other half was punctured by the tufting needle without tufting thread, at spacing corresponding to 2.0% areal tuft density. At least five samples of control and ‘2% thread-less’ were prepared and tested. Optical micrographs of the dry pre-

forms indicate a very similar extent of fibre damage in the tufted preforms with and without thread.

For all tests the obtained stress σ_t and modulus E_t values of the tufted samples were normalised against the 2D equivalent fibre volume fraction of the control laminate to compensate for small variations in the laminate thickness. As referred by Mouritz and Cox [3], such normalisation is necessary to compare the effective change in mechanical performance and to compensate for possible 'dilution' effects due to thickness increase from the insertion of the Z-reinforcement.

6.4.3 Compression test

The compression properties of the control, 0.5% and 2% tufted laminates were measured by testing specimens in an ITTRI compression jig at a constant cross-head speed of 1 mm per minute until failure, according to EN ISO 14126:1999. The compression load was transferred to the specimen by shear along the 50mm end-tabbed clamping lengths. Averaged compressive strain ε_c was derived from the local strain field at a rate of 1.7 Hz, using DIC within an analysis area of 15 mm x 10 mm on the specimen surface (resolution ~30 px/mm). Care was taken to align the samples with the loading direction.

The unclamped gauge length of 18 mm to 20 mm (±0.5 mm) was chosen to include at least three tuft rows within the DIC analysis area. As for tensile testing, the strain field was measured for half the samples on the thread and for the other half on the loop side. Samples with invalid failure within or in direct vicinity of the clamps were eliminated from analysis.

6.4.4 In-plane ±45° shear tension test

Bias [±45°] NCF and twill woven composite specimens with a gauge length of 150 mm were tested in static tension to determine the in-plane shear properties according to BS EN ISO 14129:1998. At least six samples were tested to failure, for each fabric type and tuft density, at a constant cross-head speed of 1.5 mm per minute. The average shear strain γ_{12} was derived from the sum of longitudinal and transverse strain ε_x and ε_y in relation to the load direction. Both constituents were measured as averaged values by DIC in an analysis area of 120 mm x 25 mm. According to the standard, the maximum shear strength τ_{12} was taken at a strain level γ_{12} of 5%, if ultimate failure occurred at a higher shear strain.

Additional quasi-static cyclic tests were performed on three samples each of the control, 0.5% and 2% tufted specimens to determine the damage accumulation at increasing strain levels, following the procedure of Ladevéze [129]. The matrix dominated shear damage parameter d_{12} = 1- (G_{12}/G_{12}^0) is defined as ratio of secant shear modulus G_{12} to initial elastic modulus G_{12}^0. The former was measured between the maximum total and inelastic strain constituent (x-axis intercept at F = 0 N) of five to six unloading cycles at equally spaced increasing strain increments of 0.4%. Loading and unloading for each cycle was executed at a speed of 1.5 mm per minute. The cyclic strain field was recorded during loading and unloading at a rate of 2 Hz. In-situ ultrasonic scans were made on each sample prior to testing and after each unloading cycle, without removing the sample from the test machine, using an Olympus Omniscan MX PA64 unit equipped with phased array ultrasonic probe.

Along with the damage parameter d_{12}, the force conjugate Y was calculated as partial derivative of the damaged elastic work according to equation 6-1 [130]. This parameter expresses the damage development at each loading cycle, analogous to the critical energy release rate for quasi-static delamination crack propagation in fracture mechanics [129]:

$$\underline{Y} = \sqrt{Y_{12}} = \frac{\tau_{12}}{(1-d_{12})\sqrt{2G_{12}^0}} = \sqrt{\frac{1}{2}G_{12}^0(2\varepsilon_{12}^e)^2} \qquad \textbf{6-1}$$

6.5 Quasi-static tests and damage laws

6.5.1 Tension

6.5.1.1 Tensile stiffness

Results summarised in Table 6.2 and Table 6.3 show that the presence of tufts at both 2.8 mm and 5.6 mm spacing has no significant effect on the longitudinal tensile elastic modulus E_t. This agrees with the majority of findings for conventionally stitched and Z-pinned composites of similar reinforcement density and controlled specimen thickness [2; 3; 7].

Table 6.2 - Longitudinal tensile test results for tufted UD, NCF and twill woven composites (Std.dev. in brackets)

Fabric	ρ_t (%)	# (-)	t (mm)	E_t (GPa)	$\varepsilon_{t,ult}$ (%)	$\sigma_{t,ult}$ (MPa)	$\nu_{0/90}$ (-)	$V_{f,2D}$ (%)
UD 0°	0.0	6	2.34	101 (1)	1.91 (0.05)*	2160 (52)*	0.32 (0.02)	50.2
	0.5	6	2.39	102 (2)	1.54 (0.05)	1746 (61)	0.25 (0.01)	49.2
	2.0	5	2.38	102 (1)	1.62 (0.03)	1775 (58)	0.27 (0.01)	49.4
NCF 0/90	0.0	8	4.26	62 (3)	1.33 (0.02)	837 (48)	0.028 (0.005)	53.1
	0.5	9	4.22	61 (1)	1.31 (0.04)	759 (33)	0.036 (0.012)	53.6
	2.0	9	4.29	61 (1)	1.26 (0.04)	741 (17)	0.042 (0.019)	52.7
Twill 0/90	0.0	7	4.21	55 (1)	1.32 (0.12)	662 (17)	0.053 (0.005)	51.9
	0.5	7	4.19	54 (2)	1.34 (0.09)	643 (27)	0.041 (0.003)	52.1
	2.0	7	4.31	55 (1)	1.37 (0.03)	672 (10)	0.056 (0.009)	50.7

* obtained for 1.30 mm thick $[0°]_4$ uni-weave laminate, $V_{f,2D}$=51.8%

In contrast, the transverse (90°) elastic modulus of the unidirectional composite increases by 7% and 45% for 0.5% and 2% areal tuft densities respectively. The main causes of this increase appear to be the locally increased fabric packing density around the tuft and the addition of stiff tufting thread and loops parallel to the loading direction. By reducing the tuft and row spacing from 5.6 to 2.8 mm the number of thread seams doubles and loops overlap and quadruple in volume along the transverse UD direction explaining the significant increase in stiffness for the closer tuft spacing.

Table 6.3 - Transverse tensile test results for tufted UD composite (Std.dev. in brackets)

Fabric	ρ_t (%)	Samples	t (mm)	E_t (GPa)	$\varepsilon_{t,ult}$ (%)	$\sigma_{t,ult}$ (MPa)	$V_{f,2D}$ (%)
UD 90°	0.0	6	3.09	8.2 (0.1)	0.58 (0.03)	46 (2)	54.4
	0.5	5	3.06	8.8 (0.2)	0.38 (0.03)	33 (2)	54.9
	2.0	5	3.17	11.9 (0.6)	0.30 (0.06)	32 (2)	53.0

Local fibre deviation around tufts towards the transverse load direction is assumed to contribute little to the increase as such effect would be expected at deviation levels significantly higher than the measured deviation angles of below 9°.

The increase in transverse stiffness of the unidirectional composite explains the significant reduction in the Poisson's ratio $\nu_{0/90}$. It is not possible to reach any conclusion on the effect of tufting on Poisson's ratio of the bidirectional NCF and twill woven composites, as the control value is very low and difficult to determine with accuracy.

Under longitudinal load the initial stress-strain curves are linear and identical for control, 0.5% and 2% tuft density samples but the behaviour of control samples at increasing strain levels depends on the type of laminate. As Figure 6.3 shows the stress-strain curve of the untufted NCF remains linear, while tow straightening in the uni-weave fabric causes the tangent modulus to increase by nearly 20%. In contrast, inelastic stretching between interwoven transverse and longitudinal tows causes drop in tangent modulus for the untufted twill layup which measured -18% at 1.15% tensile strain.

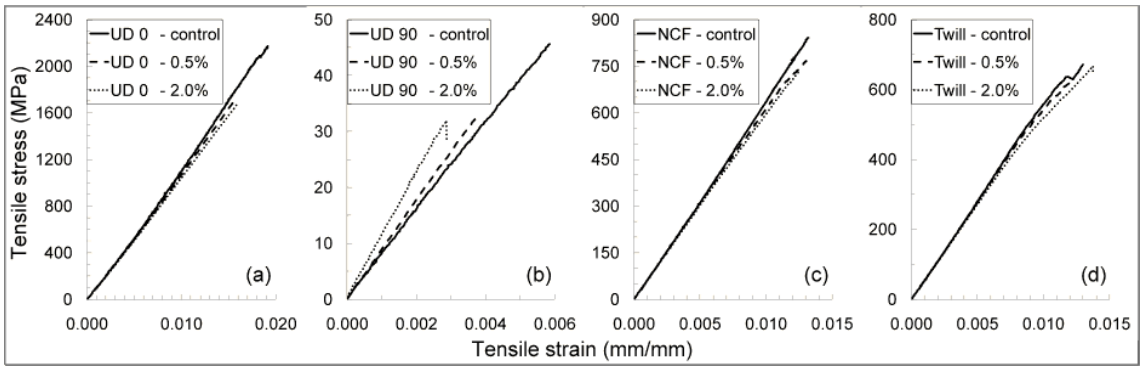

Figure 6.3 - Tensile stress-strain curves of a) longitudinal (0°) and b) transverse (90°) UD, (c) NCF and (d) twill woven specimens with 0%, 0.5% and 2% carbon tufts

At high strain the insertion of tufts caused a reduction in secant modulus of up to 7%, 17% and 18% for 2% tufted UD, NCF and twill laminates respectively, compared to the corresponding controls. Increasing the areal tuft density from 0.5% to 2% brings an earlier offset in tangent modulus from the control, from an average level of 0.6 - 0.75% tensile strain to 0.35 - 0.55% respectively.

Micrographs of specimen edges and sections parallel to the 0° plies of tufted NCF specimens revealed two types of accumulating micro-cracks at increasing strain levels. Above 0.4% tensile strain, typical tension cracks were found in the transverse 90° plies, a well known factor in the reduction of the secant modulus in multi-directional laminates [12; 119]. The crack density in both control and 0.5% tufted NCF samples increased at a comparable rate. Above 0.8% extension, micro-cracks were observed to expand along the 0°/90° ply interfaces, creating local delamination. In contrast, micro-cracks in the 2% tufted specimens were limited mostly to the resin rich regions around the tuft, without the formation of local delamination. It appears that bridging traction of closely spaced tufts limits the interfacial delamination propagation. This agrees with observations for stitched composites [119; 124].

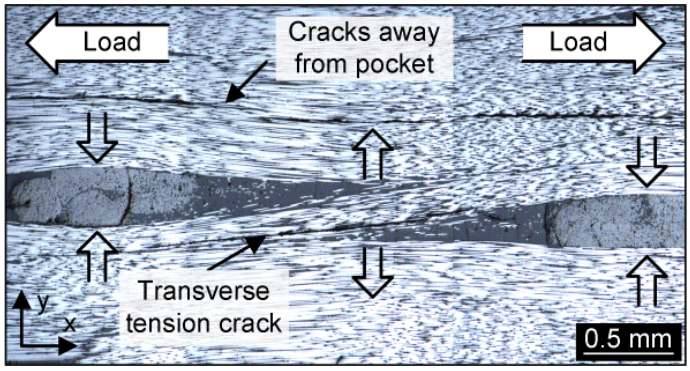

Figure 6.4 - Transverse tensile and shear cracks within the 0° ply of 2% tufted NCF at ε_t = 1.1%

In addition to the formation of micro-cracks in the transverse fabric plies, at higher strain levels splitting cracks were found to expand along the fibre direction of 0° plies in close vicinity of the tufts (see Figure 6.4). The source for the formation of such splitting cracks appears to be the undulated fabric around the inserted tufts. Transverse forces which are exerted by the gradually straightening tows on the surrounding material (see arrows in Figure 6.4) favour the formation of splitting cracks within the resin rich region away from the tuft. Thermal shrinkage cracks act as initiators for the formation of macro-cracks along the complete length of the resin rich region between neighbouring tufts. Additional splitting cracks were also found parallel to the resin rich regions within the fabric.

The formation of both transverse and longitudinal micro-cracks explains the reduction in tangent modulus of the tufted samples at increasing tensile strain. As tufted NCF and twill woven laminate contain larger resin pockets and have higher fibre undulation angles, the reduction in the secant modulus is to be expected more pronounced than in the case of the unidirectional tufted composites.

6.5.1.2 Tensile strength

As shown in Table 6.2, the change in ultimate tensile strain $\varepsilon_{t,ult}$ and strength $\sigma_{t,ult}$ of the tufted composites under longitudinal (0°) tension depends strongly on the type of fabric construction. While tufting has no significant effect on the strengths of twill woven fabric samples, the strength of 0.5% and 2% tufted NCF samples reduced by 9% and 11% respectively; the corresponding drop in the case of the UD specimens is close to 19%. As might be expected, in transverse tension (90°) the insertion of tufts is very detrimental to the strength of the UD laminate, leading to reduction of up to 30%, and does not represent a realistic loading situation.

The reduction in the measured ultimate strains of each composite type follows a similar pattern to the strength reduction.

6.5.2 Compression

6.5.2.1 Compression stiffness

Table 6.4 summarises the effect of tufting on the compressive properties of UD, NCF and twill woven composites. Similar to the tensile test, the elastic compression modulus E_c appears to be unaffected by the insertion of tufts, which agrees with the majority of studies on stitched composites [2; 3]. Initial elastic Young's moduli in tension and compression are comparable for each composite, although those from compression tests tended to be more variable. The reduction in compressive Poisson's ratio of the tufted unidirectional composite is not as prominent as for the tensile tested samples. Small measured increase and reduction in stiffness between the different tuft densities in compression are within the standard deviation of the test.

Table 6.4 - Longitudinal compression test results for tufted UD, NCF and twill woven composites (Std.dev. in brackets)

Fabric	ρ_t (%)	# (-)	t (mm)	E_c * (GPa)	$\varepsilon_{c,ult}$ (%)	$\sigma_{c,ult}$ (MPa)	$V_{f,2D}$ (%)	$\nu_{0/90}$ (-)
UD 0°	0.0	12	3.06	107 (2)	0.84 (0.12)	875 (46)	54.9	-0.38 (0.03)
	0.5	10	3.04	113 (7)	0.69 (0.06)	704 (36)	55.3	-0.37 (0.05)
	2.0	10	3.09	109 (4)	0.67 (0.08)	668 (50)	54.4	-0.35 (0.05)
NCF 0/90	0.0	9	4.27	60 (3)	0.86 (0.08)	478 (27)	52.9	-
	0.5	12	4.28	59 (3)	0.92 (0.05)	492 (29)	52.9	-
	2.0	11	4.28	60 (4)	0.82 (0.08)	451 (26)	52.8	-
Twill 0/90	0.0	10	4.18	53 (2)	1.13 (0.11)	523 (31)	52.2	-
	0.5	10	4.19	53 (2)	0.93 (0.15)	454 (58)	52.1	-
	2.0	8	4.29	51 (2)	0.83 (0.2)	377 (26)	50.9	-

*determined in accordance with the test standard between 0.05% and 0.25% compressive strain

In contrast to tension, the secant modulus in all three compression tested composites without tufting reduced at higher strain level. Inelastic deformation of the naturally waved in-plane fibre tows explains the general reduction, which was most pronounced for the untufted twill woven fabric composite as it exhibits the highest fabric waviness, measuring a drop of up to 45% before failure. The addition of Z-reinforcing tufts with introduction of fabric undulation and resin rich zones around the tufts leads to no sig-

nificant further decrease in the relative secant modulus even for a tuft density of 2% compared to the untufted response.

6.5.2.2 Compressive failure

All three sets of specimens without tufts failed by delamination between the individual fabric plies and subsequent ply buckling. In the unidirectional samples, the presence of undissolved thermoplastic weft yarn initiated the local separation of fabric plies.

The addition of tufts in the unidirectional and the twill woven fabrics resulted in considerable reduction in the compressive strength $\sigma_{c,ult}$, of around 25%, while the NCF based composite strength remained relatively unaffected by tufting.

6.5.3 In-plane ±45° shear

6.5.3.1 Quasi-static tests in tension

Table 6.5 summarises the properties of tufted [±45°] NCF and twill woven specimens, loaded in tension along the fabric bias direction. Control specimens of both types have similar elastic shear moduli G_{12}, as the response in bias direction is dominated by the resin matrix.

Table 6.5 – In-plane shear test results for tufted [±45°] NCF and twill woven composites (Std.dev. in brackets)

Fabric	ρ_t (%)	# (-)	t (mm)	G_{12} (GPa)	$\gamma_{12,m}$ (%)	τ_{12} (MPa)	$\gamma_{12,nl}$ (%)	$V_{f,2D}$ (%)
NCF ±45	0.0	6	4.20	3.9 (0.1)[b]	2.7 (0.1)	61.2 (0.7)	0.51 (0.07)	53.8
	0.5	6	4.24	4.3 (0.1)[b]	2.9 (0.1)	59.5 (1.8)	0.54 (0.02)	53.3
	2.0	6	4.26	5.5 (0.2)[b]	2.1 (0.2)	67.5 (1.2)	0.41 (0.09)	53.0
Twill ±45	0.0	6	4.17	4.1 (0.1)[b]	16.3 (1.0)	71.6 (2.5)[a]	0.35 (0.09)	52.3
	0.5	6	4.24	4.4 (0.1)[b]	14.6 (1.6)	69.7 (2.9)[a]	0.44 (0.09)	51.5
	2.0	6	4.17	5.1 (0.2)[b]	26.2 (5.5)	70.3 (3.6)[a]	0.36 (0.12)	52.3

[a] determined at γ_{12} = 5.0% according to BS EN ISO 14129:1998, [b] determined for γ_{12} = [0.1%,0.35%]

In contrast to axial compression and tension tests in fibre direction, the addition of tufts increases the elastic shear stiffness, by up to 10% and 41% for 0.5% and 2% areal tuft densities respectively. According to the classical rule of mixtures, the local deviation of fabric tows by up to 9° towards the load direction around the triangularly arranged tufts should produce only a small effect on the global shear modulus. However, when the tuft

spacing was reduced from 5.6 mm to 2.8 mm, there was an over 25% increase in the shear stiffness of the samples. This appears to be connected with the four-fold increase in thread volume, from partially aligned thread seams and loop ends on the composite surface. A similar effect was noted in tufted UD specimens, loaded in transverse tension. Thus the difference in relative stiffness change between tufted NCF and twill woven specimens can be explained by the varying tuft loop lengths (see Table 6.1).

In contrast to the shear stiffness, the insertion of tufts has only negligible effect on the shear strengths τ_{12}. The maximum reduction of 2.5%, measured for 5.6 mm spaced tufting in both NCF and twill-woven samples, lies within measurement scatter.

A strength increase of 10% was noted in the NCF composite with 2.8 mm spaced tufts. Micrographs of the failed NCF specimens indicate the suppression of delamination to be the main source for this enhancement.

6.5.3.2 Damage accumulation

The stress-strain response of both control and tufted specimens becomes non-linear above strain levels $\gamma_{12,nl}$ between 0.35% and 0.54%, due to inelastic matrix deformation and shear micro-cracking between fibre tows. Figure 6.5 shows the cyclic stress-strain curves for [±45°] NCF and twill woven composites, which are the basis for the damage master curves in Figure 6.6, defined by the damage parameter d_{12} and the force conjugate Y. In both control and tufted NCF specimens the damage accumulation is linearly dependent on the force conjugate, initiating at 0.2 $MPa^{0.5}$. At a maximum damage level of 0.3-0.35 all specimens failed by local delamination, tow rotation and fibre pull-out. In contrast, twill woven specimens give rise to a non-linear damage curve with significantly higher damage levels of 0.6-0.7 before ultimate failure by fibre pull-out. Locking between interwoven fabric tows at increasing tow rotation and enhanced friction between the tows have previously been identified as source for this non-linear damage development in woven [131] and braided fabric composites [130].

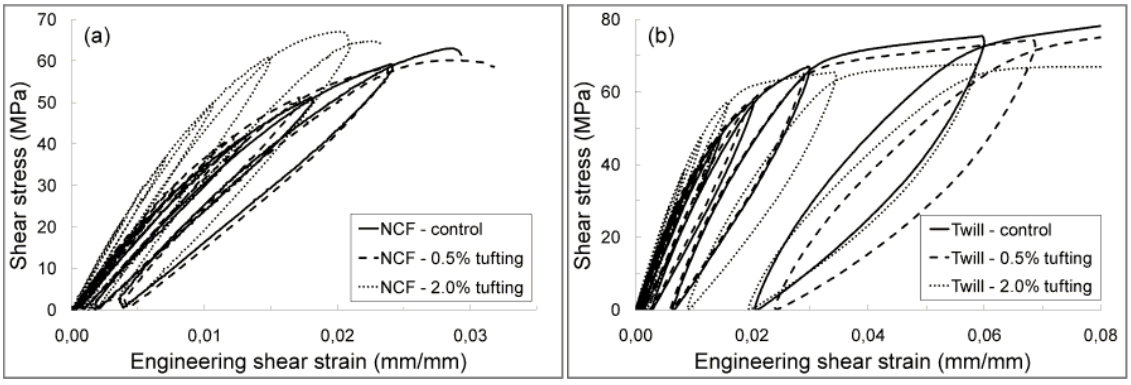

Figure 6.5 – Cyclic shear stress-strain curves of a) NCF and (b) twill woven composites with 0%, 0.5% and 2% carbon tufts

Comparing of the damage laws of tufted and untufted specimens indicates that tufting increases the susceptibility of the composite to local matrix damage under all modes of loading and a closer examination of the failure mechanisms is required.

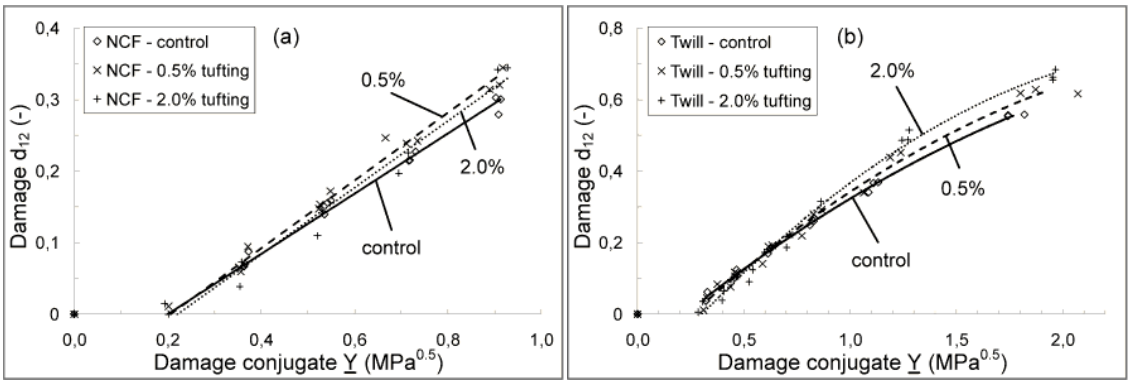

Figure 6.6 - Cyclic shear damage evolution of a) NCF and (b) twill woven composites with 0%, 0.5% and 2% carbon tufts

6.6 Failure mechanisms

6.6.1 Tensile loading

Post-failure analysis of the fracture planes of all three types of tufted composites under 0° tension revealed that the fabric tows fail in close vicinity to the inserted tufts, as shown in Figure 6.7. Stress concentrations in the highly deviated fibre tows close to the tuft appear to initiate the final ply failure. Hence, fibre undulation is a significant contributing factor to the reduction in tensile strength of the tufted specimens. The observed reduction in the maximum fibre deviation and total volume of deviated fibres in densely tufted samples (caused by the formation of continuous resin rich channels, see Chapter

5), explains why there is only a minimal difference in tensile strength between 0.5% and 2% tufted composite.

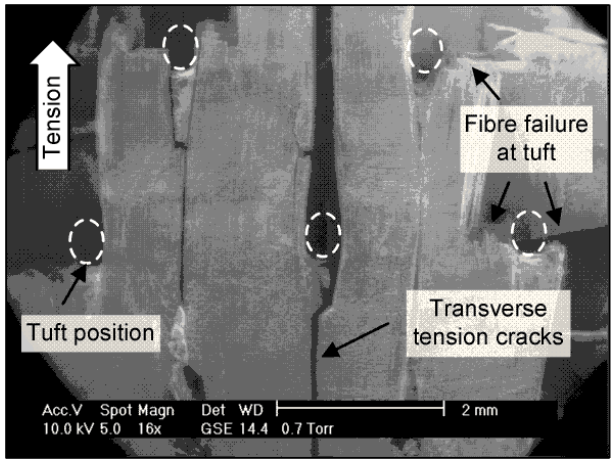

Figure 6.7 - SEM fractograph of 0° ply in 2% tufted NCF after catastrophic tensile failure

In tufted UD composite loaded along the fibre axis splitting cracks dominate the failure mechanism, even for 2% tufted samples. Under transverse load, macro-cracks were found to expand primarily along the resin rich regions parallel to the 0° fabric plies. Combined with the local stress concentration between the highly compacted fabric tows and pure resin rich pockets, the presence of thermal cracks as initiator for macro-cracks appear to be the cause for the reduced transversal tensile strength of the tufted UD composite.

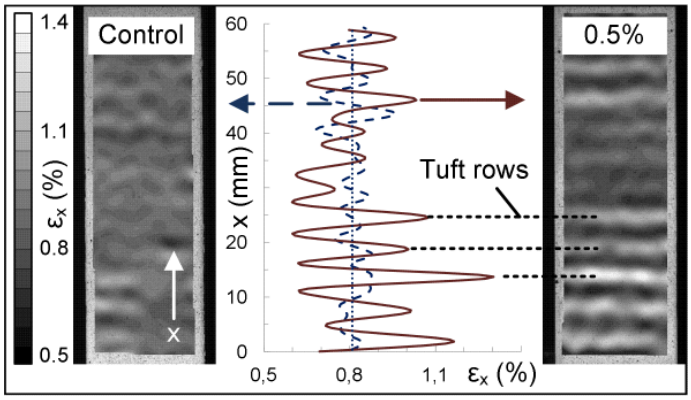

Figure 6.8 - Typical strain field ε_x of tensile loaded control (left) and 0.5% tufted (right) NCF (averaged ε_x = 0.81%, thread seam surface) and variations in the local strain ε_x measured along the specimen centre lines (in x)

Figure 6.8 compares the local strain field on the thread seam surface of control and 0.5% tufted NCF samples, showing that the presence of transverse tufting seams causes local strain and stress concentration in the load bearing 0° surface plies, reaching 60%

higher strain levels than the global average. As the deviated surface plies stretch, the resin rich areas around the thread seams are forced outwards in locally increased strain bands. Such local in-elastic stretching and associated change in stress distribution can be assumed to contribute to the reduction in tensile strength, becoming more prominent with closer tuft spacing.

Analysis of the strain field on the thread seam surface of control and tufted twill woven samples revealed the formation of local longitudinal strain concentration bands, oriented at 45° to the load direction. Closer examination showed these strain bands to coincide with the transverse 90° fabric tows on the laminate surface. As the load carrying 0° tows stretch, 3D stresses are introduced between the interwoven tows causing the transverse tows to stretch also. Above a critical strain level of 1.1% the 90° tows of the untufted samples were observed to debond, with a sudden high increase in local strain concentration, as shown in Figure 6.9. In contrast, the out-of-plane deformation and separation between plies in the tufted samples was inhibited by closure traction of the tufts. Local strain concentration due to the presence of surface thread seams was less prominent than strain variations in the weave pattern.

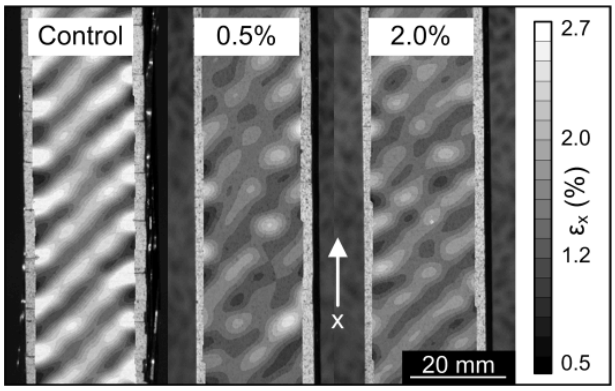

Figure 6.9 - Strain field ε_x of tensile loaded control (left), 0.5% (centre) and 2% (right) tufted twill samples before ultimate failure (averaged ε_x = 1.75%, thread seam surface)

As both NCF and twill woven tufted composites show a lower drop in tensile strength than the UD tufted composite, it would seem that the suppression of global delamination by tufting is a significant contributing factor counteracting the effect of in-plane fibre undulation. Such finding agrees with previous studies on unstitched and stitched NCF [124; 132]. By suppressing delamination, the damage zone in highly tufted NCF and twill woven laminates is limited to a small zone around the final transverse fracture surface (Figure 6.10).

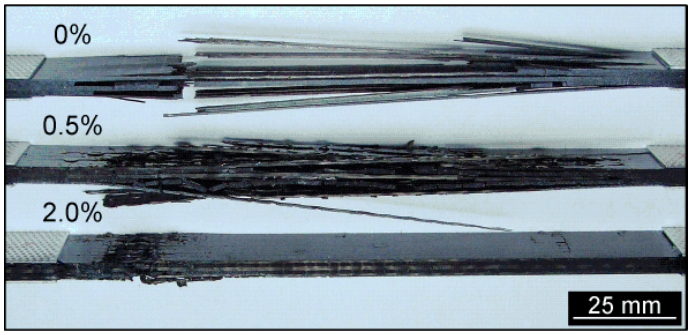

Figure 6.10 - Photographs of tensile failed NCF specimens with 0, 0.5 and 2% tuft density (from top to bottom)

Given that tuft induced fibre waviness is of a similar magnitude as the global fabric undulation within the twill woven composites, it is perhaps not surprising that this type of composite is the least affected by the presence of tufts, under tensile loading conditions.

6.6.1.1 Damage from needle insertion in NCF fabrics

Table 6.6 summarises the average elastic stiffness, ultimate strain and strength of additional control and 'thread-less' tufted NCF samples. The reduced laminate thickness of 3.93 mm explains the measured increase in stiffness and strength of both sets of samples compared to values of Table 6.2. Micrographs confirmed that by punching a tufting needle without thread in 2.8 mm intervals through the NCF panel, a similar level of fabric fibre breakage was produced as by conventional tufting. However, while the spreading of the in-plane fibre around the tufting thread of conventionally tufted samples caused a reduction in tensile strength by up to 11%, the presence of fibre damage only had no significant influence on the measured strength and strain compared to the tested control samples. Hence, tufting induced fibre damage appears to have a negligible effect on the strength degradation, while fibre spreading is the main contributing factor. This observation disagrees with most previous studies on stitched composites where fibre breakage was assumed to cause degradation of the composite tensile strength [3].

Table 6.6 - Longitudinal tensile test results for threadless tufted NCF composite (Std.dev. in brackets)

Fabric	ρ_t (%)	Samples	Thickness (mm)	E_t (GPa)	$\varepsilon_{t,ult}$ (%)	$\sigma_{t,ult}$ (MPa)	$V_{f,2D}$ (%)
NCF	0.0	6	3.93 (0.00)	66.4 (0.9)	1.41 (0.04)	916 (32)	57.5
thread-less	2.0	5	3.92 (0.01)	67.0 (1.5)	1.40 (0.05)	923 (35)	57.6

6.6.2 Compression loading

With increasing tuft density the compression failure mode of the UD specimens changed from the expected delamination and global ply buckling to formation of local kink bands and shear failure along an inclined fracture plane. Examination of the failure surface showed the formation of kink bands in zones of highly undulated fabric tows around the tufts. The fracture plane initiated always in crimped fabric plies, in close vicinity to the surface tufting thread seams. The observed reduction in unidirectional compressive strength is in line with the results of Fleck and Steeves who observed up to 30% reduction in the compressive strength of 2% Z-pinned UD laminates [26].

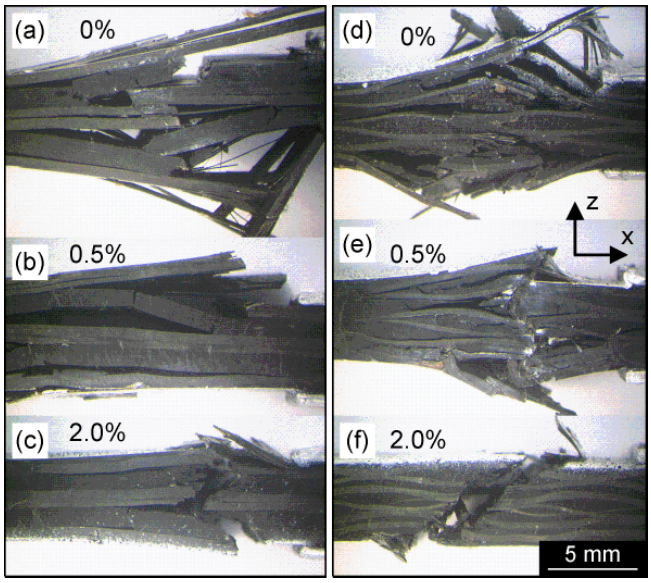

Figure 6.11 - Failed compression samples: a) to c) NCF and d) to e) twill woven composite with 0%, 0.5% and 2% tuft density (from top to bottom)

Figure 6.11 shows the failed NCF and twill compression samples with and without tufting. As can be seen, the addition of tufts to the bi-directional fabric layup reduces global delamination and ply buckling. In case of the NCF, the suppression of critical delamination by the tufts appears to balance the effect of additional fibre misalignment and crimp, as a maximum strength reduction of only 6% was measured for 2% tuft density. In the twill woven fabric the drop in compressive strength appears to decrease linearly with increasing tuft density. Such reduction can only be explained by the local increase in natural out-of-plane fabric waviness as a result of higher fabric compaction by the resin rich surface layers. Locally increased fabric undulation enhances the susceptibility to fibre kinking.

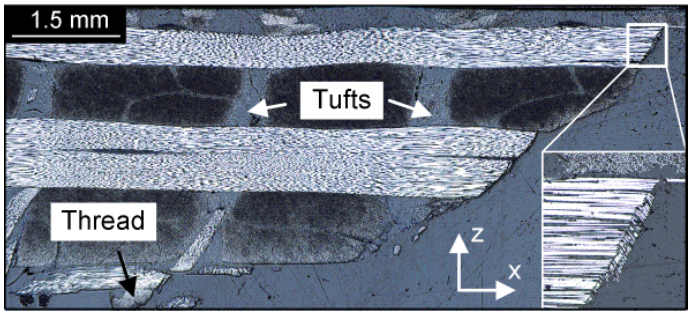

Figure 6.12 - Optical micrograph of x-z section through failed 2% tufted NCF compression specimen

Figure 6.12 confirms that local indentation of surface thread seam into the load bearing fabric plies is a critical source for the formation of kink bands and shear failure. This is supported by the observed strain concentration localisation shown in Figure 6.13. By plotting the local strain distribution before failure along two lines parallel to the compression direction, it was found that local strain doubles at the transverse tuft seams compared to the ply area between thread seams. Measured local strain concentration on the loop surface was less pronounced as the closely spaced and overlapping loops create a quasi-uniform resin rich layer with reduced out-of-plane fabric crimp. While shear failure and kink bands showed to initiate in direct vicinity to the indented tufting thread seams, no correlation could be identified between the location of the kink failure zone and loops on the opposing laminate surface.

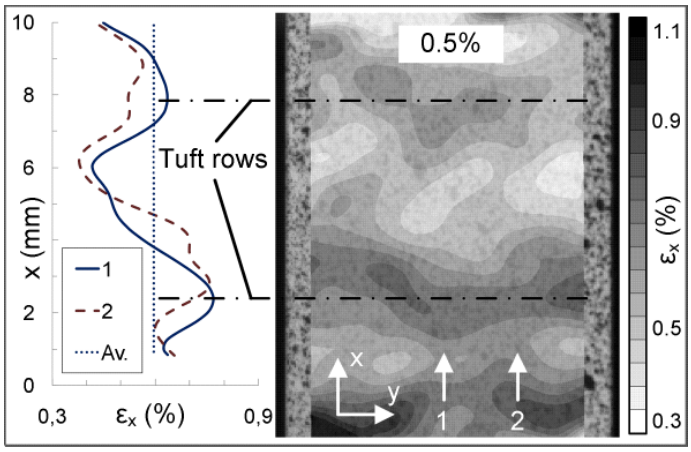

Figure 6.13 - Comparison between local (line 1 and 2) and averaged axial strain on thread seam surface of 0.5% tufted NCF compression specimen (averaged ε_x = 0.59%)

6.6.3 In-plane shear loading

Figure 6.14 shows the in-plane micrograph of a 2% tufted NCF sample, stopped at 2.0% shear strain before failure. Thermally induced large cracks within the resin rich pockets immediately around the tufts appear to be associated with long shear macro-cracks, propagating into and beyond the far edges of the resin rich pockets. In specimens with low tuft density additional shear cracks were found to extend parallel to the fibre free pockets, within each fabric ply. At a shear strain level of 1.6% the tuft loops, as well as the associated resin rich layer on the surface, debond from the underlying fabric layers.

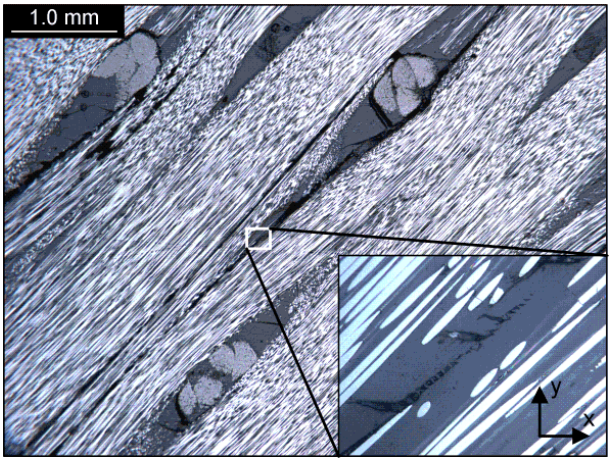

Figure 6.14 - Optical micrograph of in-plane crack distribution in 2% tufted [±45°] NCF specimen

Figure 6.15 shows a post-failure micrograph of an out-of-plane section of the 0.5% tufted NCF composite, close to the ultimate failure location. Delamination is evident between individual layers. In order for the loop layer to debond completely from the underlying composite, the loops have to become separate from the rest of the tufts. There is some indication of high shear deformation and local thread breakage at the interfaces between shearing plies.

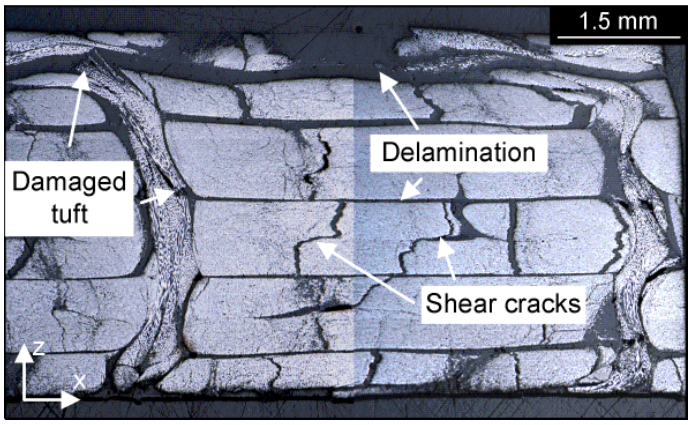

Figure 6.15 – Out-of-plane damage around tufts in 0.5% tufted [±45°] NCF specimen under in-plane shear

In contrast to the NCF composite, the twill woven control specimens were able to stretch up to 16% strain before local fibre rotation allowed the interlocked tows to separate. Tufts at close spacing further enhanced the deformability of the composite, reaching a total shear strain of up to 24% before final failure. The tufts inhibit the localised scissoring of interwoven fabric fibre tows, suppressing local necking and fibre pull-out, the typical failure modes of the control specimens, and advance global damage accumulation until final failure (see Figure 6.16 a). The deformation process is accompanied by high level of internal matrix damage (see Figure 6.16 b)).

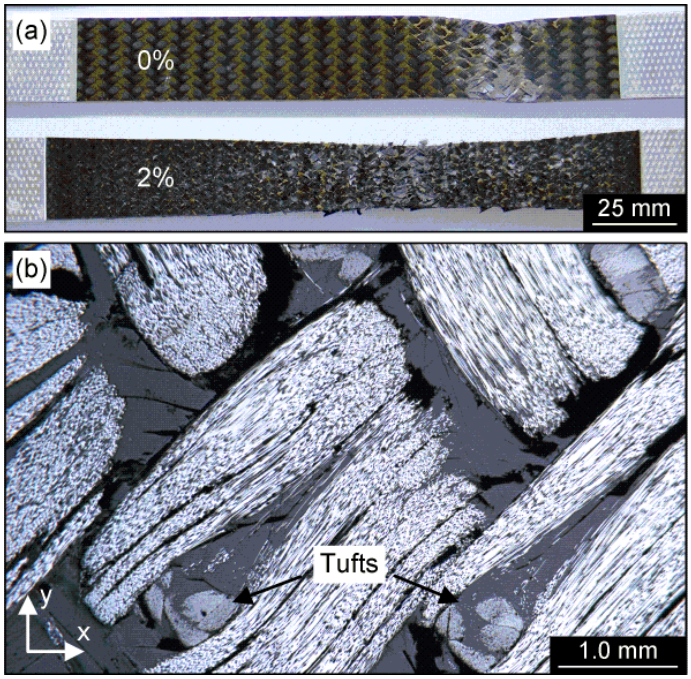

Figure 6.16 – a) Photographs of failed [±45°] twill woven specimens under in-plane shear with 0% and 2% tuft density, b) in-plane shear damage in 2% tufted twill woven specimen

The comparison of the local strain field on the laminate surface, the location of ultimate failure and ultrasonic scans of the composite after each unloading cycle confirm the observed failure mechanisms. Figure 6.17 illustrates the damage state of control, 0.5% and 2% tufted [±45°] NCF specimens after the fifth loading cycle. Strain concentration bands in the DIC strain field recording at maximum load of the fifth loading cycle, which align with the 45° fabric orientation, coincide with zones of maximum signal attenuation and the location of final specimen failure. Hence, the local strain map gives an indication of damage state and distribution in the samples. High signal attenuation on the edge of the specimen, where failure initiated (Figure 6.17 c) coincides with the location of a small area of full debond of the surface resin rich loop layer.

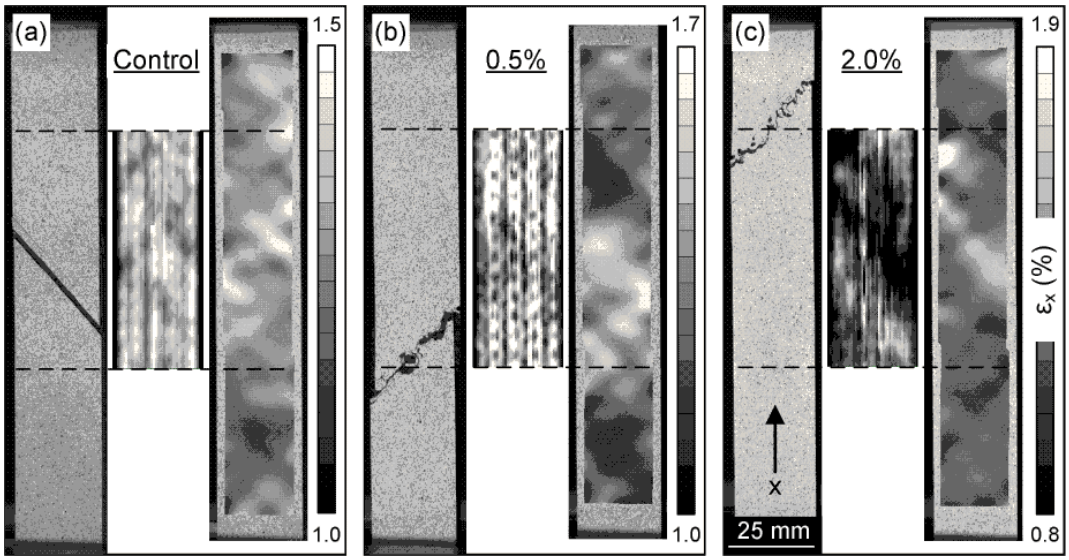

Figure 6.17 – Damage development in a) control, b) 0.5% and c) 2% tufted (±45°) NCF specimens under in-plane shear: photograph of failed specimen (left), ultrasonic scan (centre) and DIC strain field (right) at 5th loading cycle, before ultimate failure

6.7 Conclusions

Based on the extensive experimental investigation presented in this study, as well as additional data from measurements of flexural and inter-laminar shear behaviour of the same sample set [Treiber, unpublished data], it is believed that the current concerns about 'catastrophic' degradation of in-plane properties of realistic tufted fabric composites are not justified. The 2% areal tufting density is, in practice, likely to represent the higher end of tufting density to be used and the greatest property drop encountered was

the 30% reduction in transverse tensile strength in the pseudo-UD tufted fabric composite – not in itself a realistic loading situation.

No significant property degradation was found to be attributable to simple fibre breakage by the tufting needle, at least in the specific case of NCF fabrics.

The issues connected with the formation of resin rich loop layers on one surface of the tufted composite are clearly more significant in the case of relatively thin composites. While the whole issue of loop formation management requires further attention, tufting appears to show most promise in relatively thick preforms and joints. Additionally, high curing temperatures and selection of carbon thread as the Z-reinforcement will favour formation of thermally induced micro-cracking which advances the damage accumulation in the tufted composites, raising possible questions over fatigue and long- term environmental resistance.

There is a clear need for the establishment of appropriate modelling procedures, in order to predict the effects of tufting on the in-plane mechanical properties of composites. Early work by the authors indicates that both the modulus and the upper and lower bounds of the failure envelope can be predicted successfully, provided that the representative volume elements of the model are based on the true morphologically defined unit cell of the particular composite (see Chapter 5,[133]).

Chapter 7 Prediction of in-plane performance of tufted composites

7.1 Introduction

As shown in Chapter 5 and Chapter 6, the insertion of structural Z-reinforcements can cause complex changes in the 3 dimensional meso-structure of composite layups which appear to have significant effect on the macroscopic in-plane mechanical properties of the composite. In order for tufting to find application in industry as structural through-the-thickness reinforcement technology the potentially detrimental effects of the inserted Z-reinforcement on the mechanical properties need to be predictable without the need for extensive mechanical testing.

For the prediction of macroscopic behaviour of heterogeneous materials, such as the composite layup with repetitive presence of local Z-reinforcements, two approaches are possible. The composite can be described by either a representative volume element (RVE), which presents a heterogeneous material by macroscopically homogenising over a set of statistically varying meso-structural features, or by a unit cell (UC) which describes the material based on its smallest periodic heterogeneous meso-structure [134]. The two approaches differ in the scale and required boundary conditions.

Due to computational limits, early studies on the prediction of mechanical properties of general textile composites used primarily analytical methods based initially on 1D 'mosaic' [135] and later 2D and 3D 'bridging' [136-138] or 'fibre undulation' models [139; 140]. In these models the averaged elastic constants are determined from the assemblage of yarn segments, which are assumed to be either in series parallel or parallel series arrangement, using the classical laminate theory. A comprehensive overview is given by [141] and [142].

In order to estimate only the relative change in elastic properties of composites due to stitching Sickinger and Hermann [61], as well as Mouritz and Cox [2] derived simple analytical equations by incorporating experimentally observed volume and angles of deviated fabric around the inserted stitches. Junqian at al developed an analytical model

based on continuous shape functions incorporating changes in both fibre volume fraction and fibre deviation to predict the general stiffness and strength of stitched composites [143].

A large number of studies focused on the prediction of the in-plane elastic and failure behaviour of general textile composites using numerical modelling which allows the incorporation of potentially complex three-dimensional geometric features and advanced material and damage models [131; 144-151]. One of the most advanced tools to investigate textile composites with through-the-thickness features such as braided and non-structurally stitched fabric composites (NCF) is currently the software package developed by the team of Verpoest and Lomov at the Katholieke Universiteit Leuven, Belgium, incorporation WiseTex to create the geometrical fabric architecture and TexComp to predict numerically the mechanical properties of the textile composites [152-154].

The numerical unit cell approach was used in several studies to predict the in-plane elastic behaviour of Z-pinned [26; 155-157] and stitched [97; 158; 159] composites by incorporating typically a single Z-reinforcement, resin rich zones and local fibre deviation. Difference between the studies consists primarily in the detail of included features such as fibre deviation distribution or stitch geometry. In all models local fibre misalignment was identified as cause for reduction of the predicted fibre dominated tensile stiffness with increasing density of Z-reinforcement, reaching up to 11% in 2% Z-pinned UD composite [156] and 3.5% for a relatively low Z-reinforcement density of 0.3% in stitched quasi-isotropic composites [97]. Gunnion [160] introduced a voxel finite element unit cell model of stitched uni-directional and biaxial composites to overcome the complex meshing operation around the Z-reinforcement in multi-directional fabric layup. By applying the voxel approach, required element number could be reduced without loss in prediction accuracy of in-plane elastic constants. The approach ensures mesh compatibility across plies even for variable fibre and resin pocket orientation which normally requires a complex meshing operation such as the star-approach [158]. With each percent of increased stitch density the elastic longitudinal tensile modulus was predicted to decreases by 2%.

More recent studies also incorporated material failure and degradation to predict damage onset and failure of stitched composites using ply failure criteria such as Puck or Hoffmann [97; 158]. Steeves and Fleck [26] included explicitly measured fibre distribution along with fibre kinking mechanisms into a 2D finite element unit cell model to

predict the compressive elastic and failure behaviour of Z-pinned unidirectional composites. In close agreement with experimental results, local fibre deviation of up to 16° was found to be main cause for the earlier formation of kink bands, reducing the in-plane compressive strength of UD composite by at least 30% in the presence of Z-pins.

In addition to studies focusing on in-plane features such as fibre undulation, Yoshimura et al investigated the inhibiting effect of stitches on formation of delamination cracks as additional failure mechanism of multi-directional composites during in-plane loading [119]. Furthermore, Sweeting used the finite element unit cell of a Z-pinned composite to evaluate thermal stresses within the Z-reinforced composite due to curing [107]. It was found that curing of carbon Z-pinned composites with multi-axial layup at high temperature of 180°C leads inevitably to high thermal stresses in the final composite with formation of thermal shrinkage cracks in the resin rich pockets due to mismatch of thermal expansion in transverse and thickness direction between pure resin and stiffening Z-reinforcement. Huang and Waas used the representative volume element approach instead of a single unit cell to predict in-plane compression properties of Z-pinned woven composites [161; 162], enabling the investigation of both pin insertion and variable weave pattern arrangement between plies.

Although most models on the in-plane mechanical properties of Z-reinforced composites report close agreement between prediction and experimental results, correlation between simplified and experimentally determined disruptions such as fibre volume fraction and fibre deviation are often missing. Change in local fibre volume fraction was generally either omitted or simplified by assuming a uniformly enhanced fibre compaction across the unit cell, although several studies on Z-reinforced composites have reported significant variations in fibre volume fraction in the presence of the Z-reinforcement [96; 98; 103] which can affect the prediction of both elastic constants and initiation of damage [163].

In this chapter in-plane elastic constants and failure behaviour of uni- and bi-directional fibre composites with 0, 0.5 and 2% tufting are predicted and compared to experimental results on in-plane tension and shear (see Chapter 6) by developing a meso-structural 3 dimensional finite element unit cell approach. In-plane fibre undulation, change in the local fabric fibre compaction as well as discretisation of tuft loop features are considered. Geometric layup, morphologic tuft and fabric features and corresponding dimensions are included based on detailed meso-structural characterisation of corresponding composites in Chapter 5.

7.2 Unit cell model

A three-dimensional parametric finite element unit cell model was developed to identify critical changes to the meso-structure of composites due to the insertion of tufts and to predict its effect on the macroscopic response and stress-strain field in the unit cell of the tufted composite. Three separate combinations of fabric layup and tuft arrangement have been considered which affect the formulation of the unit cell model: uni-directional fabric layup with triangular and square tuft arrangement, as well as bi-axial ply stacking with square tuft pattern. Figure 7.1 shows the in-plane view (*x*-*y*) of a 0° ply for all three models with meso-structural features and corresponding dimensional parameters.

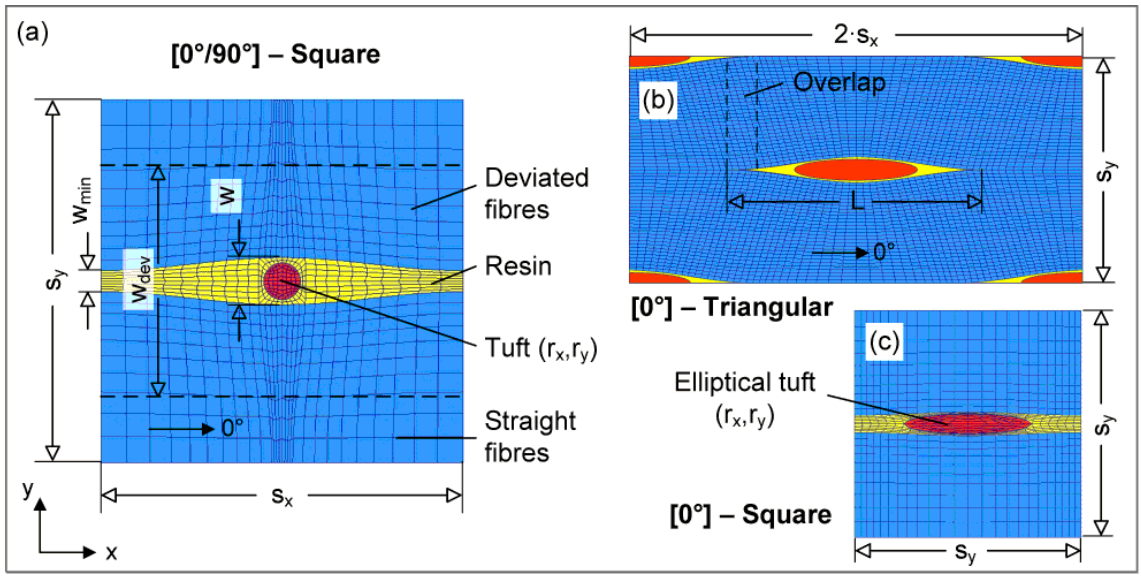

Figure 7.1 – In-plane view (x-y) of unit cell models for a) bi-axial layup with square and unidirectional layup with b) triangular and c) square tuft pattern; geometric parameter definition for single tuft, resin rich region and homogenised fabric ply features

The parametric model is capable to consider number, orientation and thickness of the individual composite layers, the outer dimensions of the unit cell (defined by the specimen thickness t and tuft to tuft spacings s_x and s_y), width, length and orientation of the fibre free resin pockets which are created by local fabric undulation around the tuft, cross-sectional area of the tuft, and fibre deviation and compaction distribution within the plies.

While in tested unidirectional and bi-axial NCF specimens of Chapter 6 a perfect square tuft arrangement was aimed for, small deviations in the robotic tuft insertion process

showed to cause local irregularities in the tuft arrangement. In order to characterise the effect of such irregularities both extremes, i.e. perfectly square and perfectly triangular tuft arrangement, are considered for the modelling of the unidirectional composite. Square tuft pattern is defined as regular insertion of tufts at constant pitch s_y (along tufting row) and spacing s_x (between tuft rows) with parallel tuft alignment between adjacent tuft rows in relation to the orientation of the undisturbed fabric plies. Triangular tuft pattern is characterised by constant shift of $s_y/2$ between neighbouring tufting rows.

For the unit cell approach of this study the single plies of the composite layup are considered to be uni-directional and flat, i.e. without textile features such as non-structural stitching or weave. Hence, the required unit cell size to present the smallest periodic structure within the tufted composite is defined by the tuft spacings. The coordinates x and y in the unit cell define the longitudinal and transverse in-plane direction of the 0° ply. The origin of the coordinate system at the bottom centre of the unit cell coincides with the centre of the single tuft. The z axis determines the through-the-thickness direction of the composite within the unit cell.

Based on observations during the experimental morphology analysis in Chapter 5 the following meso-structural features are incorporated into the 3D unit cell of tufted UD and bi-directional composite.

Each unit cell incorporates a single tuft at its centre, which is simplified as cylindrical, straight through-the-thickness entity of uniform cross-section with homogeneous fibrous material properties, aligned with the z directional of the unit cell. The individual thread yarns and thread twist are not considered in the geometry, but accounted for in the adapted material properties. In unidirectional layup the tuft is assumed to adopt an elliptical cross-section shape with major and minor radius r_x and r_y, as the uni-axial ply stacking enables spreading of the yarns within the resin pocket. In bi-axial layup a circular tuft shape is assumed (r_x=r_y). Minor and major tuft radii are derived from the measured infused tuft cross-section area A_t.

The tuft is surrounded by fibre-free resin filled zones (resin pocket) which align in each composite layer with the original fibre orientation of the ply. The resin pockets have a maximum width w at the tuft with w>2r_y, i.e. tuft and surrounding fabric plies are separated by a small volume of neat resin. For triangular tuft arrangement the resin zones are closing over a distance $L/2$ from the tuft centre, creating individual resin pockets. In square arrangement the resin zones reduce in width to w_{min} at the unit cell boundary, but

remain continuous open channels, a phenomenon specific to the small chosen tuft spacings of 2.8 and 5.6 mm. Through all layers the dimensions of the resin rich zones are assumed to be constant.

The individual composite layers are assumed to be uni-directional with orthotropic, transversely isotropic material properties and constant thickness for each ply. In order to accommodate the tuft the fibres of the ply are locally compacted and deviate from the original in-plane ply orientation, creating the resin rich zones. Fibre deviation reaches a maximum at the flanks of the resin pocket and reduces in transverse ply direction with increasing distance to the tuft, before aligning with the original ply orientation at a distance $w_{dev}/2$. Fibre waviness due to non-structural stitching and weave is not taken into consideration since micro-graphs confirmed their size to be a magnitude smaller than the tuft induced changes to the meso-structure. Shape functions and distribution models for local fibre compaction and fibre deviation are presented in detail in section 7.2.1.

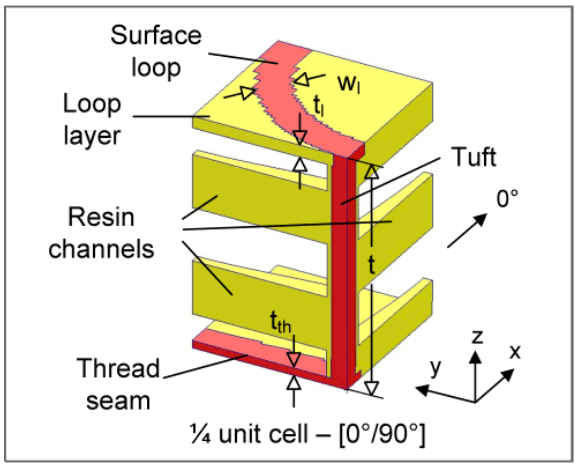

Figure 7.2 – Through-the-thickness features of 3D quarter unit cell of 0°/90° fabric layup with resin rich areas of resin pockets, surface loop and surface thread layer (fabric plies omitted)

For simplification of the meshing operation both thread seam and free tuft loop end are assumed to create resin rich layers of constant thicknesses t_{th} and t_l on the specimen surfaces, as shown for a quarter unit cell in Figure 7.2. Out-of-plane surface crimp in fabric plies close to the surface thread and tuft loop was not considered as its effect was limited typically to the outermost fabric plies. Within the surface layers thread and loop are implemented as discrete entity, surrounded by neat resin. The thread seam is aligned with the transverse fibre direction of the outermost ply, the generally chosen tuft row direction in this study. The surface loop, which is normally free to arrange arbitrarily on the specimen surface, was modelled as semicircular arch bridging to the next tuft posi-

tion (see Figure 7.2). In order to account for the absolute fibre volume of the potentially overlapping surface loops, the loop width w_l was calculated with $w_l=(A_t \cdot l_l)/(2 \cdot s_x \cdot \pi \cdot t_l)$, based on the measured free loop length l_l and an assumed infused cross-sectional area half of the tuft.

It has to be noted that meso-structural imperfections, such as voids or broken fabric filaments, and curing stresses as well as shrinkage cracking were not considered. The latter were found to affect the matrix dominated failure of the uni-directional and biaxial NCF, as thermal micro-cracks initiated macroscopic transverse tension and shear failure in the composite.

Table 7.1 – Geometric parameters of 3D in-plane unit cells

Fabric	ρ_t	Pattern	$s_x=s_y$	t	L	w	w_{min}	w_{dev}	$r_{x/y}$	t_l	t_{th}
(-)	(%)	(-)	(mm)	(mm)	(mm)	(mm)	(mm)	(mm)	(mm)	(mm)	(mm)
UD [0]	0.5	Squ.	5.6	3.01	-	0.49	0.16	2.8	0.51/0.19	0.16	0.08
		Tri.	5.6	-	5.31	0.43	-	2.6	0.57/0.17	0.16	0.08
	2.0	Squ.	2.8	3.03	-	0.29	0.21	1.5	0.79/0.12	0.38	0.07
		Tri.	2.8	-	3.2	0.30	-	2.8	0.76/0.12	0.38	0.07
NCF [0/90]	0.5	Squ.	5.6	4.18	-	0.73	0.32	3.9	0.28	0.21	0.14
	2.0	Squ.	2.8	4.19	-	0.64	0.40	1.9	0.28	0.23	0.09

For comparison with the tested composites of Chapter 6 the same material and stacking sequence of 10 individual 0° carbon fibre plies with areal weight of 300 g/m^2 was used for the unidirectional unit cell. The bi-axial unit cell had eight unidirectional carbon fabric plies of 500 g/m^2 each, arranged in symmetric stacking of $[(0°/90°)_s]_2$. The corresponding fabric fibre volume fractions $V_{f,2D}$ of the untufted composites were calculated from the areal weight and number of fabric plies, the density of the carbon filaments and thickness of the unit cell (see Chapter 3.1)

For both layup configurations 2k carbon thread tufting at spacings ($s_x=s_y$) of 5.6 and 2.8 mm was considered, corresponding to areal tuft densities of 0.5% and 2%. The corresponding dimensions of all introduced unit cell features, which were determined experimentally for square and triangular tuft arrangement at 0.5% and 2% tuft density in uni-directional and bi-axial ply stacking in Chapter 5, are summarised in Table 7.1.

7.2.1 Fibre distribution and deviation

From the experimental morphology analysis in Chapter 5 the implementation of variable fibre deviation angles and fibre compaction were found to be necessary within the fabric plies of the tuft unit cell.

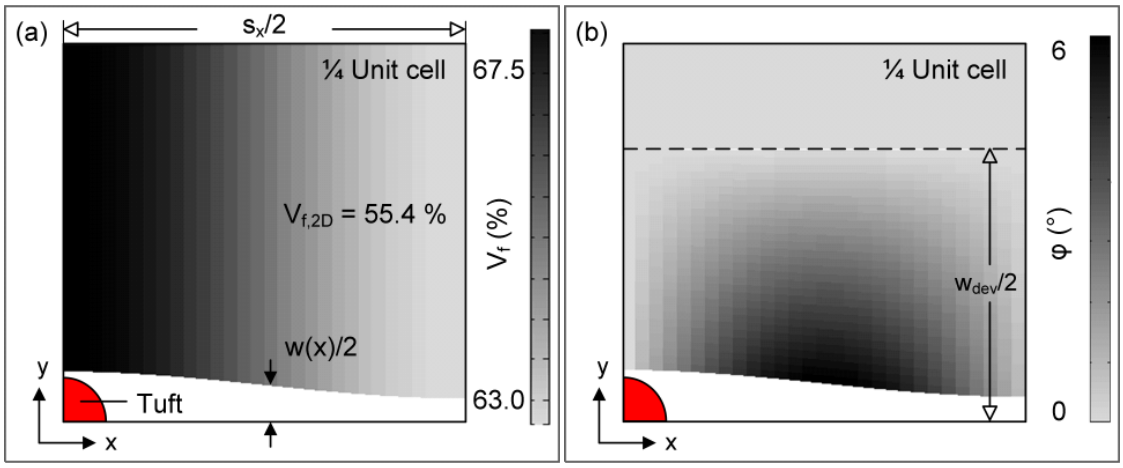

Figure 7.3 – Fibre compaction and deviation distribution for ¼ unit cell of 0.5% biaxial NCF

The increase in fibre volume fraction of the fibrous ply around the resin rich pockets is assumed to be directly related to the ratio of local resin pocket width *w(x)* to spacing length s_y between adjacent resin pockets. Global compaction by resin rich loop and thread layers of constant thickness t_l and t_{th} is also taken into account. Such assumption is in close agreement with the observed fibre volume fractions measured for both UD and NCF in Chapter 5. Between adjacent resin pockets transverse to the local ply orientation a constant enhanced fibre volume fraction is assumed. The enhancement can be derived from the original fibre volume fraction $V_{f,2D}$ of the undisturbed fabric using equation 5-3 in Chapter 5, assuming that the specimen thickness remains constant. Figure 7.3 a) shows the according fibre volume fraction distribution in a quarter unit cell for the plies of 0.5% tufted bi-axial layup.

In order to validate the effect of the chosen fibre compaction distribution model on the elastic and strength properties of the unit cell, parametric studies were performed using also two other fabric distribution models. The most simplistic approach only accounts for global enhancement of fabric volume fraction $V_{f,c}$ in the plies due to constant compaction by the resin rich surface layers (see equation 7-1). The other approach, as used by studies of Heß and Koissin [97; 158], assumes a uniformly enhanced constant fibre

volume fraction $V_{f,A}$ within the entire ply by taking the area A_{rp} of the fibre free resin pockets into account (see equation 7-2).

$$V_{f,c}(\%) = V_{f,2D} \cdot \frac{t}{(t - t_{th} - t_l)} \quad \textbf{7-1}$$

$$V_{f,A}(\%) = V_{f,2D} \cdot \frac{t}{(t - t_{th} - t_l)} \cdot \frac{s_x \cdot s_y}{s_x \cdot s_y - A_{rp}} \quad \textbf{7-2}$$

Fibre deviation from the original fabric orientation, which was found to be maximal at the boundary of the resin rich pocket, is assumed to be limited to the length of the resin rich zone L (or s_x for resin rich channels) and a width w_{dev} in transverse direction to the resin rich zones where the fibres align with the orientation of the undeviated fabric. Both parameters were confirmed by experimental observations in chapter 5.4. The deviation angle is assumed to reduce linearly between the resin rich pocket and outer boundary w_{dev} with increasing transverse distance to the fibre free pocket.

A cosine shaped function was chosen to predict the shape of the resin rich pocket and subsequently the fibre deviation distribution. The use of a continuous shape function over other fibre deviation models, such as the linear deviation by Grassi [155], is essential for the correct strength prediction. Discontinuous geometric features and sharp changes in fibre orientation can cause invalid stress concentration and failure prediction in the unit cell model.

The boundary of closed resin pockets of length L and width w, as found in the triangular tuft unit cell, is defined by:

$$y_0(x) = \frac{w}{4} \cdot \left(1 + \cos\left(\frac{2x\pi}{L}\right)\right) \quad \textbf{7-3}$$

In case of continuous resin rich channels with a minimal channel width w_{min} the boundary definition adapts to:

$$y_0(x) = \left(\frac{w}{4} - \frac{w_{min}}{4}\right) \cos\left(\frac{2x\pi}{s_x}\right) + \left(\frac{w}{4} + \frac{w_{min}}{4}\right) \quad \textbf{7-4}$$

The angle of fibre deviation along the boundary of the resin rich region can be derived using the first derivative of equations 7-3 and 7-4.

With the assumption of linear reduction and straightening of the deviated fibre over a width w_{dev} the fibre misalignment angle φ at each position (x,y) within the boundaries of deviated fabric for continuous resin channels can be derived as follows:

$$\varphi(x,y) = \arctan\left[-\frac{\pi}{s_x}\cdot\left(y^*\left(1-\frac{s_y-w_{min}}{s_y-w}\right)+\frac{w\left(s_y-w_{min}\right)}{2\left(s_y-w\right)}-\frac{w_{min}}{2}\right)\cdot\sin\left(\frac{2\pi x}{s_x}\right)\right] \quad \textbf{7-5}$$

$$y^* = \frac{2y-\left(\frac{w\left(s_y-w_{min}\right)}{2\left(s_y-w\right)}-\frac{w_{min}}{2}\right)\left(\cos\left(\frac{2\pi x}{s_x}\right)-1\right)}{\left(1-\frac{s_y-w_{min}}{s_y-w}\right)\cos\left(\frac{2\pi x}{s_x}\right)+\left(1+\frac{s_y-w_{min}}{s_y-w}\right)} \quad \textbf{7-6}$$

Fibre angle distribution for discrete resin pockets can be calculated from equation 7-5 by setting w_{min} to zero and substituting s_x against the pocket length L.

Table 7.2 shows a comparison between the measured and predicted maximum fibre deviation angles at the flanks of the resin rich pockets. Corresponding standard deviations for measured results are shown in brackets.

Table 7.2 – Comparison of average measured and predicted maximum fibre deviation angle φ_{max}

		Square pattern		Triangular pattern	
Fabric	ρ_t (%)	Exp. (°)	Model (°)	Exp. (°)	Model (°)
UD [0]	0.5	4.6 (0.7)	5.3	4.7 (0.4)	7.3
	2.0	3.4 (0.7)	2.6	6.3 (0.9)	8.5
NCF [0/90]	0.5	7.3 (1.1)	6.5	-	-
	2.0	3.9 (0.9)	7.7	-	-

For large tuft spacing the assumed cosine shape is in agreement with the experimentally determined fibre deviation angles. Only for small spacing the shape function over-predicts the local fibre deviation angles by 2° to 3.5°. In order to assess the effect of maximum fibre deviation and volume of deviated fabric, a parametric study was performed with variation of φ_{max} and w_{dev} within the maximum range of measured parameters.

7.2.2 Material properties

The features of the tuft unit cell, i.e. the resin matrix, homogenised fibrous plies and the tuft are assumed to behave linearly elastically until initiation of failure. This assumption is an acceptable simplification as a brittle matrix resin is chosen and both longitudinal and transverse tension tests showed that the material response of uni-directional un-tufted composite remained quasi-linear up to failure (see Chapter 6.4.2). Only in experimental shear tests the accumulation of damage caused a non-linear response of the composite material at high shear strains, leading to potential mismatch between the following numerical simulation and experimental results.

7.2.2.1 Elastic constants

For the matrix within the fibre-free pockets and surface layers the epoxy resin ACG MVR 444 was assigned, assuming homogeneous, isotropic resin behaviour. Corresponding elastic constants of Young's modulus E_r and Poisson's ration v_r in Table 7.3 were derived from compression tests on neat epoxy samples, as detailed in chapter 3.4.1. The resin shear modulus G_r was calculated from measured axial Young's modulus and Poisson's ratio using the well known relationship $G_r=E/2\cdot(1+v_r)$.

The unidirectional plies as well as the tufting thread were treated as homogenised orthotropic, transversely isotropic material. As the fibre volume fraction and subsequently the elastic properties vary in each fabric ply and in the tufting thread depending on the relative shape and dislocation of fibres by the fibre free resin pockets around the tuft, the elastic properties for each transversely isotropic fibre/epoxy element have to be determined separately depending on the location within the fibre compaction distribution model, see section 7.2.1.

Direct experimental determination of the elastic properties for the current unit cell model is unpractical due to the large range of required elastic parameters at variable fibre compaction. Hence, a micro-mechanical homogenisation model has been adopted to determine the homogenised elastic properties of each composite element based on the elastic behaviour of the fibre and resin constituents. Several approaches including analytical [164; 165] and numerical fibre/matrix micro-models [151; 152; 166; 167] are available.

To ease the computational effort the analytical closed form solution of Chamis has been implemented derived from the Rule of Mixtures (ROM) [168]. In contrast to the conventional Rule of mixture the model assumes the reinforcing fibres to be orthotropic, transversely isotropic. Lomov et al showed that this analytical model is in good agreement with detailed numerical micro-homogenisation models [152], predicting closely the empirically observed relationship between fibre and neat resin properties on the 'smeared' elastic behaviour.

The homogenised elastic constants of axial Young's moduli $E_{||}$ (= E_1) and $E_{\perp}$ (= E_2 = E_3), shear moduli $G_{||\perp}$ (= G_{12} = G_{13}) and $G_{\perp\perp}$ (= G_{23}) and Poisson's ratios $\nu_{||\perp}$ (= ν_{12} = ν_{13}) and $\nu_{||\perp}$ (= ν_{23}) parallel (||) and transverse ($\perp$) to the fibre direction within each uni-directional ply element are derived from the properties of the fibre (*f*) and matrix (*r*) constituents as follows:

$$E_{\parallel} = V_f \cdot E_{f,\parallel} + \left(1 - V_f\right) \cdot E_r \qquad E_{\parallel} = \frac{E_r}{1 - \sqrt{V_f} \cdot \left(1 - \frac{E_r}{E_{f,\perp}}\right)} \tag{7-7}$$

$$G_{\parallel\perp} = \frac{G_r}{1 - \sqrt{V_f} \cdot \left(1 - \frac{G_r}{G_{f,\parallel\perp}}\right)} \qquad G_{\perp\perp} = \frac{G_r}{1 - \sqrt{V_f} \cdot \left(1 - \frac{G_r}{G_{f,\perp\perp}}\right)} \tag{7-8}$$

$$\nu_{\parallel\perp} = V_f \cdot \nu_{f,\parallel\perp} + \left(1 - V_f\right) \cdot \nu_r \qquad \nu_{\perp\perp} = \frac{E_{\perp}}{2G_{\perp\perp}} - 1 \tag{7-9}$$

In absence of manufacturers' data the required elastic transverse and shear constants of the fibre constituent were derived by matching the predicted homogenised parameters of equations 7-7 to 7-9 with experimental test results for the untufted uni-directional composite specimens in Chapter 6. The longitudinal fibre modulus was adjusted separately for the uni-directional and biaxial unit cells to account for reductions in uni-axial response of the tested composite due to the textile structure of the two different types of uni-weave and non-crimped fabric. Table 7.3 summarises the used elastic constants for both isotropic epoxy matrix and fibre types. The 'equivalent' axial stiffness of the highly twisted tuft filaments was determined from tensile test results on infused thread rodstock (see chapter 3.2.1).

Table 7.3 – Elastic properties of resin and fibre constituents for UC models

	E_r (GPa)		ν_r (-)	G_r (GPa)	
Epoxy MVR 444	3.1		0.35	1.1	
	$E_{f,\parallel}$ (GPa)	$E_{f,\perp}$ (GPa) *	$\nu_{f,\parallel\perp}$ (-)**	$G_{f,\parallel\perp}$ (GPa) **	$G_{f,\perp\perp}$ (GPa)
UD (Grafil 34-700)	200 (234)	19	0.25	24	7.6
NCF (HTS)	214 (240)	19	0.25	24	7.6
Tuft (HTA)	196 (238)	19	0.25	24	7.6

* derived from transverse tension test on UD composite; ** from in-plane shear test on NCF

Bracketed values state the fibre properties given by the manufacturers.

While empirical fitting of the properties of the constituents is discouraged for the independent prediction of the absolute mechanical response of the composite, this study focuses primarily on the investigation of the relative effect of tuft insertion. The adjustment of the constituents' properties is only limited to the untufted composite to enable direct comparison with the experimental results. As expected for the weave and twist in the uni-directional fabric and helical tuft, the derived longitudinal fibre stiffness values are reduced between 10 and 15%. Property changes within the tufted unit cells are only related to change in volume fraction without further adjustment of elastic parameters.

7.2.2.2 Strength

For prediction of damage initiation in the composite the dependence of the strength parameters in each ply on the locally varying fibre volume content needs to be considered. Several analytical [169-172] and micro-mechanical finite element approaches [151; 167; 173] are available to determine the homogenised strength of uni-directional composite plies based on the strengths of fibre and resin constituents. As the fibre volume content in the unit cells of this study changes continuously within the deviated plies in a relatively large range from 50% to beyond 70% an analytical prediction method by Chamis [171] was preferred over the computational expensive prediction by micro-mechanical finite element models. According formulae are given as:

$$R_{\parallel}{}^{t} = V_f \cdot R_f{}^{t} + \left(1 - V_f\right) \cdot R_r{}^{t} \cdot \frac{E_r}{E_{f,\parallel}} \qquad \textbf{7-10}$$

$$R_{\parallel}{}^{c} = \frac{G_r}{1 - V_f \cdot \left(1 - \frac{G_r}{G_{f,\parallel\perp}}\right)} \quad \textbf{7-11}$$

$$R_{\perp}{}^{t/c} = \left[1 - \left(\sqrt{V_f} - V_f\right) \cdot \left(1 - \frac{E_r}{E_{f,\perp}}\right)\right] \cdot R_r{}^{t/c} \quad \textbf{7-12}$$

$$R_{\parallel\perp} = \left[1 - \left(\sqrt{V_f} - V_f\right) \cdot \left(1 - \frac{G_r}{G_{f,\parallel\perp}}\right)\right] \cdot R_{r,\parallel\perp} \quad \textbf{7-13}$$

$$R_{\perp\perp} = \left[\frac{1 - \sqrt{V_f} \cdot \left(1 - \frac{G_r}{G_{f,23}}\right)}{1 - V_f \cdot \left(1 - \frac{G_r}{G_{f,23}}\right)}\right] \cdot R_{r,\parallel\perp} \quad \textbf{7-14}$$

The empirical approach distinguishes between axial strengths $R_{||}{}^{t,c}$ (= $R_1{}^{t,c}$) and $R_{\perp}{}^{t,c}$ (= $R_2{}^{t,c} = R_3{}^{t,c}$) and shear strengths $R_{||\perp}$ (=$R_{12} = R_{13}$) and $R_{\perp\perp}$ (= R_{23}) parallel (||) and transverse (⊥) to the fibre direction within each unidirectional ply element. Subscripts *f* and *r* indicate the corresponding strengths of the fibre and matrix constituents. Superscripts *t* and *c* are used to distinguish between strength in tension and compression respectively.

The compressive strength of the resin matrix was measured in compression tests on neat resin samples. Tensile and shear resin strengths were derived from transverse tension and shear tests on the uni-directional and bi-axial composite by inverting equations 7-12 and 7-13. The axial fibre strengths were determined separately for uni-directional and biaxial NCF, as well as the tuft from experimental results on untufted composites. Table 7.4 summarises the determined strength parameters for the material constituents, and if available the corresponding data stated by the manufacturers (in brackets).

Table 7.4 – Selected strengths of fibre and resin constituents of UC model

	R^t_r (MPa)	R^c_r (MPa)	$R_{r,12}$ (MPa)
Epoxy MVR 444	56 (78)	149	73
		R^t_f (MPa)	
Grafil 34-700 (UD)		4120 (4830)	
HTS (NCF)		3120 (4300)	
HTA (Tuft)		3540 (3950)	

As described in 7.2.2.1 the constituents' strengths were adjusted to match experimental strength results in order to account for property reduction due to the textile structure of

the composite fabric plies which are simplified as perfectly unidirectional in the unit cells.

7.2.3 Material failure and degradation

In order to predict onset of failure and damage propagation the local 3D stress distribution within the meso-structural features of the unit cells has to be evaluated against the direction-dependent strengths of the materials by incorporating suitable failure and degradation criteria. In the following, σ, τ, ε and γ are used for stress and strain in normal and shear direction while subscripts 1, 2 and 3 refer to longitudinal fibre, transverse and through-the-thickness direction within the plies.

7.2.3.1 Failure initiation

Failure initiation in the neat epoxy matrix of the fibre-free pockets was calculated with the widely accepted maximum stress criterion for isotropic materials. The criterion evaluates the ratio of maximum (normal) principle stress to corresponding material strength in tension and compression, determining a stress exposure value f_e. Failure occurs if the fracture condition $f_e \geq 1$ is reached.

For the failure analysis of individual homogenised unidirectional plies a large number of failure criteria have been developed in the past, part of which are summarised in [174]. The first World-Wide Failure Exercise (WWFE) by Hinton et al. [175; 176] helped to assess the strength and weakness of 19 advanced failure theories to generally predict the strength of different layup configurations of unidirectional plies under various load cases. Promising approaches appear to be the 'interactive' Tsai-Wu criterion [177] and the physically based approach of Puck [178]. The advantage of the general accepted 'interactive' ply failure criterion is its need for only a very small number of parameters to determine the composite strength as no distinction is made between the internal failure mechanisms within the ply, explaining its common use in industry and commercial finite element solutions. However, due to missing phenomenological basis of this approach the more advanced continuum mechanics based action plane strength criterion by Puck [178-181] was selected for the failure initiation prediction of this work.

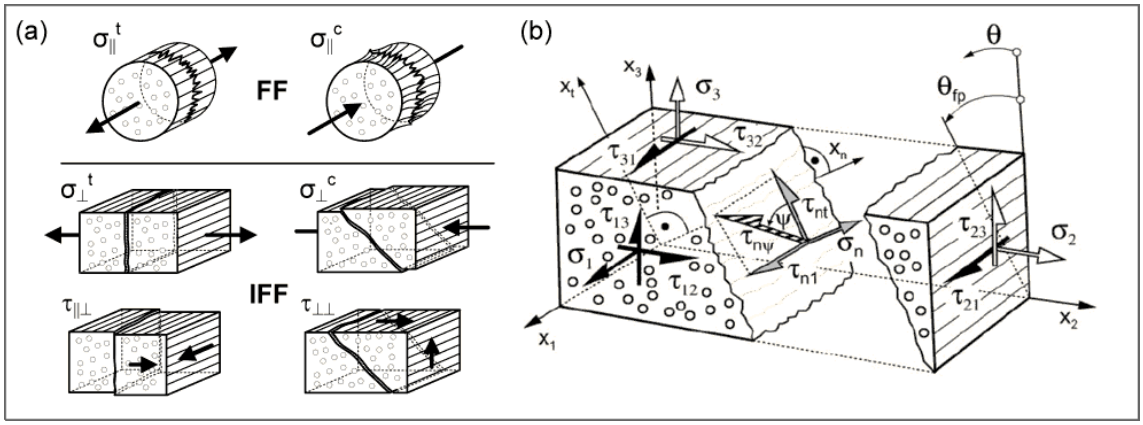

Figure 7.4 – a) Fibre (FF) and inter fibre failure (IFF) modes under different types of stressing, adapted from [181]**, b) definition of fracture plane (parallel to fibre direction), fracture angle θ_{fp}, stress components σ_1, σ_2, σ_3, τ_{31} , τ_{32} and τ_{21} in the ply coordinate system and σ_n, τ_{n1} and τ_{nt} acting on the fracture plane** [180]

The Puck criterion distinguishes between two failure types within a homogenised unidirectional composite element, which are fibre fracture (FF) and matrix dominated inter-fibre fracture (IFF). As shown in Figure 7.4 six basic types of 'stressing' $\sigma_{\parallel}^{t}$, $\sigma_{\parallel}^{c}$, $\sigma_{\perp}^{t}$, $\sigma_{\perp}^{c}$, $\tau_{\parallel\perp}$ and $\tau_{\perp\perp}$ can produce the two types of fracture. The term 'stressing' was introduced by Puck as the more general distinction between longitudinal (||) and transverse stresses (⊥) to the fibre direction appears to be more appropriate in case of a 3 dimensional stress state in orthotropic, transversely isotropic material than distinction between ply coordinates 1,2 and 3. For each stressing case a corresponding strength $R_{\parallel}^{t}$, $R_{\parallel}^{c}$, $R_{\perp}^{t}$, $R_{\perp}^{c}$, $R_{\parallel\perp}$ and $R_{\perp\perp}$ exists (see section 7.2.2.2).

For the two fracture types independent failure criteria are applied. The fracture condition is evaluated by calculating a stress exposure f_e which relates the three-dimensional local stress state to the corresponding strength properties of the composite.

For decoupled fibre fracture (FF) the maximum stress criterion is used to calculate the corresponding stress exposure f_e^{FF}, with:

$$f_e^{FF} = \frac{\sigma_1}{R_{\parallel}^{t}} \quad \text{for } \sigma_1 > 0 \qquad f_e^{FF} = \frac{\sigma_1}{R_{\parallel}^{c}} \quad \text{for } \sigma_1 < 0 \qquad \textbf{7-15}$$

Fibre fracture is assumed to be a catastrophic failure mode of the entire composite ply as the released high strain energy results normally in a compressive shock wave causing full disintegration of the ply.

In contrast to fibre fracture, the matrix dominated inter-fibre fracture (IFF) is not necessarily appearing in the plane normal to applied stressing (see Figure 7.4 a). Based on the Coulomb-Mohr fracture hypothesis for brittle materials, an acceptable assumption for the epoxy polymer composites, inter-fibre fracture is assumed to take place in a fibre-parallel (fp) stress-action plane, the so called fracture plane, which is inclined at an angle θ_{fp} against the ply thickness direction (see Figure 7.4 b) [180]. For each arbitrary angle θ a stress exposure $f_e(\theta)$ can be calculated based on the locally acting stress components σ_n, τ_{n1} and τ_{nt}, which are derived by transformation of the stress components σ_2, σ_3, τ_{21}, τ_{31} and τ_{32} of the ply coordinate system (1,2,3) to the locally rotated fracture plane, as follows:

$$\sigma_n(\theta) = \sigma_2 \cdot \cos^2\theta + \sigma_3 \cdot \sin^2\theta + 2 \cdot \tau_{23} \cdot \sin\theta \cdot \cos\theta \qquad \textbf{7-16}$$

$$\tau_{nt}(\theta) = -\sigma_2 \cdot \sin\theta \cdot \cos\theta + \sigma_3 \cdot \sin\theta \cdot \cos\theta + \tau_{23} \cdot \cdot (\cos^2\theta - \sin^2\theta) \qquad \textbf{7-17}$$

$$\tau_{n1}(\theta) = \tau_{31} \cdot \sin\theta + \tau_{21} \cdot \cos\theta \qquad \textbf{7-18}$$

with (-90°≤θ≤90°). The shear stresses τ_{n1} and τ_{nt} can be merged to a single shear stress $\tau_{n\psi}$ acting at an angle ψ to the transverse fracture plane direction (see Figure 7.4 b).

The stress exposure f_e for inter-fibre fracture as a function of the stress-plane angle θ needs to be calculated separately for tensile and compressive normal stresses σ_n at the fracture plane, as tensile normal stress $\sigma_n>0$ with or without shear stress $\tau_{n\psi}$ was found to promote and compressive normal stress $\sigma_n<0$ to impede inter-fibre fracture [180]. Subsequently, the stress exposure calculates as follows:

$$f_e(\theta) = \sqrt{\left[\sigma_n(\theta) \cdot \left(\frac{1}{R_\perp^t} - \frac{p_{\perp\psi}^t}{R_{\perp\psi}^A}\right)\right]^2 + \left(\frac{\tau_{nt}(\theta)}{R_{\perp\perp}^A}\right)^2 + \left(\frac{\tau_{n1}(\theta)}{R_{\perp\parallel}}\right)^2} + \sigma_n(\theta) \cdot \frac{p_{\perp\psi}^t}{R_{\perp\psi}^A} \qquad \text{for } \sigma_n \geq 0 \qquad \textbf{7-19}$$

$$f_e(\theta) = \sqrt{\left[\sigma_n(\theta) \cdot \frac{p_{\perp\psi}^c}{R_{\perp\psi}^A}\right]^2 + \left(\frac{\tau_{nt}(\theta)}{R_{\perp\perp}^A}\right)^2 + \left(\frac{\tau_{n1}(\theta)}{R_{\perp\parallel}}\right)^2} + \sigma_n(\theta) \cdot \qquad \textbf{7-20}$$

$$\cdot \frac{p_{\perp\psi}^{c}}{R_{\perp\psi}^{A}} \qquad \text{for } \sigma_n \leq 0$$

$$\frac{p_{\perp\psi}^{t,c}}{R_{\perp\psi}^{A}} = \frac{p_{\perp\perp}^{t,c}}{R_{\perp\perp}^{A}} \cdot \cos^2\psi + \frac{p_{\perp\parallel}^{t,c}}{R_{\perp\parallel}^{A}} \cdot \sin^2\psi \qquad \textbf{7-21}$$

$$\text{with} \quad \cos^2\psi = 1 - \sin^2\psi = \frac{\tau_{nt}^2}{\tau_{nt}^2 + \tau_{n1}^2}$$

$$R_{\perp\perp}^{A} = \frac{R_{\perp}^{c}}{2 \cdot (1 + p_{\perp\perp}^{c})} \qquad \textbf{7-22}$$

As the IFF failure criterion is based on the stresses σ_n, τ_{n1} and τ_{nt} in the fracture plane, corresponding fracture resistances R^A of the fracture plane are required (indicated by superscript A) instead of the basic strengths $R_{||}^{t}$, $R_{||}^{c}$, $R_{\perp}^{t}$, $R_{\perp}^{c}$, $R_{||\perp}$ and $R_{\perp\perp}$ which are related to the ply stressings. For pure transverse tensile stressing $\sigma_{\perp}^{t}$ or transverse/longitudinal shear stressing $\tau_{\perp||}$ the fracture plane coincides always with the action-plane of pure stresses σ_n or τ_{n1}. Hence, the basic strengths $R_{\perp}^{t}$ and $R_{\perp||}$ can be directly used for the fracture resistances $R_{\perp}^{A}$. and $R_{\perp||}^{A}$.

In contrast, for transverse/transverse shear stressing $\tau_{\perp\perp}$ the fracture plane is rotated against the pure shear plane requiring a different approach to determine the fracture resistance $R_{\perp\perp}^{A}$. Based on experimentally observed fracture angles in pure transverse compression loading Puck suggests to relate the fracture resistance to the transverse compressive strength $R_{\perp}^{t}$ (equation 7-22) [180].

Fracture is always assumed to occur in the plane with the highest stress exposure factor $f_e(\theta_{fp})$. Closed form analytical solutions for the required fracture plane angle in relation to the applied stressings are only available for plane stress condition. In three-dimensional stress state the fracture angle θ_{fp} needs to be determined by numerical search, as discussed in [178].

By applying the fracture condition ($f_e = 1$) to equations 7-19 to 7-22 the master fracture body can be determined for full 3D stress state, as shown in Figure 7.5 a). The additional inclination parameters $p_{\perp||}^{t,c}$ and $p_{\perp\perp}^{t,c}$ for the determination of the stress exposure in equations 7-19 to 7-22 are illustrated in Figure 7.5 b).

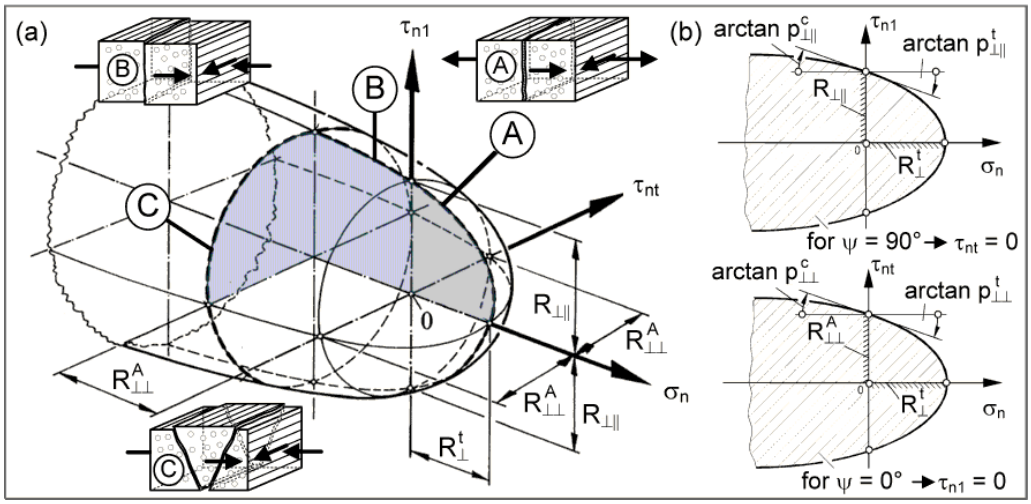

Figure 7.5 – a) Master fracture body ($\sigma_1 = 0$) for IFF in (σ_n, τ_{n1}, τ_{nt}) stress space, adapted from [179]**, b) definition of inclination parameters $p_{\perp\parallel}^{t,c}$ and $p_{\perp\perp}^{t,c}$ for fracture body** [180]

In absence of experimental data the values of equation 7-23 were assigned to the inclination parameters of Figure 7.5 b), as suggested for carbon/epoxy composites by Puck [180].

$$p_{\perp\parallel}^{t} = 0.35 \qquad p_{\perp\parallel}^{c} = 0.3 \qquad p_{\perp\perp}^{t,c} = 0.3 \tag{7-23}$$

Depending on the combination and orientation of the stress components at the fracture plane three modes of inter-fibre fracture need to be considered (see A to C in Figure 7.5 a). In IFF mode A transverse tensile stressing $\sigma_\perp^t$, longitudinal shear stressing $\tau_{\perp\parallel}$ or a combination of both are causing fracture. Due to the transverse tensile stress at the fracture plane the fracture surfaces are assumed to open, resulting in significant degradation of both macroscopic transverse tensile Young's modulus $E_\perp$ and shear modulus $G_{\perp\parallel}$. For compressive normal stressing $\sigma_\perp^c$ in failure mode B below a ratio $|\sigma_\perp^c/R_\perp^c| \leq \sim 0.4$, combined with longitudinal shear stressing $\tau_{\perp\parallel}$, fracture is caused only by the shear stress component, while the compressive transverse stressing forces the crack surfaces together. As consequence the degradation of stiffness is expected to be smaller than for mode A. Mode C is characterised by compressive transverse stressing exceeding the ratio $|\sigma_\perp^c/R_\perp^c|$ of about 0.4 and a combination of transverse and longitudinal shear stressing. The high compressive stress causes the fracture plane to incline $\theta_{fp} \neq 0°$. Resulting wedge effect of the broken layer with inclined fracture plane can lead to separation from neighbouring layers by delamination.

In the numerical damage analysis both failure criteria were implemented using the already integrated failure modules within the finite element analysis software package of MSC Software Corporation.

7.2.3.2 Degradation

For the degradation analysis of this study a phenomenological continuum damage mechanics based approach was chosen which relates degradation of the mechanical properties of the material to the local 3D stress state and corresponding fibre and inter-fibre fracture modes within each ply [182]. Such an approach allows the discrete local prediction of different failure modes, which is of specific interest for the complex features within the single tuft unit cell, although the appropriate definition of damage evolution laws is difficult due to the lack of experimental material data. While many studies relied on the discount method [150; 158; 183], i.e. the very conservative immediate degradation of all or specific elastic constant to a relatively low residual value or directly to zero at initiation of local failure, experimental data suggests a more gradual degradation for the matrix dominated inter-fibre fracture (IFF) [182; 184].

The onset of fibre failure (FF) in the fibrous plies is assumed to be ultimate failure and subsequently not considered as degradation mechanisms of the unit cell behaviour. As soon as fibre failure was detected in the first ply of the unit cell the model was stopped and the resulting maximum strength was taken as macroscopic material strength.

The matrix dominated inter-fibre failure modes A and B in the fibrous plies are assumed to reduce the load bearing capability of the individual layers, as discussed in section 7.2.2.1. At failure initation at the fracture plane local stiffnesses E_n, G_{n1}, G_{nt} and G_{t1} of the damaged elements are reduced to a stable numerical residual as soon as the stress exposure exceeds the fracture condition.

A simplified exponential degradation evolution law was used to determine the degradation factors for normal and shear modulus at the fracture plane, considering the local stress exposure and minimum residual stiffness factors η_{Er} and η_{Gr}.

$$\begin{Bmatrix} E_n \\ G_{n1} \\ G_{nt} \\ G_{t1} \end{Bmatrix}_{deg} = \begin{Bmatrix} \eta_E \cdot E_n \\ \eta_G \cdot G_{n1} \\ \eta_G \cdot G_{nt} \\ \eta_G \cdot G_{t1} \end{Bmatrix} \qquad \textbf{7-24}$$

$$\text{with } \eta_{E/G} = 1 - \left(1 - e^{1-f_e}\right) \cdot \left(1 - \eta_{Er/Gr}\right)$$

For IFF mode A failure the normal tensile stress σ_n^t causes the fracture plane surfaces to open. To determine the locally degenerated stiffnesses $E_{n,d}$, $G_{n1,d}$, $G_{nt,d}$ and $G_{t1,d}$ the following residuals were considered following suggestions by [184]:

$$\text{IFF mode A: } \eta_{E,r} = 0.01 \quad \eta_{G,r} = 0.70 \qquad \textbf{7-25}$$

The relatively high reduction of normal modulus to a residual of only 1% is justified as load can no longer be transferred between the opening failure surfaces. However, shear stresses in all three directions are still assumed to be carried equally by local bridging fibres and general surface roughness.

In case of mode B inter-fibre fracture the present compressive normal stress can still be transferred across the fracture plane. Hence, only the shear moduli are reduced:

$$\text{IFF mode B: } \eta_{E,r} = 1.0 \quad \eta_{G,r} = 0.70 \qquad \textbf{7-26}$$

From the reduced stiffness parameters at the fracture plane the reduced elastic constants of the ply are determined by transformation of the compliance matrix from the fracture plane coordinate system into the ply coordinate system [158].

Based on experimental observations by [184] the Poisson's ratios are assumed to be unaffected and to remain constant.

For degradation of the neat resin within the fibre free pocket the Young's modulus corresponding to the critical stress component is immediately reduced to 10% of its original stiffness if failure is predicted by the maximum stress criterion.

7.2.4 Numerical unit cell implementation

For numerical simulation the meso-structural unit cells for unidirectional and bi-directional fabric layup have been implemented into 3 dimensional finite element models, consisting of eight-node hexahedral elements. Each node provides three degrees of freedom u, v and w, corresponding to the displacement components in x, y and z direction. The parametric model code was written in the FE pre-processor software MSC Patran® (MSC Software Corporation) to enable simple adaptation of the geometric model parameters. For elastic and non-linear failure and degradation analysis the para-

metric model data was transferred to and analysed with the non-linear implicit solver MSC Marc® (MSC Software Corporation).

As failure initiation and degradation depend on the local stress distribution within the element grid, a convergence study was performed by increasing the element number within the unit cell until the resulting averaged global strength varied by less than 1% between iterations. The quarter unit cell of tufted biaxial $[(0°/90°)_s]_s$ non-crimped fabric composite for axial in-plane loading contained typically 17300 elements with one element layer for each composite ply. Figure 7.1 a) shows a single ply of the full 3 dimensional unit cell with the typical mesh distribution (for easier perception the element number is reduced to 2000 elements per quarter unit cell).

Within the finite element mesh fibre orientation as well as elastic and strength material properties were determined and assigned to each fibre/epoxy ply element separately depending on the position of the element centre within the distribution field of fibre deviation and compaction.

7.2.4.1 Averaged stresses and strains

According to [185], the heterogeneous composite medium can be described by effective engineering constant of an assumed macroscopically homogeneous composite, as is the modelling approach in classical laminate theory. Based on the strain energy equivalence macroscopically uniform average stress and strain tensors $\bar{\sigma}_{ij}$ and $\bar{\varepsilon}_{ij}$ are typically derived by averaging the local stress and strain tensors σ_{ij} and ε_{ij} over the volume of the unit cell V, as follows:

$$\bar{\sigma}_{ij} = \frac{1}{V} \cdot \int_V \sigma_{ij}(x,y,z)dV \qquad \textbf{7-27}$$

$$\bar{\varepsilon}_{ij} = \frac{1}{V} \cdot \int_V \varepsilon_{ij}(x,y,z)dV \qquad \textbf{7-28}$$

with $i,j = [x,y,z]$ orientation index within unit cell coordinate system.

Since the use of equations 7-27 and 7-28 can be computational expensive for unit cells with large number of degrees of freedom, which is the case for this study, the Gauss theorem was applied to derive the macroscopic averaged strain vector from the boundary displacements of the unit cell. In that case, equation 7-28 changes to:

$$\bar{\varepsilon}_{ij} = \frac{1}{V} \cdot \int_V \varepsilon_{ij} dV = \frac{1}{2V} \cdot \int_S \left(u_i n_j + u_j n_i\right) dS \qquad \textbf{7-29}$$

where S is the boundary surface area of the unit cell, u_i is the ith component of nodal displacement and n_j the jth component of the unit vector outward normal to the boundary surface S.

The validity of the Gauss theorem on elements with strain continuity ε_{ij} within the unit cell can be extended to only piecewise continuous strain fields, as present in the current model unit cell due to the different materials of Z-reinforcement, resin pocket and homogenised fabric plies, if the displacements are continuous across the interfaces between the constituents [185]. As long as bonding is ensured between the constituents, an assumption used in the current unit cell model, equation 7-29 can still be applied to derive the averaged uniform strain of an equivalent macroscopically homogenised unit cell.

Based on the equivalence of total strain energy U, stored in the volume V of the unit cell and external work, done by external displacement and corresponding load P_i, the following applies:

$$\frac{1}{2} \cdot P_i \cdot u_i = \frac{1}{2} \cdot \bar{\sigma}_{ii} \cdot \bar{\varepsilon}_{ii} \cdot V \qquad \textbf{7-30}$$

where u_i is the boundary surface displacement, applied in different load cases or extracted as resultant from the finite element analysis. The total force P_i, acting on the individual boundary surfaces, can be derived by summing the corresponding nodal force components from the finite element solution.

By applying a set of normal and pure shear displacement loading cases and deriving the corresponding force resultants and transverse displacement components, see following section, the effective elastic engineering constants for an equivalent macroscopic homogenised unit cell can be calculated from the combined equations 7-29 and 7-30 as follows:

$$E_i = \frac{\bar{\sigma}_{ii}}{\bar{\varepsilon}_{ii}} \qquad \nu_{ij} = \frac{\bar{\varepsilon}_{jj}}{\bar{\varepsilon}_{ii}} \qquad G_{ij} = \frac{\bar{\sigma}_{ij}}{\bar{\gamma}_{ij}} \qquad \textbf{7-31}$$

with

$$\bar{\gamma}_{ij} = \bar{\varepsilon}_{ij} + \bar{\varepsilon}_{ji} = \frac{1}{V} \cdot \int_S \left(u_i n_j + u_j n_i\right) dS \qquad \textbf{7-32}$$

Where E_i is the uni-axial elastic Young's modulus normal to the ith surface, v_{ij} the Poisson's ratio between ith and jth surfaces, G_{ij} the elastic shear modulus and γ_{ij} the averaged engineering shear strain.

7.2.4.2 Load and boundary conditions

In order to determined the engineering elastic constants and strengths of the different unit cell geometries four load cases together with the appropriate periodic displacement boundary conditions were applied to the geometric models, as summarised in Figure 7.6. The applied displacement boundary conditions have to ensure that the unit cell deforms as if part of an infinite continuum, requiring periodic response at its boundaries. For the uni-axial load cases parallel to x, y and z the analysis of a quarter unit cell of tufted uni-directional and [0/90] composite was sufficient using the symmetric behaviour within the unit cell. Only for in-plane shear the analysis of the full unit cell was necessary.

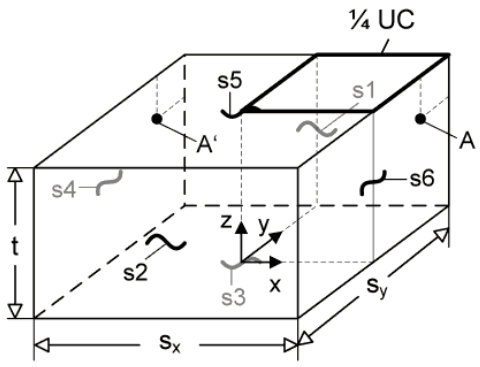

LC	Coordinate (x,y,z)	Displacement BC
x,y,z	(0,y,z)	$u_x=0$
	(x,0,z)	$u_y=0$
	(s_x/2,y,z)	$u_x=\varepsilon_x \cdot s_x/2$
	(x,s_y/2,z)	$u_y=\varepsilon_y \cdot s_y/2$
z	(x,y,t)	$u_z=\varepsilon_z \cdot t$
	(x,y,0)	$u_z=0$
xy	($\pm s_x$/2,y,z)	$u_y=\gamma_{xy} \cdot \pm s_x/2$
	(x,$\pm s_y$/2 ,z)	$u_x=\gamma_{xy} \cdot \pm s_y/2$

Figure 7.6 – Boundary conditions (BC) and applied displacements for the load cases (LC) of axial tension in x, y and in-plane shear in x,y

For all load cases the three displacement components at the model origin x=y=z=0 were restricted to avoid rigid body motion. The free boundaries s3 and s5 on the upper and lower specimen surface remained unrestricted for in-plane axial stretching in x and y direction and in-plane shear as is the case for the tested specimens. Only for out-of-plane loading case uniform displacement was enforced along the straight surfaces.

The homogenised axial moduli E_0, E_{90} and E_z, associated Poisson's ratio $v_{0/90}$ and strengths R_0, R_{90} and R_z in parallel (x), transverse (y) and normal (z) direction of the unit cell were determined on a quarter unit cell. Uniform, uni-axial displacement u_i was applied to the outer boundary surface orthogonal to the intended axial analysis direction i, while the normal displacement components at the inner boundaries (0,y,z) and (x,0,z) were constrained. The boundary parallel to the displacement direction was free to deform to avoid biaxial stress condition. However, both outer surfaces were forced to remain straight and parallel to the undeformed boundary planes by using multi-point constraints (MPC) ensuring periodic displacement between neighbouring unit cells. This limitation is acceptable as all tested unit cell geometries exhibit a symmetric fabric layup. Unsymmetrical coupling of axial strain and curvature due to variations in the material properties of loop and thread layer is neglected as the relative fibre volume content and thickness of these layers was small compared to the fabric layers of the unit cell.

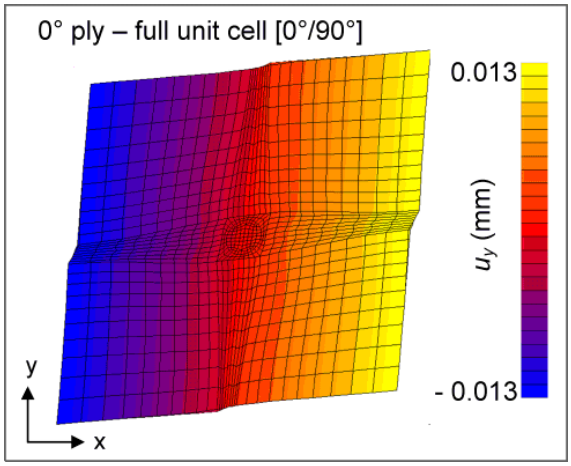

Figure 7.7 – Typical deformation of unit cell with periodic boundary conditions under pure shear ([0/90] layup with 0.5% areal tuft density)

To determine the in-plane shear modulus $G_{0/90}$ and shear strength $R_{0/90}$, uniform displacements were applied parallel to all four lateral unit cell boundaries s1, s2, s4 and s6 of the full unit cell. Following the recommendation by [134], multi-point constraints enforced equal normal displacements between mirrored nodes (A-A') on opposing shear boundaries to ensure pure shear loading across the outer unit cell surface. The boundaries are no longer limited to deformation with straight surfaces, an essential requirement for heterogeneous unit cell models [185], see Figure 7.7.

7.3 Results and discussion

7.3.1 Elastic behaviour

Table 7.5 and Table 7.6 summarise the predicted initial elastic properties of control, 0.5% and 2% tufted unidirectional and biaxial fabric layup respectively.

Table 7.5 –Predicted elastic constants of control, 0.5% and 2% tufted UD ($V_{f,2D}$ = 55.7%)

ρ_t (%)	Pattern	E_x (GPa)	E_y (GPa)	v_{xy} (-)	E_z (GPa)
0.0	-	**112.7**	**8.3**	**0.30**	**8.3**
0.5	Squ.	**112.5**	**9.7**	**0.30**	**9.5**
	Tri.	**110.4**	**9.8**	**0.31**	**9.5**
2.0	Squ.	**113.8**	**11.9**	**0.30**	**13.1**
	Tri.	**110.7**	**11.9**	**0.34**	**13.0**

For both layup configurations the through-the-thickness Young's modulus E_z is predicted to increase linearly by about 30% for each areal percent of added Z-reinforcement. This is expected as local alignment of the stiff Z-reinforcing thread with the Z-direction of the composite contributes significantly to the otherwise matrix dominated out-of-plane stiffness of flat composites. The fabric layup and tuft arrangement have only minor influence.

Table 7.6 – Predicted elastic constants of control, 0.5% and 2% tufted biaxial NCF ($V_{f,2D}$ = 54.1%)

ρ_t (%)	Pattern	E_x (GPa)	E_y(GPa)	v_{xy} (-)	G_{xy} (GPa)	E_z (GPa)
0.0	-	**62.8**	**62.8**	**0.04**	**3.8**	**8.9**
0.5	Squ.	**63.1**	**63.6**	**0.05**	**4.7**	**10.1**
2.0	Squ.	**63.2**	**64.5**	**0.05**	**5.8**	**13.7**

Although more than 50% of fabric in the tufted unit cell is deviated from original alignment with the load direction, the longitudinal modulus E_x remains quasi unaffected by the insertion of tufts with a maximum reduction of 2% for triangular tuft arrangement in UD which can be attributed to the increased maximum fibre undulation angles of the fabric. Increase in transverse (y) stiffness of up to 2.7% for biaxial layup is caused by the alignment of the surface thread seams with the y-axis, contributing to the overall stiffness of the composite.

Such small effects of the insertion of tufts disagrees with models of Dickinson and Grassi, which predicted a 10% reduction in UD for an areal Z-pin density of 2% (with a

maximum fibre undulation angle of 11°) [156; 157]. The difference appears to be caused by the incorporation of different fibre compaction models, as enhanced local fibre volume fraction would balance partially the reduced fabric stiffness due to fibre undulation (further discussed in section 7.3.4).

For transverse tension (UD) and shear stiffness (biaxial layup) the addition of tufts including surface loops results in a tuft density dependent linear increase of up to 44 and 52% respectively.

In Figure 7.8 and Figure 7.9 comparisons are given between the predicted and experimentally obtained relative change of stiffness for in-plane tension and shear results of UD and biaxial NCF respectively. It becomes clear that the predicted changes by the model for the elastic parameters are in very close agreement with the experimentally observed results for both axial (x, y) and shear stiffness.

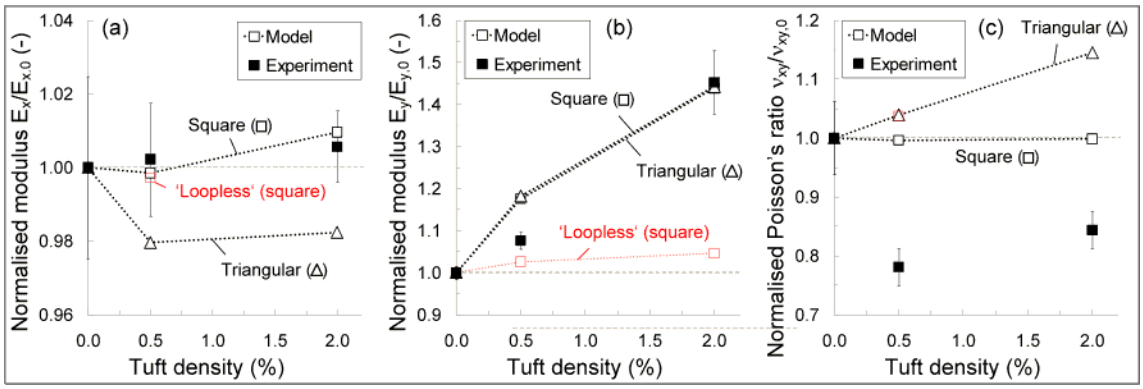

Figure 7.8 – Comparison of predicted and measured elastic properties on 0, 0.5 and 2% tufted UD composite: a) longitudinal modulus E_x, b) tranverse modulus E_y for square and triangular unit cell (shaded: results for unit cell without surface tuft loop and thread)

By substituting the discrete surface loops and threads on the unit cell surface with a neat resin layer, indicated by the additional shaded data points ('Loopless') in both graphs, it can be distinguished between contribution of local fibre deviation and compaction and additional stiffening due to the surface layers. While the axial stiffness in fibre direction is not affected, the significant increase in transverse and shear modulus is primarily caused by the surface loops, confirming the experimental observations of Chapter 6. Hence, the discrete loop geometry of the tuft must be included into the numerical simulation if correct predictions are required for matrix dominated responses of the composite, such as the transverse modulus of unidirectional specimens and through-the-thickness stiffness of any composite layup.

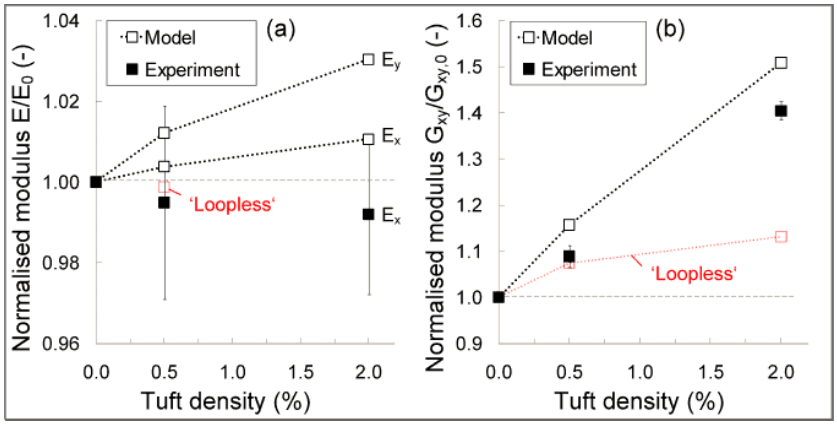

Figure 7.9 – Comparison of predicted and measured elastic property changes, normalised against untufted values, on 0, 0.5 and 2% tufted biaxial NCF: a) longitudinal and transverse modulus, E_x and E_y, and b) in-plane shear modulus G_{xy}

7.3.2 Stress field around tufts

7.3.2.1 Uni-axial loading ε_x

Figure 7.10 a) and b) show the longitudinal (σ_1) and transverse (σ_2) stress distribution and Figure 7.11 the corresponding shear stress (σ_{12}) distribution in the 0° ply of the bi-axial unit cell layup under uni-axial tension loading ε_x parallel to the x-axis of the unit cell, coinciding with the 0° ply fibre orientation. Although just uni-axial external loading is applied, the internal stress field around the inserted tuft Z-reinforcement becomes three-dimensional. High stress concentration of the axial stress σ_1 is shown in close vicinity to the tuft (see Figure 7.10 a), exceeding the far-field stress in the undisturbed fabric region by more than 15%. The extent of stress concentration is directly related to the volume of deviated fabric, as can be seen from the indicated zone of misalignment (w_{dev}).

The transverse stress σ_2 field in Figure 7.10 b) depends highly on the local fibre undulation distribution. Directly at the tuft a compressive transverse stress field is observed, which inverts to a high tensile stress with both increasing transverse and longitudinal distance to the tuft, before balancing to a uniform far-field stress distribution outside the undulated fabric volume. Such stress reversal can be related directly to the continuous fibre undulation distribution within the unit cell. At increasing uni-axial loading, the undulated fibres straighten towards the load direction and by such applying a tensile force to the neat resin rich region while compressing the tuft (see arrows in Figure 7.10 b). In the far-field, the transverse stress reduces to a small positive tensile value, which

is expected in the 0° ply of a bi-axial layup under uni-axial tension as the stiff transverse fabric plies inhibit transverse contraction of the 0° plies.

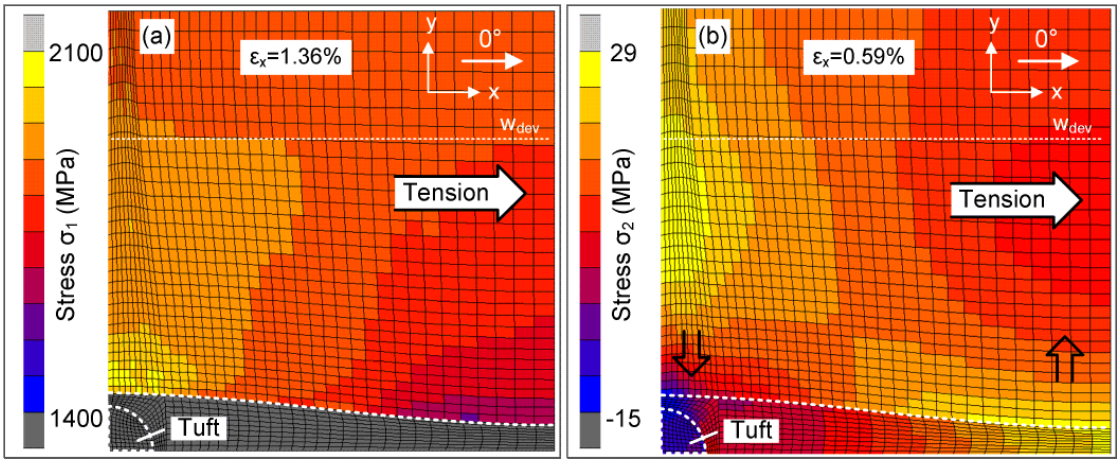

Figure 7.10 – a) Longitudinal and b) transverse stress field in 0° ply (quarter unit cell) of 0.5% tufted biaxial NCF under uni-axial in-plane tension (0°)

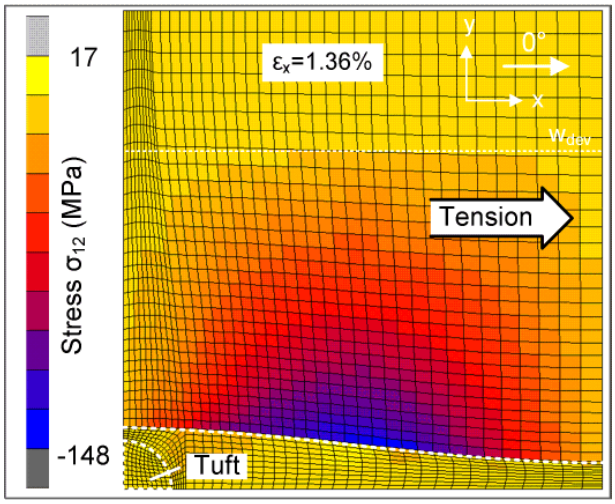

Figure 7.11 – Shear stress field in 0° ply (quarter unit cell) of 0.5% tufted biaxial NCF under uni-axial in-plane tension (0°)

In order for the undulated fibres to straighten under longitudinal tension, high shear stresses appear in the undulated fibre volume, with concentration at the zone of maximum fibre deviation at the flank of the resin pocket (see Figure 7.11). Shear stress is limited to the zone of fibre undulation. For unidirectional layup all three stress components are similarly distributed.

7.3.2.2 Shear loading γ_{xy}

The axial and shear stress distribution within the 0° ply of the full unit cell of biaxial fabric layup is shown in Figure 7.12 for applied shear γ_{xy} at the boundaries of the unit cell. Similar to uni-axial loading, the stress distribution in the composites becomes three-dimensional.

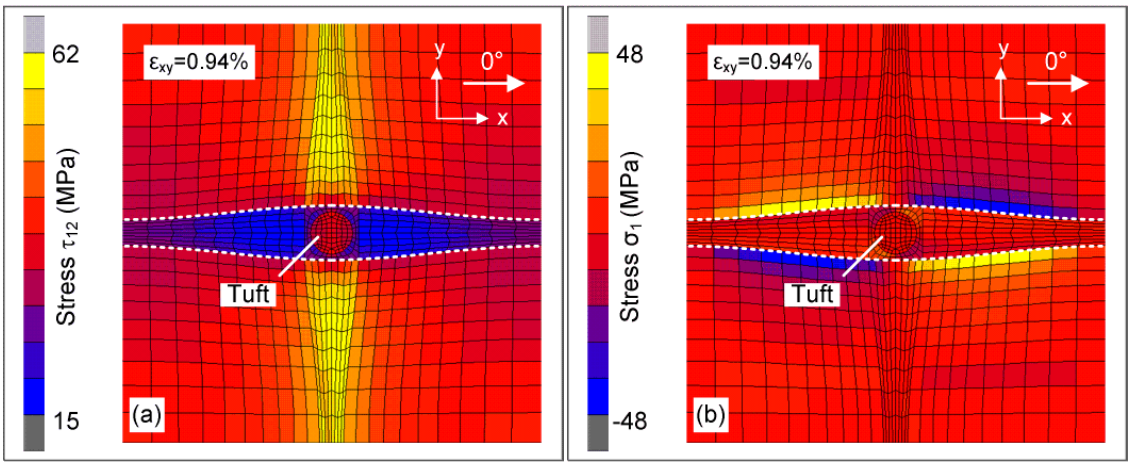

Figure 7.12 – a) In-plane shear and b) longitudinal stress field in 0° ply (full unit cell) of 0.5% tufted biaxial NCF under pure in-plane shear γ_{xy}

While low shear stress is present in the resin pocket, due to the low stiffness of the neat resin compared to the surrounding composite, the shear stress distribution in the composite ply is locally affected by the interaction between longitudinal and transverse plies. As shown in Figure 7.7, shear deformation in the resin rich regions is high compared to the surrounding composite (periodic boundary condition), opposed by relatively stiff adjacent fabric plies with transverse fibre orientation. This explains the presence of high shear stress concentration within the 0° ply at the position of the resin pocket in adjacent 90° plies. With increasing fibre undulation, shear deformation of the unit cell is opposed by axial stress in the undulated fibre tow, concentrating in the zone of maximum fibre undulation (see Figure 7.12).

7.3.3 Strength prediction and failure

In order to understand and to predict the effect of tuft insertion on the ultimate macroscopic strength of the composite layup, development of damage has to be considered, taking non-critical matrix failure modes for the fabric plies into account. In the following the failure progression is presented for the investigated biaxial and unidirectional unit cell models.

7.3.3.1 Failure progression in axial loading

Figure 7.13 a) presents the macroscopic stress-strain curves for the biaxial unit cell model with 0%, 0.5% and 2% carbon tuft density under axial loading case parallel to the 0° plies of the unit cell (ε_x). Comparable to the experimentally determined tensile behaviour of the corresponding NCF with 0%, 0.5% and 2% carbon tuft density (see Chapter 6), the model predicts non-linear macroscopic stress-strain behaviour with increasing tensile strain, see Figure 7.13 a), which becomes more pronounced at increasing tuft densities. For the unit cell with 0.5% tuft density three strain levels are indicated which are critical for failure initiation and degradation of the 0° and 90° plies of the unit cell.

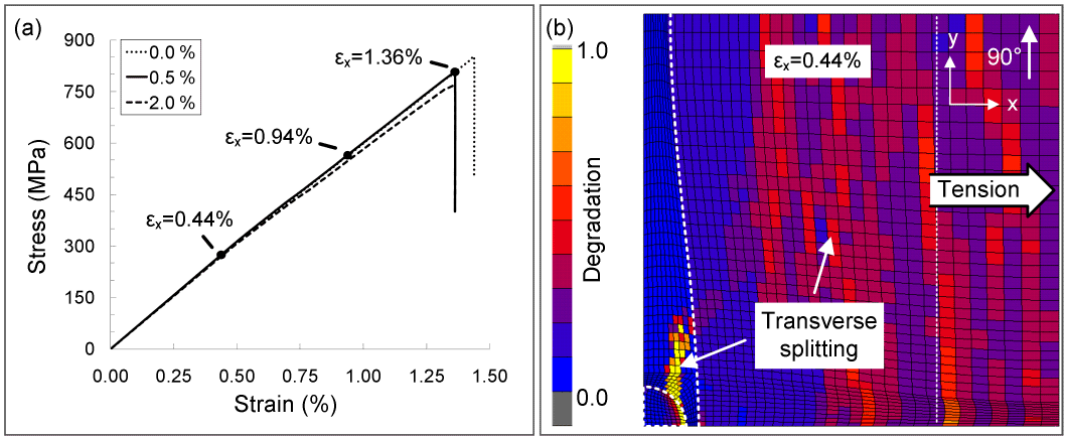

Figure 7.13 – a) Macroscopic stress-strain curves of biaxial unit cell with 0°, 0.5% and 2% tuft density for longitudinal loading (ε_x), b) degradation in 90° ply (ε_x=0.44%) due to formation of transverse matrix failure

At an axial strain level of ε_x=0.44%, transverse tensile matrix failure initiates in the 90° fabric plies within the neat resin pocket between tuft and surrounding highly compacted fabric, and in the fabric plies, as shown in Figure 7.13 b). Both such failure modes are expected for the transverse plies of a bi-directional fabric layup under axial loading and have been observed to initiate at a comparable strain level of 0.4% within the tufted NCF composite (see Chapter 6). With increasing fabric deviation from the 90° ply orientation the load is carried partially by the fibres and not purely by the matrix. Hence, transverse tensile cracks appear primarily outside or within low levels of deviated fabric in the 90° ply.

At tensile strain of 0.94% the transverse tensile stress distribution in the 0° plies of the biaxial stacking, as introduced in section 7.3.2.1, causes the formation of transverse

matrix failure, enabling further fibre straightening of the deviated fibre tows. Figure 7.14 a) shows the corresponding stress exposure distribution f_e in the 0° ply at failure initiation for inter-fibre failure mode A of the Puck failure criterion (σ_n>0). Matrix tensile failure initiates not only in the resin rich pocket away from the tuft, but also in the 0° fibre ply transverse to the tuft in a zone were adjacent plies contain a fibre free pocket. It becomes apparent that for the biaxial fabric layup the transverse fibre plies support the deviated fibre regions of the 0° plies against straightening. With the support missing in the resin rich region of the adjacent ply, transverse matrix failure initiates in the 0° plies. In the experimental tension tests on NCF such transverse failure was observed to develop as discrete longitudinal splitting cracks along the fibre direction at strain level of 1.1% strain, as shown in Figure 6.4 of Chapter 6. Figure 7.14 b) shows the level of degradation of the 0° ply due to tensile inter-fibre failure at ultimate strain, before initiation of fibre failure.

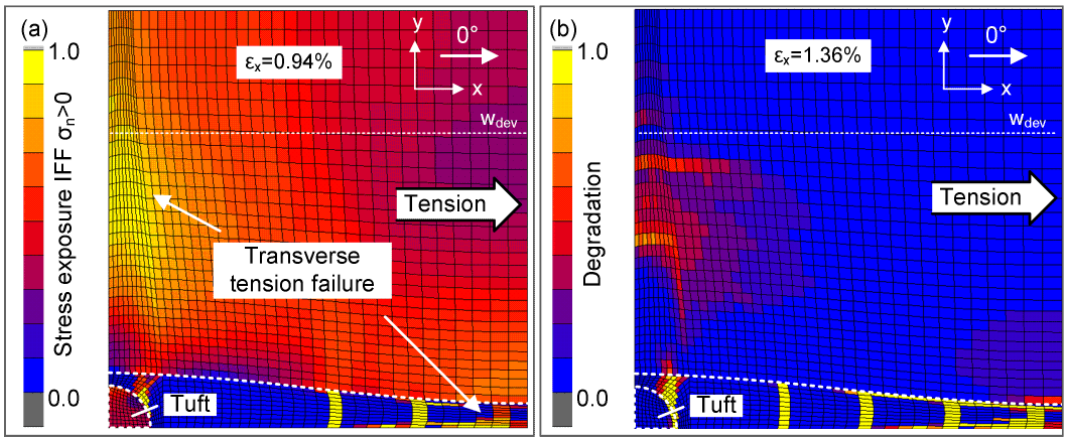

Figure 7.14 – Failure progression in 0° ply under axial load: a) stress exposure distribution for mode A IFF at transverse failure initiation (ε_x=0.94%), b) degradation of elements at ultimate strain due to mode A IFF (ε_x=1.36%)

Fibre failure was predicted to initiate in the fibre bundles closest to the tuft, in a zone of enhanced axial stress concentration, as shown by the stress exposure distribution for fibre failure in Figure 7.15 a). This failure location for fibre failure coincides with observations on failed NCF specimens, as shown in Figure 6.7 of Chapter 6. As shown in Figure 7.15 a), a zone of undeviated fabric within the far-field of the tuft is also highly loaded due to reducing fibre volume fraction and corresponding strength in the fibre ply at increasing longitudinal distance to the tuft. However, the exposure level was found to remain about 10% below the level at the tuft.

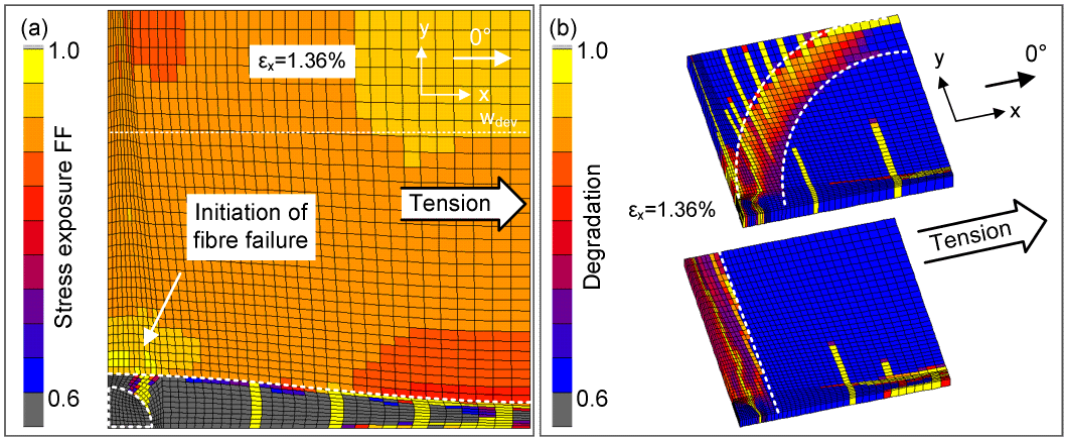

Figure 7.15 – Ultimate failure of biaxial unit cell: a) stress exposure distribution for fibre failure in 0° ply (ε_x=1.36%), b) degradation of surface loop and thread layers

For 0° loading the surface loop and thread contribute little to the total strength as only segments of the loop are aligned with the load direction. However, significant level of inter-fibre failure is predicted in the off-axis segments of the surface threads, as shown in Figure 7.15 b).

Failure initiation and development in the uni-directional unit cell were found to be comparable to the 0° ply behaviour of the biaxial unit cell. Only, stabilising transverse fibre plies are not present. Hence, expansion of transverse tensile inter-fibre failure parallel to the tuft is not retarded, leading to large damage bands of combined transverse tension and shear, as shown in Figure 7.16 for the equivalent 0.5% tufted UD unit cell with square tuft arrangement.

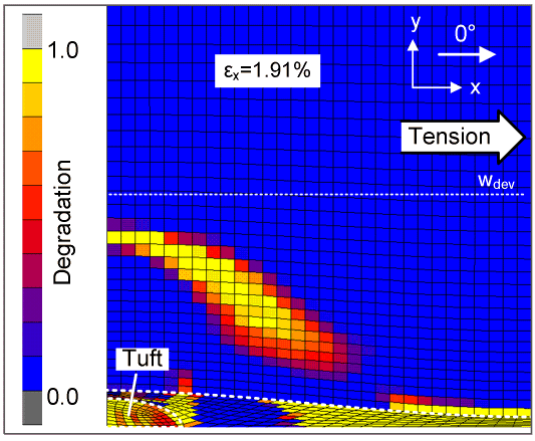

Figure 7.16 – Degradation of 0.5% tufted unidirectional unit cell under uni-axial in-plane tension (quarter unit cell) at ultimate strain (ε_x=1.91%)

7.3.3.2 Shear load case

Figure 7.17 shows the experimentally measured and predicted shear stress-strain curves of biaxial layup with 0%, 0.5% and 2% tuft density. While the initial modulus and slope are predicted accurately, significant non-linear behaviour was not reproduced by the model. Main cause for the insufficient prediction appears to be the assumption of linear elastic material and relatively brittle damage evolution. The tested specimens were found to exhibit significant damage accumulation due to initiation of shear cracks from thermal cracks within the resin rich regions, which are not present in the current model. To account for such features either a combined model of continuum mechanics based ply failure criterion and discrete fracture mechanical approach or a continuum damage mechanics based approach as the Cachan model [129] are required.

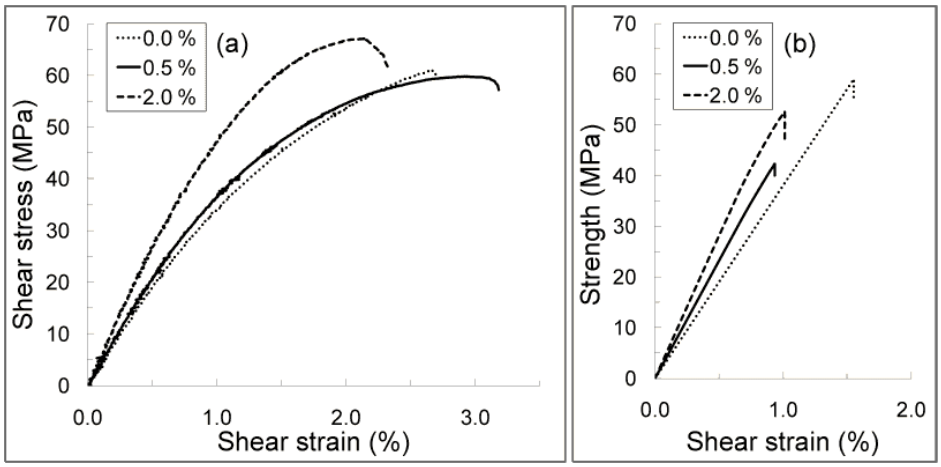

Figure 7.17 – Comparison of a) measured and b) predicted shear stress-stain curves for 0, 0.5% and 2% tufted NCF

7.3.3.3 Strength comparison

Figure 7.18 a) shows the comparison of predicted and measured relative change of axial tensile strengths for UD composite layup for 0.5% and 2% areal tuft density, normalised against the strength of the untufted material. While the perfectly square tuft arrangement creates an upper bound for the minimum reduction in axial strength, predicting reductions between 4% and 6%, the triangular pattern defines the lower bound, the maximum possible reduction, in axial strength, which can reduce by 22%. The measured strength for uni-directional test specimens in longitudinal loading is found to range within the given boundary. As general failure is governed by individual critical imperfections, small variations to triangular arrangement in the otherwise square tuft pattern within the

UD test specimens explains the relatively low values of the experiment within the boundaries.

The model is able to predict correctly the measured non-linear trend of significant initial reduction for 0.5% tuft density, but only small additional reduction for increase to 2% tuft density. Main cause for the non-linear trend is the only small additional increase in fibre deviation angle with closer tuft spacing, the critical factor for the reduction of axial strength.

It has to be noted that for triangular unit cells a small number of elements were highly skewed or had large aspect ratios in a small zone at the tapered end of the resin pockets. While subsequent prediction of local failure within these elements is potentially affected, the global strength remains unaltered as failure propagation in the regular meshed areas determines final failure of the composite unit cell.

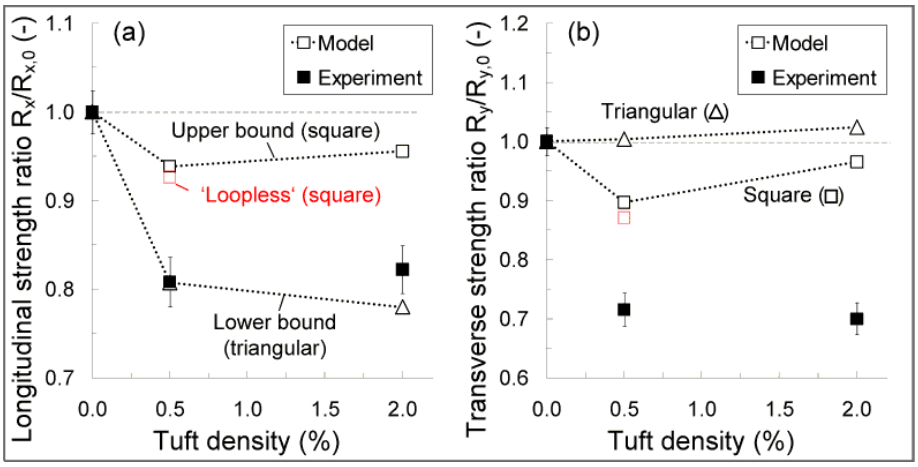

Figure 7.18 – Comparison of predicted and measured relative strength reductions on 0.5 and 2% tufted unidirectional composite: a) longitudinal strength R_x and b) transverse strength R_y

The transverse tensile strength of the unidirectional layup was predicted to be less dependent on the tuft pattern and maximum fibre deviation angle. Significant differences between predicted maximum reduction of 10% and measured reduction of up to 30% is eplained with the observed failure initiation at thermal cracks in the experiments, an imperfection not presented in the current unit cell model.

In contrast to prediction of the corresponding elastic properties, the implementation of the discrete surface loop and thread are not critical for the strength prediction in both longitudinal and transverse loading case, as indicated by the additional data points for 0.5% tuft density ('Loopless').

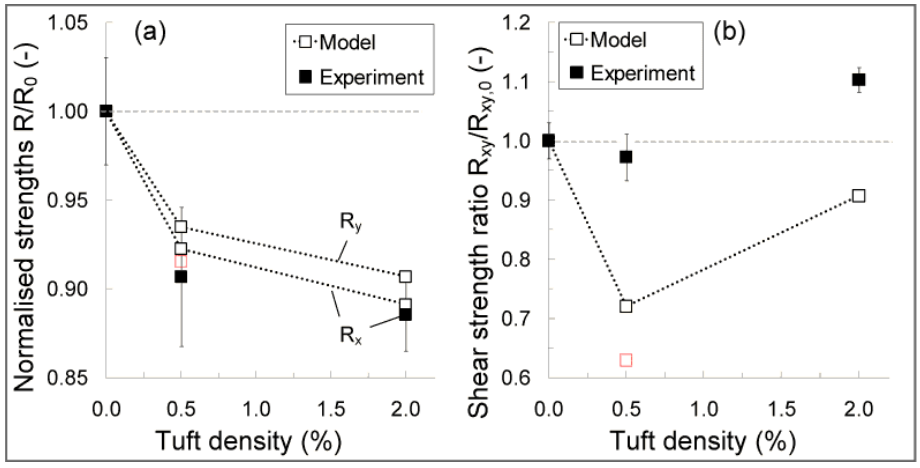

Figure 7.19 – Comparison of predicted and measured relative change in strengths of 0.5 and 2% tufted biaxial NCF composite: a) longitudinal and transverse strengths, R_x and R_y and b) in-plane shear strength R_{xy}

Figure 7.19 a) shows the relative reduction in predicted tensile strength parallel (0°) and transverse (90°) to the x-axis of the biaxial unit cell, together with relative changes determined from experimental results in x-direction. For the fibre dominated transverse strength of the biaxial unit cell the presence of aligned surface thread contributes only little, increasing the strength by 2%. For biaxial layup the unit cell model with square tuft arrangement predicts axial strength values in close agreement with reductions found in experiments of Chapter 6.5.1.2, as local variations in square tuft arrangement were less pronounced compared to the unidirectional composite specimens.

It has to be noted that suppression of delamination, a beneficial effect of tufting on the tensile strength found in the experimental testing, is not incorporated in this model. The close agreement between test and prediction, despite the potential presence of local pattern shifts in the tested specimens, is expected to be partially due to superposition of detrimental pattern shift effects and suppressed delamination in the experimental results.

For shear loading, the model predicts a significant reduction in shear strength of up to 30%, deviating significantly from the measured properties as additional damage mechanisms and non-linear material properties are present in the experimental test specimens (see above).

7.3.4 Effect of fibre volume fraction distribution

Figure 7.20 shows the relative prediction results of uni-axial strength (R_x) and stiffness (E_x) for the biaxial unit cell with 0.5% tufting, normalised against corresponding ex-

perimental results, for three different fibre compaction models. If change in local fibre volume fraction is disregarded ($\Delta V_f=0$) both the predicted stiffness and strength are underestimated by 7% and 8%, while an assumed uniform enhancement of fibre volume fraction based on the resin pocket cross-section area ($\Delta V_f=f(A_{rp})$) causes an over-prediction of 13% and 10% respectively. For both assumptions the deviation of prediction is significantly higher than the corresponding standard deviation in the experimental results. Only, if local fabric compaction variation is taken into account the strength and especially the modulus are in agreement with the experimental results. Similar effects were also found for the uni-directional unit cell, although slightly reduced, as the maximum resin pocket width is smaller.

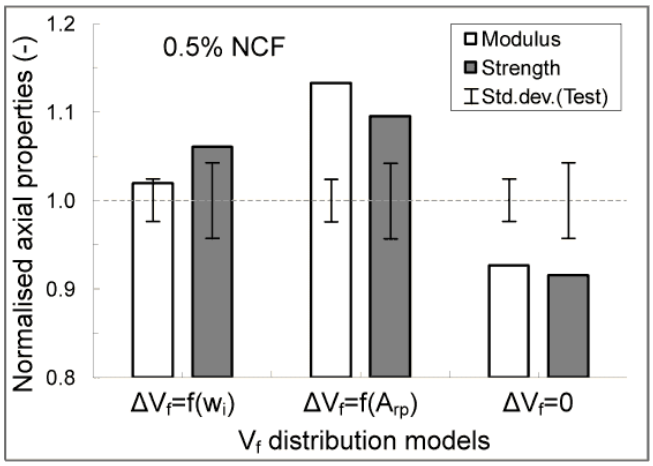

Figure 7.20 – Comparison of predicted longitudinal moduli and strengths normalised against the experimental results of 0.5% tufted NCF for three different fibre distribution models

It becomes apparent that the correct identification of the fibre compaction distribution within the deviated fabric is essential for prediction of both true elastic and strength prediction, a parameter which has been disregarded or simplified in most comparable studies to date [97; 156; 158; 160; 173]. On meso-structural level in the unit cell, disregarding of fibre compaction causes an underestimation of tensile strength in the ply zone of local tensile stress concentration next to the tuft, resulting in the reduced strength prediction. On the other hand, averaged increase in fibre volume fraction assumes an increased transverse tensile and shear strength at the resin pocket away from the tuft which leads to inhibition of strength degrading formation of longitudinal splitting cracks and over-prediction of strength.

7.3.5 Effect of fibre deviation

Figure 7.21 shows the relative change in uni-axial tensile strength R_x, compared to the strength $R_{x,0}$ of the untufted material, for increased maximum fibre undulation and relative volume of deviated fabric in 0.5% tufted UD and biaxial unit cells with square tuft arrangement. The maximum fibre undulation in Figure 7.21 a) was varied by changing the minimal width of the resin rich channels of the unit cell model while keeping all other feature dimensions constant. Hence, changes in strength can be related directly to the unique changes to the stress field due to fibre undulation, while fibre compaction induced improvements are avoided (which would be the case for changing the maximum pocket width w).

As can be seen in Figure 7.21 a), both biaxial and unidirectional fabric layup are very sensitive to the maximum angle of fibre undulation, as the load bearing capability of the deviated fabric plies reduces. A quasi-linear strength reduction can be observed for increasing fibre deviation angles. Due to the presence of transverse fibre plies, which oppose the development of large damage and transverse splitting zones in the 0° plies, the biaxial fabric layup is less sensitive to angle of fabric deviation than the unidirectional composite, explaining partially the improved strength of experimentally tested NCF in Chapter 6. Modulus changes remain small with enhanced fibre deviation.

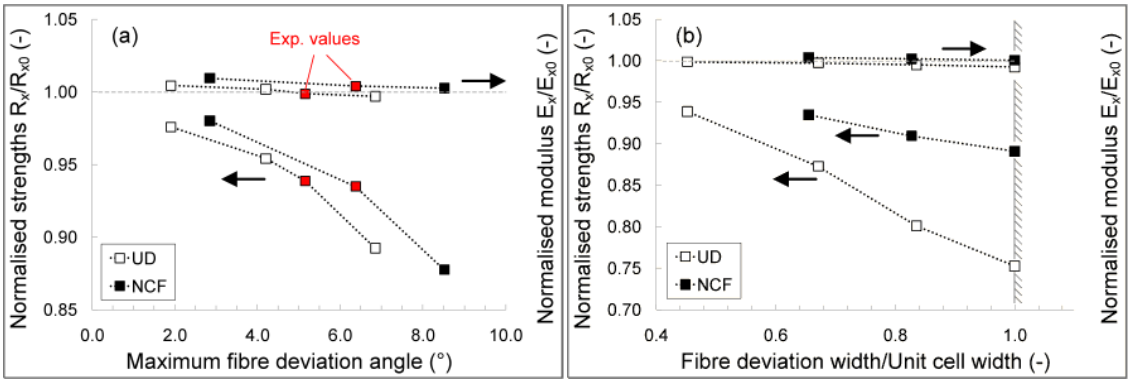

Figure 7.21 – Change in relative strength and modulus (normalised against untufted UC) for 0.5% tufted UD and NCF unit cell with changing a) maximum fibre deviation angle and b) volume of deviated fabric

By changing the width w_{dev} at which fabric deviation reduces to zero in transverse distance to the tuft the total volume of deviated fabric could be varied. From Figure 7.21 b) it becomes apparent that the strength, especially of unidirectional composite layup, is highly affected by the assumed volume of deviated fabric, reducing linearly with relative increase in volume. Primary cause is the reduced volume of straight fibres which

are carrying the axial load and increased damage zone, resulting in earlier fibre failure at the stress concentration point in direct vicinity to the tuft. Such effect has been generally not accounted for in previous modelling approaches with failure prediction [97; 158].

Hence, the correct identification of both maximum fibre deviation and volume of deviated fabric is important to predict accurately the strength changes due to insertion of tufts. While the maximum fibre deviation angle can be determined easily by micrography of sectioned composite samples, the measurement of volume of deviated fabric in naturally inhomogeneous textile fabrics remains a challenge.

7.4 Conclusions

Detailed implementation of both variable fibre deviation and fibre packing distribution showed to be essential for the correct prediction of elastic and strength properties. An averaged fibre volume fraction model is not sufficient as it leads either to over- or under-prediction of modulus and strength of the unit cell.

The developed parametric unit cell model provides the basis for a detailed strength analysis of various tuft arrangements and fabric stacking sequences based on empirically determined meso-structural tuft features, such as local fabric undulation, formation of resin rich regions and compaction of the fabric.

With implementation of the detailed morphologic features not only elastic constants and strength could be predicted with good agreement to experimental tests but also the local failure and degradation mechanisms were captured accurately for the axial loading. Only, the simplification of linear-elastic material behaviour resulted in under-prediction of shear strength for the tufted composites.

Local increase in fibre compaction compensates the effect of local fabric undulation around the tuft on the fibre dominated elastic response of the composite. Fibre undulation is the most critical parameter on the reduction of strength, suggesting the avoidance of triangular tuft arrangement in load bearing fabric plies. By incorporating the two most extreme tuft arrangements of perfectly square or triangular tuft to tuft arrangement with respect to the uni-axial or biaxial ply stacking an upper and lower bound can be determined for the potential reduction in in-plane strengths. As already observed in experimental tests the unidirectional fabric is more sensitive to local fibre undulation than

biaxial fabric stackings with stabilising transversely orientated fabric plies. Surface loop and thread seam have a negligible effect on the fibre dominated axial response, but can highly affect matrix dominated shear and transverse tension in unidirectional material. Increased local fabric compaction also contributes to increased shear and transverse tensile stiffness, while the effect of fibre undulation is negligible.

Chapter 8 Delamination behaviour of tufted composites

8.1 Introduction

Improvements in resistance to delamination of 2D continuous fibre reinforced epoxy matrix composites by the inclusion of through-the-thickness (Z-direction) reinforcements are well documented [27; 91; 92; 110-112]. Z-Fiber ® pinning [5] is suitable for reinforcement of prepreg based laminates while structural stitching and tufting are currently used with dry fabric preforms. Dransfield et al. gave an early review of the conventional stitching techniques and dependency of thread selection on the improvement of the delamination toughness in under mode I and II loadings. Advantages of stitching, besides the improved delamination toughness, are perceived as better preform handling, free edge stabilisation and hence the possibility of automation of the manufacturing process. The main disadvantages were seen to be in-plane fibre damage and consequent reduction of the in-plane properties of the composite [6]. Subsequent studies by other authors confirmed the enhancement in the delamination resistance and established good impact damage resistance and joint strength of stitched composite. The presence of interlocking thread knots was shown to reduce the through thickness strength of the stitches [186] and laminate in-plane properties by disrupting and damaging the in-plane fabric [2; 3].

Extensive studies of Mode I delamination in stitched composites point to delamination resistance increases of between ten and fiftyfold, with reproducible measurements obtained for a given set of samples. Simple stitch failures are characterised by local debonding, in-elastic stretching, and frictional pull-out after thread failure [91].

To date, significant variability and disagreement persists in attempts to characterise the mode II delamination performance of the same sets of samples. This variability in mode II delamination resistance values has its root in the complex stitch failure mechanisms and often reported insufficient bridging lengths, as compressive forces cause flexural failure of the stitched specimens exerted by test fixtures such as the 3-point-End-Notched-Flexure (ENF). Hence Jain et al. suggested the use of the End-Loaded-Split (ELS) test to achieve full-scale Z-reinforcement bridging [92].

This chapter concentrates on detailed evaluation of the delamination resistance of tufted carbon fibre composites, specifically those based on the so called non-crimped fabrics (NCFs) which are in themselves an example of a (non-structurally) stitched preform. Very limited information is currently available on the out-of-plane mechanical performance of tufted composites. Previous work in this laboratory has reported an improvement of an order of magnitude in the apparent mode I delamination toughness of 1% glass thread tufted five-harness woven and quasi-isotropic non-crimped fabric material [85]. It has been established that delamination initiation is unaffected by the presence of the Z-reinforcement and the studies therefore concentrate on evaluating the resistance to crack propagation. Some mode II delamination studies have also been carried out on biaxial non-crimped fabric with 0.3% areal density carbon thread tufts, leading to a threefold increase in the apparent mode II delamination toughness [187].

The major issue with determination of delamination propagation resistance of any Z-direction reinforced composite is the fact that the values are sample geometry dependent. Specifically, the thickness of the sample, or rather the length / depth of insertion of the Z-direction element determine the traction forces exerted by the Z-pin, stitch or tuft as it bridges the propagating delamination crack. The data reduction methods in current use for delamination testing of composites are based on linear elastic fracture mechanics assuming negligible plasticity around the crack tip and no fibre bridging. The presence of large scale tuft bridging in the delamination crack introduces a structural component into the otherwise material property. In their work on Z-pinned composites, Partridge and Cartié [5] suggest the use of the term 'apparent toughness' or 'G_{Ip}', 'G_{IIp}' to account for this fact.

Studies of delamination response under forward shear (mode II) loading represent a specific challenge. Even for simple unidirectional laminates, development of standard test protocol or data reduction have been hampered for many years by the difficulties associated with correct identification of the crack tip [188]. The present chapter describes an experimental technique based on digital image correlation, by which the position of the crack tip may be identified with a higher degree of certainty.

8.2 Materials and manufacturing

Dry carbon fibre preforms, 200 mm x 200 mm, were assembled from four layers of bidirectional (0°/90°) non-crimped carbon fibre fabric (Sigmatex®) with an areal weight of 1010 g/m^2, stacked in a symmetric $[(0/90)_s]_2$ layup with two 0° plies at the preform

mid-plane. Each 0°/90° NCF layer contained equally arranged 24k HTS carbon fibre tows from Tenax, held together by non-structural stitching with 8g/km polyester yarn in tricot/chain pattern. The chain pattern was oriented orthogonal to the 0° ply direction. A 10 μm thick PTFE crack starter film was placed in the mid-plane of the preform, between the two central 0° plies, extending 65 mm from the edge.

One half of each preform panel was then structurally tufted through-the-thickness with high-twist 2k HTA carbon fibre sewing thread (Schappe Techniques). The other half was left untufted for control samples, designated as '0%'. The tufts were inserted normal to the laminate plane in square pattern with 5.6 mm x 5.6 mm spacing, resulting in areal tuft density of 0.5%. Tufting seams were aligned orthogonal to the 0° ply orientation, with the first tuft row positioned 16 mm from the end of the release film, covering a total delamination length of 100 mm. The free thread loops, which protrude from the bottom preform surface (opposite the tuft insertion side) and lock in a resin rich layer during resin injection and cure, had average height of 3.3 mm. For characterisation of the tufting thread material, tensile tests were performed on infused thread rodstock according to BS EN ISO 10618:2004. These tests reveal an average infused thread stiffness of 199 (±10) GPa and ultimate strength of 3544 (±72) MPa.

Each panel was injected with epoxy resin (MVR 444, Advanced Composites Group) using the vacuum assisted resin transfer moulding process. After successful resin injection at 1 bar and 70°C, the panels were cured at 4 bar and 160°C for 75 minutes, followed by free standing oven postcure at 180°C for 90 minutes. Heating and cooling rates of 2°C per minutes were controlled carefully, using an Isojet RTM injection controller. By injecting the panels in a rigid steel mould, a consistent laminate thickness of 4.0 (±0.01) mm was achieved, resulting in a carbon fabric fibre volume fraction of 56 %. The insertion of carbon tufting thread at 5.6 mm spacing increased the global fibre volume fraction within the tufted sections by an extra 1.4% (i.e. to 57.4%).

8.3 Experimental

8.3.1 Specimen preparation

Figure 8.1 shows the schematic of sample dimensions and tuft row positioning used in the delamination tests. The longitudinal axis of the double cantilever beam (DCB) specimen was parallel to the 0° ply orientation in the mid-plane of the specimen. Cut edges were polished to tolerance with 1200 grit silicon carbide paper on a flat disk pol-

ishing machine to remove any machining damage and facilitate the identification of the crack tip during crack propagation. The sample ends with insert film were trimmed with a slow speed water-cooled diamond wheel saw to ensure correct alignment of the required load blocks. After trimming, the insert film in each sample had a length of 61 mm (±0.5mm), giving an initial crack length a_{insert} of 50 mm from the load line.

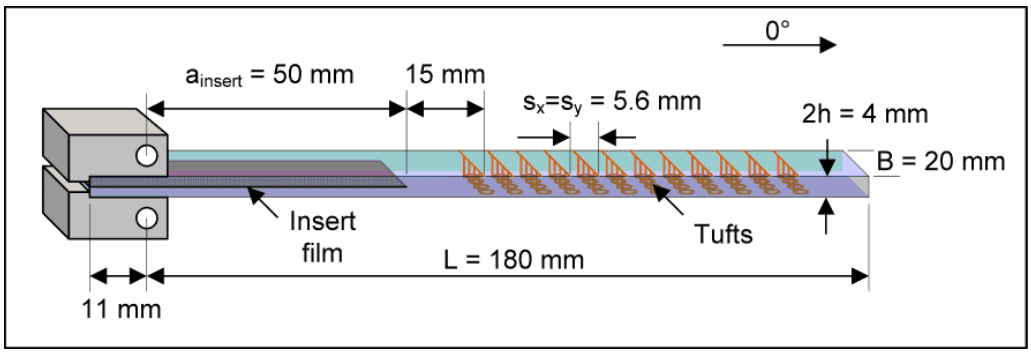

Figure 8.1 – Schematic of specimen configuration for DCB/ELS delamination testing

One side of each beam was coated with a thin layer of brittle white spray-on paint and marked with millimetre increments to enable visual monitoring of the crack tip position. On the opposite side a black and white speckle pattern was applied for monitoring of crack propagation and measurement of opening and shear displacements along the cracked beam halves with the digital image correlation system (Limess VIC 2D and VIC 3D).

In initial mode I delamination trials on 0.5% tufted NCF samples of 4 mm thickness the delamination crack stopped propagating as it reached the first Z-reinforcement row. Any additional beam opening caused flexural beam failure. To avoid such flexural failure, 3 mm thick strips of cured unidirectional composite were bonded to both sides of the tufted DCB samples with a structural adhesive (Araldite A/B 420 from Huntsman), as suggested by [91; 189]. The unidirectional laminate contained 10 layers of carbon fibre uniweave fabric (OCV Technical Fabrics™, 12k Grafil 34-700) with an areal weight of 310 g/m^2, infused with MVR 444 epoxy resin and cured. Steel load blocks were bonded onto the pre-cracked sample ends with cyanoacrylate adhesive, to enable load introduction by steel pins. Before testing all specimens were conditioned in standard atmosphere.

8.3.2 Delamination testing

Delamination tests on DCB and ELS specimens were performed on a universal test machine Instron 5500R, with 5kN load cell, at a constant cross-head speed of 1 mm/min in a temperature controlled laboratory (21°C ±2). Load *P* and crack displacement δ at the load line were measured at a rate of 1 Hz.

In absence of standardised procedures for testing and data reduction of through-the-thickness reinforced bi-directional laminates, mode I tests were performed following the procedure for unidirectional composites without Z-reinforcement (ISO 15024:2001). Mode II delamination tests followed the current ELS protocol, which was developed originally by the ESIS TC4 committee for unidirectional laminates [190; 191]. Prior to mode II testing the compliance of clamping mechanism was measured using the 'inverse' ELS procedure. The root rotation beam length correction factor Δ_{clamp} was determined as 9.0 mm and 9.8 mm for control and 0.5% tufted ELS samples respectively. Prior to delamination testing the initial pre-crack was propagated from the insert film for 5 mm by opening the beam halves in mode I and unloading. The new crack tip a_0 ensures the measured initiation values to be independent of the insert film tip. For crack propagation testing, mode II samples were clamped with a defined force at a span of 100mm from the load line in an aluminium ELS jig which allows the necessary horizontal sliding as the sample bends under the applied transverse load.

Crack extension *a* was determined by visual observation with the aid of a magnifying glass and by derivation from the displacement field via digital image correlation (DIC). With DIC the local variation in the displacement field between the upper and lower beam halves was calculated and evaluated from a set of recorded pictures, taken at 1Hz. In the case of the DCB samples two digital 1.4 megapixel cameras were positioned orthogonal to the specimen surface, each recording a 50 mm long section in 2D starting at the crack initiation film a_0 and covering a total delamination length of 100 mm. For the ELS tests the cameras were set in a 3D configuration covering the total delamination length of 50 mm from initiation film tip to the clamp. Measurement of the opening and shear displacement components directly at the crack interface was not possible as the crack singularity disturbs the image correlation algorithm. Hence, both components were calculated from the measured displacements at equidistant lines 0.7 mm above and below the laminate mid-plane (plane of crack propagation) using elastic beam theory. The crack tip was identified as position at which the relative opening and shear dis-

placement between the adjacent lines dropped below a threshold level of 0.003 mm. The threshold value was chosen based on the natural level of noise in the DIC measurement.

In mode II flexure the ENF beam exhibits elastic shear deformation which is captured in the DIC measurement due to the separation of the two analysis lines. To eliminate the elastic shear component from the actual shear displacement between the separated beam halves in the DIC measurement the stabilised shear measurement beyond the crack tip was averaged and deduced as constant term from the measured total shear displacement. The relative offset due to elastic shear deformation accounted typically for less than 2 μm in the measured shear displacement.

As the measurement plane in the DIC system is fixed with the orientation of the cameras, rotation of each beam half was taken into account to derive the relative opening and shear in relation to the local crack plane. The calculated displacement resolution, which depends on the analysis area and camera resolution, was verified by a series of pictures taken at zero beam flexure. A standard deviation in opening and shear displacement of less than 1.3 μm and 1.9 μm was determined for mode I and II setup respectively, which is below the chosen threshold for identification of the crack tip.

8.3.3 Data reduction

8.3.3.1 Mode I - DCB

The corrected beam theory (CBT) was used as the data reduction method according to (ISO 15024:200). Large scale bridging by the tufts affects the validity of the conventional derivation of delamination toughness based on linear elastic fracture mechanics. Hence, the data were re-analysed with a modified procedure for the corrected beam theory, which was originally proposed by Robinson and Das [192] to correct for changes in the beam compliance for developing and developed large scale bridging zones. Robinson and Das showed that values closer to the true delamination toughness for Z-reinforced laminates can be determined by using separate length correction factors Δ for the unreinforced and for the fully developed bridging zones. Each factor is calculated as intercept of the linear interpolation determined only for values of the unreinforced or of the fully developed section in the $(C/N)^{1/3}$ versus crack length plot (see Figure 8.2).

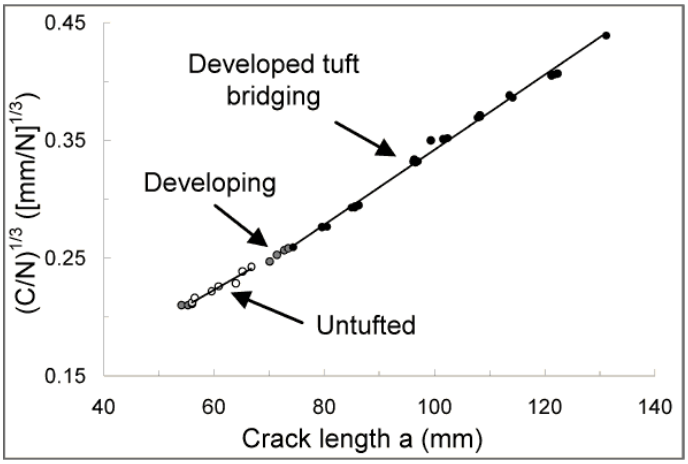

Figure 8.2 – $(C/N)^{1/3}$ versus a plot of 0.5% tufted NCF laminate, obtained in DCB mode I delamination test

8.3.3.2 Mode II - ELS

As the flexural stiffness in the bi-directional laminate depends on the chosen ply-layup, the separated beam halves have a higher flexural stiffness E_a than the complete, unbroken laminate, E_b for the chosen NCF layup. In absence of a standardised procedure, the ELS protocol of the ESIS TC4 committee was adapted to apply to beams of variable stiffness.

In the experimental compliance method (ECM) for the calculation of the delamination toughness G_{IIc} the change in stiffness is represented within the slope m, measured in the compliance C versus crack length a^3 plot. As the ECM is sensitive to errors in the measured crack length, test data were also analysed with the corrected beam theory with effective crack length (CBTE) and an experimentally determined clamp correction. In the CBTE the measured crack length a is substituted by an effective crack length a_c which is calculated from the changing compliance of the ELS specimen, including the compensation for load blocks and root rotation. The required corrected compliance C/N of the delaminated ELS beam with variable stiffness can be derived from the standard beam theory as follows:

$$\frac{C}{N} = \frac{\delta}{PN} = \frac{2a^3}{Bh^3E_a} + \frac{\left(L + \Delta_{clamp}\right)^3 - a^3}{2Bh^3E_b} \qquad \textbf{8-1}$$

where N is the load block correction factor and Δ_{clamp} corrects for beam rotation in the ELS fixture (determined via the 'inverse' ELS test).

By inverting equation 8-1 the effective crack length a_c can be calculated from the measured beam and half beam stiffness, the load P and beam deflection δ, making the problematic visual determination of the crack tip position unnecessary. With the effective crack length the delamination toughness G_{IIc} is calculated as follows:

$$G_{IIc} = \left(\frac{3P^2 {a_c}^2}{B^2 h^3 E_a} + \frac{3P^2 {a_c}^2}{4B^2 h^3 E_b} \right) \cdot F \qquad \textbf{8-2}$$

where F corrects for large beam displacement effects.

Besides the layup, the flexural stiffness of the beam is also affected by the presence of the tufts as the free loops and tufting seams on the laminate surface compress the plies and reduce the effective area moment of inertia. For equation 8-2, an effective beam stiffness E^* was derived from standard beam theory which results in an equivalent deflection as the combination of partially untufted and tufted beams. For the beam halves the crack length dependent effective stiffness ${E_a}^*$ is determined as follows (for $a > x_t$):

$${E_a}^*(a) = \frac{E_{f,r} \cdot E_{f,t} \cdot a^3}{E_{f,t} \cdot {x_t}^3 + E_{f,r} \cdot (a^3 - {x_t}^3)} \qquad \textbf{8-3}$$

where $E_{f,r}$ and $E_{f,t}$ are the flexural stiffnesses of the untufted and the tufted beam halves respectively, and x_t is the distance between the load line and the start of the tufted area.

Table 8.1 – Flexural moduli of control and 0.5% tufted ELS samples and delaminated half beams, determined by 3 point bending (Std.dev. in brackets)

3pt flexure		Full beam	Beam arms
ρ_t (%)	# spec.	$E_{f,b}$ (GPa)	$E_{f,a}$ (GPa)
0%	4	69 (4)	101 (1)
0.5%	3	63 (2)	94 (2)/96 (3)*

* with UD stiffeners

The effective stiffness ${E_b}^*$ for the unbroken beam was derived in an equivalent way. The required flexural moduli E_r and E_t for control and for the tufted sections were determined for both the unbroken samples and for separated beam arms in an independent 3point bending test, as summarised in Table 8.1.

8.4 Results

8.4.1 DCB mode I

Figure 8.3 a) and b) shows the resistance curves for the tested DCB samples without and with 0.5% tufts, determined by standard CBT. After an initial increase within the first 10 mm to 15 mm the R-curves of the control samples remain flat as the delamination propagates along the laminate mid-plane, at an average propagation toughness value of 460 J/m^2. All average values quoted in this section are determined from measurements on at least three separated samples, using both arrest and re-initiation values within the zone of crack propagation if stick-slip behaviour prevailed (for further discussion see below).

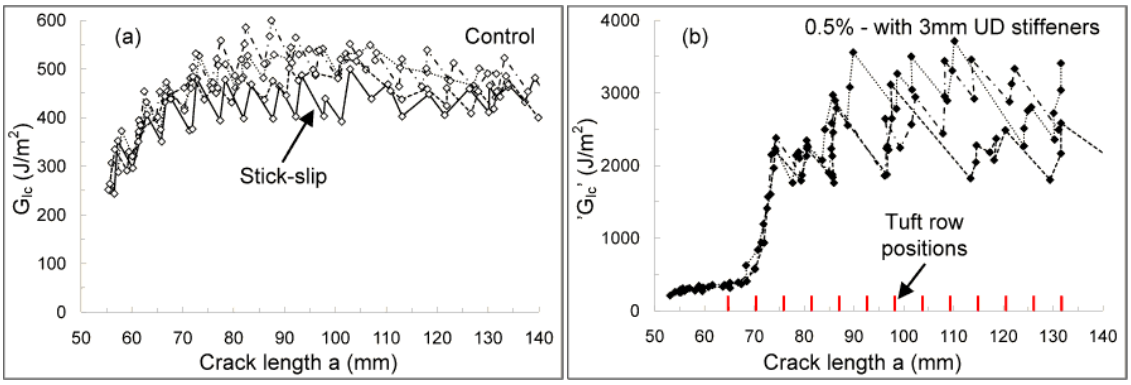

Figure 8.3 – R-curves for mode I testing of a) control and b) 0.5% tufted DCB specimens

The initial increase can be attributed to local bridging by the non-structural stitches. Even without intended connection between the mid-plane layers the 5 mm spaced polyester stitching seams on the crack interface appear to remain attached to both sides of the separating beam arms, as shown in Figure 8.4 a), applying some small but measurable closure traction. The audible failure of the bridging stitch rows was always followed by unstable crack propagation to the next non-structural stitching row, resulting in the 'stick-slip' fracture of the untufted samples.

In the tufted DCB samples, delamination propagated initially through an untufted region of 16 mm length, at a constant averaged delamination resistance of around 300 J/m^2. The reduction in averaged propagation toughness compared to the untufted (and untabbed) samples is likely to be a consequence of the presence of the stiffening tabs. The attached UD tabs increase the flexural stiffness of the laminate and reduce the relative opening displacement for a given crack length, resulting in a lower bridging trac-

tion by the non-structural stitches within the same delamination zone. Furthermore, the unified derivation of the crack length correction factor over both unreinforced und tufted zone plays an important role, as discussed in data reduction methods section.

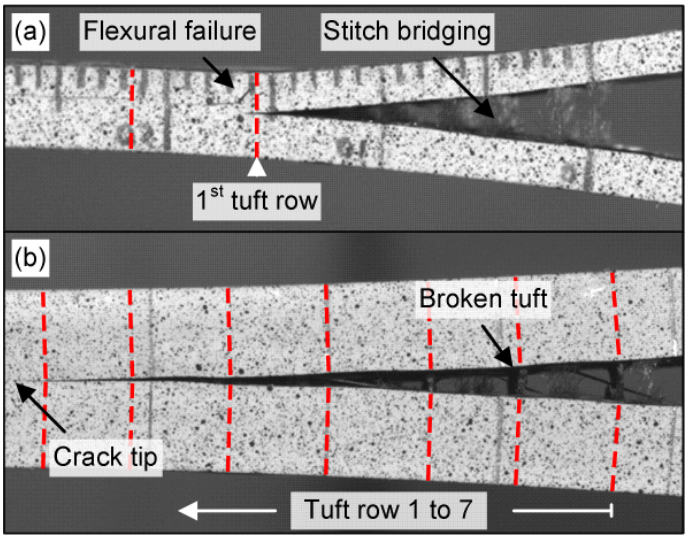

Figure 8.4 – (a) DIC image of untabbed DCB specimen, failed in flexure at first tuft row; (b) large scale tuft bridging in DCB sample with 0.5% tufting, reinforced by UD stiffeners

As the crack reaches the first tuft row, the load increases significantly, by up to 130%. In contrast to a previous study on Z-pinned composites [193], the increase appeared only after the crack propagated 4-5 mm beyond the first tuft row, as illustrated in Figure 8.3 b). This is expected as the increasing bridging traction of the stretched tufts acts only in an already developed crack.

On continuing loading the crack continues to propagate through the tufted area, causing progressive tuft rows to stretch and rupture. With failure of the first tuft row a tuft bridging zone is developed and the apparent delamination toughness reaches a plateau, with average value of 2490 J/m^2. The stick-slip behaviour is present for all tufted DCB samples as energy released by failing tuft rows causes unstable propagation of the crack. As can be seen in Figure 8.3 b), the crack typically jumps through one to two tuft rows before being arrested by the bridging traction of newly opening tuft rows.

A full summary of the analysis parameters and results for each tested DCB specimen according to the standard CBT is given in Table 8.2.

Table 8.2 – Analysis results for mode I DCB specimens by corrected beam theory

Mode I - CBT standard			Untufted*			Tufted		
ρ_t (%)	Sample	Δ (mm)	$E_{f,r}$ (GPa)	'$G_{I\,ini}$' (J/m^2)	'$G_{I\,prop}$' (J/m^2)	$E_{f,t}$ (GPa)	'$G_{I\,prop}$' (J/m^2)	# pts
0%	S1	-2.2	102	352	431	-	-	34
	S2	-1.2	97	306	474	-	-	43
	S3	-3.2	107	324	497	-	-	41
	S4	-3.0	103	263	433	-	-	41
0.5%	S2	-12.0	100	247	336	105	2709	38
	S3	-11.8	99	249	308	104	2582	36
	S4	-9.5	95	274	325	103	2171	35

* first 16 mm in 0.5% tufted DCB samples

8.4.2 ELS mode II

Figure 8.5 shows the R-curves for the control and 0.5% tufted samples, determined by CBTE. In control samples quasi-stable crack propagation was observed only within the first 5-20 mm of crack growth, despite the fact that the initial delamination to total beam length exceeded the required ratio of 0.55 as requirement for stable crack propagation [190]. The crack then jumped to within 5 mm of the clamping fixture when testing was stopped. Even in quasi-stable propagation, stick-slip was observed with unstable crack jumps of 2-5 mm in length between neighbouring non-structural stitching rows. From the limited number of data points an average mode II delamination resistance of 1751 J/m^2 was calculated (CBTE). The arrest values close to the clamps were excluded from the calculation of the average mode II resistance values. The crack initiation toughness was 1369 J/m^2, the R-curve rising to averaged maximum of 2084 J/m^2 before failure. It is assumed that the bridging traction of non-structural stitching caused this rise in crack propagation resistance.

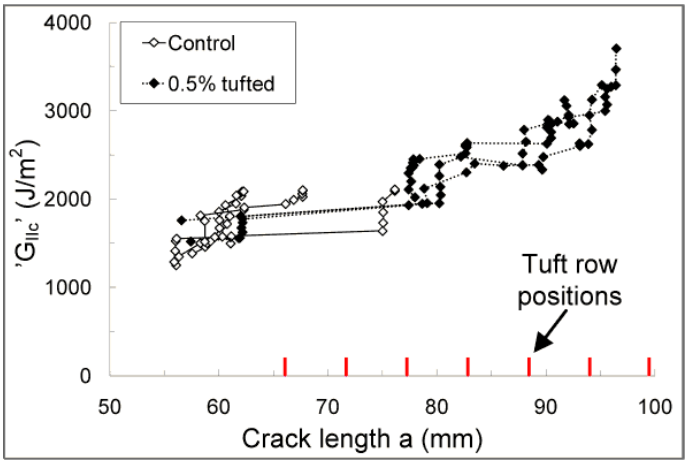

Figure 8.5 – R-curves for mode II tested ELS specimens with and without tufts

Unstable crack propagation was also observed within the untufted region of the 0.5% tufted ELS specimens. However, the crack arrested within the tufted region and propagated subsequently in a stable manner with increasing load and beam flexure. Thus the tufts affect the stability of crack propagation, as already reported for Z-pinned composites in mode II loading [5; 30]. In general, three tuft rows or a bridged crack length of 12 mm was necessary to arrest the unstable propagation. The test was stopped when the crack propagated to a length of 95 mm, i.e. within 5 mm of clamping. The crack initiation toughness was calculated as 1415 J/m^2. In the tufted region, the delamination

toughness increased continuously reaching a maximum apparent delamination toughness of 3396 J/m^2.

8.5 Discussion

8.5.1 Crack propagation and tuft bridging

8.5.1.1 Mode I loading

Given that visual inspection of the sides of the opening crack already provides accurate determination of the crack tip position in mode I loading, the use of digital image correlation for the identification of the crack tip brings limited further improvement. The measured crack length difference between the two acquisition methods was typically less than 1 mm, which is within the natural variability between the opposing specimen edges.

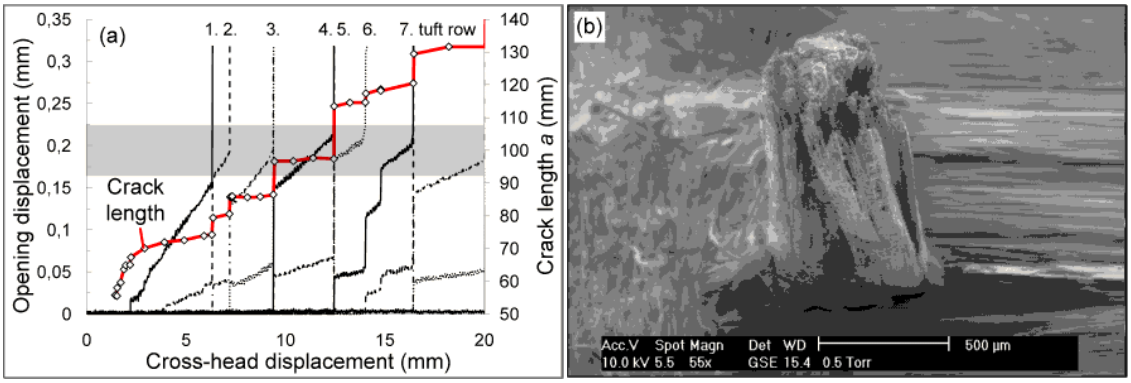

Figure 8.6 – (a) Relative opening at individual tuft rows and crack lengths versus cross-head displacement of tufted mode I DCB specimens; (b) SEM micrograph of failed tuft after pull-out in mode DCB specimen

Main benefit of the use of DIC in mode I delamination test on tufted specimens was the identification of the bridging behaviour of the tufts by measuring the relative opening displacement of each individual tufting row. Figure 8.6 a) shows the relationship between the opening displacement, measured with the DIC system at each individual tuft row, and crack length versus cross-head displacement. As soon as the delamination crack passes a tuft row the tufts stretch and apply a closure traction which retards further propagation of the crack. With increasing opening debonding cracks were found to expand around the tuft, separating the tuft from the surrounding resin rich region. The debonding cracks always started at the delamination plane and extended towards the laminate surface. When debonding reached the laminate surface tuft thread seams and loops on the laminate surface prevent actual pull-out of the debonded tufts.

At a crack opening of 0.20 (±0.02) mm on each tuft location the delamination propagation turned unstable. In micrographs this critical value was identified as rupture of the tufting threads, occurring primarily on (60%) or within 1 mm (30%) of the delamination plane. Figure 8.6 b) shows a tuft which ruptured away from the delamination plane and subsequently pulled out from the opposite beam arm.

This rupture location, which differs from that observed in conventional chain or modified lock stitched composites [112], is to be expected as tufts do not suffer from the weakening thread interlocking point at the laminate surface. Interfacial friction along the debonding surfaces reduces the axial stress in the tuft with increasing distance to the laminate mid-plane and favours rupture at the delamination plane, as described in several bridging models [113; 194; 195].

The maximum opening at tuft failure significantly exceeds the theoretical elastic limit of 0.07 mm which can be derived from the laminate thickness and measured thread properties. The difference can only be explained by in-elastic deformation of the interlocking surface threads and surrounding laminate, at the cross-over of through-thickness to surface tuft segment. Visual observations during initial trials on tufted specimens without UD stiffeners confirmed this assumption, as significant local indentation was found at the specimen surface, in direct vicinity of the bridging tufts, prior to the final flexural failure of the specimens. Hence, ploughing of the surface threads into the surface layers appears to be the main energy absorbing contribution to the tuft bridging response in mode I loading.

While failure at the laminate surface and subsequent frictional pull-out in conventional stitched composites could be seen as preferential due to increased energy dissipation, the avoidance of thread locking and absence of stress concentration suggests improved strength and bridging traction of the tuft [186]. With failure of the first tuft row the large-scale tuft bridging zone is fully developed, always containing two intact tuft rows for the given laminate layup with UD stiffeners.

In contrast to control specimens, partial bridging by single fabric tows was observed in the tufted DCB samples, as shown in Figure 8.7 a). Initiators for the local tow bridging appear to be increased fabric waviness, out-of-plane crimp and fabric damage, all introduced by the insertion of the tufts.

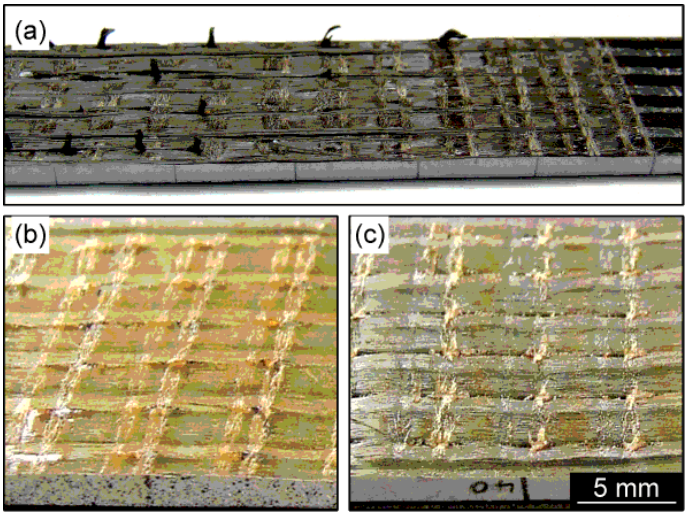

Figure 8.7 – (a) Mode I fracture surface of 0.5% tufted DCB specimen; (b) and (c) opposing fracture surfaces of mode II ELS control specimen with non-structural stitching yarns

8.5.1.2 Mode II loading

The delamination crack propagated in mode II loading with the typical formation of resin hackles in the central plane. The necessary rupture between non-structural stitching seams at the crack plane and the out-of-plane stitching threads, as shown in Figure 8.7 b) and c), is believed to be the initiator for unstable crack propagation in the untufted ELS specimens. Furthermore, the presence of the non-structural stitching seams appears to be a source of significant crack opening displacement in the untufted ELS specimens, as shown in Figure 8.8 a).

The imprint of the stitching seams causes local fabric waviness which leads to some opening up of the ELS specimen as the separated beam halves shear against each other. By monitoring the relative opening and shear displacements along the untufted ELS samples it was found that the opening displacement reaches similar magnitude as the relative shear displacement, away from the crack tip (see Figure 8.8 b). However, the opening displacement drops to below the DIC measurement threshold some 1 mm ahead of the crack tip, while the shear displacement was still measured at 8 μm. Hence, it can be assumed that mode II condition prevailed at the actual crack tip.

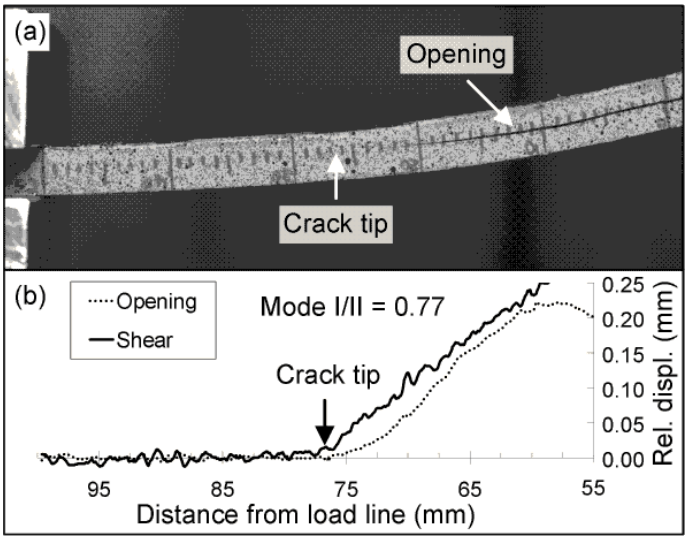

Figure 8.8 – (a) DIC image of control ELS specimen for crack length of 76.4 mm; (b) relative opening and shear displacements of crack interface along the ELS sample

The definition of 'true' crack length in mode II delamination has been subject of discussion in several publications [188; 196] as the creation of an extended micro-damage zone without actual formation of a continuous crack impedes the clear definition of the crack tip. In the current study, the use of DIC with relative shear displacement as criterion to identify the crack tip seems to offer significant improvement in the identification of the actual mode II crack tip, compared to visual inspection. Optical micrographs of the physical crack tip along the failed specimens (Figure 8.9 a)) confirmed the DIC measurements to be within 1 mm of the maximum extent of the micro-damage zone, characterised by local cusps in the resin rich interface. While the typical S-shaped resin micro-cracks were very small away from the tufts, the resin rich regions around tufts and non-structural stitching yarns enabled the micro-cracks to expand, creating a micro-damage zone of up to 0.5 mm in length.

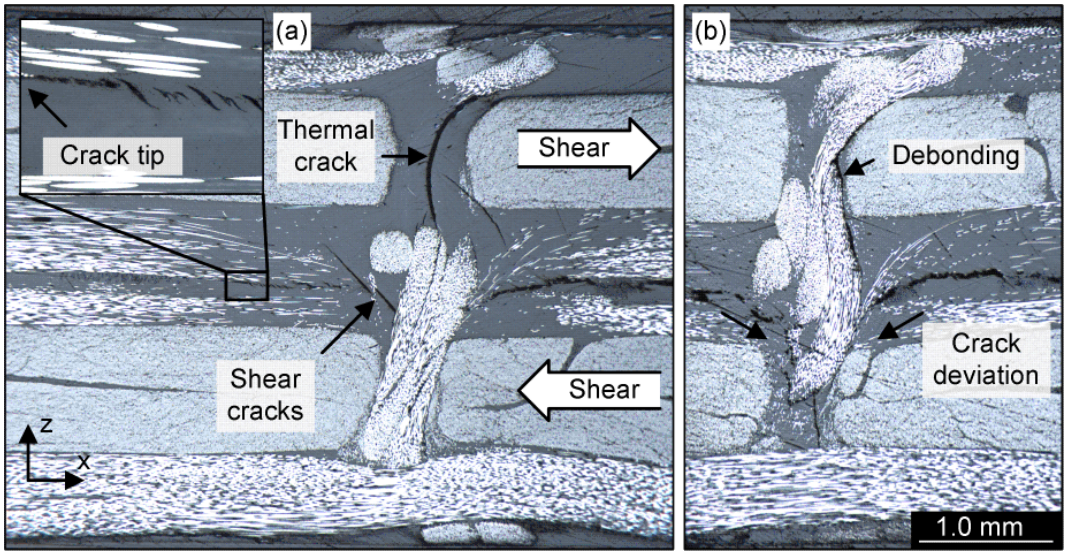

Figure 8.9 – Micrographs of shear damage around tufts in delaminated mode II ELS specimen: (a) 1.5 mm and (b) 18 mm away from crack tip

The visually determined crack length always underestimated the actual crack length, differing by up to 6 mm from the DIC measurement. It has to be noted that DIC records only the displacement field and subsequently the crack length at the specimen edge, while the crack extension is known to be potentially longer within the laminate [92].

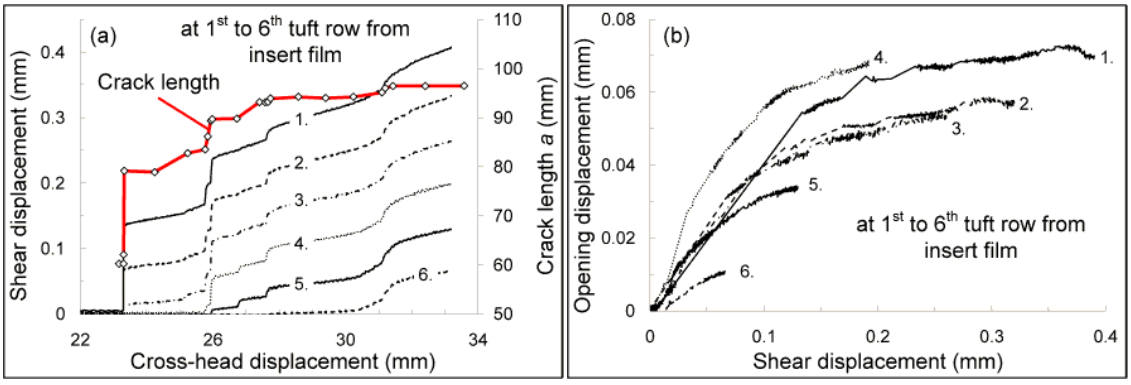

Figure 8.10 – (a) Relative shear displacement at individual tuft rows and crack lengths versus cross-head displacement of tufted mode II ELS specimen; (b) relative opening versus shear displacement of individual tufting rows

The meso-structural bridging and the ways in which the tufts fail in mode II loading differ substantially from those observed in mode I loading. Relative shear displacement at the tuft rows in the ELS test can exceed 0.4 mm, without tuft rupture (Figure 8.10 a)). This corresponds to 75% of the average maximum tuft diameter, defined by the width of the surrounding resin rich pocket. In order to sustain such displacement without thread failure by shear the tuft must be able to deform significantly at the crack plane. In the

chosen NCF laminate layup the tufts sit within a fibre free pocket, which is created by fabric spreading around the inserted tufting thread and being filled with resin during injection. As the resin pockets align with the relatively thick 0° ply in the crack plane, coinciding with the load direction, the tufts are able to bend and rotate locally in the crack plane by ploughing into the relatively soft resin. This phenomenon has previously been referred to as 'snubbing' [197]. Micrographs of tufts at different distances from the crack tip showed that the delamination crack deviates from the mid-plane along the tuft, as is passes the tuft rows (see Figure 8.9 a) and b)). Furthermore, small cracks develop on the tensile side of the shearing tuft within the resin pocket which allow the tuft to further rotate in the crack plane. With increasing distance from the delamination tip the transverse debonding zone expands around the tuft towards the laminate surface, separating it from the surrounding laminate as the rotating tuft carries on stretching. Out-of-plane forces, which are exerted by the surrounding resin to oppose the ploughing of the bent tuft, appear to contribute to the significant opening at the tufts. As shown in Figure 8.10 b), at relatively small shear deformation of only 0.1 - 0.15 mm between the beam halves each tuft row shows an opening displacement of up to 0.07 mm. At increasing shear displacement, the relative opening displacement reaches a plateau as axial tension within the increasingly stretched tufts counteracts the opening mechanisms. In contrast to the untufted specimens, the growing closure traction by the bridging tufts restricts the overall opening of the beam (Figure 8.11 a) and b)).

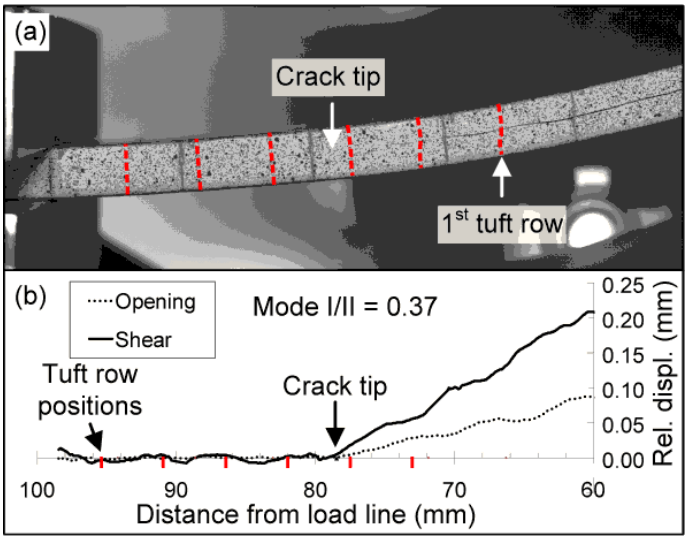

Figure 8.11 – (a) DIC image of 0.5% tufted ELS specimen for crack length of 76.4 mm; (b) relative opening and shear displacements of crack interface along the ELS sample

Although the ELS test setup ensures pure mode II loading at the crack tip of the NCF laminate, the tufts are subject to mixed mode loading, reaching a mode I to II ratio of up to 0.6 depending on the constraints and geometry of the surrounding laminate.

In contrast to mode I delamination, the maximum shear displacement of 0.4 mm was not sufficient to fail any tuft when the crack reached the clamped region of the specimen. Hence, at the test finish the tuft bridging zone was still developing, already containing six bridging tuft rows. This means that the current ELS setup, albeit being the best testing set-up available, still has only a limited capability to determine the full tuft bridging potential and mode II delamination resistance in the type of sample used in this study.

8.5.2 Data reduction methods

In the locally tufted specimens the presence of tufts significantly alters the compliance and resistance curve under both modes of loading, characterised by three identifiable zones which are influenced by different bridging mechanisms of the non-structural stitching and structural tufting (see section 8.4).

It is not possible to use a unified treatment of these 'unreinforced', 'developing' and 'developed' tuft bridging zones by use of the standard CBT and determination of a single compliance correction value Δ for all data points (except crack initiation), as the compliance curve changes slope for each zone (see Figure 8.2). By using the modified CBT of Robinson and Das [192] for analysis of the fully developed tuft bridging zone, average correction factors Δ_t of -7.6 (±2.8) mm were calculated, compared to the unified values of -11.1 (±1.4) mm according to the standard CTB. This has for effect a slight increase in the averaged propagation toughness for the tufted zone, to 2567 (±261) J/m^2, with reduced scatter. The inversely calculated apparent flexural stiffness of the beam halves reduces from 104 (±1) GPa (all data points) to 94.5 (±5) GPa for data points in the tuft bridged zone only. This agrees better with the measured flexural stiffness of 96 (±3) GPa of the delaminated tufted beam halves with UD stiffener, making the modified CBT the preferred analysis method. Table 8.3 summarises the analysis results for the individual tufted specimens using the modified CBT.

Table 8.3 – Results for 0.5% tufted mode I DCB specimens analysed according to [192]

Mode I - modified CBT									
	Untufted first 16 mm					Developed tuft bridging			
Spec.	$E_{f,r}$	Δ_r	'$G_{I\,ini}$'	'$G_{I\,prop}$'	# pts	$E_{f,t}$	Δ_{dev}	'$G_{I\,prop}$'	# pts
(-)	(GPa)	(mm)	(J/m^2)	(J/m^2)	(-)	(GPa)	(mm)	(J/m^2)	(-)
S2	265	-39.8	174	243	5	101	-10.4	2748	29
S3	161	-24.5	210	262	8	93	-7.6	2684	24
S4	172	-25.0	222	268	7	90	-4.8	2268	24

In contrast, the separate analysis of the initial untufted zone of the 0.5% tufted DCB specimens shows significant increase in the scatter and absolute values for compliance correlation (-30 (±9) mm), apparent flexural stiffness (199 (±57) GPa) and delamination propagation toughness (258 (±13) J/m^2). Two possible reasons exist for such deviation. Small errors in the measurement of the short crack propagation length with only 5 to 8 data points can cause significant variability in the toughness. Furthermore, the development of a large scale bridging zone of non-structural stitching with distinct stick-slip behaviour contributes to the error. The uncertainty in the initial untufted zone implies that the evaluation of the true enhancement of the apparent delamination toughness due to tuft bridging cannot be derived from delamination toughness of the initial unreinforced zone ahead the block of tufts in DCB samples. Data derived from control samples are necessary for evaluation of mode I delamination toughness enhancement due to tufting.

The use of the continuous automated DIC displacement monitoring enables the accurate capture of load, beam displacement and crack length not only at crack arrest after unstable crack propagation, but also before crack re-initiation for both mode I and mode II delamination. The omission of arrest values and averaging of propagation toughness values according to the mode I test standard is justified for unidirectional composites without Z-reinforcements as stick-slip can be expected to be small. In contrast, stick-slip due to non-structural and structural Z-reinforcements in this study causes significant variability in the delamination propagation toughness of control and tufted samples. While the majority of previous studies either relied on simple averaging of the stabilised R-curve values or use of only arrest values [198] a differentiation between re-initiation and arrest values as upper and lower bound is suggested for the characterisation of stick-slip in the tufted composites. The lower boundary gives a very conservative value to describe the large scale bridging behaviour of the Z-reinforced composite, the upper

boundary relates to the actual energy which is required to physically fail each individual bridging tuft row.

Table 8.4 – Mode I boundary analysis of R-curves with stick-slip behaviour

Mode I – modified CBT		Arrest	Re-initiation
ρ_t	Spec.	'$G_{I\,prop}$'	'$G_{I\,prop}$'
(%)	(-)	(J/m^2)	(J/m^2)
0%	S1	393	465
	S2	443	482
	S3	463	517
	S4	412	466
0.5%*	S1	2426	3176
	S2	2352	3077
	S4	1866	2615

* Results for fully developed tuft bridging zone

Table 8.4 summarises the averaged upper and lower boundary toughness values for mode I delamination propagation, determined for the fully developed bridging zones of non-structural stitching and structural tufting in the control and 0.5% tufted specimens respectively. The R-curves were determined using the modified CBT procedure. For tufting stick-slip behaviour can contribute to a span of boundaries of up to 29% relative to the average delamination toughness, determined for arrest, re-initiation and propagation values.

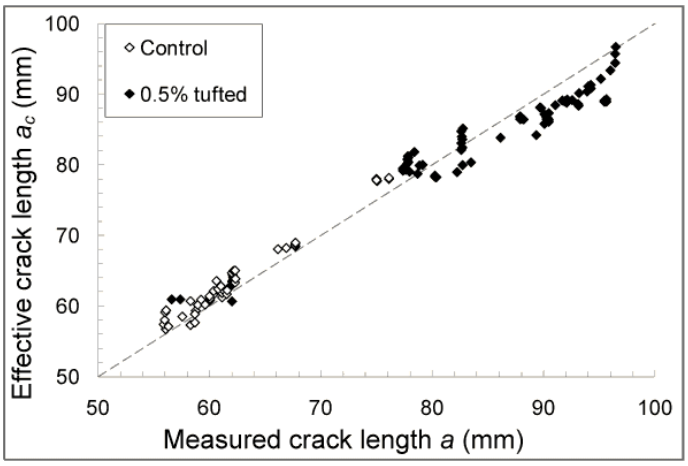

Figure 8.12 – Measured mode II crack lengths a versus effective crack lengths a_c

Under mode II loading the evaluation of the delamination resistance is further complicated by the practical inability to reach the 'steady state' situation of fully developed

tuft bridging. Table 8.5 summarises the measured parameters for the determination of apparent delamination toughness using the experimental compliance method (ECM) and corrected beam theory with effective crack length (CBTE).

Table 8.5 – Analysis results for mode II ELS specimens

Mode II			ECM			CBTE*		
ρ_t	Spec.	a_0	m	'$G_{II\,ini}$'	max. '$G_{II\,prop}$'	'$G_{II\,ini}$'	max. '$G_{II\,prop}$'	# pts
(%)	(-)	(mm)	($1/Nm^2 \cdot 10^{-8}$)	(J/m^2)	(J/m^2)	(J/m^2)	(J/m^2)	(-)
0%	S1	59.6	8.9	1652	2218	1498	2111	9
	S2	54.8	7.4	1201	1895	1382	2085	13
	S3	56.1	3.8	591	970	1248	2041	11
	S4	56.0	8.0	1302	2034	1348	2099	13
0.5%	S1	56.5	5.4	1086	2454	1387	3271	23
	S2	57.4	5.7	1069	2436	1486	3116	35
	S4	60.2	5.8	1390	2865	1371	3796	21

* Δ_c = 9.0mm, Δ_t = 9.8 mm;

Although the crack length measurement could be improved by DIC, the low number of data points and short stable propagation zone in the untufted control samples significantly increases the variability in compliance calibration and both initiation and propagation toughness based on the ECM. By using the CBTE, with implementation of the experimentally determined flexural stiffness values for each delamination zone, variability in the initiation and propagation toughness values is reduced for both control and 0.5% tufted specimens. However, the true enhancement of delamination propagation toughness in mode II with tuft bridging still cannot be determined as no stable propagation zone was developed. As shown in Figure 8.12 the combination of DIC crack identification together with derivation of the effective flexural stiffness provides good agreement between the measured and theoretical effective crack length a_c in both control and tufted specimens with an average maximum deviation of 2.9 (±0.4) mm and 5.4 (±1.2) mm respectively. In both control and tufted samples the theoretical crack length is slightly underestimated in the zone without tufting, and overestimated in the developing tuft bridging zone.

8.6 Conclusions

The presence of a block of just 0.5% areal tuft density in NCF has the potential to enhance its mode I delamination propagation resistance in the tufted zone sixfold over the equivalent unreinforced region. Such reinforcement is already sufficient to shift the failure in a 'standard' DCB specimen from delamination to flexural failure of one of the beam arms. Thick and/or stiffened specimens need to be used and the data analysis altered accordingly. Under Mode II loading, even for a partially developed bridging zone an enhancement of 63% was achieved, comparing the R-curve stick-slip maxima for control and tufted samples. Tufts are able to arrest unstable crack propagation, although a significant bridging zone of three tuft rows at 5.6 mm spacing was required in mode II loading. Rotation of tufts in the crack wake under shear displacement causes local crack opening, which has a potential effect on the mode mixity at the crack tip.

Measurement of the relative opening and shear displacement components along the progressing delamination, using digital image correlation, allows an operator-independent accurate localisation of the crack tip within a tolerance of 1 mm.

Finally, the presence and rupture of non-structural stitching in the delamination plane of NCF-based samples can initiate local and global unstable crack propagation in both mode I and mode II. Furthermore, it enhances the development of opening displacement in mode II testing, affecting the applicability and validity of the ELS tests on untufted bidirectional NCF laminates. Similar effects must be expected in other fabric based or stabilised pseudo-UD specimens with localised reinforcement.

Chapter 9 Crack bridging laws of single tufts and Z-pins

9.1 Introduction

Tufts and Z-pin are both examples of discrete Z-direction elements that are incorporated into polymer matrix/continuous fibre composites with the aim to increase the delamination crack resistance of such materials. There is an obvious need for parametric studies, to determine the effect of reinforcement diameter, spacing and geometric arrangement on the resulting delamination resistance. Experience indicates that it is not feasible to carry out all such parametric studies experimentally, especially given the fact that the Z-pin or tuft response is highly dependent on the architecture of the prepreg/preform that it is inserted into. The interactions between the preform architecture and the geometric factors of the reinforcement are complex, making it extremely difficult to vary just one parameter at a time.

A number of studies have focused on the prediction of the delamination toughness enhancement by using analytical or numerical models, incorporating the Z-reinforcement either as discrete elements (beam elements) or smeared properties via superposition of cohesive elements. Massabo and Cox [199-201] have demonstrated that the main contribution of the Z-reinforcement to increased delamination toughness is the formation of large scale bridging zones. A lower and upper bridging limit were defined as 'small-scale bridging', when the bridging zone is constant and small compared to the crack length, and 'ACK' limit (following the work of Aveston, Cooper and Kelly [202]) respectively, when the critical applied stress becomes independent of the crack length in the presence of large scale bridging. However, the majority of these studies, while accurately predicting the general effect of large scale bridging, rely on simplified bridging models, such as bi- and tri-linear models for the Z-pin pull-out [114; 115; 203; 203; 204] or linear and square root laws for continuous stitches [201; 205].In order to close this gap several studies have focused on the characterisation and prediction of the single Z-reinforcement bridging laws, i.e. the relation of crack displacement to applied closure force by the Z-reinforcement (Bridging law $F[\delta]$, relation between bridging force vector $\boldsymbol{F}$ and displacement vector $\boldsymbol{\delta}$ acting on the delamination plane). Dai [206] has performed a detailed study on pull-out of single Z-pins, while Iwahori and colleagues [112; 207;

208] have investigated the pull-out of single modified lock stitches. Other experimental investigation focused on the determination of matrix-stitch bond strength from thread pull-out tests [209; 210], although interlocking surface threads are not considered. The identified failure mechanisms for mode I are: - debonding and elastic stretching in mode I including surface deformation, rupture and potential frictional pull-out of failed Z-reinforcement.

The crack bridging mechanisms of the Z-reinforcements under Mode II loading have been the subject of considerably fewer studies [27; 29; 111; 117; 211]. Typical mode II pin bridging mechanisms were identified as:

- transverse ploughing into surrounding matrix under Z-reinforcement rotation, enhanced friction in ploughing zone and potential effect of initial angled insertion [29; 197; 212].

Several micro-mechanical models have been developed in order to predict the bridging response of the different types of Z-reinforcement. Simple bridging models assume only elastic stretching of the Z-reinforcement, opposed solely by interfacial friction within a rigid substrate [92; 116; 213]. For mode II the Z-reinforcement is assumed to behave as a stretching rope within a rigid substrate [116; 204; 214]. Bi-linear or tri-linear bridging models solely recreate the measured bridging curves by curve fitting on experimental bridging data.

Cox [195; 197; 212; 215] has developed a detailed analytical model to predict the pin bridging laws for orthogonal or even inclined discrete rods, including surface ploughing at increased local interfacial friction, supported by experimental study on single lap shear specimens reinforced with angled Z-pins. Tong [113; 216] extended the model to include flexural properties of the Z-reinforcement, which applies primarily for ductile Z-reinforcements such as metal pins.

The study presented here investigates the different bridging mechanisms and their effects on the bridging response of interconnected tufts and makes a comparison with the response of solid carbon rods (Z-pins). The comparison is made for several different fabric geometries and three different tufting threads (glass, 2k carbon and 1.2k carbon). Additional single tuft bridging results for aramid thread are summarised in appendix B. Single tuft/pin specimens and specially designed pull-out and shear fixtures are used.

9.2 Manufacturing

Unidirectional, biaxial non-crimped and biaxial woven carbon fabric preforms of 200 x 200 mm^2 were used in this part of the study. The UD preforms were assembled from 14 layers of uni-weave fabric (OCV Technical Fabrics®) with an areal weight of 300 g/m^2, stacked in $[0°]_{14}$ layup. Each layer was made of 12k 34-700 carbon fibre tows from Grafil, held together in plain weave pattern by hotmelt weft yarns of 10 g/m^2 areal weight. Biaxial NCF preforms were assembled of four bi-directional (0°/90°) carbon fibre layers (Sigmatex®) with an areal weight of 1010 g/m^2, stacked in symmetric $[(0/90)_s]_2$ layup. Each (0°/90°) layer contained equally arranged 24k HTS carbon fibre tows from Tenax, held together by non-structural stitching with 8 g/km polyester yarn in tricot/chain pattern. Additional biaxial preforms (Twill) were assembled of six layers of woven carbon fibre fabric with an areal weight of 650 g/m^2, stacked in $[(0/90)_3]_s$ layup. The woven fabric layers were made of equally distributed 12k 34-700 carbon fibre tows from Grafil, woven in 2x2 twill weave pattern. In the mid-plane of each preform artificial delamination was created by inserting a 20 μm thick PTFE film between the central fabric plies, covering an area of 190 mm x 190 mm.

Preforms for each layup configuration were structurally tufted through-the-thickness with commercially available E-glass (3x411 filaments, Saint Gobain Vetrotex) and 2k HTA carbon fibre sewing thread (Schappe Techniques), both featuring a comparable dry fibre cross-section $A_{th,dry}$ of 0.77 mm^2 and 0.078 mm^2. As each tuft is made of a closed thread loop the actual tuft cross-section area $A_{t,dry}$ is twice the thread area. An additional NCF panel was tufted with thinner 1.2k HTA carbon fibre sewing thread (Schappe Techniques) to investigate the influence of thread size ($A_{th,dry}$ = 0.045 mm^2). The tufts were inserted vertically at a square tuft to tuft spacing of 20 mm, penetrating the inserted release film. Tufting seams were aligned orthogonal to the fabric orientation on the preform surface. Each tuft featured a free loop end of 3 to 5 mm length which was left to protrude from the preform surface, opposite the insertion side. During mould closure, resin injection and cure, the free thread loops were bent and locked into a resin rich layer on the composite surface.

To make the samples for tuft-Z-pin comparisons, single carbon fibre Z-pins (Albany International) were inserted by hand vertically into a dry NCF preform, at 20 mm pin to pin spacing. The fully cured carbon fibre T300/BMI resin pins had a diameter of 0.51 mm and a dry fibre cross-section of 0.12 mm^2, the closest commercially available pin

size to the selected 2k carbon and glass thread tufts. Each pin featured a 45° chamfered end to facilitate pin insertion. To minimise pin rotation within the dry fabric preform during mould closure, the pins were cut 0.2 mm to 0.4 mm shorter than the intended panel thickness.

The preforms were injected with aerospace grade epoxy resin (MVR 444, Advanced Composites Group) using the vacuum assisted resin transfer moulding process. Injection was executed at 70°C and 1 bar (±0.01) pressure, followed by cure at 160°C and 4 bar (±0.01) for 90 minutes and freestanding post-cure at 180°C for 120 minutes in an oven. By using a rigid steel mould tool, each cured panel achieved thickness of 4.00 mm (± 0.01 mm), resulting in fabric fibre volume fractions of 58.8% (UD), 56.5% (NCF) and 54.6% (Twill), not including the Z-reinforcements.

9.3 Experimental testing

9.3.1 Characterisation of through-the-thickness reinforcements

Initial tensile tests were performed on impregnated thread and Z-pin rodstock specimens of 250 mm length according to BS EN ISO 10618:2004 in order to determine the mechanical properties of the selected types of through-the-thickness reinforcement (TTR). Thread rodstock was manufactured by impregnating glass and carbon threads of 600 mm length with epoxy resin, followed by cure under pretension of 0.25 cN/tex. Each rodstock end was tabbed with 8 layers of 0.125 mm thick ±45° woven glass prepreg (Hexply® 913), before tensile testing at a constant crosshead speed of 1 mm/min.

In order to identify the morphological effects of the Z-reinforced composite on the bridging response of the through-the-thickness reinforcement its meso-structure was determined by sectioning and micrographical analysis parallel and normal to the cured composite plane of at least five specimens per configuration.

9.3.2 Specimen preparation

To measure the bridging law of single Z-reinforcements, i.e. the applied force $\boldsymbol{F}=[F_1,F_3]$ versus displacement $\boldsymbol{\delta}=[v_t,u_t]$ parallel and normal to the delamination plane, cubical specimens of 20 x 20 mm^2 were cut from each panel with a slow speed diamond coated saw. Each specimen comprised two symmetric composite halves separated by

the inserted release film and only connected by a single Z-reinforcement at its centre, as illustrated in Figure 9.1 a). At least eight samples of each material and Z-reinforcement combination were prepared for the two considered test configurations of pure mode I pull-out and mixed mode shear loading. Care was taken during cutting to avoid damage to the pre-delaminated single Z-reinforcement samples.

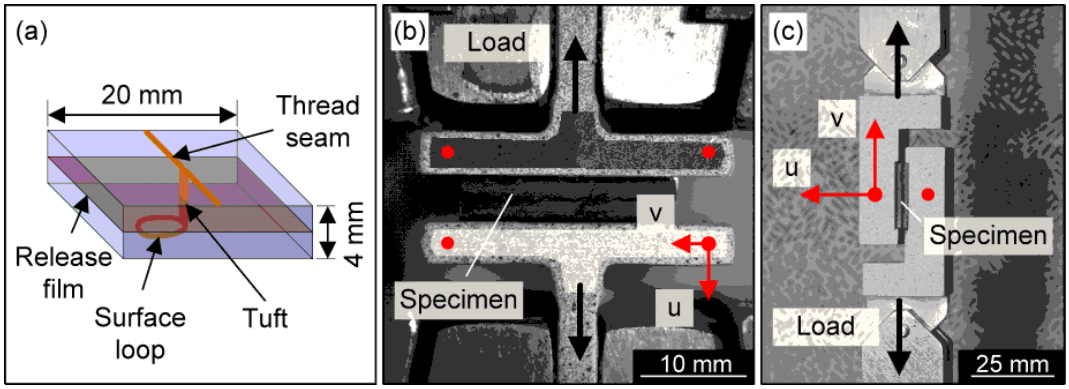

Figure 9.1 - Experimental setup for single tuft bridging: a) specimen geometry, b) single tuft specimen between steel T-tabs for tensile pull-out testing, c) shear fixture

To investigate the effect of interlocking surface threads on the tuft bridging behaviour, additional 2k carbon tufted UD and NCF specimens were modified by removing a surface layer of 0.5 mm thickness including the interlocking surface thread loops from one side of the specimens on a circular grinding machine with 1200 grit silicon carbide paper.

9.3.3 Mode I pull-out

For pure mode I bridging (Pull-out), single tuft and Z-pin specimens were bonded with top and bottom surface between two aligned T-shaped steel tabs (25 x 25 mm^2) using cyanoacrylate. The brittle nature and low viscosity of the used adhesive ensured negligible deformation of the bondlines between test specimen and test fixture as verified by compliance tests using mounted steel blocks. The tabs were held in the grips of a universal test machine Instron 5500R, with 5kN load cell, and loaded in tension normal to the delamination plane at a constant cross-head speed of 0.25 mm/min (see Figure 9.1 b).

A digital image correlation system was employed to measure the relative opening and shear displacement components u and v on the opposing fixture surfaces. Measurement positions and relative displacement orientation are indicated by round dots in Figure 9.1 b) and c). In mode I, the relative opening was derived from averaged displacements at

the eight corners of the test fixture, captured by two opposing 1.4 megapixel CCD cameras at a resolution of 46 pix/mm and rate of 5 Hz, and analysed by the 2D correlation software Vic2D.

9.3.4 Mixed mode shear testing

A special steel fixture was designed to test the single Z-reinforcement specimens in shear, as illustrated in Figure 9.1 c). Samples were bonded into the manufactured slots of each fixture arm with cyanoacrylate and loaded parallel to the delamination plane at a constant crosshead speed of 0.25 mm/min. Damage to the single tufts was avoided during test setup by bonding the samples between the test fixtures only after these were clamped and aligned in the test machine. The detailed design of the shear fixture can be found in appendix C.

In contrast to previously reported single Z-pin shear tests [27], the potential crack opening during shear testing was not restricted, in order to investigate possible opening mechanisms caused by the presence of the Z-reinforcement and other textile features within the delamination plane. The pivot-mounted fixture arms allowed opening of the delamination crack while retaining mode II loading on the bridged specimens. Consequently, mixed mode (not pure mode II) delamination bridging is tested in the shear test configuration, although only mode II contribution of the bridging load is captured by the load cell. Out-of-plane bridging force due to opening of the delamination crack cannot be measured in this test configuration.

In order to investigate the influence of layup geometry specimens were tested in shear, both parallel (0°) and transverse (90°) to the fabric fibre orientation at the delamination plane. All tests were carried out in a temperature controlled laboratory (21°C ±2) after sample conditioning for at least 24 hours in standard atmosphere. Both opening and shear displacements in mixed mode testing were derived from stereo pictures of the opposing fixture arm surfaces using the 3D DIC software Vic3D. Load-displacement curves were recorded until failure and complete pull-out of the bridging Z-reinforcements.

After shear testing, the roughness of the artificial delamination surface was measured on at least three failed and sectioned specimens to distinguish between potential contribution of the Z-reinforcement and unevenness of the delamination surface to the opening displacement in shear loading. The maximum variation in surface height within length

increments of 0.5 mm, the maximum required length to fail all Z-reinforced specimens in shear, was used as measure for roughness and determined on the failed specimen surface within 10 mm of the tuft position along the shear direction.

9.4 Results and discussion

9.4.1 Tensile properties of TTR rodstock

Table 9.1 summarises the tensile rodstock test results for elastic modulus E_t^*, ultimate strain ε_t and tensile strength σ_t^* of the four types of selected Z-reinforcement. According to the test standard, strength and modulus were determined by the ratio of load divided by dry fibre cross-sectional area, indicated by the superscript '*'. While glass thread and carbon Z-pin measured elastic moduli comparable to the pristine filaments according to the manufacturers' data, the high twist in the carbon thread caused a reduction of both strength and modulus of 10% and 16%.

Table 9.1 - Tensile properties of tufting thread and Z-pin rodstock (Std.dev. in brackets)

Reinforc.	V_f (%)	E_t^* (GPa)	σ_t^* (MPa)	ε_t (%)
Carbon 2k	63.6	199 (10)[a]	3544 (72)	1.7 (0.1)
Carbon 1.2k	72.6	200 (22)[a]	3721 (359)	1.7 (0.1)
Glass	60.3	70 (2)[a]	2382 (39)	3.5 (0.1)
Z-pin	56.5	217 (19)[b]	3099 (460)	1.3 (0.2)

[a] determined for strain interval [0.1%,0.6%]; [b] [0.1%,0.3%]

9.4.2 In-plane morphology

Figure 9.2 shows the typical resin rich pockets and in-plane fabric fibre deviation which are caused by the insertion of tufts and Z-pins into UD and biaxial fabrics. Both well documented effects for stitched and Z-pinned composites [3; 7] have been quantified by measuring the average resin pocket length L, maximum resin pocket width w and impregnated cross-sectional area A_t of the Z-reinforcements at 25% and 75% thickness of the analysed samples. The fibre-free zones align always with the main fabric fibre orientation in each ply. Table 9.2 gives a summary of the averaged dimensions.

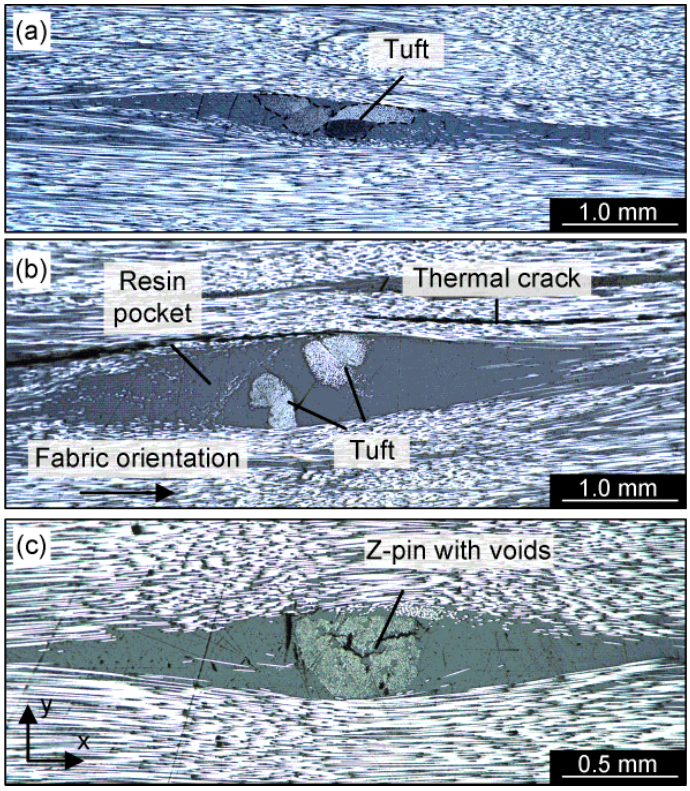

Figure 9.2 - Typical fabric disruption around single tuft in a) UD and b) NCF composite, c) Z-pin in NCF composite

As expected, the fixed diameter of the cured Z-pin rodstock defines the maximum width of the fibre free resin pocket around the pin (see Figure 9.2 c). In contrast, the cross-section of the tufting thread is affected by the geometry of the surrounding fabric layup. If inserted in UD layup the tuft expanded along the resin rich region resulting in an elliptic tuft cross-sectional shape with increased circumference, but reduced internal fibre volume fraction (Figure 9.2 a). In the biaxial non-crimped fabric and twill woven samples the resin pockets were significantly wider than necessary to accommodate the tufts allowing the two tufting threads to arrange arbitrarily within the centre of the resin rich pockets (Figure 9.2 b). For both glass and 2k carbon tufts similar resin pocket dimensions were measured. A reduction in tuft cross-section for 1.2k carbon thread resulted in only small reduction of pocket width and length. It is assumed that due to friction between crossing plies the biaxial fabric layers are not fully closing around the tufts after thread insertion with a relatively large needle cross-section (1.5 x 1.9 mm^2), explaining the wider than necessary resin pockets.

Table 9.2 - Average dimensions of resin rich pockets around tufts and Z-pins (Std.dev. in brackets)

Reinforcement		L(mm)	w (mm)	A_t (mm^2)
Carbon 2k	UD	4.8 (0.5)	0.40 (0.05)	0.32 (0.02)
	NCF	5.6 (0.8)	0.55 (0.08)	0.27 (0.03)
Carbon 1.2k	NCF	5.0 (0.7)	0.50 (0.09)	0.17 (0.03)
Glass	NCF	5.1 (0.7)	0.58 (0.05)	0.29 (0.03)
Z-pin	NCF	3.1 (0.5)	0.53 (0.02)	0.20 (0.01)

It has to be noted that for close tuft to tuft spacing (<5 mm) of the selected thread thicknesses the local compaction of deviated fabric around the resin pockets potentially affects the resin pocket and tuft geometry and subsequently the bridging behaviour of the tufts (see Chapter 5). Such effect can be considered in the current test with only single tufts by aiming for a higher fibre volume fraction of the undisturbed fabric preform in the first place.

Out-of-plane sectioning showed that the tufts remained relatively straight without significant deviation from the vertical insertion direction, although twist and random arrangement of the two tufting threads, caused by low thread tension, impede the measurement of definite orientation. The Z-pins were found to deviate at an average of 9.8° (+-3.9°) from the originally vertical insertion direction. The offset can be attributed to insertion into loose dry fabric layup, mould closure and resin injection, but lies within typical range achieved for conventional pre-impregnated laminates [7].

9.4.3 Mode I pull-out

9.4.3.1 Single tuft bridging law

Figure 9.3 shows the measured load-opening displacement curve, known as the mode I bridging law, of a single carbon tuft in biaxial NCF composite. The bridging response under mode I pull-out of the single tuft specimen is characterised by four stages. Initially, the bridging load increases rapidly under relatively small opening displacement with linear slope. At a load between 65 N to 75 N and corresponding total opening displacement of only 0.015 mm for the carbon tuft the slope of the load-displacement curve reduces significantly, characterising the second stage of the bridging behaviour.

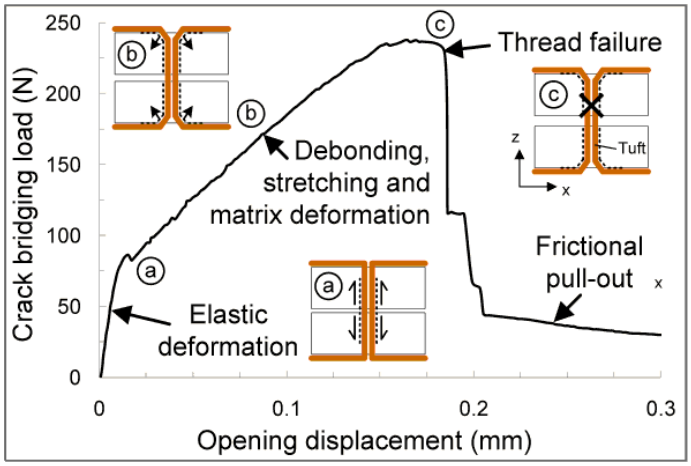

Figure 9.3 – Typical failure mechanisms of single tufts in pull-out – bridging law for single carbon tuft in NCF

When reaching a peak force F_{fail} and a corresponding critical opening displacement $u_{t,fail}$ the load drops suddenly to zero, corresponding to the tensile rupture of the tufting thread. In some cases, a small force is retained which reduces linearly to zero over a relatively large further crack opening displacement $u_{t,max}$, characterising the fourth stage of the bridging law. Table 9.3 summarises the number of tested specimens and measured bridging parameters for each configuration of tested fabric layups, thread materials and thread diameters in mode I pull-out.

Table 9.3 – Pull-out: single tuft bridging parameters (Std.dev. in brackets)

Thread	Fabric	#	F_{fail}	$u_{t,fail}$	$u_{t,max}$	U_{fail}	U_{max}
		(-)	(N)	(mm)	(mm)	(Nmm)	(Nmm)
Carbon 2k	UD	8	247 (29)	0.15 (0.02)	0.31 (0.04)	32 (5)	37 (4)
	NCF	10	232 (29)	0.20 (0.04)	0.89 (0.30)	34 (7)	50 (15)
	Twill	11	232 (45)	0.23 (0.03)	0.53 (0.29)	36 (11)	41 (19)
Carbon 1.2k	NCF	8	168 (34)	0.14 (0.04)	0.24 (0.08)	17 (3)	18 (4)
Glass	UD	8	184 (23)	0.15 (0.03)	0.35 (0.07)	20 (2)	22 (3)
	NCF	9	162 (17)	0.20 (0.02)	0.52 (0.20)	23 (2)	28 (9)
	Twill	10	165 (32)	0.22 (0.03)	0.45 (0.13)	27 (6)	29 (7)

9.4.3.2 Mode I bridging mechanisms

By sectioning specimens, which were stabilised under load by applying epoxy adhesive (Araldite® 420 A/B) into the opened crack wake and removed from the test at different stages of the mode I bridging response, the following corresponding failure mechanisms were identified for each bridging stage, as illustrated in Figure 9.3.

In the first stage, the fully bonded tuft stretches elastically within the surrounding composite. At transition from linear to non-linear stage debonding cracks were found to propagate from the delamination plane towards the outer specimen surface between the tuft and the surrounding resin matrix, allowing the tuft to straighten and stretch further. Helical features of the two tufting threads caused the debonding crack not to follow perfectly the fibrous tuft surface, but to bridge through pure resin regions and between the two tufting threads, indicating variability in thread tension between the two thread segments of the tufting loop (see Figure 9.4 a).

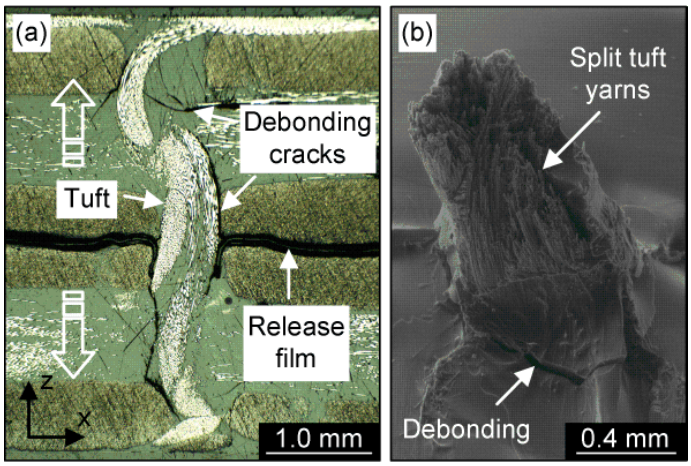

Figure 9.4 – Pull-out: a) partially debonded and stretched carbon tuft under load in NCF at u = 0.10 mm, b) SEM of ruptured and pulled-out carbon tuft

At peak force the tufting threads rupture by fibre failure, causing a significant drop in bridging load. In the majority of cases failure occurred at the delamination plane, causing the force to drop directly to zero. This failure location is expected, as interfacial shear friction along the debonded tuft reduces the axial stress within the tuft with increasing distance to the delamination plane.

Only if the tuft rupture occurs within the composite away from the delamination plane, the frictional pull-out (with linearly reducing bridging force) contributes to the energy dissipation in the last bridging stage. Figure 9.4 b) shows a ruptured carbon tuft after frictional pull-out which failed about 1 mm from the delamination plane. All ruptured tufts featured a tapered failure surface which reduces the effective length which contributes to the frictional pull-out at failure away from the delamination plane. Both the dissipated energies U_{fail} and U_{max} of single tuft bridging to maximum load and total pull-out respectively were determined by summing the area under the different stages of load-displacement curve.

While similar observations on the failure mechanisms have been made on mode I bridging of conventional stitches [91; 112], both studies and thereupon based bridging model [217] refer to elastic stitch stretching and straightening as main causes for relatively large crack opening after stitch debonding, which was typically beyond the feasible limit for solely elastic deformation of the vertical Z-reinforcement. In the tested single carbon tuft specimens of this study the total opening to failure corresponds to a theoretical axial strain of 5% within the tuft, a value three times as high as measured for the straight carbon thread rodstock at failure.

Instead, in this study small indentations were found at the cross-over between vertical tuft segment and interlocking surface loop and thread seam at increasing load within the second bridging stage. As the crack closure force is transferred from the delamination plane along the debonded tuft to the interlocking surface threads the thread seams appear to be forced into the composite under plastic deformation of the supporting matrix. Experimental observation of local surface indentation at the insertion points of bridging tufts in mode I tests of tufted NCF double cantilever beam specimens with similar layup confirms this failure mechanism (see Chapter 8).

By comparing the theoretical elastic deformation limit of 0.03 mm at tuft failure, derived from the stiffness of the straight rodstock, the specimen thickness and the given maximum bridging force, with the maximum measured opening displacement of 0.20 (±0.04) mm it becomes apparent that inelastic straightening and matrix deformation are the main contributing factors to the opening displacement in mode I bridging. This confirms previous suggestions on stitch failure in the micromechanical model for prediction of single stitch bridging by Cox [195; 212; 215].

9.4.3.3 Effect of fabric layup

Figure 9.5 shows representative measured load-opening displacement curves for single carbon tufts in UD, biaxial NCF and biaxial twill woven fabric layup. Specimens for all three fabric layup configurations show the typical introduced bridging stages with high reproducibility within each configuration.

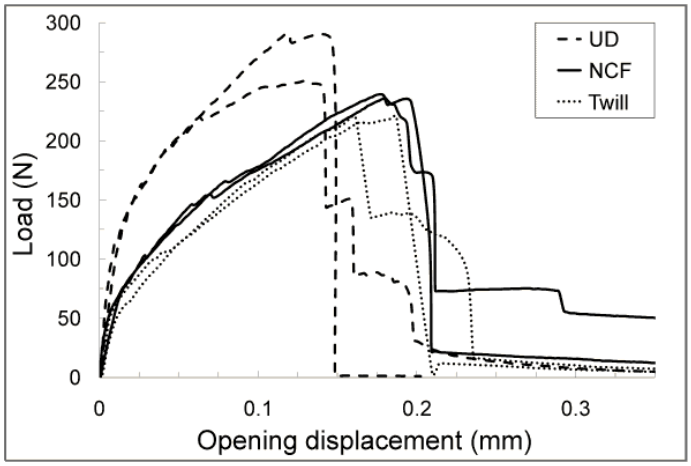

Figure 9.5 – Mode I bridging load versus opening displacement curves for single 2k carbon tufts in UD, NCF and twill woven composite

However, while the mode I bridging laws for carbon tufts in NCF and twill woven composite are almost identical, with comparable onset of non-linearity, maximum bridging load, displacement and energy dissipation to tuft failure, the bridging laws for UD are significantly enhanced with an increased debonding load of 105 to 115 N at only 70% critical opening displacement at tuft failure.

A comparison of the bridging laws for the different fabric layups with the tuft morphology within each layup configuration suggests that the increased tuft circumference, the only significant changed morphological parameter for UD, is the main contributing factor to the change in bridging behaviour. By normalising the measured forces at onset of debonding with the corresponding tuft circumference of 3.25 (±0.62) mm and 2.24 (±0.14) mm for UD and NCF respectively, comparable force residuals of 33.5 and 35.4 N/mm were derived for the two fabric composites, confirming the suggestion.

With larger circumference both the maximum force to debonding and interfacial shear traction opposing axial stretching after debonding increase, explaining the higher bridging forces at reduced opening displacement for the UD composite. Hence, the local fabric layup can have a significant effect even on the mode I bridging response of tufts, if it changes the morphology of the tuft.

The axial stress within the carbon thread tufts at failure, derived from the peak force F_{fail} divided by the dry tuft thread cross-section area A_t, reaches only 43% to 45% of the measured thread rodstock strength for NCF and UD respectively. Such uniform reduction for all layup configurations is assumed to be caused by mismatch in straightness

between the two tufting threads leading to uneven loading between the thread components. Furthermore, stress concentration between debonded tuft and surrounding fabric layup contributes potentially to the reduction.

9.4.3.4 Effect of thread material and diameter

Figure 9.6 shows measured mode I bridging laws for smaller 1.2k carbon and additional glass tufts, which have a comparable diameter as the reference 2k carbon thread. Further mode I pull-out results for glass tufted NCF, twill and UD and 1.2k carbon thread tufted NCF specimens are summarised in Table 9.3.

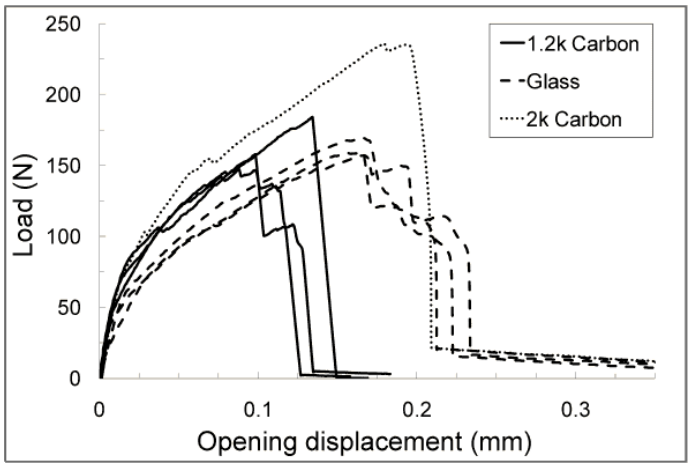

Figure 9.6 – Effect of thread material and size on single tuft bridging laws in NCF composite

The general bridging trend of specimens with single glass tuft or smaller carbon thread tuft remained unchanged, showing the typical enhancement of debonding and maximum bridging force at reduced maximum opening if inserted in UD. Only, the absolute measured values for the slope of the initial linear elastic bridging curve, maximum bridging force and consequential energy dissipation values were reduced by 44%, 30% and 32% respectively, as expected for the reduced stiffness and strength of the glass tufts (see Table 9.1).

A reduction of cross-sectional area by 40% for the 1.2k carbon tufts resulted in the expected reduction in initial slope and maximum bridging force of 29%, which translates to a ratio of tuft to rodstock strength reduction of 50%, a value comparable to ratios for thicker glass and 2k carbon tufts.

However, while the measured ultimate tensile strains for the thread rodstock tests would suggest that the two carbon tufts of different diameter exhibit a similar maximum crack

opening displacement at failure while glass tufts fail at larger maximum opening, opposite effects were found in the single tuft specimens under mode I pull-out. The glass tufts failed at crack opening displacements comparable to the 2k carbon tufts, while the maximum opening at failure of the smaller 1.2k carbon tufts reduced by 30%.

Two morphological aspects appear to cause this discrepancy. On one hand, the carbon tufts featured large curvature at the transition from vertical tuft to surface thread seams, due to the high flexural stiffness of the carbon filaments allowing larger in-elastic stretching after debonding resulting from the straightening of the tuft. On the other hand, thread ploughing into the specimen surface under plastic deformation of the surrounding matrix, the main contribution to the total opening displacement at failure, is directly dependent on the maximum transverse force and width w_{th} of the interlocking surface thread seams over which the transverse load is transferred to the surrounding composite. While glass and 2k carbon thread seams in NCF were found to have a similar width of 1.04 (±0.16) and 1.07 (±0.13) mm, a reduction in thread cross-section by 40% for the 1.2k carbon tufts resulted only in a 20% reduced surface thread width of 0.84 (±0.10) mm. If set in relation to the maximum bridging force at tuft failure both the smaller 1.2k carbon and glass tuft apply smaller absolute pressure to the surrounding composite, resulting in lower contribution of surface ploughing.

9.4.3.5 Frictional pull-out of Z-pins and tufts

Figure 9.7 shows measured bridging laws of single carbon Z-pins with 0.51 mm diameter and 2k carbon thread tufts with removed surface loop in NCF. In contrast to the single tuft specimens of section 9.4.3.1 the modified tufts and Z-pins feature no interlocking surface thread seams, enabling the Z-reinforcement to pull-out under interfacial friction along the full insertion length after debonding. A summary of the averaged bridging parameters of peak force, maximum crack opening and dissipated energy for modified tufts in UD and NCF as well as Z-pins in NCF is given in Table 9.4.

Table 9.4 – Pull-out: bridging parameters of 'loopless' tufts and Z-pins (Std.dev. in brackets)

Thread	Fabric	#	F_{max}	$u_{t,max}$	U_{max}	s_t	τ
		(-)	(N)	(mm)	(Nmm)	(mm)	(MPa)
Carbon 2k	UD	6(2)	238 (18)	1.27 (0.12)	85 (13)	3.25 (0.62)	30 (4)
	NCF	6(5)	141 (8)	1.54 (0.17)	99 (16)	2.24 (0.14)	36 (6)
Z-pin	NCF	8(7)	98 (17)	1.12 (0.19)	14 (5)	1.60 (0.05)	9.9 (3)

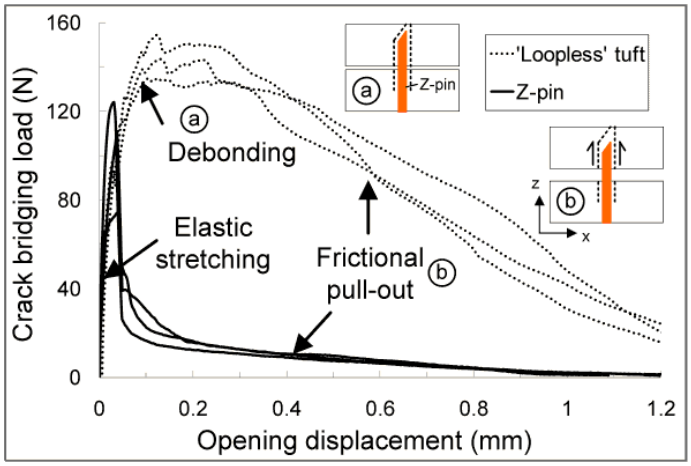

Figure 9.7 – Mode I bridging laws of single carbon thread tufts without interlocking surface loop and 0.51 mm diameter Z-pins in NCF

Similar to the conventional tufts both bonded Z-pins and 'loop-less' tufts stretch initially within the surrounding matrix up to an average bridging force of 70 to 90 N and corresponding opening displacement of 0.029 (±0.007) mm when debonding cracks were found to develop and propagate along the surface of the Z-reinforcements. The relatively high force to debonding compared to previous studies on similar Z-pins in pull-out [29; 206] indicates good bonding between the pin and chosen matrix resin. Scanning electron micrographs of the extracted pin surface in Figure 9.8 a) show typical shear damage of the resin at the fibrous surface of the Z-reinforcements.

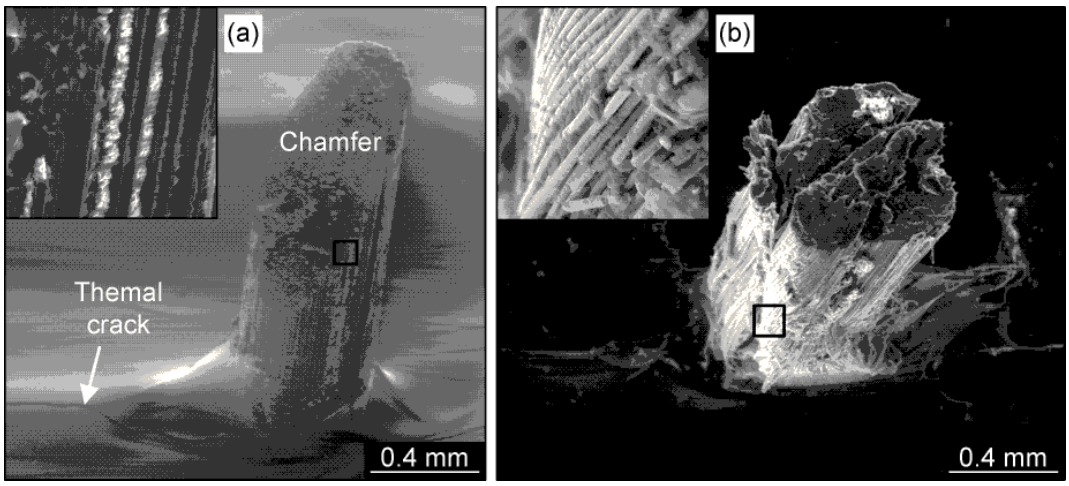

Figure 9.8 – Frictional pull-out: a) carbon Z-pin with chamfered end and b) carbon tuft with removed surface loop after frictional pull-out

After full debonding at an average peak load of 98 (±17) N, the Z-pins exhibit a rapid load drop to between 20 and 35 N at very small additional opening displacement, followed by linearly reducing load over a relatively large total opening displacement. This

characterises the typical frictional pin pull-out observed by numerous studies on Z-pinned composites [27; 29; 206]. For the tested Z-pin specimens of this study, it was always the chamfered end of the pin which was extracted from the opposing specimen half (see Figure 9.8 a). The chamfer appears to reduce the length of the effective load bearing pin surface favouring the pull-out of only one pin half. Measured differences between average maximum opening displacement of 1.12 (±0.19) mm at which the bridging load reduces to zero and the actual length of the protruding pin of 1.47 (±0.14) mm support this observation. By applying simple shear lag theory and assuming a uniform stress distribution along the Z-reinforcement the friction stress τ acting over the debonded surface can be derived from the maximum force after debonding F_d , the circumference of the Z-reinforcement s_t and the effective pull-out length, corresponding to the maximum crack opening displacement u_{max}, as follows:

$$\tau = \frac{F_d}{s_t \cdot u_{max}} \qquad \textbf{9-1}$$

For frictional Z-pin pull-out from NCF an average interfacial shear stress of 9.9 (±2.7) MPa was determined.

In contrast, the bridging force applied by the modified tufts after onset of debonding increases up to a peak value of 141 N for NCF layup before reducing linearly to zero. The corresponding averaged interfacial shear stress was calculated to 35.9 MPa, a threefold increase compared to the smooth carbon Z-pins. Modified single tufts in UD composite exhibited a similar interfacial shear stress of 30.1 MPa, although only for two of the eight specimens was frictional pull-out observed. The other specimens ruptured during pull-out as the circumference and subsequently the interfacial debonding surface was increased, leading to an increase in bridging load up to critical strength of the tuft.

In both NCF and UD composite the calculated enhancement in averaged shear stress along the modified tufts compared to the tested Z-pin specimens appears to be superposition of interfacial friction along the twisted debonding surface and additional plastic deformation of the surrounding matrix and thread splitting caused by the pull-out of the interlocking helical tuft geometry. Over the typical pull-out length of 1.5 mm the carbon threads exhibit at least one half twist, which has to uncoil or plough through the surrounding matrix under significant internal damage and separation between the thread segments (see Figure 9.8 b).

By removing the surface loop and enabling frictional pull-out in mode I loading for the 4 mm thick specimens of this study, the energy dissipated increased by 195% , due to high interfacial friction and energy dissipating ploughing mechanisms. In contrast, the relatively low interfacial friction stress on the smooth Z-pin surface reduced the energy dissipated by the Z-pins by 42% compared to the conventional tufts and even 81% compared to the modified tufts. Hence, frictional pull-out of the Z-reinforcement as only bridging mechanisms compared to the more complex surface ploughing and elastic stretching of the tuft at higher bridging load appears to be only beneficial if high interfacial friction stresses can be achieved.

Contradicting results on reduced energy dissipation of modified lock stitches with removed interlocking surface knots during mode I delamination propagation tests by Dransfield et al [91] appear to originate from the presence of frictional pull-out even for stitches with knot, as the surface knot always initiated stitch failure on the composite surface.

It has to be noted that evaluation of the effectiveness of the Z-reinforcement to enhance the delamination toughness in mode I opening depends not only on the dissipated energy and maximum bridging force but also on the ratio of maximum opening to bridging force at failure as it affects the formation of large scale bridging zones [213]. For the tested thin composites a change from smooth to helical surface geometry at comparable pull-out length appears to be always beneficial as long as the enhanced friction does not lead to changed failure mechanism by thread rupture, agreeing with suggestion by [218].

9.4.4 Mixed mode shear

9.4.4.1 Shear tuft bridging laws

Figure 9.9 shows the measured shear force versus shear displacement curves for single 2k carbon tufts in NCF under mixed mode loading with applied load parallel (0°) and transverse (90°) to the fabric orientation at the delamination plane. Averaged results of maximum bridging force parallel to delamination plane F_{fail}, shear displacement to tuft failure v_{fail} and to full separation between the delamination halves v_{max}, as well as corresponding dissipated energies V_{fail} and V_{max} for at least 8 tested specimens per configuration are summarised in Table 9.5.

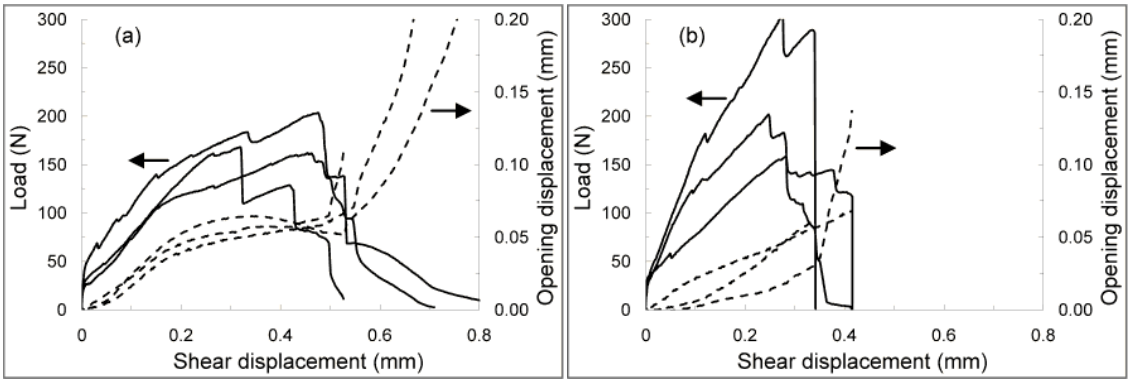

Figure 9.9 - Shear bridging of single carbon tufts in NCF under a) parallel (0°) and b) transverse (90°) loading; shear to opening displacement curves (dashed lines)

In both loading directions the bridging curves increase rapidly to a load of 22 to 30 N before becoming highly non-linear. Further increase in shear displacement causes the load to increase gradually until thread rupture. While for parallel loading (0°) to the fibre direction the tufting threads fail gradually, characterising the stepwise reduction in bridging load, the load in transverse shear drops rapidly to zero. From the differences in maximum load and shear displacement between the two loading cases it becomes apparent that the surrounding fabric geometry in relation to the loading direction has a significant effect on the tuft bridging behaviour in shear. Transverse instead of parallel loading to the fabric orientation causes about 25% increase in maximum load at equivalent reduction of shear displacement and energy dissipation for carbon tufts in NCF.

Table 9.5 - Shear: bridging parameters of single carbon and glass tufts (Std.dev. in brackets)

Thread	Fabric		#	F_{max}	$v_{t,fail}$	$v_{t,max}$	V_{fail}	V_{max}
			(-)	(N)	(mm)	(mm)	(Nmm)	(Nmm)
Carbon 2k	UD	0°	10	179 (22)	0.42 (0.08)	0.57 (0.06)	55 (16)	59 (17)
	NCF	0°	10	180 (34)	0.51 (0.12)	0.66 (0.20)	65 (13)	69 (14)
		90°	11	222 (59)	0.37 (0.05)	0.41 (0.06)	51 (12)	52 (13)
	Twill	0°/90°	10	270 (87)	0.38 (0.09)	0.49 (0.18)	71 (20)	74 (21)
Glass	UD	0°	10	136 (47)	0.37 (0.08)	0.48 (0.07)	35 (5)	36 (6)
	NCF	0°	10	168 (29)	0.35 (0.03)	0.40 (0.07)	41 (7)	42 (7)
		90°	10	177 (50)	0.30 (0.09)	0.34 (0.10)	31 (6)	32 (6)
	Twill	0°/90°	10	174 (65)	0.36 (0.09)	0.50 (0.13)	41 (14)	44 (15)

Compared to equivalent mode I pull-out bridging results of Figure 9.5 the single carbon tuft specimens in shear are able to deform almost threefold before tuft failure (see Figure 9.9). However, the maximum bridging force at failure showed to be only similar or even reduced by 25% compared to the maximum crack closure force in mode I pull-out. Such increase in necessary crack displacement to achieve similar crack bridging traction explains the reduced effectiveness of tufts and stitches to enhance the delamination toughness of composites in mode II delamination, as has been reported repeatedly for stitches and tufted composites (see Chapter 8 and [95; 219]).

As opening displacement was not restricted, Figure 9.9 also presents the measured relationship between applied shear and measured opening displacement for each of the shear bridging curves. For both loading directions in NCF the absolute opening displacement before tuft failure never exceeded 0.06 mm while the shear displacement reached between 0.35 to 0.51 mm at tuft failure, suggesting that the specimens were loaded primarily in mode II shear delamination.

Differences in the development of opening to shear displacement for parallel and transverse loading in NCF were found to be caused by the natural surface waviness of the artificially created delamination crack. The thin delamination film nestled to fabric dependent features such as non-structural stitching seams between the centre plies of the NCF or the natural waviness of fabric tows.

9.4.4.2 Tuft failure mechanisms in shear

In order to identify the bridging and failure mechanisms of the tufts which are associated to the measured bridging curves of Figure 9.9 single carbon tufts in NCF were loaded parallel and transverse to fabric direction at the delamination plane and removed from the test fixture under load at the first significant drop in bridging load. The following shear tuft bridging mechanisms were identified: - In the initial stage the tuft deforms elastically under pure shear displacement within the composite causing the very steep slope of the bridging curve. Subsequent onset of non-linearity at very small shear displacements was found to be directly related to the formation of debonding cracks on the tensile side between tuft and surrounding substrate (see Figure 9.10), as well as internal plastic shear deformation within the tuft. At increasing shear displacement, lateral pressure which is applied by the shearing Z-reinforcement on the adjacent substrate over the width of the tuft causes the substrate to deform plastically in close vicinity to the delamination plane. Subsequently the tuft is able to rotate at the delamination plane,

adopting locally an 'S'-shaped curvature (see Figure 9.10 a) and b)). The rotating tuft no longer transfers the shear bridging load across the delamination plane only by internal shear within the tufting threads, but increasingly by axial tension. Axial tuft stretching as consequence of the increasing axial load within the pin causes debonding cracks to propagate along the tuft circumference towards the interlocking surface threads on the specimen surface. Flexural stiffness of the quasi-circular tuft in NCF is assumed to contribute only little to the bridging traction as local tuft rotation was accompanied by separation and extensive internal plastic shear of the tufting threads.

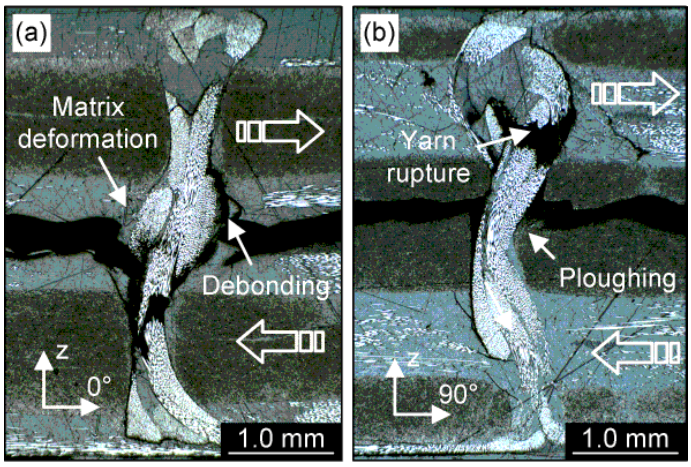

Figure 9.10 – Sections through partially stretched carbon tufts in NCF, loaded in shear a) parallel (0°) and b) transverse (90°) to fabric orientation at delamination plane

It has to be noted that the measured shear load for the single tuft specimens is only the transverse component of the axial load carried within the tuft. As frictional pull-out of the tuft is inhibited by the interlocking surface threads and loops it is expected that the tuft applies increasing closure traction to the delamination crack while rotating and stretching elastically at increasing shear displacement. Balancing of crack opening displacement at larger shear displacement with a sudden increase after tuft rupture (see Figure 9.9) confirms this assumption.

As shown in Figure 9.11, the lateral ploughing zone, characterised by local tuft rotation from the original insertion position, appears to be distributed quasi-uniformly in both specimen halves. For transverse shear displacement (90°) the ploughing zone height z_0 in each specimen half is about 30% smaller, measuring 0.55 mm, at 65% higher maximum rotation angle, measuring 33°, if compared to parallel shearing. If compared to the applied shear displacement and resulting shear bridging force, it becomes apparent that

the resistance of the supporting substrate highly affects the total shear displacement and the capability of the single tuft specimens to apply transverse shear bridging forces.

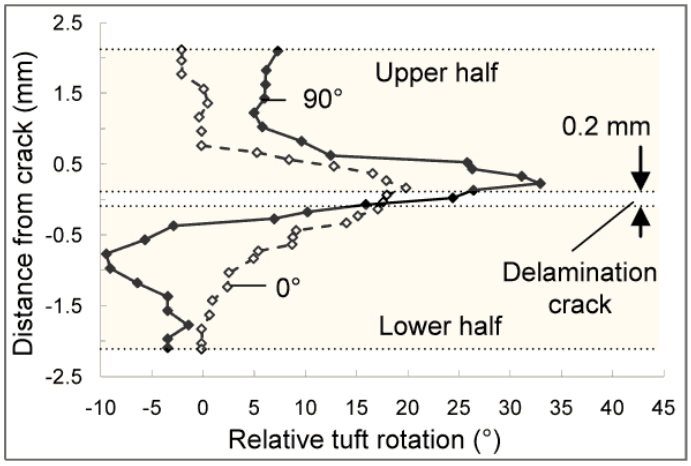

Figure 9.11 - Local rotation of sheared carbon tufts through specimen thickness in NCF, loaded parallel (0°) and transverse (90°) to fibre direction

In parallel loading the tuft ploughs into neat resin within the fibre free pocket. Under the applied lateral pressure a relatively large resin volume deforms plastically (without cracking - see Figure 9.10 a), enabling significant shear displacement at only small overall rotation of the tuft. In contrast, under transverse shear the orthogonal fabric tows distribute the applied pressure of the shearing tuft along the fabric fibre direction, creating significantly higher resistance against ploughing. This explains the reduced ploughing height and resulting higher tuft rotation angle at the delamination plane with generally smaller total shear displacement to tuft failure. Lateral pressure against the fabric tows resulted in local cracking and fibre breakage within the fabric tows (see Figure 9.12 b).

Difference in the ploughing resistance also explains the variable tuft rupture location of the tufting thread. While in parallel loading local stress concentration at the transition of 0° to 90° fabric ply 0.5mm from the delamination plane initiated thread rupture, for transverse loading the tuft failed in the majority of cases directly at the delamination plane due to high contact pressure with the transverse fabric tows.

Variability in the arrangement of the two tufting threads at the delamination plane causes the generally increased variability in the bridging curves for shear loading compared to mode I pull-out.

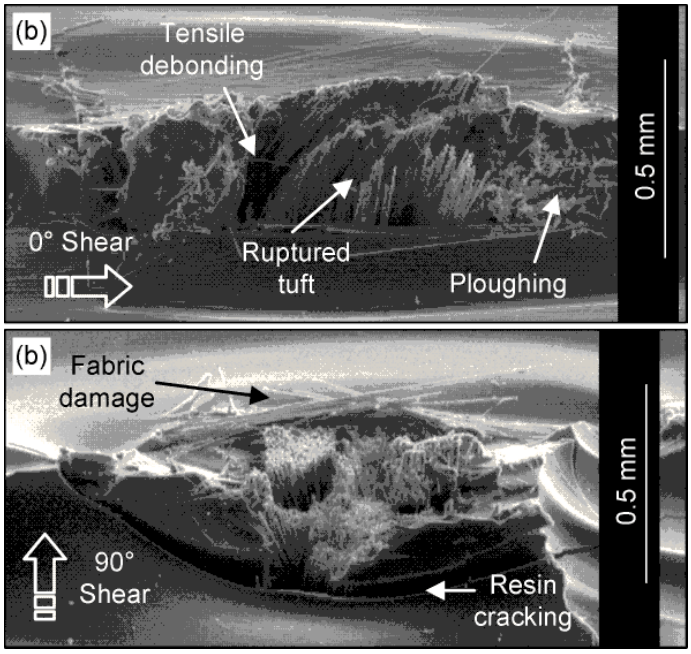

Figure 9.12 – Scanning electron micrographs of failed carbon tufts in NCF, loaded a) parallel (0°) and b) transverse (90°) to fabric orientation at delamination plane

9.4.4.3 Effect of thread material and fabric layup

Similar to mode I pull-out testing, the change from carbon to glass thread tufts in the mixed mode shear tests resulted in reduction of maximum bridging force at similar maximum shear displacement values (see Table 9.5), although the reduction was less prominent than in mode I. As both threads exhibit comparable cross-sections, the ploughing resistance of the surrounding composite remains unchanged, but the reduced strength of the glass material causes failure of the glass tufts at lower shear displacement.

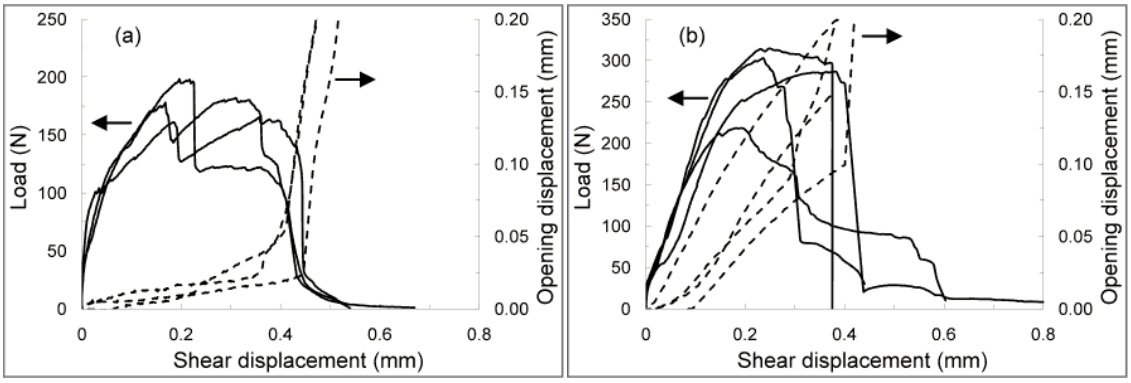

Figure 9.13 - Shear bridging of single carbon tufts in a) UD (0°) and b) twill woven composite; shear to opening displacement curves (dashed lines)

Figure 9.13 a) and b) shows the measured shear bridging curves for single carbon tufts in unidirectional and twill woven composite, with loading parallel to the 0° fibre orientation.

The increase in tuft circumference and alignment of the main axis of the elliptically shaped tuft with the shear displacement direction appear to affect the slope of the shear bridging curves in the UD composite. While reaching a similar maximum bridging force as carbon tufts in NCF, loaded parallel to the fibre direction, the average maximum shear displacement is reduced by 20%. The opening displacement was negligible for the tested UD specimens. Due to the longitudinal spreading of the tufting threads within the resin rich pocket, thread fibre failure was preceded by significant internal shear damage and axial splitting between the tufting threads.

Uncontrolled position of the tuft in relation to the weave pattern of the twill composite appears to be the source of high variability in the twill shear tests. Depending on the local orientation of the surrounding fabric tows shear deformation of the tuft is either opposed by transverse fabric tows, neat resin of the aligned resin pockets or a combina-

tion of both on opposing delamination surfaces. In general, the increased waviness on the delamination surface due to fabric weave caused significantly larger opening to shear displacement ratios. Subsequent axial stretching of the tuft results in increased contact pressure between the adjacent delamination planes, explaining the high shear bridging forces.

9.4.4.4 Shear bridging of Z-pins

Figure 9.14 shows measured shear bridging laws for single Z-pins in NCF, loaded parallel and transverse to the fabric fibre orientation at the delamination plane. In both loading directions the bridging load of the Z-pins increases rapidly to about 20 N, a similar level as for the single tuft specimens in shear, when first debonding cracks and plastic shear deformation were observed at the pins.

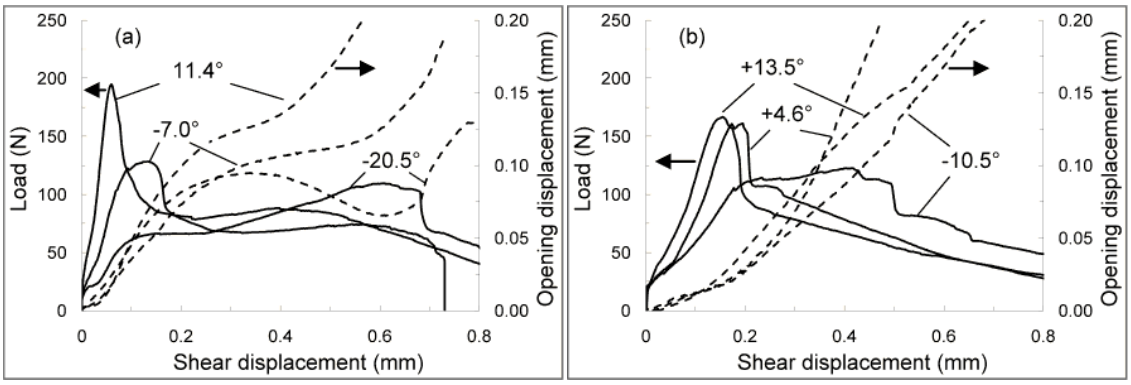

Figure 9.14 - Shear bridging of single Z-pins in NCF under a) parallel (0°) and b) transverse (90°) loading; shear to opening displacement curves (dashed lines)

The further development of the bridging curve appears to depend highly on the original pin insertion angle in relation to the loading direction. If originally angled towards the shear direction (with the nap), defined by positive rotation angles in Figure 9.14, the bridging curves rise to a peak bridging force of up to 200 N as the shear bridging load is transferred through the Z-pin at increasing axial tension. Subsequent rapid drop to between 70 and 80 N was found to coincide with full debonding of one pin half, mostly the chamfered end, from the surrounding matrix, allowing the pin to extract from the opposing specimen half under interfacial friction. During subsequent frictional pull-out the pins remained intact with only little internal splitting (see Figure 9.15 a), which appears to be caused by the initial shear deformation of the pin in order to align with the shear direction.

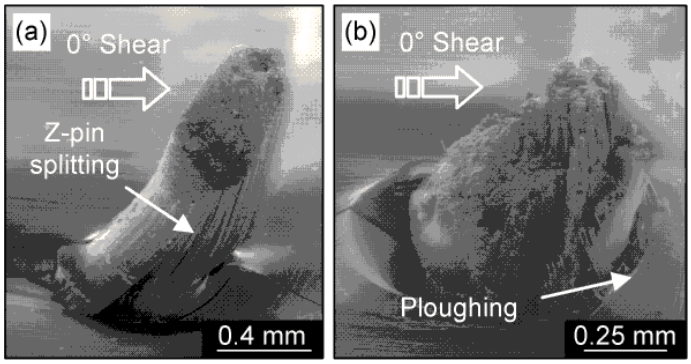

Figure 9.15 – Angled Z-pins after failure under shear displacement parallel to fabric fibre orientation (0°) at the delamination plane, loaded a) with the nap and b) against the nap

If originally orientated against the shear displacement direction (against the nap, negative angles in Figure 9.14), the initial peak in the bridging curve was not detected. Instead, the bridging force increases gradually before showing a sudden drop at relatively large displacements of 0.4 to 0.6 mm. The load drop was found to coincide with local rupture of the tuft at the delamination plane (see Figure 9.15 b). This is expected as loading against the nap causes initial axial compressive within the pin. In order to carry the shear load between the delamination planes the pin has to rotate significantly under extensive internal splitting and shear damage within the pin. Frictional pull-out at higher shear displacement and rotation of the pin was limited.

By analysing the local rotation of similarly orientated Z-pins, which were removed from the test fixture after partial shearing parallel and transverse to the fabric orientation at the delamination plane, a similar trend in lateral ploughing was found as for the conventional tufts. Ploughing into neat resin parallel to the fabric orientation results in smaller maximum fibre rotation angles at increasing volume of plastically deformed resin compared to loading in transverse direction against adjacent fabric tows.

Although the shear bridging force is smaller for the discrete Z-pins, the maximum rotation angles of sheared Z-pins were found to be significantly higher than for shearing tufts, measuring 34.6° and 40.4° at comparable shear displacements of 0.42 and 0.39 mm for parallel and transverse loading respectively, while the heights of plastically deformed surrounding substrate reduced to 0.55 and 0.36 mm (see Figure 9.16). This is expected as the shear load is no longer transferred to the interlocking surface threads through axial stress within the rotated Z-reinforcement, but only transferred to the surrounding composite by interfacial friction along the debonded pin surface. Consequential reduction in out-of-plane closure force, further reduced by increased rotation of the

pin, explains the significantly larger crack opening displacement for Z-pins compared to carbon tufts in shear (see Figure 9.14).

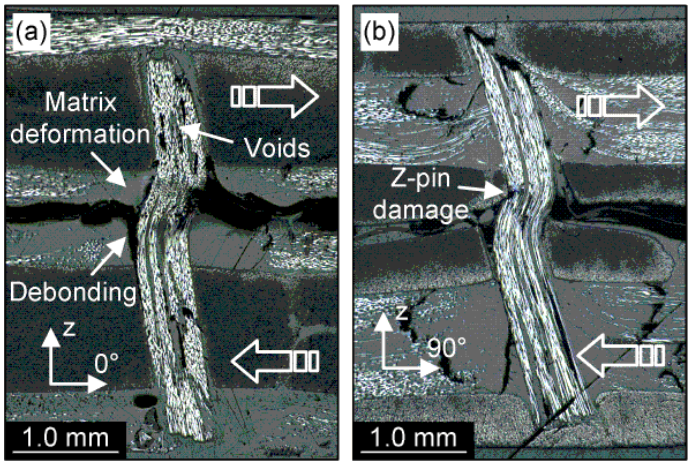

Figure 9.16 – Micrographs of partially sheared Z-pin, loaded a) parallel (0°) and b) transverse (90°) to fabric orientation at the delamination plane

9.4.4.5 Enhanced interfacial friction in shear

Although tested Z-pins in both mode I and mode II failed primarily by frictional pull-out, the measured bridging forces during frictional pull-out in shear were significantly higher, resulting in dissipated energy levels similar to the conventional sheared single tuft specimens.

Based on the observed extensive internal splitting and shear damage within the pin at larger shear displacement, which appears to be facilitated by insufficient internal wet-out of the supplied Z-pin rodstock (see Figure 9.16), contribution of flexural and shear stiffness of the pin can be assumed to be negligible. Hence, enhanced interfacial friction within the zone of ploughing is expected to be the main cause for the increased shear traction, as the Z-pin is forced against the surrounding substrate at high lateral pressure. This agrees with observations of the shear response of single titanium pins in UD composite [29].

By assuming a constant friction enhancement along the zone of ploughing, straight insertion angle and alignment of the sheared Z-pin with the shear direction at the delamination plane the enhancement factor μ of the original shear traction τ during frictional extraction can be estimated based on simple shear lag analysis [197] as follows:

$$\mu = \frac{1}{z_{0,i}} \cdot \left(\frac{F_i}{\tau s} - l_i \right) \qquad \textbf{9-2}$$

where F_i is the resulting shear traction for a given shear displacement v_i, τ is the initial shear stress in the undeflected section of the Z-pin, s is the circumference of the pin, l_i is the remaining embedding length of the extracting pin half and $z_{0,i}$ the corresponding height of the debonding zone within the specimen half. By assuming equal friction within the undeflected segment of the pin as measured for mode I pullout and inserting the applied shear displacements, corresponding bridging forces and measured ploughing zone heights for the Z-pins of Figure 9.16 into equation 9-2, enhancement factors of 4.8 and 7.3 were calculated for parallel and transverse shearing of the carbon Z-pins in NCF. Similar enhancement factors of 6.7 to 9.6 have been found necessary to predict the mode II bridging response of comparable carbon T300/BMI Z-pins from unidirectional composite [197].

The presence of local friction enhancement was further confirmed by shear tests on modified carbon tufts with removed surface loop in NCF. For both parallel and transverse shear loading, the modified carbon tufts responded almost identical to its unmodified counterpart (see Table 9.6). Although debonding cracks were found to develop along the full tuft surface, the modified tufts were not pulled out from the opposing specimen surface under increasing shear displacement, but failed always by tuft rupture at the delamination plane. Local enhancement within the zone of ploughing of the already high friction stress on the debonded surface of the helical tuft appears to increase the resistance of the tuft against pull-out to a level beyond the axial strength, resulting in tuft rupture instead of friction pull-out.

Table 9.6 - Shear: bridging parameters of loopless tufts in NCF (Std.dev. in brackets)

Thread	Fabric		#	F_{max}	$v_{t,fail}$	$v_{t,max}$	V_{fail}	V_{max}
			(-)	(N)	(mm)	(mm)	(Nmm)	(Nmm)
Carbon 2k	NCF	0°	8	172 (32)	0.71 (0.08)	1.01 (0.40)	92 (19)	103 (26)
		90°	7	156 (36)	0.45 (0.06)	0.48 (0.10)	47 (10)	47 (10)
Z-pin	NCF	0°	8	160 (69)	-	1.01 (0.41)	-	64 (12)
		90°	8	151 (26)	-	1.22 (0.17)	-	59 (13)

Hence, the modification of the tuft failure mechanisms and increase in total interfacial friction is less beneficial for mode II shear testing compared to mode I pull-out. More

significant effect on the bridging behaviour has the ploughing resistance of the surrounding composite, explaining the variation in effective enhancement of delamination toughness in reported conventional mode II crack propagation tests.

9.5 Conclusions

The bridging laws of both interlocked single tufts and Z-pins have been tested in mode I and mixed mode delamination configuration. Single tuft bridging behaviour in mode I pull-out depends on the stiffness and strength of the tufting thread, but also the geometrical arrangement of the tuft within the surrounding composite. Debonding and local pull-in of surface seams with plastic deformation of the surrounding composite at the transition from through-thickness tuft segment to surface seams are the main contributions to maximum opening displacement and energy dissipation before failure in mode I loading. Frictional pull-out of tufts plays a minor role, as the tufts fail primarily at the delamination plane. In contrast, the major energy dissipation mechanism for out-of-plane loaded Z-pins is frictional pull-out. For thin composites, the mode I bridging effectiveness of Z-pins is reduced compared to tufts of similar diameter due to the ineffective chamfer region and low interfacial friction along the smooth pin surface, resulting in 42% lower energy dissipation. The energy dissipation of tufts can be enhanced further by removing the interlocking surface loop resulting in frictional pull-out under highly enhanced frictional shear stress due to the threaded surface geometry of the tuft with 170% increased energy dissipation.

Mixed mode shear failure is more complex, as relative arrangement of local fabric orientation to shear direction, geometrical arrangement of the tuft within the composite and mechanical properties of thread and surrounding composite play a significant role. A modified shear jig allows the specimens to open under shear displacement in order to overcome natural fracture surface waviness and opening mechanisms exerted by the locally deforming Z-reinforcement. After debonding, both tufts and Z-pins cause significant local plastic deformation of the surrounding composite close to the crack surface, resulting in Z-reinforcement rotation of up to 45°. Size of the ploughing zone and maximum rotation angle depend on the resistance of the surrounding matrix against ploughing and the applied lateral pressure of the shearing Z-reinforcement. Removal of the surface loop in mixed mode shear brings only little improvement over conventional tufts and even Z-pins as enhanced friction within the ploughing zone causes tensile failure of the tufts before frictional pull-out. By using a digital image correlation system

both shear and opening displacement could be measured, with dependence on the loading direction and Z-reinforcement type.

The introduced single Z-reinforcement bridging tests are an essential tool to validating the implemented failure mechanisms and necessary mechanical parameters in existing micro-mechanical bridging models. They are used to characterise the critical material parameters of these models required to predict accurately not only mode I but also mixed mode delamination bridging.

Chapter 10 Overall discussion/future work

10.1 Discussion

Tufting appears to be an attractive form of structural Z-reinforcement of composites. During the course of this study, there has been a steady increase in external interest from potential industrial users with current development mainly concentrated in Germany. There has also been a real growth in practical applications, currently still limited to defence and aerospace users – examples include an IAI application of a tufted component with foam core and the new tufted landing gear for the Boeing 787 (Aircelle - Safran Group). Compared to the equivalent state of knowledge in the sister technology of Z-Fiber® pinning a decade ago, the rise in interest in tufting is significantly faster. This is likely to be due to its connection to the promise of relatively low-cost high performance structures, to be achieved via liquid moulding processes.

This study has established some requirements on the control of the manufacturing processes involved in the preparation of tufted composite structures. It has also provided an extensive data-base of carefully documented relationships between the resulting meso-structures of tufted cured samples and their mechanical performance under a range of loading modes. Finally, it offers some usable modelling approaches for quantitative treatment and prediction of the very complex structure-property relationships in this new type of material/structure.

10.1.1 Manufacturability and meso-structure control

Fabric support and external stabilisation of the preform during the tufting process are the critical parameters to manage in order to achieve a high rate of manufacturing at low failure rate. The initial preform thickness and fabric selection are not critical as long as internal stabilisation is minimal; in very highly bindered preforms there will be increased thread breakage and resistance to tuft insertion.

In an accompanying study, co-supervised by the author, the introduction of an external preform support structure was essential to ensure uniform tuft insertion and minimal

fabric compaction related crimping of the tuft in the final composite (see appendix F and [88]) .

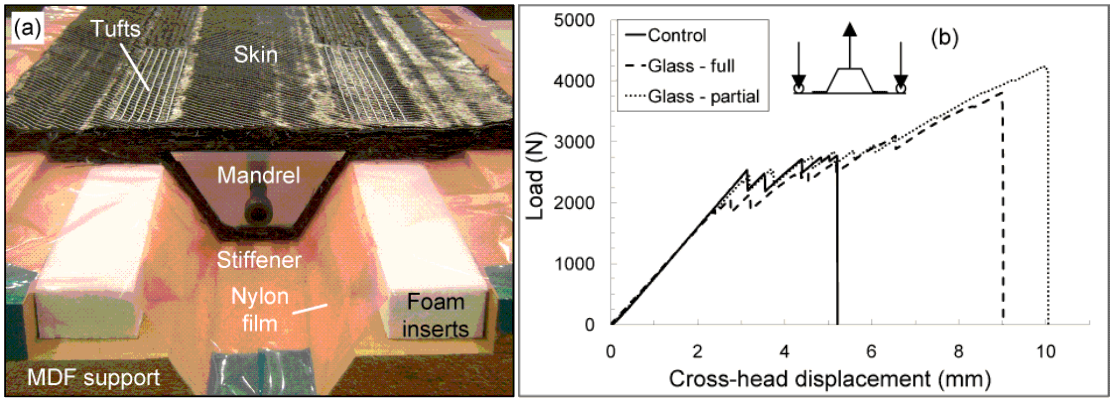

Figure 10.1 - a) Tufting support structure for omega stiffener-to-skin joint, b) load-displacement curves for 3 point bending pull-off of stiffener with full and partially inserted glass tufts

The set-up shown in Figure 10.1 a) made it possible to tuft an omega stiffener-to-skin joint with final joint thickness of 14.5 mm. A wooden (MDF) support with replaceable foam inserts for needle penetration proved sufficient for good compaction to be achieved, resulting in straight tufts despite the high preform thickness. The final RTM processed joint showed a significant enhancement in the load carrying capability, compared with an untufted joint, in a standard pull-off test (see Figure 10.1 b).

As shown in Chapter 5, the pattern of tuft arrangement relative to the load-bearing fabric plies can have significant effect on the morphological changes of the composite and subsequently the mechanical properties. The local fibre volume fraction changes have to be considered carefully, both for manufacturing reasons (local fabric permeability) and for mechanical property implications as even 2.8 mm tuft spacing can result in local fibre volume fraction in excess of 75%. Close tuft spacing in square arrangement leads inevitably to formation of continuous resin rich channels, which are prone to thermal cracking on cooling from high temperature cure.

In thin tufted composite structures the inevitable surface loops and the accompanying surface resin-rich layer cause a significant reduction in the load bearing cross-section, thus compromising the flexural performance of the part (see Figure 10.2). In addition, the increased compaction causes further kinking of even naturally undulated fabrics (e.g. twill weave), with detrimental effects on compressive behaviour.

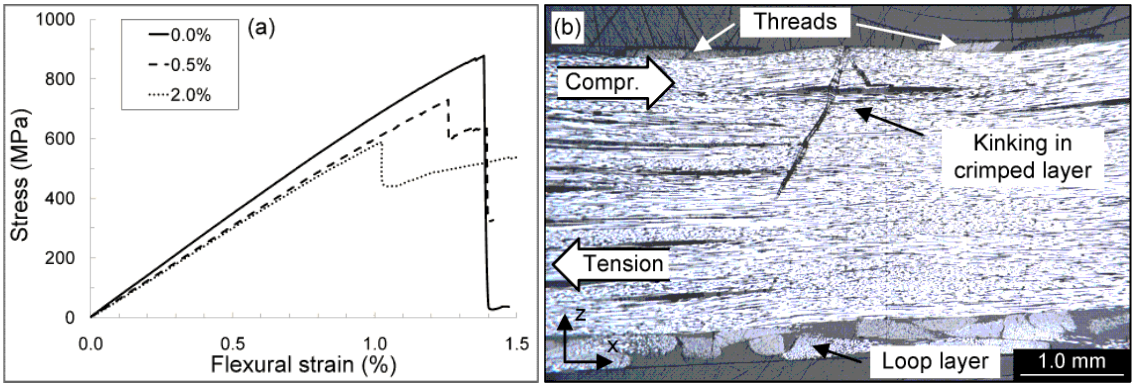

Figure 10.2 – Flexural failure of tufted composites: a) flexural stress-strain curves for 0%, 0.5% and 2% tufted NCF, b) micrograph (x-z) of kink failure of 2% tufted UD

Indeed, fibre undulation brought about by the insertion of tufts is seen as the most detrimental effect. In contrast, fibre fracture appears to have no significant effect on the composite as the dry fabric creates little resistance to the penetrating needle.

10.1.2 Characterisation and prediction of mechanical performance

It is important to be clear about the motivation for the use of tufting which defines the scope of a particular study. Some research groups look at tufting as a means of stabilising preforms besides improving the out-of-plane performance with the areal tuft density even below 0.1% [96; 97]. In this study tufting is looked at very much as a means of enhancing the toughness/damage tolerance of highly loaded composite structures and consequently the range of tuft-to-tuft spacing considered is between 2 and 6 mm, corresponding to areal densities of 0.5% to 2%, a similar range as typically used for Z-pinned composites. The generalisations and comments made here are therefore pertinent to this relatively narrow subsection of all possible tufting arrangements.

Given the prior knowledge on the effects of stitching and Z-pinning, as well as some tufting data, on the delamination resistance enhancement in composites, the toughening benefits of tufting were taken as expected. Considerable effort was therefore devoted to filling in the knowledge gap concerning the in-plane characteristics of tufted composites, for a representative range of fabric architectures. There are currently considerable fears in the industrial community about unsustainable penalties in the in-plane property drop-offs.

Recent experience within the group in Z-pinning also indicated that modelling means of carrying out parametric studies are essential.

10.1.2.1 In-plane performance

The outcome of tufting, in terms of in-plane stiffness and strength, is found to be highly dependent on the starting fabric/preform architecture. While this was expected, from previous Z-pinning work, the situation is considerably more complicated than in the case of Z-pinning. There is no identifiable single or even linear tendency in any given mode of loading, as found in Z-pinned laminates, but instead there is a strong dependency on type of tuft and its interaction with its immediate environment. The solid Z-pins produce an easily identifiable perturbation to the laminate, whereas the tufts become in themselves a part of the immediate environment during the resin infusion and cure process.

The effects of tuft insertion on in-plane stiffness are generally negligible. The effects on the strength of thin (< 4mm) carbon fabric composites are generally detrimental, but to very different degrees (Chapter 6, see also Figure 10.3).

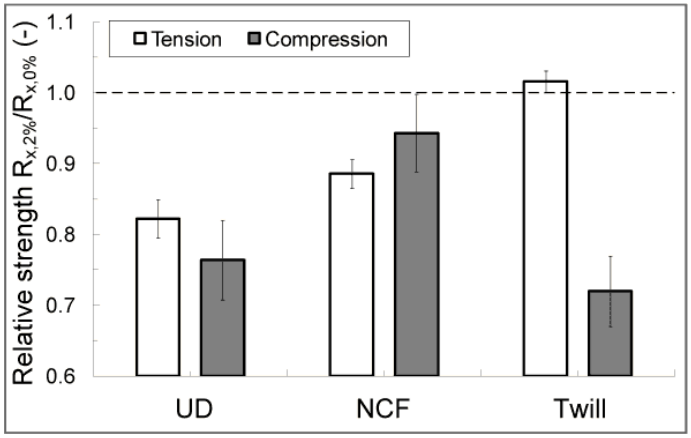

Figure 10.3 – Comparison of relative reduction of in-plane strength for 2% carbon tufted UD, NCF and Twill woven composite

The cause of these differences is the combination of several meso-structural changes around the tuft which were identified as local fabric undulation, resin rich regions and change in local fabric fibre volume fraction. The insertion pattern and spacing highly affect the local 3D morphology of tufted composite, as identified via 2D optical micrographs and sectioning/polishing, as in the many examples given in Chapter 5. The pattern proves to be critical to resulting fibre undulation angles and formation of resin rich zones. A square pattern, in relation to the load bearing fabric plies, should be preferable

as the fibre undulation reduces with increasing tuft spacing. However, the same pattern favours the formation of resin rich channels, which may prove to be detrimental for thermo-mechanical stability and potentially fatigue performance.

The reduction in compressive strength in tufted woven composites is one serious drawback for the use of the technique for structural applications (see chapter 6.5.2). The modern NCF fabrics are more forgiving and appear to be ideally suited to modification by tufting. The tufts suppress local delamination between the multi-directional fabric layers, which otherwise have a detrimental effect even on the in-plane properties of NCF, in the absence of Z-reinforcements. If a fixed geometry process, such as RTM, is to be used, the tuft loop size should be kept as small as possible, to minimise the compaction of the preform.

The FE model presented in Chapter 7 shows itself capable of determining the upper and lower bounds of the expected strength performance. The proviso is that the unit cell used in the model is based on the true experimental identification of the tuft pattern and some minimum necessary meso-structural parameters, i.e. the resin pocket dimensions and volume proportion of deviated fabric. In addition, accurate fibre deviation and compaction distributions need to be assigned.

10.1.2.2 Out-of plane performance

The common questions that may be posed by a potential user concern “the best tuft density” and the “best tuft diameter”. The complex interactions between tufting parameters, specimen thickness, fabric architecture and in-plane property drop-off mean that there is no simple answer to the question. Tufting is very effective in improving the mode I delamination toughness. Just 0.5% tufting density already increases the resistance to delamination crack propagation so much that the DCB arms may fail in flexure. In contrast, the same tufting density under mode II loading is insufficient to ensure the existence of a fully developed bridging zone in the specimen (see Chapter 8.5.1.2). The ‘apparent’ delamination toughness enhancement depends on the bridging zone length, which itself is affected by both the bridging properties of the Z-reinforcement and by the structural properties of the host material.

The DIC assisted observations of mode II test crack tip (Chapter 8.5.1.2) clearly demonstrate that a significant proportion of crack opening exists in the far-field of the crack at what should (nominally) be a pure mode II test, in tufted ELS specimens. This is par-

ticularly the case in woven fabric samples, where the natural pre-existing fibre crimp forces the faces of the beam sample apart under shear. Thus the local strain field/mode mixity at the crack tip is different to that experienced at the tuft location and different from one tuft location to the next. The addition of a mode I component to what should be a mode II test was predicted in early work by Massabò et al [117], but not previously documented in the way presented here.

The use of the single tuft specimens offers a possible solution to the characterisation of the complexity of the shear response. The single tuft delamination tests described in Chapter 9 support the identification of bridging mechanisms not only in mode I but also in mixed I/II modes. Besides frictional pull-out surface deformation and ploughing mechanisms were identified as contributing to the energy absorption and maximum opening displacement before failure, an important parameter for the development of large scale bridging. Single tuft testing is considered to be preferable over multiple Z-reinforcement tests. It offers the possibility to determine the intrinsic variability in single Z-reinforcement performance, required for eventual statistical approach to modelling.

As shown in Table 10.1, the dissipated energy and critical opening to failure of tufts in carefully performed single tuft tests are in very close agreement to results from delamination tests, derived from DIC monitored crack displacement at individual tuft rows along the delamination specimen surface (see Figure 8.6 and Figure 8.10 in Chapter 8) and by dividing the total energy dissipated by a fully separated delamination specimen by the number of failed tufts.

Table 10.1 – Comparison of single carbon tuft bridging parameters of critical opening ($u_{t,fail}$) to failure and maximum dissipated energy ($U_{t,max}$), derived from single tuft bridging and DCB tests (Std.dev. in brackets)

Test	$u_{t,fail}$ (mm)	U_{max} (Nmm)
Single tuft pull-out	0.20 (0.04)	50 (15)
DCB test	0.19 (0.02)	52 (4)

Hence, single tuft bridging tests are a suitable alternative to conventional delamination tests to determine the independent bridging performance of tufts. They eliminate the often disregarded influence of the beam geometry on the development of large scale bridging in a conventional delamination test.

In order to implement the bridging behaviour of tufts into mechanical models of composite structures with continuously changing delamination modes, as determined experimentally in the omega stiffener-to-skin joint under flexure [88], the use of an analytical bridging model is suggested. This is capable of predicting tuft bridging for any mode mixity. Appendix D contains the adaptation of an earlier analytical model by Cox [195; 212; 215], which incorporates the critical failure mechanisms identified in the single tuft bridging tests.

The required geometric parameters can be determined relatively easily by preparing micro-graphical samples of tufted laminates with sufficiently accurate estimations of surface thread shape. A number of critical material properties, i.e. tuft stiffness and surface ploughing resistance, can be measured or even estimated from general material data on fibre and resin constituents. However, the factors of frictional stress, enhancement in local friction under lateral pressure and corresponding ploughing resistance of the composite at the delamination plane can only be derived from the single tuft bridging tests (see Chapter 9.4.4) as all three parameters are directly related to the local interaction of the tuft with the surrounding meso-structure of the composite. Instead of oversimplified, limited validity constituent tests for crushing strength and interfacial friction, as proposed in [210], it is suggested to use a combination of the single tuft delamination test in mode I and in mixed mode loading, allowing the separate adjustment of interfacial friction from mode I test and of the ploughing resistance and friction enhancement from mode II tests.

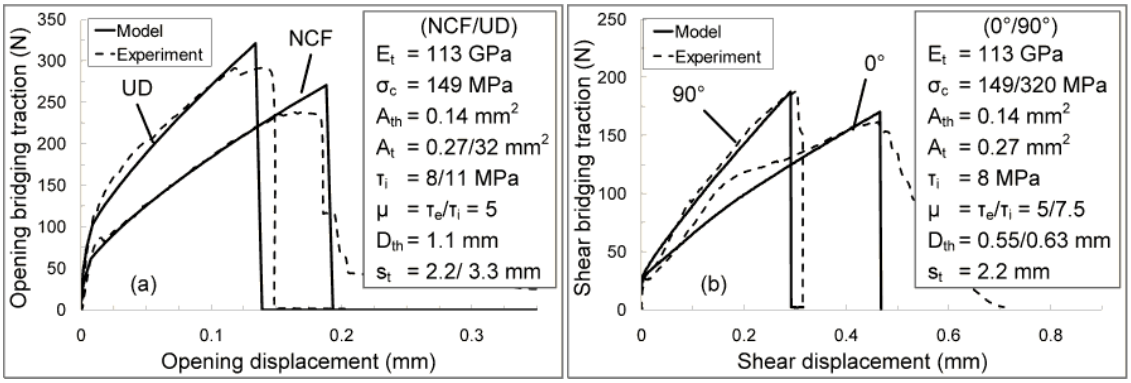

Figure 10.4 – Comparison of analytically predicted and measured single carbon tuft bridging laws in a) mode I (UD and NCF) and b) mixed mode loading (NCF, 0° and 90° loading to fabric direction at crack plane)

Figure 10.4 shows the close agreement that can be achieved between the model prediction and experiment, not only for the case of mode I loading but also for the mixed mode case, by only adjusting the frictional stress to mode loading and enhancement

factor and lateral ploughing resistance. There is a difference between the relatively low resulting interfacial friction in the adjusted model and the experimental results by frictional pull-out of modified tufts. However, this indicates only the shortcoming of the experimental determination method of interfacial friction on helical threads, as for full thread pull-out, the underlying test method, significant inelastic matrix deformation and crumbling is necessary, contributing to the overprediction of the apparent measured friction. For small elastic stretching of the interlocked tuft, local interfacial friction can be expected to be significantly lower. The adjusted ploughing resistance agrees well with measured corresponding compressive material properties such as the compressive resin yield strength (for ploughing into the resin rich region) and with values reported by Cox [212].

It is interesting to note that the bridging effectiveness of carbon thread tufts is better than that of glass thread tufts, as the maximum bridging load is higher at comparable displacement (see Chapter 9.4.3.4). Thus the thread material of choice in tufting for toughness would appear to be carbon. Furthermore, reduction of the tuft diameter appears to be not beneficial for the bridging performance in mode I (see Chapter 9.4.3.4) as relative enhancement of the interfacial friction surface, main cause for higher bridging loads and increased energy dissipation at unchanged maximum bridging displacement of Z-pins, is only secondary for interlocked tuft. For the thinner tufts, relative increase in surface thread width and corresponding reduction of surface deformation result in reduced bridging displacement, i.e. an areal equivalent tuft density of thinner tuft diameters dissipates less energy than thick tufts with larger crack opening displacement to failure.

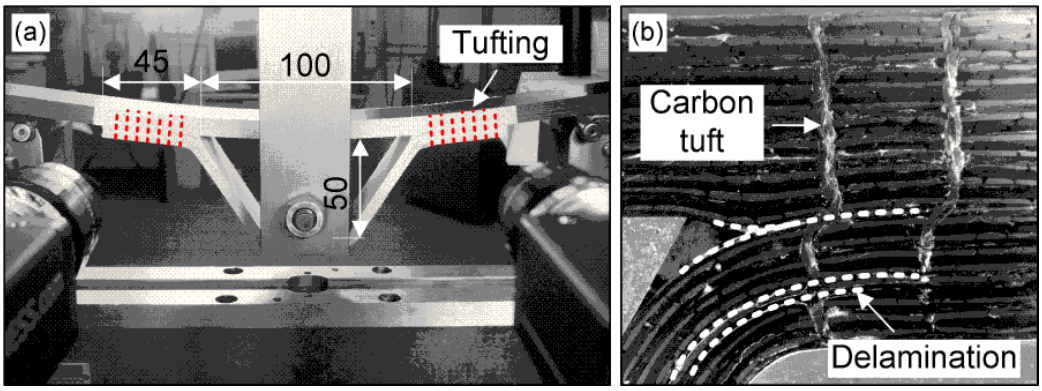

Figure 10.5 – a) Pull-off configuration of omega stiffener-to-skin joint, b) micrograph of locally bridged delamination cracks by carbon tufts

Finally, since the additional in-plane property drop off at tufting densities over 0.5% is relatively low, but there is potential for further delamination resistance increase, it may be advantageous to use higher tufting densities in practical, thicker, structures, such as the omega-stiffener demonstrator shown in Figure 10.5

10.2 Future work

The study presented here has addressed mechanical response of tufted composites to quasi-static loading, and has touched on the mechanisms of damage accumulation. It has not addressed in-plane fatigue behaviour, nor the issues of effects on delamination crack growth rates. Both of these should be addressed in future work. Also, given the significant thermal cracking in the resin-rich pockets, there are some questions regarding possible water ingress via such cracks. Effects of hot-wet conditioning on the mechanical performance are deserving of attention, as is more general environmental resistance.

Given the intrinsic variability in single tuft response, further developments of modelling approaches to delamination modelling, using single tuft bridging laws, should include stochastic distribution considerations.

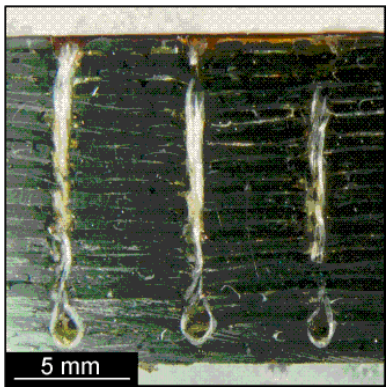

Figure 10.6 – Micrograph of partially through-the-thickness inserted glass thread tufts in section of omega stiffener-to-skin flange

In terms of practicalities of manufacturing, the management of the loops remains the major issue. The external loop-resin layer creation is an undesirable effect, on a number of levels. As work in this laboratory has demonstrated, the issue can be resolved in sufficiently thick preforms, by the use of partially inserted tufts (see Figure 10.6) and with no apparent detriment to the mechanical out-of-plane performance (see stiffener pull-off results in Figure 10.1 b) for partially inserted glass tufts) [88].

This is not an option for the typically thin (< 3mm) structures that fully exploit other desirable properties of carbon fibre composites. There are some current limitations inherent in the tufting equipment design which needs further optimisation targeted specifically on thin composites. Improvements would include reduction in the needle diameter, shorter stroke and tight positional control.

Potential users are already expressing their wish to be able to tuft on the tool, with no further transfer of the tufted preform. Indeed, this has been suggested as primary advantage of tufting compared to other Z-reinforcing techniques. Significant attention therefore now needs to be given to tooling design, to enable tufting on the mould while minimising subsequent post-finishing operations.

Chapter 11 Conclusions

- The manufacturing process of automated tufting has been improved by optimising critical manufacturing parameters, such as fabric compaction, thread tension and fabric support.

- Tufts introduce structural defects into the cured composite. Extent of in-plane fibre misalignment, resin rich pockets and channels around the tufts, local fibre breakage and thermal cracking within the resin pockets depends highly on the fabric layup, tuft spacing and control of the tuft insertion pattern.

- For the manufacturing route of resin transfer moulding, free tufting loops and thread seams on the composite surface can cause significant out-of-plane fibre fabric crimp and compaction of the fabric stacking if loops overlap at close tuft spacing.

- Surface loops can be completely avoided in thicker composites by inserting tufts only through part of the thickness.

- Local fibre deviation around the tufts and formation of resin rich surface layers cause significant increase in local fabric fibre volume fraction, to about 75% for 2% areal tuft density in 4 mm thick specimens.

- Axial in-plane Young's moduli for tension and compression of UD (in fibre direction), twill woven and non-crimped fabric composites are unaffected by tufting as fibre misalignment is balanced by locally increased fabric compaction.

- Fibre misalignment and local stress concentration are critical factors for the observed reduction in axial tensile strength of up to -19% in unidirectional composites. Suppression of delamination and natural fibre waviness (in woven laminates) reduce the detrimental effect to only -11% and -1.5% for biaxial non-crimped and woven fabrics respectively. Fibre breakage from needle penetration has no effect on the tensile strength.

- Tuft induced out-of-plane fabric crimp assists the formation of kink bands under in-plane compression, causing strength reductions of up to -28% for both UD

and woven composite. Delamination suppression in NCF balances the reduction to only -6%.

- Both compressive and tensile strength reductions are already present for 0.5% tuft density while a further decrease in tuft spacing (from 5.6 mm to 2.8 mm) causes only a little further reduction of both properties. This is due to formation of continuous resin rich channels and consequential straightening of fabric.

- Random orientation of the surface loops can increase matrix dominated shear and transverse tensile modulus (for UD) by up to 50%, while the in-plane shear strength remains unaffected by the insertion of tufts.

- A parametric finite element unit cell model enables prediction of both in-plane elastic and strength properties of UD and NCF composites by incorporating empirically determined morphologic changes and Puck's failure criterion with a simple damage model. By analysing the two extremes of square and triangular tuft arrangement a boundary for maximum changes to the in-plane tension properties can be predicted. Accurate knowledge of distributions of fibre deviation and of fabric compaction is necessary for correct failure prediction.

- The insertion of carbon tufts at only 5.6 mm spacing is sufficient to increase the apparent delamination propagation resistance of biaxial NCF in a DCB test eightfold, which can cause a change in failure mode from delamination to flexural failure for thinner samples (~4mm).

- ELS mode II testing of 0.5% carbon tufted NCF showed a 61% increase in apparent delamination toughness at maximum crack extension. Tufts have the ability to stop unstable crack propagation.

- Digital image correlation improves the detectability of the true crack tip and hence clarification of the bridging behaviour of tufts in mode I and II delamination tests, by measuring the relative opening and shear displacement components of opposing beam halves.

- Insufficient development of tuft bridging and presence of mode I opening as a result of the textile nature of the fabric limit the usefulness of the ELS test in determining the effect of tufting on the mode II delamination propagation. The use of a controlled single tuft bridging test is suggested as a suitable alternative.

- Bridging laws of single tuft and solid Z-pin specimens have been determined in mode I and mixed mode, for various fabric architectures. Tuft bridging laws can be used to calibrate analytical bridging models which are required for the eventual independent prediction of delamination suppression in composite structures.

- Tuft bridging mechanisms in mode I pull-out are debonding, elastic tuft stretching and composite deformation around the interlocking surface thread. Frictional pull-out, the main energy dissipation mechanism in case of the Z-pins, is negligible after tuft failure.

- Local tuft rotation (up to 30°) and lateral ploughing into the surrounding composite allow for crack shear displacements beyond the tuft diameter, explaining the low toughness enhancement in ELS delamination tests. Mode II tuft bridging laws are highly dependent on the load direction in relation to fibre orientation at the delamination plane.

- For thin (< 4mm) composites the mode I energy dissipation by single tufts is significantly higher than that achieved by equivalent Z-pins. Removal of the tuft surface loop additionally improves the mode I energy dissipation by the tuft threefold, by allowing supplementary pull-out mechanism under enhanced friction, arising from the helical tuft geometry.

- 'Management' of the tufting loops remains a relevant challenge in the optimised exploitation of the technology.

References

[1] Mouritz, A. P., Leong, K. H. and Herszberg, I. (1997), "A review of the effect of stitching on the in-plane mechanical properties of fibre-reinforced polymer composites", Composites Part A: Applied Science and Manufacturing, vol. 28, no. 12, pp. 979-991.

[2] Mouritz, A. P. and Cox, B. N. (2000), "Mechanistic approach to the properties of stitched laminates", Composites Part A: Applied Science and Manufacturing, vol. 31, no. 1, pp. 1-27.

[3] Mouritz, A. P. and Cox, B. N. (2010), "A mechanistic interpretation of the comparative in-plane mechanical properties of 3D woven, stitched and pinned composites", Composites Part A: Applied Science and Manufacturing, vol. 41, no. 6, pp. 709-728.

[4] Bannister, M. K. (2004), "Development and application of advanced textile composites", Proceedings of the Institution of Mechanical Engineers, Part L: Journal of Materials: Design and Applications, vol. 218, no. 3, pp. 253-260.

[5] Partridge, I. K. and Cartié, D. D. R. (2005), "Delamination resistant laminates by Z-Fiber® pinning: Part I manufacture and fracture performance", Composites Part A: Applied Science and Manufacturing, vol. 36, no. 1, pp. 55-64.

[6] Dransfield, K. A., Baillie, C. and Mai, Y. W. (1994), "Improving the delamination resistance of cfrp by stitching-a review", Composites Science and Technology, vol. 50, no. 3, pp. 305-317.

[7] Mouritz, A. P. (2007), "Review of z-pinned composite laminates", Composites Part A: Applied Science and Manufacturing, vol. 38, no. 12, pp. 2383-2397.

[8] Mouritz, A. P., Bannister, M. K., Falzon, P. J. and Leong, K. H. (1999), "Review of applications for advanced three-dimensional fibre textile composites", Composites Part A: Applied Science and Manufacturing, vol. 30, no. 12, pp. 1445-1461.

[9] Wittig, J. (2001), "Recent development in the robotic stitching technology for textile structural composites", in Falcone, A., Nelson, K. M., Alvers, R., et al (eds.), 33rd International SAMPE Technical Conference -Advancing Affordable Materials Technology, Vol. 33, 5 - 8 November, Seattle, WA, pp. 540.

[10] Dickinson, L. C., Farley, G. L. and Hinders, M. K. (1999), "Translaminar Reinforced Composites: A Review", Journal of Composites Technology and Research, vol. 21, no. 1, pp. 3-15.

[11] Tong, L., Mouritz, A. P. and Bannister, M. K. (2002), 3D Fibre Reinforced Polymer Composites, Elsevier.

[12] Truong, T. C., Vettori, M., Lomov, S. V. and Verpoest, I. (2005), "Carbon composites based on multi-axial multi-ply stitched preforms. Part 4. Mechanical properties of composites and damage observation", Composites Part A: Applied Science and Manufacturing, vol. 36, no. 9, pp. 1207-1221.

[13] Yang, Q. D., Rugg, K. L., Cox, B. N. and Shaw, M. C. (2003), "Failure in the junction region of T-stiffeners: 3D-braided vs. 2D tape laminate stiffeners", International Journal of Solids and Structures, vol. 40, no. 7, pp. 1653-1668.

[14] Greenhalgh, E. and Hiley, M. (2003), "The assessment of novel materials and processes for the impact tolerant design of stiffened composite aerospace structures", Composites Part A: Applied Science and Manufacturing, vol. 34, no. 2, pp. 151-161.

[15] Brandt, J., Drechsler, K. and Arendts, F. J. (1996), "Mechanical performance of composites based on various three-dimensional woven-fibre preforms", Composites Science and Technology, vol. 56, no. 3, pp. 381-386.

[16] Guénon, V. A., Chou, T. W. and Gillespie Jr., J. W. (1989), "Toughness properties of a three-dimensional carbon-epoxy composite", Journal of Materials Science, vol. 24, no. 11, pp. 4168-4175.

[17] Lee, L., Rudov-Clark, S., Mouritz, A. P., Bannister, M. K. and Herszberg, I. (2002), "Effect of weaving damage on the tensile properties of three-dimensional woven composites", Composite Structures, vol. 57, no. 1-4, pp. 405-413.

[18] Kuo, W. S., Ko, T. -. and Chen, C. P. (2007), "Effect of weaving processes on compressive behavior of 3D woven composites", Composites Part A: Applied Science and Manufacturing, vol. 38, no. 2, pp. 555-565.

[19] Freitas, G. (1993), "Z-Fiber Insertion Process for Improved Damage Tolerance in Aircraft Laminates", Proceedings, 25th International SAMPE Technical Conference.

[20] Freitas, G., Fusco, T., Campbell, T., Harris, J. and Rosenberg, S. (1996), "Z-fiber technology and products for enhancing composite design", AGARD Conf. Proc., pp. 17-1-17-8.

[21] Cartié, D. D. R. (2000), Effect of Z-Fibres™ on the Delamination Behaviour of Carbon Fibre / Epoxy Laminates (unpublished PhD thesis), School of Applied Sciences, Cranfield University, Cranfield, UK.

[22] Chang, P., Mouritz, A. P. and Cox, B. N. (2006), "Properties and failure mechanisms of z-pinned laminates in monotonic and cyclic tension", Composites Part A: Applied Science and Manufacturing, vol. 37, no. 10, pp. 1501-1513.

[23] Chang, P., Mouritz, A. P. and Cox, B. N. (2004), "Tensile fatigue properties of z-pinned carbon/epoxy composite", 49th International SAMPE Symposium and Exhibition: Materials and Processing Technology, Vol. 49, 16 - 20 May, Long Beach, CA, pp. 1023.

[24] Chang, P., Mouritz, A. P. and Cox, B. N. (2007), "Flexural properties of z-pinned laminates", Composites Part A: Applied Science and Manufacturing, vol. 38, no. 2, pp. 244-251.

[25] Mouritz, A. P. (2007), "Compression properties of z-pinned composite laminates", Composites Science and Technology, vol. 67, no. 15-16, pp. 3110-3120.

[26] Steeves, C. A. and Fleck, N. A. (2006), "In-plane properties of composite laminates with through-thickness pin reinforcement", International Journal of Solids and Structures, vol. 43, no. 10, pp. 3197-3212.

[27] Cartié, D. D. R., Troulis, M. and Partridge, I. K. (2006), "Delamination of Z-pinned carbon fibre reinforced laminates", Composites Science and Technology, vol. 66, no. 6, pp. 855-861.

[28] Cartié, D. D. R. and Partridge, I. K. (2003), "Prediction of the delamination behaviour of z-fiber® reinforced laminates", 44th AIAA/ASME/ASCE/AHS/ASC Structures, Structural Dynamics, and Materials Conference, Vol. 1, 7 - 10 April, Norfolk, VA, pp. 707.

[29] Cartié, D. D. R., Cox, B. N. and Fleck, N. A. (2004), "Mechanisms of crack bridging by composite and metallic rods", Composites Part A: Applied Science and Manufacturing, vol. 35, no. 11, pp. 1325-1336.

[30] Rugg, K. L., Cox, B. N., Ward, K. E. and Sherrick, G. O. (1998), "Damage mechanisms for angled through-thickness rod reinforcement in carbon-epoxy laminates", Composites Part A: Applied Science and Manufacturing, vol. 29, no. 12, pp. 1603-1613.

[31] Lander, J. K. (2008), Designing with z-pins: locally reinforced composite structures (unpublished PhD thesis), School of Applied Sciences, Cranfield University, Cranfield, UK.

[32] McBeath, S. (2002), "Safety pins", Racecar Engineering, vol. 12, pp. 56-62.

[33] Hall, T. (2002), Automation of Z-Fiber for Complex Shapes, available at: cmtc.scra.org/pubs/fall_2002.pdf (accessed Aug. 2010).

[34] Schuerfeld, G. W. (2003), Joint Technology Exchange Group - CMTC Brief 2003, available at: www.jdmag.wpafb.af.mil/v%20composite%20manufacturing%20technology%20center.ppt (accessed Sept. 2010).

[35] Marasco, A. I. (2005), Analysis and evaluation of mechanical performance of reinforced sandwich structures: X-CorTM and K-CorTM (unpublished PhD thesis), School of Applied Sciences, Cranfield University, Cranfield, UK.

[36] Cartié, D. D. R. and Fleck, N. A. (2003), "The effect of pin reinforcement upon the through-thickness compressive strength of foam-cored sandwich panels", Composites Science and Technology, vol. 63, no. 16, pp. 2401-2409.

[37] Marasco, A. I., Cartié, D. D. R., Partridge, I. K. and Rezai, A. (2006), "Mechanical properties balance in novel Z-pinned sandwich panels: Out-of-plane properties", Composites Part A: Applied Science and Manufacturing, vol. 37, no. 2, pp. 295-302.

[38] Dow, M. B. and Smith, D. L. (1989), "Damage-tolerant composite materials produced by stitching carbon fabrics", 21st International SAMPE Technical Conference, Vol. 21, 25 - 28 September 1989, Atlantic City, NJ, USA, pp. 595.

[39] Benson Dexter, H. and Funk, J. G. (1986), "Impact resistance and interlaminar fracture toughness of through-the-thickness reinforced graphite/epoxy", AIAA Paper 86-1020-CP , Vol. 1, pp. 700.

[40] Dow, M. and Dexter, H. B. (1997), "Development of stitched, braided and woven composite structures in the ACT program and at Langley Research Center (1985 to 1997)", NASA TP 97-206234.

[41] Karal, M. (2005), "AST composite wing program - Executive summary", NASA Report, vol. NASA-CR-2001-210650.

[42] Beier, U., Fischer, F., Sandler, J. K. W., Altstädt, V., Weimer, C., Spanner, H. and Buchs, W. (2008), "Evaluation of preforms stitched with a low melting-temperature thermoplastic yarn in carbon fibre-reinforced composites", Composites Part A: Applied Science and Manufacturing, vol. 39, no. 5, pp. 705-711.

[43] Lee, C. and Liu, D. (1990), "Tensile strength of stitching joint in woven glass fabrics", Journal of Engineering Materials and Technology, Transactions of the ASME, vol. 112, no. 2, pp. 125-130.

[44] Ogale, A., Weimer, C. and Mitschang, P. (2004), "Selection of sewing threads for preform manufacturing", Advanced Composites Letters, vol. 13, no. 4, pp. 199-206.

[45] Lowe, J., Schneider, M. and Kinsella, M. (2005), "Carbon fibre sewing yarn for structural reinforcement of textile composite applications", International SAMPE Technical Conference, 31 October - 3 November, Long Beach, CA, USA.

[46] Plain, K. P. and Tong, L. (2010), "The effect of stitch incline angle on mode I fracture toughness - Experimental and modelling", Composite Structures, vol. 92, no. 7, pp. 1620-1630.

[47] Morales, A. (1990), "Structural stitching of textile performs", in Michelove, L. D., Caruso, R. P., Adams, P., et al (eds.), 22nd International SAMPE Technical Conference, Vol. 22, 6 - 8 November, Boston, MA, USA, pp. 1217.

[48] Klopp, K., Moll, K. U. and Wulfhorst, B. (2000), "Stitching technology for technical textiles and composites", Technische Textilien, vol. 43, no. 4, pp. 278.

[49] Talvensaari, H., Ladstätter, E. and Billinger, W. (2005), "Permeability of stitched preform packages", Composite Structures, vol. 71, no. 3-4, pp. 371-377.

[50] Rieber, G. and Mitschang, P. (2010), "2D Permeability changes due to stitching seams", Composites Part A: Applied Science and Manufacturing, vol. 41, no. 1, pp. 2-7.

[51] Schuster, M., Ogale, A., Peetz, L., Schuster, J. and Mitschang, P. (2008), "Analysis of sewed preforms by visual on-line monitoring of stitch-hole variations under compaction", Composites Science and Technology, vol. 68, no. 1, pp. 312-320.

[52] Zhao, N., Rödel, H., Herzberg, C., Gao, S. L. and Krzywinski, S. (2009), "Stitched glass/PP composite. Part I: Tensile and impact properties", Composites Part A: Applied Science and Manufacturing, vol. 40, no. 5, pp. 635-643.

[53] Zhao, N. (2007), Nähen als Montageverfahren textiler Preforms und Wirkungen der Nähte auf lokale mechanische Eigenschaften thermoplastischer Faserverbundwerkstoffe (unpublished PhD thesis), Fakultät Maschinenwesen, Technical University Dresden, Dresden, Germany.

[54] Potluri, P., Kusak, E. and Reddy, T. Y. (2003), "Novel stitch-bonded sandwich composite structures", Composite Structures, vol. 59, no. 2, pp. 251-259.

[55] Grundmann, T., Gries, T., Kordl, M. T. and Corves, B. (2006), "Robot-supported joining of reinforcement textiles with one-sided sewing heads", Technische Textilien, vol. 49, no. 4, pp. 262.

[56] Gries, T. and Klopp, K. (2007), Füge- und Oberflächentechnologien für Textilien: Verfahren und Anwendungen, Springer Verlag, Berlin.

[57] Geßler, A. and Schouten, M. (2007), "Textiltechnik für Luftfahrt - Lessons Learnt", Cluster-Treff Neue Werkstoffe, 2. October, Naila, Germany.

[58] Thurm, T. (2005), "Applications of one-sided stitching techniques for resin infusion preforms and structures", SAMPE Journal, vol. 41, no. 1, pp. 64-67.

[59] Neitzel, M. and Mitschang, P. (2004), Handbuch Verbundwerkstoffe: Werkstoffe, Verarbeitung, Anwendung, Carl Hanser Verlag, Munich, Germany.

[60] Filsinger, J., Dittmann, R. P. and Bischoff, T. (2003), "Nähen als textile Preform-Technik zur Herstellung von Faserverbundstrukturen für Luftfahrtanwendungen am Beispiel der A380-Druckkalotte", DGLR-Kongress, 17 - 20 November, Munich, Germany.

[61] Sickinger, C. and Herrmann, A. (2001), "Structural stitching as a method to design high-performance composites in future", Proceeding of TechTextil Symposium, 24 - 26 April, Frankfurt am Main, Germany.

[62] Herzberg, C., Rodel, H., Fodisch, J. and Marker, M. (2000), "Sewing of reinforcement textiles for composites in the example of high-performance rotors", Technische Textilien, vol. 43, no. 2, pp. E30-E33+124-128.

[63] Klopp, K. (2003), Analyse des Nahtbildungsprozesses von Verstärkungstextilien fur Faserverbundkunststoffe (unpublished PhD thesis), School of Mechanical Engineering, RWTH Aachen, Aachen, Germany.

[64] Klopp, K. and Moll, K. U. (2007), "Stitching Process with One-sided Approach of the Textile for the Production of Reinforcing Textiles for Composites and Other Technical Textiles", The 5th International Conference on Textile Composites, 18–20 September, Leuven, Belgium.

[65] Laourine, E. (2005), Einseitige Naehtechnik fuer die Herstellung von dreidimensionalen Faserverbundbauteilen (unpublished PhD thesis), School of Mechanical Engineering, RWTH Aachen, Aachen, Germany.

[66] Grundmann, T., Gries, T., Flachskampf, P., Henning, K., Kordi, M. T., Corves, B., Wisner, G., Brecher, C. and Kempf, T. (2006), "Autopreforms - Economic production of fibre-reinforced-plastic parts by automated production of textile preforms", DWI Reports, no. 130.

[67] Schiebel, P. and Herrmann, A. (2008), "Textile preform technologies in the aviation sector – chances and challenges for the automotive sector", Industrial Fabrics Association International - Advanced Textiles Europe Conference, 12.06.2008, Berlin, Germany.

[68] Geßler, A., Gliesche, K., Keilmann, R., Laourine, E., Kröber, J. and Pickett, A. (2002), Textile Integrationstechniken zur Herstellung Vorkonfektionierter Verstärkungsstrukturen für FVK "INTEX".

[69] Brandt, J., Drechsler, K. and Filsinger, J. (2001), Advanced Textile Technologies for the Cost Effective Manufacturing of High Performance Composites, available at: ftp://ftp.rta.nato.int//PubFullText/RTO/MP/RTO-MP-069(II)/MP-069(II)-(SM1)-20.pdf (accessed Sept. 2010).

[70] Stickler, P. B., Ramulu, M. and Johnson, P. S. (2000), "Experimental and numerical analysis of transverse stitched T-joints in bending", Composite Structures, vol. 50, no. 1, pp. 17-27.

[71] Stickler, P. B. and Ramulu, M. (2001), "Investigation of mechanical behavior of transverse stitched T-joints with PR520 resin in flexure and tension", Composite Structures, vol. 52, no. 3-4, pp. 307-314.

[72] Stickler, P. B. and Ramulu, M. (2006), "Damage progression analyses of transverse stitched T-joints under flexure and tensile loading", Advanced Composite Materials: The Official Journal of the Japan Society of Composite Materials, vol. 15, no. 2, pp. 243-261.

[73] Stickler, P. B. and Ramulu, M. (2006), "Experimental study of composite T-joints under tensile and shear loading", Advanced Composite Materials: The Official Journal of the Japan Society of Composite Materials, vol. 15, no. 2, pp. 193-210.

[74] Stickler, P. B. and Ramulu, M. (2002), "Parametric analyses of stitched composite T-joints by the finite element method", Materials and Design, vol. 23, no. 8, pp. 751-758.

[75] Henao, A., Carrera, M., Miravete, A. and Castejón, L. (2010), "Mechanical performance of through-thickness tufted sandwich structures", Composite Structures, vol. 92, no. 9, pp. 2052-2059.

[76] Havar, T. (2007), Towards Design and Calculation of 3D-reinforced Composite Force Introduction Loops (unpublished PhD thesis), University Stuttgart, Stuttgart, Germany.

[77] Poulin, E. (2004), Reinforcement of a T-joint by Z-Fiber® pinning and 'tufting' (unpublished MSc thesis), School of Applied Sciences, Cranfield University, Cranfield, UK.

[78] Morillot, H. (2007), Delamination resistance of tufted composites (unpublished MSc thesis), School of Applied Sciences, Cranfield University, Cranfield, UK.

[79] Jones Vinchery, J. A. (2007), Reinforcement of composite aircraft structures using tufting (unpublished MSc thesis), School of Engineering, Cranfield University, Cranfield, UK.

[80] Mills, A. R. and Jones, J. (2010), "Investigation, manufacture, and testing of damage-resistant airframe structures using low-cost carbon fibre composite materials and manufacturing technology", Proceedings of the Institution of Mechanical Engineers, Part G: Journal of Aerospace Engineering, vol. 224, no. 4, pp. 489-497.

[81] Bjorndalen, D. F. (2010), Analysis and Modelling of Thin Skin Composite Pi-Section T-Joints with Tufting (unpublished MSc thesis), School of Engineering, Cranfield University, Cranfield, UK.

[82] Dell'Anno, G. (2007), Effect of tufting on the mechanical behaviour of carbon fabric/epoxy composites (unpublished PhD thesis), School of Applied Sciences, Cranfield University, Cranfield, UK.

[83] Hodgkinson, J. M. (ed.) (2000), Mechanical testing of advanced fibre composites, Woodhead Publishing, Cambridge.

[84] Ma, J., Qi, Q., Bayley, J., Du, X. S., Mo, M. S. and Zhang, L. Q. (2007), "Development of SENB toughness measurement for thermoset resins", Polymer Testing, vol. 26, no. 4, pp. 445-450.

[85] Dell'Anno, G., Cartié, D. D. R., Partridge, I. K. and Rezai, A. (2007), "Exploring mechanical property balance in tufted carbon fabric/epoxy composites", Composites Part A: Applied Science and Manufacturing, vol. 38, no. 11, pp. 2366-2373.

[86] Beier, U., Fischer, F., Sandler, J. K. W., Altstädt, V., Weimer, C. and Buchs, W. (2007), "Mechanical performance of carbon fibre-reinforced composites based on stitched preforms", Composites Part A: Applied Science and Manufacturing, vol. 38, no. 7, pp. 1655-1663.

[87] Wittig, J. (2002), "In-mold-reinforcement of preforms by 3-dimensional tufting", 47th International SAMPE Symposium and Exhibition, Vol. 47 II, 12 - 16 May, Long Beach, CA, pp. 1043.

[88] Preau, M. (2010), Manufacture and performance of tufted omega stiffenes composite structures (unpublished MSc thesis), School of Applied Sciences, Cranfield University, Cranfield, UK.

[89] Ogale, A. and Mitschang, P. (2007), "Compaction behavior of assembled fiber reinforced preforms", Journal of Industrial Textiles, vol. 37, no. 1, pp. 15-29.

[90] Koissin, V., Ruopp, A., Lomov, S. V., Verpoest, I., Witzel, V. and Drechsler, K. (2006), "On-surface fiber-free zones and irregularity of piercing pattern in structurally stitched NCF preforms", Advanced Composites Letters, vol. 15, no. 3, pp. 87-94.

[91] Dransfield, K. A., Jain, L. K. and Mai, Y. W. (1998), "On the effects of stitching in CFRPs - I. Mode I delamination toughness", Composites Science and Technology, vol. 58, no. 6, pp. 815-827.

[92] Jain, L. K., Dransfield, K. A. and Mai, Y. W. (1998), "On the effects of stitching in CFRPs - II. Mode II delamination toughness", Composites Science and Technology, vol. 58, no. 6, pp. 829-837.

[93] Stringer, L. and Hiley, M. (2003), "Through-thickness reinforcement of composites: stitching, Z-pinning and 3D weaving", Proc. 14th Int. Conf. Comp. Mats., 11 - 14 July, San Diego, California, USA.

[94] Larsson, F. (1997), "Damage tolerance of a stitched carbon/epoxy laminate", Composites Part A: Applied Science and Manufacturing, vol. 28, no. 11, pp. 923-934.

[95] Colin de Verdiere, M., Pickett, A. K., Skordos, A. A. and Witzel, V. (2009), "Evaluation of the mechanical and damage behaviour of tufted non crimped fabric composites using full field measurements", Composites Science and Technology, vol. 69, no. 2, pp. 131-138.

[96] Koissin, V., Kustermans, J., Lomov, S. V., Verpoest, I., Van Den Broucke, B. and Witzel, V. (2009), "Structurally stitched NCF preforms: Quasi-static response", Composites Science and Technology, vol. 69, no. 15-16, pp. 2701-2710.

[97] Koissin, V., Kustermans, J., Lomov, S. V., Verpoest, I., Nakai, H., Kurashiki, T., Hamada, K., Momoji, Y. and Zako, M. (2009), "Structurally stitched woven preforms: Experimental characterisation, geometrical modelling, and FE analysis", Plastics, Rubber and Composites, vol. 38, no. 2-4, pp. 98-105.

[98] Lomov, S. V., Belov, E. B., Bischoff, T., Ghosh, S. B., Truong Chi, T. and Verpoest, I. (2002), "Carbon composites based on multiaxial multiply stitched preforms. Part 1. Geometry of the preform", Composites Part A: Applied Science and Manufacturing, vol. 33, no. 9, pp. 1171-1183.

[99] Chun, H. J., Kim, H. W. and Byun, J. -. (2006), "Effects of through-the-thickness stitches on the elastic behavior of multi-axial warp knit fabric composites", Composite Structures, vol. 74, no. 4, pp. 484-494.

[100] Mouritz, A. P. (2004), "Fracture and tensile fatigue properties of stitched fibreglass composites", Proceedings of the Institution of Mechanical Engineers, Part L: Journal of Materials: Design and Applications, vol. 218, no. 2, pp. 87-93.

[101] Reeder, J. R. (1995), "Stitching vs. a toughened matrix: compression strength effects", Journal of Composite Materials, vol. 29, no. 18, pp. 2464-2487.

[102] Mouritz, A. P. (2008), "Tensile fatigue properties of 3D composites with through-thickness reinforcement", Composites Science and Technology, vol. 68, no. 12, pp. 2503-2510.

[103] Koissin, V., Ruopp, A., Lomov, S. V., Verpoest, I., Witzel, V. and Drechsler, K. (2006), "Internal structure of structurally stitched NCF preform", Proceedings of 12th European conference on composite materials (ECCM-12), 29 Aug - 01 Sep, Biarritz, France.

[104] Liotier, P. J., Alain, V. and Christine, D. (2010), "Characterization of 3D morphology and microcracks in composites reinforced by multi-axial multi-ply stitched preforms", Composites Part A: Applied Science and Manufacturing, vol. 41, no. 5, pp. 653-662.

[105] Farley, G. L. and Dickinson, L. C. (1992), "Mechanical response of composite materials with through-the-thickness reinforcement", FIBER-TEX, pp. 123-143.

[106] Shim, S. B., Ahn, K., Seferis, J. C., Berg, A. J. and Hudson, W. (1995), "Cracks and microcracks in stitched structural composites manufactured with resin film infusion process", Journal of Advanced Materials, vol. 26, no. 4, pp. 48-62.

[107] Sweeting, R. D. and Thomson, R. S. (2004), "The effect of thermal mismatch on Z-pinned laminated composite structures", Composite Structures, vol. 66, no. 1-4, pp. 189-195.

[108] Farley, G. L. (1992), "Mechanism responsible for reducing compression strength of through-the-thickness reinforced composite material", Journal of Composite Materials, vol. 26, no. 12, pp. 1784-1795.

[109] Cann, M. T., Adams, D. O. and Schneider, C. L. (2008), "Characterization of fiber volume fraction gradients in composite laminates", Journal of Composite Materials, vol. 42, no. 5, pp. 447-466.

[110] Mouritz, A. P., Baini, C. and Herszberg, I. (1999), "Mode I interlaminar fracture toughness properties of advanced textile fibreglass composites", Composites Part A: Applied Science and Manufacturing, vol. 30, no. 7, pp. 859-870.

[111] Chen, L., Sankar, B. V. and Ifju, P. G. (2001), "Mode II fracture toughness of stitched composites", 42nd AIAA/ASME/ASCE/AHS/ASC Structures, Structural Dynamics, and Materials Conference and Exhibit Technical Papers, Vol. 3, 16 - 19 April, Seattle, WA, pp. 2253.

[112] Iwahori, Y., Ishikawa, T., Watanabe, N., Ito, A., Hayashi, Y. and Sugimoto, S. (2007), "Experimental investigation of interlaminar mechanical properties on carbon fiber stitched CFRP laminates", Advanced Composite Materials: The Official Journal of the Japan Society of Composite Materials, vol. 16, no. 2, pp. 95-113.

[113] Plain, K. P. and Tong, L. (2009), "Traction law for inclined through-thickness reinforcement using a geometrical approach", Composite Structures, vol. 88, no. 4, pp. 558-569.

[114] Dantuluri, V., Maiti, S., Geubelle, P. H., Patel, R. and Kilic, H. (2007), "Cohesive modeling of delamination in Z-pin reinforced composite laminates", Composites Science and Technology, vol. 67, no. 3-4, pp. 616-631.

[115] Liu, H. Y., Yan, W. and Mai, Y. W. (2003), "Z-pin bridging force in composite delamination", in Blackman, B. R. K., Pavan, A. and Williams, J. G. (eds.) European Structural Integrity Society, Elsevier, pp. 491-502.

[116] Jain, L. K. and Mai, Y. W. (1994), "Analysis of stitched laminated ENF specimens for interlaminar mode II fracture toughness", International Journal of Fracture, vol. 68, no. 3, pp. 219-244.

[117] Massabò, R., Mumm, D. R. and Cox, B. N. (1998), "Characterizing mode II delamination cracks in stitched composites", International Journal of Fracture, vol. 92, no. 1, pp. 1-38.

[118] Grassi, M. and Zhang, X. (2003), "Finite element analyses of mode I interlaminar delamination in z-fibre reinforced composite laminates", Composites Science and Technology, vol. 63, no. 12, pp. 1815-1832.

[119] Yoshimura, A., Yashiro, S., Okabe, T. and Takeda, N. (2007), "Characterization of tensile damage progress in stitched CFRP laminates", Advanced Composite Materials: The Official Journal of the Japan Society of Composite Materials, vol. 16, no. 3, pp. 223-244.

[120] Beier, U., Sandler, J. K. W., Altstädt, V., Spanner, H. and Weimer, C. (2009), "Mechanical performance of carbon fibre-reinforced composites based on stitched and bindered preforms", Composites Part A: Applied Science and Manufacturing, vol. 40, no. 11, pp. 1756-1763.

[121] Kang, T. J. and Lee, S. H. (1994), "Effect of stitching on the mechanical and impact properties of woven laminate composite", Journal of Composite Materials, vol. 28, no. 16, pp. 1574-1587.

[122] Kamiya, R. and Chou, T. W. (2000), "Strength and failure behavior of stitched carbon/epoxy composites", Metallurgical and Materials Transactions A: Physical Metallurgy and Materials Science, vol. 31, no. 3, pp. 899-909.

[123] Pang, F., Wang, C. H. and Bathgate, R. G. (1997), "Creep response of woven-fibre composites and the effect of stitching", Composites Science and Technology, vol. 57, no. 1, pp. 91-98.

[124] Aymerich, F., Priolo, P. and Sun, C. T. (2003), "Static and fatigue behaviour of stitched graphite/epoxy composite laminates", Composites Science and Technology, vol. 63, no. 6, pp. 907-917.

[125] Piggott, M. R. (1995), "The effect of fibre waviness on the mechanical properties of unidirectional fibre composites: A review", Composites Science and Technology, vol. 53, no. 2, pp. 201-205.

[126] Heß, H. and Himmel, N. (2010), "Structurally Stitched NCF CFRP Laminates. Part 1: Experimental Characterization of In-Plane and Out-of-Plane Properties", Composites Science and Technology, currently in press.

[127] Yang, B., Kozey, V., Adanur, S. and Kumar, S. (2000), "Bending, compression, and shear behavior of woven glass fiber–epoxy composites", Composites Part B: Engineering, vol. 31, no. 8, pp. 715-721.

[128] Mouritz, A. P. (1996), "Flexural properties of stitched GRP laminates", Composites Part A: Applied Science and Manufacturing, vol. 27, no. 7, pp. 525-530.

[129] Ladevéze, P. and Le Dantec, E. (1992), "Damage modelling of the elementary ply for laminated composites", Composites Science and Technology, vol. 43, no. 3, pp. 257-267.

[130] Pickett, A. K. and Fouinneteau, M. R. C. (2006), "Material characterisation and calibration of a meso-mechanical damage model for braid reinforced composites", Composites Part A: Applied Science and Manufacturing, vol. 37, no. 2, pp. 368-377.

[131] Greve, L. and Pickett, A. K. (2006), "Modelling damage and failure in carbon/epoxy non-crimp fabric composites including effects of fabric pre-shear", Composites Part A: Applied Science and Manufacturing, vol. 37, no. 11, pp. 1983-2001.

[132] Mattsson, D., Joffe, R. and Varna, J. (2007), "Methodology for characterization of internal structure parameters governing performance in NCF composites", Composites Part B: Engineering, vol. 38, no. 1, pp. 44-57.

[133] Treiber, J. W. G., Cartié, D. D. R. and Partridge, I. K. (2011), "Effects of mesostructure on the in-plane properties of tufted carbon fabric composites", 5th International Conference on Composites Testing and Model Identification, 14-16 Feb., Lausanne, Switzerland.

[134] Drago, A. and Pindera, M. J. (2007), "Micro-macromechanical analysis of heterogeneous materials: Macroscopically homogeneous vs periodic microstructures", Composites Science and Technology, vol. 67, no. 6, pp. 1243-1263.

[135] Ishikawa, T. and Chou, T. W. (1983), "One-dimensional micromechanical analysis of woven fabric composites", AIAA Journal, vol. 21, no. 12, pp. 1714-1721.

[136] Scida, D., Aboura, Z., Benzeggagh, M. L. and Bocherens, E. (1999), "A micromechanics model for 3D elasticity and failure of woven-fibre composite materials", Composites Science and Technology, vol. 59, no. 4, pp. 505-517.

[137] Scida, D., Aboura, Z., Benzeggagh, M. L. and Bocherens, E. (1998), "Prediction of the elastic behaviour of hybrid and non-hybrid woven composites", Composites Science and Technology, vol. 57, no. 12, pp. 1727-1740.

[138] Donadon, M. V., Falzon, B. G., Iannucci, L. and Hodgkinson, J. M. (2007), "A 3-D micromechanical model for predicting the elastic behaviour of woven laminates", Composites Science and Technology, vol. 67, no. 11-12, pp. 2467-2477.

[139] Naik, N. K. and Shembekar, P. S. (1992), "Elastic behavior of woven fabric composites: I-lamina analysis", Journal of Composite Materials, vol. 26, no. 15, pp. 2196-2225.

[140] Shembekar, P. S. and Naik, N. K. (1992), "Elastic behavior of woven fabric composites: II-laminate analysis", Journal of Composite Materials, vol. 26, no. 15, pp. 2226-2246.

[141] Tan, P., Tong, L. and Steven, G. P. (1997), "Modelling for predicting the mechanical properties of textile composites—A review", Composites Part A: Applied Science and Manufacturing, vol. 28, no. 11, pp. 903-922.

[142] Onal, L. and Adanur, S. (2007), "Modeling of elastic, thermal, and strength/failure analysis of two-dimensional woven composites - A review", Applied Mechanics Reviews, vol. 60, no. 1-6, pp. 37-50.

[143] Junqian, Z. and Yuqing, W. (2007), "A predictive approach to the in-plane mechanical properties of stitched composite laminates", Acta Mechanica Solida Sinica, vol. 20, no. 2, pp. 130-140.

[144] Li, X. K. and Bai, S. L. (2010), "Tensile properties of multilayered biaxial weft knitted fabric reinforced composite material", Plastics, Rubber and Composites, vol. 39, no. 2, pp. 91-98.

[145] Barbero, E. J., Trovillion, J., Mayugo, J. A. and Sikkil, K. K. (2006), "Finite element modeling of plain weave fabrics from photomicrograph measurements", Composite Structures, vol. 73, no. 1, pp. 41-52.

[146] Barbero, E. J., Lonetti, P. and Sikkil, K. K. (2006), "Finite element continuum damage modeling of plain weave reinforced composites", Composites Part B: Engineering, vol. 37, no. 2-3, pp. 137-147.

[147] González, A., Graciani, E. and París, F. (2008), "Prediction of in-plane stiffness properties of non-crimp fabric laminates by means of 3D finite element analysis", Composites Science and Technology, vol. 68, no. 1, pp. 121-131.

[148] Drapier, S. and Wisnom, M. R. (1999), "Finite-element investigation of the compressive strength of non-crimp-fabric-based composites", Composites Science and Technology, vol. 59, no. 8, pp. 1287-1297.

[149] Drapier, S. and Wisnom, M. R. (1999), "A finite-element investigation of the interlaminar shear behaviour of non-crimp-fabric-based composites", Composites Science and Technology, vol. 59, no. 16, pp. 2351-2362.

[150] Zhao, L. G., Warrior, N. A. and Long, A. C. (2006), "Finite element modelling of damage progression in non-crimp fabric reinforced composites", Composites Science and Technology, vol. 66, no. 1, pp. 36-50.

[151] Ernst, G., Vogler, M., Hühne, C. and Rolfes, R. (2010), "Multiscale progressive failure analysis of textile composites", Composites Science and Technology, vol. 70, no. 1, pp. 61-72.

[152] Lomov, S. V., Ivanov, I., Verpoest, I., Zako, M., Kurashiki, T., Nakai, H. and Hirosawa, S. (2007), "Meso-FE modelling of textile composites: Road map, data flow and algorithms", Composites Science and Technology, vol. 67, no. 9, pp. 1870-1891.

[153] Verpoest, I. and Lomov, S. V. (2005), "Virtual textile composites software WiseTex: Integration with micro-mechanical, permeability and structural analysis", Composites Science and Technology, vol. 65, no. 15-16 SPEC. ISS., pp. 2563-2574.

[154] Lomov, S. V. and Verpoest, I. (2003), "WiseTex - Virtual textile reinforcement software", Proceedings of the 48th International SAMPE Symposium and Exhibition, Vol. 48 II, pp. 1320.

[155] Grassi, M. (2004), Numerical modelling of composite laminates with through-thickness-reinforcements (unpublished PhD thesis), School of Engineering, Cranfield University, Cranfield, UK.

[156] Grassi, M., Zhang, X. and Meo, M. (2002), "Prediction of stiffness and stresses in z-fibre reinforced composite laminates", Composites Part A: Applied Science and Manufacturing, vol. 33, no. 12, pp. 1653-1664.

[157] Dickinson, L. C., Farley, G. L. and Hinders, M. K. (1999), "Prediction of effective three-dimensional elastic constants of translaminar reinforced composites", Journal of Composite Materials, vol. 33, no. 11, pp. 1002-1029.

[158] Heß, H. and Himmel, N. (2010), "Structurally Stitched NCF CFRP Laminates. Part 2: Finite Element Unit Cell Based Prediction of In-Plane Strength", Composites Science and Technology, currently in press.

[159] Heß, H., Roth, Y. C. and Himmel, N. (2007), "Elastic constants estimation of stitched NCF CFRP laminates based on a finite element unit-cell model", Composites Science and Technology, vol. 67, no. 6, pp. 1081-1095.

[160] Gunnion, A. J., Scott, M. L., Thomson, R. S. and Hachenberg, D. (2002), "A linear 3-D finite element unit cell model for fibre waviness in composite materials", Proceedings of the 23rd Congress of the International Council of the Aeronautical Sciences (ICAS 2002), pp. 313.1-313.10.

[161] Huang, H. and Waas, A. M. (2009), "Compressive response of Z-pinned woven glass fiber textile composite laminates: Modeling and computations", Composites Science and Technology, vol. 69, no. 14, pp. 2338-2344.

[162] Huang, H. J. and Waas, A. M. (2009), "Modeling and predicting the compression strength limiting mechanisms in Z-pinned textile composites", Composites Part B: Engineering, vol. 40, no. 6, pp. 530-539.

[163] Summerscales, J. and Russell, P. M. (2004), "Observations on the fibre distribution and fibre strain in a woven fabric reinforcement", Advanced Composites Letters, vol. 13, no. 3, pp. 135-140.

[164] Halpin, J. C. and Kardos, J. L. (1976), "HALPIN-TSAI EQUATIONS: A REVIEW.", Polymer Engineering and Science, vol. 16, no. 5, pp. 344-352.

[165] Huang, Z. M. (2001), "Simulation of the mechanical properties of fibrous composites by the bridging micromechanics model", Composites Part A: Applied Science and Manufacturing, vol. 32, no. 2, pp. 143-172.

[166] Carvelli, V. and Poggi, C. (2001), "A homogenization procedure for the numerical analysis of woven fabric composites", Composites Part A: Applied Science and Manufacturing, vol. 32, no. 10, pp. 1425-1432.

[167] Zhao, L. G., Warrior, N. A. and Long, A. C. (2006), "A micromechanical study of residual stress and its effect on transverse failure in polymer-matrix composites", International Journal of Solids and Structures, vol. 43, no. 18-19, pp. 5449-5467.

[168] Chamis, C. C. (1983), "Simplified composite micromechanics equations for hygral, thermal and mechanical properties", NASA TM-83320.

[169] Rosen, B. W. (1965), "Mechanics of composite strengthening", Fiber Composite Materials, pp. 37-75.

[170] Aboudi, J. (1988), "Micromechanical analysis of the strength of unidirectional fiber composites", Composites Science and Technology, vol. 33, no. 2, pp. 79-96.

[171] Chamis, C. C. (1984), "Simplified composite micromechanics equations for strength, fracture toughness, impact resistance and environmental effects", S.A.M.P.E.quarterly, vol. 15, no. 4, pp. 41-55.

[172] Kwon, Y. W. and Berner, J. M. (1995), "Micromechanics model for damage and failure analyses of laminated fibrous composites", Engineering Fracture Mechanics, vol. 52, no. 2, pp. 231-242.

[173] Mikhaluk, D. S., Truong, T. C., Borovkov, A. I., Lomov, S. V. and Verpoest, I. (2008), "Experimental observations and finite element modelling of damage initiation and evolution in carbon/epoxy non-crimp fabric composites", Engineering Fracture Mechanics, vol. 75, no. 9, pp. 2751-2766.

[174] Orifici, A. C., Herszberg, I. and Thomson, R. S. (2008), "Review of methodologies for composite material modelling incorporating failure", Composite Structures, vol. 86, no. 1-3, pp. 194-210.

[175] Hinton, M. J., Kaddour, A. S. and Soden, P. D. (2004), Failure criteria in fibre reinforced polymer composites: The World-Wide Failure Exercise, Elsevier, Amsterdam.

[176] Soden, P. D., Hinton, M. J. and Kaddour, A. S. (1998), "A comparison of the predictive capabilities of current failure theories for composite laminates", Composites Science and Technology, vol. 58, no. 7, pp. 1225-1254.

[177] Tsai, S. W. and Wu, E. M. (1971), "General theory of strength for anisotropic materials", Journal of Composite Materials, vol. 5, pp. 58-80.

[178] Puck, A. and Schürmann, H. (2002), "Failure analysis of FRP laminates by means of physically based phenomenological models", Composites Science and Technology, vol. 62, no. 12-13 SPECIAL ISSUE, pp. 1633-1662.

[179] Puck, A. and Schürmann, H. (1998), "Failure analysis of FRP laminates by means of physically based phenomenological models", Composites Science and Technology, vol. 58, no. 7, pp. 1045-1067.

[180] Puck, A., Kopp, J. and Knops, M. (2002), "Guidelines for the determination of the parameters in Puck's action plane strength criterion", Composites Science and Technology, vol. 62, no. 3, pp. 371-378.

[181] Knops, M. (2008), Analysis of Failure in Fiber Polymer laminates: The Theory of Alfred Puck, Springer, Berlin.

[182] Schuecker, C. and Pettermann, H. E. (2008), "Fiber reinforced laminates: Progressive damage modeling based on failure mechanisms", Archives of Computational Methods in Engineering, vol. 15, no. 2, pp. 163-184.

[183] Sun, C. T. and Tao, J. (1998), "Prediction of failure envelopes and stress/strain behaviour of composite laminates", Composites Science and Technology, vol. 58, no. 7, pp. 1125-1136.

[184] Knops, M. and Bögle, C. (2006), "Gradual failure in fibre/polymer laminates", Composites Science and Technology, vol. 66, no. 5, pp. 616-625.

[185] Sun, C. T. and Vaidya, R. S. (1996), "Prediction of composite properties from a representative volume element", Composites Science and Technology, vol. 56, no. 2, pp. 171-179.

[186] Mouritz, A. P. and Jain, L. K. (1999), "Further validation of the Jain and Mai models for interlaminar fracture of stitched composites", Composites Science and Technology, vol. 59, no. 11, pp. 1653-1662.

[187] Colin de Verdiere, M., Pickett, A. K., Skordos, A. A. and Witzel, V. (2008), "Evaluation of the mechanical and damage behaviour of tufted non crimped fabric composites using full field measurements", Composites Science and Technology, vol. 69, no. 2 pp. 131-139.

[188] Brunner, A. J. (2000), "Experimental aspects of Mode I and Mode II fracture toughness testing of fibre-reinforced polymer-matrix composites", Computer Methods in Applied Mechanics and Engineering, vol. 185, no. 2-4, pp. 161-172.

[189] Jain, L. K., Dransfield, K. A. and Mai, Y. W. (1998), "Effect of reinforcing tabs on the mode I delamination toughness of stitched CFRPs", Journal of Composite Materials, vol. 32, no. 22, pp. 2016-2041.

[190] ESIS TC4 (2008), Fibre-composites - The determination of the mode II fracture resistance, GIIC, of unidirectional fibre-composites using the calibrated end loaded split (C-ELS) test and an effective crack length approach.

[191] Blackman, B. R. K., Brunner, A. J. and Williams, J. G. (2006), "Mode II fracture testing of composites: a new look at an old problem", Engineering Fracture Mechanics, vol. 73, no. 16, pp. 2443-2455.

[192] Robinson, P. and Das, S. (2004), "Mode I DCB testing of composite laminates reinforced with z-direction pins: A simple model for the investigation of data reduction strategies", Engineering Fracture Mechanics, vol. 71, no. 3, pp. 345-364.

[193] Cartié, D. D. R., Laffaille, J. M., Partridge, I. K. and Brunner, A. J. (2009), "Fatigue delamination behaviour of unidirectional carbon fibre/epoxy laminates reinforced by Z-Fiber® pinning", Engineering Fracture Mechanics, vol. 76, no. 18, pp. 2834-2845.

[194] He, M. and Cox, B. N. (1998), "Crack bridging by through-thickness reinforcement in delaminating curved structures", Composites Part A: Applied Science and Manufacturing, vol. 29, no. 4, pp. 377-393.

[195] Cox, B. N. (1999), "A constitutive model for through-thickness reinforcement bridging a delamination crack", Advanced Composites Letters, vol. 8, no. 5, pp. 249-256.

[196] Blackman, B. R. K., Kinloch, A. J. and Paraschi, M. (2005), "The determination of the mode II adhesive fracture resistance, GIIC, of structural adhesive joints: an effective crack length approach", Engineering Fracture Mechanics, vol. 72, no. 6, pp. 877-897.

[197] Cox, B. N. (2005), "Snubbing effects in the pullout of a fibrous rod from a laminate", Mechanics of Advanced Materials and Structures, vol. 12, no. 2, pp. 85-98.

[198] Tanzawa, Y., Watanabe, N. and Ishikawa, T. (1999), "Interlaminar fracture toughness of 3-D orthogonal interlocked fabric composites", Composites Science and Technology, vol. 59, no. 8, pp. 1261-1270.

[199] Massabò, R. and Cox, B. N. (1999), "Concepts for bridged Mode II delamination cracks", Journal of the Mechanics and Physics of Solids, vol. 47, no. 6, pp. 1265-1300.

[200] Massabò, R. and Cox, B. N. (2001), "Unusual characteristics of mixed-mode delamination fracture in the presence of large-scale bridging", Mechanics of Composite Materials and Structures, vol. 8, no. 1, pp. 61-80.

[201] Cox, B. N., Massabò, R., Mumm, D. R., Turrettini, A. and Kedward, K. T. (1997), "Delamination fracture in the presence of through-thickness reinforcement", Proc. 11th Int. Conf. Composite Materials, 14 – 18 July, Gold Coast, Australia, pp. 159-177.

[202] Aveston, J., Cooper, G. A. and Kelly, A. (1971), "Single and multiple fracture. The properties of fiber composites ", Proc. The Properties of Fibre Composites, pp. 15-26.

[203] Yan, W., Liu, H. Y. and Mai, Y. W. (2003), "Numerical study on the mode I delamination toughness of z-pinned laminates", Composites Science and Technology, vol. 63, no. 10, pp. 1481-1493.

[204] Yan, W., Liu, H. Y. and Mai, Y. W. (2004), "Mode II delamination toughness of z-pinned laminates", Composites Science and Technology, vol. 64, no. 13-14, pp. 1937-1945.

[205] Sonik, V. and Sankar, B. V. (1996), "Modeling the effects of translaminar reinforcements on mode II fracture toughness", in Lavine, A. S., Chandra, U., Chen, M. M., et al (eds.), Proceedings of the 1996 ASME International Mechanical Engineering Congress and Exposition, Vol. 52, 17 - 22 November, Atlanta, GA, USA, pp. 61.

[206] Dai, S. C., Yan, W., Liu, H. Y. and Mai, Y. W. (2004), "Experimental study on z-pin bridging law by pullout test", Composites Science and Technology, vol. 64, no. 16, pp. 2451-2457.

[207] Iwahori, Y., Nakane, K. and Watanabe, N. (2009), "DCB test simulation of stitched CFRP laminates using interlaminar tension test results", Composites Science and Technology, vol. 69, no. 14, pp. 2315-2322.

[208] Tan, K. T., Watanabe, N. and Iwahori, Y. (2010), "Experimental investigation of bridging law for single stitch fibre using Interlaminar tension test", Composite Structures, vol. 92, no. 6, pp. 1399-1409.

[209] Dransfield, K. A., Bader, M. G., Baillie, C. and Mai, Y. W. (1995), "On a novel test for determining the matrix-thread bond strength in stitched carbon fibre composites", Proceedings of 10th International conference on composite materials (ICCM-10), 14–18 August, Vancouver, Canada.

[210] Plain, K. P. and Tong, L. (2009), "Experimental validation of theoretical traction law for inclined through-thickness reinforcement", Composite Structures, vol. 91, no. 2, pp. 148-157.

[211] Chen, L., Ifju, P. G. and Sankar, B. V. (2005), "Analysis of mode I and mode II tests for composites with translaminar reinforcements", Journal of Composite Materials, vol. 39, no. 15, pp. 1311-1333.

[212] Cox, B. N. and Sridhar, N. (2002), "A traction law for inclined fibre tows bridging mixed mode cracks", Mechanics of Advanced Materials and Structures, vol. 9, pp. 229-331.

[213] Jain, L. K. and Mai, Y. W. (1994), "On the effect of stitching on mode I delamination toughness of laminated composites", Composites Science and Technology, vol. 51, no. 3, pp. 331-345.

[214] Jain, L. K. and Mai, Y. W. (1995), "Determination of mode II delamination toughness of stitched laminated composites", Composites Science and Technology, vol. 55, no. 3, pp. 241-253.

[215] Cox, B. N. (1999), "Constitutive model for a fiber tow bridging a delamination crack", Mechanics of Composite Materials and Structures, vol. 6, no. 2, pp. 117-138.

[216] Tong, L. and Sun, X. (2004), "Bending effect of through-thickness reinforcement rods on mode I delamination toughness of DCB specimen. I. Linearly elastic and rigid-perfectly plastic models", International Journal of Solids and Structures, vol. 41, no. 24-25, pp. 6831-6852.

[217] Jain, L. K. and Mai, Y. W. (1994), "Mode I delamination toughness of laminated composites with through-thickness reinforcement", Applied Composite Materials, vol. 1, no. 1, pp. 1-17.

[218] Byrd, L. W. and Birman, V. (2006), "Effectiveness of z-pins in preventing delamination of co-cured composite joints on the example of a double cantilever test", Composites Part B: Engineering, vol. 37, no. 4-5, pp. 365-378.

[219] Mouritz, A. P. and Jain, L. K. (1997), "Interlaminar fracture properties of stitched fibreglass composites", Proc. 11th Int. Conf. Composite Materials, 14 – 18 July, Gold Coast, Australia, pp. V116-V127.

Appendix A - Robotic tufting programme

The following appendix presents the code for robotic tufting with KSL KL 150 tufting head mounted to a Kawasaki F20N six axis robot arm, adapted from the initial design of Dell'Anno and modified according to Chapter 4. The programme is written in the simple AS robot programming language. All necessary parameters are requested by the programme prior to tufting via the user interface software KCWin. By including input verification and both software and physical limits the programme is designed to allow easy setup and safe operation of the tufting equipment with sufficient range for individual adaptation depending on the required tufting zone. The tufting programme is started by entering the command '*execute tufting'* into the KCWin command window.

At setup the operator is required to move the robot arm manually to the origin of the tufting arrangement. With the needle in the upper most position, the tufting foot is supposed to be lowered onto the preform surface until the spring element starts to compress and apply an initial compaction pressure on the dry preform. The programme automatically stores the defined start position in the controller memory, enabling the operator to recall the position for batch production or restart of the manufacturing process after an unscheduled stop. As the robot arm moves in a fixed global coordinate system without feedback of the relative distance between foot element and the preform surface, precise alignment of table, support and preform to the robot coordinate system must be ensured.

Due to the potentially high tufting speed and inertial mass of the rotating system it was found disadvantageous to stop the tufting process directly if the tufting thread ruptured. Instead, it was preferred to thread the needle after completion of the according tuft row, although the re-tufting contributes potentially further to local fabric damage by the tufting needle. Based on the row count and saved start position the omitted row can be re-tufted after completion of the full tufting routine. Acceleration and deceleration commands were implemented to reduce the inertial load of the rotating system on the drive components of the tufting head at start and finish of each tufting row.

Main programme *tufting*

```
.PROGRAM tufting()
        CALL sp_reset
```

```
        OUTSPEED 0
        FLOWRATE OFF
        SIGNAL -33,-35,-36,-38,-40
        TOOL tuftheadu
        WEIGHT 15
        ACCEL 100 ALWAYS
        DECEL 100 ALWAYS
        ACCURACY 0.5 ALWAYS
        SPEED 200 MM/S ALWAYS
        ALIGN
        ONI -1034 CALL sp_safetypos,100
        ALIGN
        needoff = 35
        PRINT "  ROBOTIC TUFTING PROGRAM"
        PRINT "  revised by   J. Treiber"
        PRINT "  Last update: 10/08/2010"
        PRINT " "
        PRINT "_____________ Main Menu _____________"
        PRINT " "
200     PRINT "Please choose an option from the following list:"
        PRINT "1 - Tufting a row along the X axis"
        PRINT "2 - Tufting a row along the Y axis"
        PRINT "3 - Tufting a rectangular area with rows parallel to x-axis"
        PRINT "4 - Tufting an angled row along X axis"
        PROMPT "Option:",main
        CASE main OF
        VALUE 1:
        CALL sp_needleup
        CALL sp_startpoint
        CALL sp_tuftxline
        VALUE 2:
        CALL sp_needleup
        ACCEL 0.1
        DRAW ,,,,,90
        BREAK
        CALL sp_startpoint
        CALL sp_tuftyline
        VALUE 3:
        CALL sp_needleup
        CALL sp_startpoint
        CALL sp_tuftmove
        VALUE 4:
        CALL sp_needleup
        CALL sp_anglex
        CALL sp_startpoint
        CALL sp_tuftxangline
```

```
        ANY :
        PRINT "The option has not been recognised. Enter again."
        GOTO 200
        END
.END
```

Subrouting *sp_reset*

```
.PROGRAM sp_reset()
        anglex = 0
        pos = 0
        lift = 0
        stitchspace = 0
        maxrps = 0
        maxtuftspeed = 0
        decision = 0
        decision1 = 0
        distx = 0
        disty = 0
        posneed = 0
        linespace = 0
        linestart = 0
        st = 0
        tuftend = 0
        maxline = 0
        counter = 0
        lcounter = 0
        lineno = 0
        posneedd = 0
        spot = 0
        maxcycles = 0
        main = 0
        min = 0
        sec = 0
        dur = 0
        pat = 0
        maxtmod = 0
        tuftingspeed = 0
        perctsp = 0
        patcorr = 0
.END
```

Subrouting *sp_safetypos*

```
.PROGRAM sp_safetypos()
```

```
        SPEED 200 MM/S ALWAYS
        OUTSPEED 0
        OUTDA 0,1; cease voltage supply to tufting head
        SIGNAL -33,34,-35,-36
        PRINT "Programme execution was stopped by emergence button."
        PRINT "Check for any error condition before restart of programme execution"
        HALT
.END
```

Subrouting *sp_check*

```
.PROGRAM sp_check()
        PRINT " "
        PRINT "_____________ Final Check _____________"
        PRINT " "
        PRINT "Make sure the foam support under the fabric is thick enough."
        PRINT "Make sure the fabric is clamped flat on the tufting table in the XY
        plane."
        PRINT " "
        PRINT /S,"When ready, "
        PRINT "press CYCLE START on the control panel or enter CONTINUE to start
        tufting."
        PAUSE
.END
```

Subrouting *sp_needledown*

```
.PROGRAM sp_needledown()
        HERE posneed
        TWAIT 1
        maxtmod = 0.1*maxtuftspeed
        ONI -1033 GOTO 110
        OUTSPEED
        SIGNAL 33
        ACCEL 0.2
        TDRAW 50,,,,,,maxtmod MM/S
        BREAK
110     BRAKE
        SIGNAL -33
        OUTSPEED 0
        IGNORE 1033
        HERE posneedd
        DECOMPOSE t[1] = posneedd
.END
```

Subrouting *sp_needleup*

```
.PROGRAM sp_needleup()
        PRINT " "
        PRINT "...moving the needle to the uppermost position..."
        PRINT " "
        HERE posneed
        TWAIT 3
        tuftspeed = 500/20
        maxtmod = 0.1*tuftspeed
        SPEED 30 MM/S ALWAYS
        SETOUTSIG 3000,8,1
        SETOUTSPEED 0,tuftspeed,10,0
        OUTSPEED
        SIGNAL -33,-34,35
        OUTSPEED 0
        ONI 1033 GOTO 110
        OUTSPEED
        SIGNAL 33
        ACCEL 0.2
        TDRAW 50,,,,,,maxtmod MM/S
        BREAK
110     BRAKE
        SIGNAL -33,34,-35
        OUTSPEED 0
        IGNORE 1033
        BREAK
        LMOVE posneed
        BREAK
        SPEED 30 MM/S ALWAYS
        PRINT "Done."
.END
```

Subrouting *sp_startpoint*

```
.PROGRAM sp_startpoint()
        PRINT " "
        PRINT "_____________ Definition of Startpoint _____________ "
        PRINT " "
        PRINT /S,"A starting position and needle penetration depth "
        PRINT /S,"are already stored in memory, you can use these settings "
        PRINT "or define new ones."
102     PRINT /S,"Do you want to define new starting position/needle "
        PROMPT "penetration depth? (yes=1 no=0)",pos
        CASE pos OF
```

```
        VALUE 0:
        PRINT " "
        PRINT "...moving the robot to the starting position..."
        PRINT " "
        LMOVE starttuft
        BREAK
        PRINT "Done."
        GOTO 106
        VALUE 1:
        GOTO 104
        ANY :
        GOTO 102
        END
104     PRINT " "
        PRINT "Set needle penetration depth using the wheel on the tufting head."
        PRINT /S,"Put the head in the position you want to start tufting from "
        PRINT "with the needle in  the upmost position."
        PRINT "The needle foot must just touch the fabric."
        PRINT /S,"When finished enter CONTINUE NEXT to continue (not just CON-
        TINUE"
        PRINT "or CYCLE START!!!)."
        PAUSE
        BRAKE
        BREAK
        lift = needoff
        LDEPART lift
        BREAK
        HERE starttuft
106     PRINT " "
        PRINT /S,"The robot will start tufting from the present position."
        PROMPT "Do you want to keep such settings? (yes=1 no=0)",decision
        CASE decision OF
        VALUE 0:
        GOTO 102
        VALUE 1:
        GOTO 108
        ANY :
        GOTO 106
108     END
.END
```

Subrouting *sp_threadcut*

```
.PROGRAM sp_threadcut()
        TWAIT 1
```

```
        LDEPART needoff
        BREAK
        PRINT " "
        PRINT "_____________ Tufting Finish _____________ "
        PRINT " "
        PRINT "Tufting finished, cut thread manually!"
        PRINT " "
        PRINT /S,"When cut, press CYCLE START on the controller panel"
        PRINT "or enter CONTINUE to return tufting head to starting point."
        PAUSE
        time = TIMER(1)
        min = INT(time/60)
        sec = INT(time-(min*60))
        PRINT " "
        PRINT "Task completed in ",min," minutes and ",sec," seconds."
.END
```

Subrouting *sp_tuftxline*

```
.PROGRAM sp_tuftxline()
120     PRINT " "
        PRINT "_____________ Definition of Tufting Pattern _____________"
        PRINT " "
        PRINT "    ->| |<- tuft spacing"
        PRINT "       | |"
        PRINT "  .-.-.-.-.-.-.-.-.-< SP   <-- (+) x-axis"
        PRINT " |                   |"
        PRINT " |< row length >|"
        PRINT " "
        PRINT "Enter the tuft spacing between each tuft along"
        PROMPT "the x-axis (in mm, max.10).",stitchspace
        IF stitchspace>10 OR stitchspace<0 THEN
        PRINT "VALUE ABOVE or BELOW LIMITS. Please enter again."
        GOTO 120
        END
        maxrps = 500/60
        tuftspeed = maxrps*stitchspace
121     PRINT " "
        PRINT "Enter the total tuft row length"
        PROMPT " along the x-axis (in mm, max. 900mm).",distx
        IF distx>900 OR distx<0 THEN
        PRINT "Distance above or below limits. Please enter again."
        GOTO 121
        END
        tuftno = distx/stitchspace
```

```
        maxtuftno = INT(tuftno)+1
        PRINT " "
        PRINT "Tuft spacing: ",(stitchspace)," mm, total row length: ",(distx)," mm."
        PRINT "--> Tufts per tuft row:",(maxtuftno)," "
        PRINT " "
        PROMPT "Do you want to keep these settings? (yes=1 no=0)?",decision1
        CASE decision1 OF
        VALUE 0:
        GOTO 120
        VALUE 1:
        GOTO 122
        any:
        GOTO 121
        END
122     PRINT " "
        PRINT "_____________ Definition of Tufting Speed _____________ "
        PRINT " "
        PRINT "Enter the tufting speed"
        PRINT "(as % value of the max. absolute tufting speed v= ",(tuftspeed)," mm/s,
        in general 80%)"
        PROMPT "(between 5 ... 100 %):",perctsp
        IF perctsp>100 OR perctsp<5 THEN
        PRINT "Speed above or below limits. Please enter again."
        GOTO 122
        END
        maxtuftspeed = tuftspeed*perctsp/100
        SPEED maxtuftspeed MM/S ALWAYS
        SETOUTSIG 3000,8,1
        SETOUTSPEED 0,tuftspeed,10,0
        OUTSPEED
        SIGNAL -33,-34,35
        OUTSPEED 0
        PRINT " "
        PRINT "...moving the needle to the lowest position..."
        CALL sp_needledown
        LMOVE posneed
        BREAK
124     DECOMPOSE s[1] = starttuft
        POINT tuftend = TRANS(s[1]+distx,s[2],s[3]-needoff,s[4],s[5],s[6])
        CALL sp_check
        PRINT " "
        PRINT "_____________ Tufting Start _____________ "
        PRINT " "
        TIMER 1 = 0
        TWAIT 5
        SIGNAL 33
```

```
        LAPPRO starttuft,-needoff
        BREAK
        SIGNAL -33
        TWAIT 2
        OUTSPEED
        SIGNAL 33
        TWAIT 0.2
        ACCEL 0.4
        DECEL 0.4
        LMOVE tuftend
        BREAK
        SIGNAL -33
        OUTSPEED 0
        CALL sp_needledown
        OUTSPEED
        SIGNAL -33,34,-35; servo lock, parking pos.
        OUTSPEED 0
        CALL sp_threadcut
        CALL sp_needleup
        GOTO 130
130     PRINT " "
        PRINT "ATTENTION! Tufting head moves back to starting point."
        TWAIT 3
        SPEED 200 MM/S ALWAYS
        LMOVE starttuft
        BREAK
.END
```

Subrouting *sp_tuftyline*

```
.PROGRAM sp_tuftyline()
220     PRINT " "
        PRINT "_____________ Definition of Tufting Pattern _____________ "
        PRINT " "
        PRINT "   ->| |<- tuft spacing"
        PRINT "     | |"
        PRINT "  .-.-.-.-.-.-.-.-.-< SP    <-- (+) y-axis"
        PRINT " |                   |"
        PRINT " |< row length >|"
        PRINT " "
        PRINT "Enter the tuft spacing between each tuft along"
        PROMPT "the y-axis (in mm, max.10).",stitchspace
        IF stitchspace>10 OR stitchspace<0 THEN
        PRINT "VALUE ABOVE or BELOW LIMITS. Please enter again."
        GOTO 220
```

```
        END
        maxrps = 500/60
        tuftspeed = maxrps*stitchspace
221     PRINT " "
        PRINT "Enter the total tuft row length"
        PROMPT "along the y-axis (in mm, max.500).",disty
        IF disty>500 OR disty<0 THEN
        PRINT "Distance above or below limits. Please enter again."
        GOTO 221
        END
        tuftno = disty/stitchspace
        maxtuftno = INT(tuftno)+1
        PRINT " "
        PRINT "Tuft spacing: ",(stitchspace)," mm, total tuft row length: ",(disty)," mm."
        PRINT "--> Tufts per tuft row:",(maxtuftno)," "
        PRINT " "
        PROMPT "Do you want to keep these settings? (yes=1 no=0)?",decision1
        CASE decision1 OF
        VALUE 0:
        GOTO 220
        VALUE 1:
        GOTO 222
        any:
        GOTO 221
        END
222     PRINT " "
        PRINT "_____ Definition of Tufting Speed _____ "
        PRINT " "
        PRINT "Enter the tufting speed"
        PRINT "(as % value of the max. absulute tufting speed v= ",(tuftspeed)," mm/s, in general 80%)"
        PROMPT "(between 5 ... 100 %):",perctsp
        IF perctsp>100 OR perctsp<5 THEN
        PRINT "Speed above or below limits. Please enter again."
        GOTO 222
        END
        maxtuftspeed = tuftspeed*perctsp/100
        SPEED maxtuftspeed MM/S ALWAYS
        SETOUTSIG 3000,8,1
        SETOUTSPEED 0,tuftspeed,10,0
        OUTSPEED
        SIGNAL -33,-34,35
        OUTSPEED 0
        PRINT " "
        PRINT "...moving the needle to the lowest position..."
```

```
        CALL sp_needledown
        LMOVE posneed
        BREAK
        224
        DECOMPOSE s[1] = starttuft
        POINT tuftend = TRANS(s[1],s[2]+disty,s[3]-needoff,s[4],s[5],s[6])
        CALL sp_check
        PRINT " "
        PRINT "_____________ Tufting Start _____________ "
        PRINT " "
        TIMER 1 = 0
        TWAIT 5
        HERE spot
        SIGNAL 33
        LAPPRO spot,-needoff
        BREAK
        SIGNAL -33
        TWAIT 2
        OUTSPEED
        SIGNAL 33
        TWAIT 0.2
        ACCEL 0.4
        DECEL 0.4
        LMOVE tuftend
        BREAK
        SIGNAL -33
        OUTSPEED 0
        CALL sp_needledown
        OUTSPEED
        SIGNAL -33,34,-35; servo lock, parking pos.
        OUTSPEED 0
        CALL sp_threadcut
        CALL sp_needleup
        GOTO 230
230     PRINT " "
        PRINT "ATTENTION! Tufting head moves back to starting point."
        TWAIT 5
        SPEED 200 MM/S ALWAYS
        LMOVE starttuft
        BREAK
        ACCEL 0.1
        DRAW ,,,,,-90
        BREAK
.END
```

Subrouting *sp_tuftmove*

```
.PROGRAM sp_tuftmove()
318     PRINT " "
        PRINT "_____________ Definition of Tufting Pattern _____________ "
        PRINT " "
        PRINT "      ->| |<- tuft spacing"
        PRINT "        | |"
        PRINT "     --  .-.-.-.-.-.-.-.-.-.    <--   (+) x-axis"
        PRINT "      /\  .-.-.-.-.-.-.-.-.-.       ||"
        PRINT "      ||  .-.-.-.-.-.-.-.-.-.       ||"
        PRINT " width .-.-.-.-.-.-.-.-.-.-.       \/ (+) y-axis"
        PRINT "      ||  .-.-.-.-.-.-.-.-.-."
        PRINT "      \/  .-.-.-.-.-.-.-.-.-."
        PRINT "     --  .-.-.-.-.-.-.-.-.-.< Start Point"
        PRINT "       |                    |"
        PRINT "       |<  row length  >|"
        PRINT " "
        PROMPT "Select the tufting pattern: Square (0), Triangle (1):",pat
        CASE pat OF
        VALUE 0:
        GOTO 320
        VALUE 1:
        GOTO 320
        ANY :
        PRINT "The option has not been recognised. Enter again."
        GOTO 318
        END
320     PRINT " "
        PRINT "Enter the tuft spacing between each tuft along"
        PROMPT "the x-axis (in mm, max.10).",stitchspace
        IF stitchspace>10 OR stitchspace<0 THEN
        PRINT "VALUE ABOVE or BELOW LIMITS. Please enter again."
        GOTO 320
        END
322     PRINT " "
        PRINT "Enter the total tuft row length"
        PROMPT " along the x-axis (in mm, max. 1100mm).",distx
        IF distx>1100 OR distx<0 THEN
        PRINT "Distance above or below limits. Please enter again."
        GOTO 322
        END
324     PRINT " "
        PRINT "Enter the tuft spacing between two tuft rows"
        PROMPT "along the y-axis (in mm, max.30).",linespace
```

```
        IF linespace>30 OR linespace<0 THEN
        PRINT "Distance above or below limits. Please enter again."
        GOTO 324
        END
326     PRINT " "
        PRINT "Enter the total tufting area width"
        PROMPT "along the y-axis (in mm, max.500).",disty
        IF disty>500 OR disty<0 THEN
        PRINT "Distance above or below limits. Please enter again."
        GOTO 326
        END
327     PRINT " "
        PRINT "Is a correction of row spacing required:"
        PROMPT "No (0), Yes (1):",pat
        CASE pat OF
        VALUE 0:
        linecorr = 0
        GOTO 328
        VALUE 1:
        GOTO 3271
        ANY :
        PRINT "The option has not been recognised. Enter again."
        GOTO 327
        END
3271    PRINT "Shift of every second (return) row along (+) y-axis"
        PROMPT "(in mm, between (-) and (+) tuft spacing).",linecorr
        IF linecorr>linespace OR linecorr<-linespace THEN
        PRINT "Correction above or below limits. Please enter again."
        GOTO 3271
        END
328     PRINT " "
        lineno = disty/linespace
        maxline = INT(lineno)+1
        tuftno = distx/stitchspace
        maxtuftno = INT(tuftno)+1
        PRINT "Tuft spacing in x: ",(stitchspace)," mm, total tuft row length in x:
        ",(distx)," mm."
        PRINT "--> Tufts per tuft row:",(maxtuftno)," "
        PRINT "Tuft row spacing in y: ",(linespace)," mm, total tuft area width in y:
        ",(disty)," mm:"
        PRINT "--> No. of tuft rows:",(maxline)," ."
        PRINT " "
        PROMPT "Do you want to keep these settings? (yes=1 no=0)?",decision1
        CASE decision1 OF
        VALUE 0:
        GOTO 320
```

```
        VALUE 1:
        GOTO 330
        any:
        GOTO 328
        END
330     maxrps = 500/60
        tuftspeed = maxrps*stitchspace
332     PRINT " "
        PRINT "_____________ Definition of Tufting Speed _____________ "
        PRINT " "
        PRINT "Enter the tufting speed"
        PRINT "(as % value of the max. absolute tufting speed v= ",(tuftspeed)," mm/s,
        in general 80%)"
        PROMPT "(between 5 ... 100 %):",perctsp
        IF perctsp>100 OR perctsp<5 THEN
        PRINT "Speed above or below limits. Please enter again."
        GOTO 332
        END
        maxtuftspeed = tuftspeed*perctsp/100
        SPEED maxtuftspeed MM/S ALWAYS
        SETOUTSIG 3000,8,1
        SETOUTSPEED 0,tuftspeed,10,0
        OUTSPEED
        SIGNAL -33,-34,35
        OUTSPEED 0
        PRINT " "
        PRINT "...moving the needle to the lowest position..."
        CALL sp_needledown
        LMOVE posneed
        BREAK
340     DECOMPOSE s[1] = starttuft
        lineno = disty/linespace
        maxline = INT(lineno)
        lcounter = 0
        counter = 0
        CALL sp_check
        PRINT " "
        PRINT "_____________ Tufting Start _____________ "
        PRINT " "
        TIMER 1 = 0
        TWAIT 5
        PRINT "Tufting line No.:"
        POINT linestart = TRANS(s[1],s[2]-(lcounter*linespace),s[3],-180,180,0)
        POINT tuftend = TRANS(s[1]+distx,s[2]-(lcounter*linespace),s[3]-needoff,-
        180,180,0)
350     SPEED maxtuftspeed MM/S ALWAYS
```

```
lrcounter = lcounter+1
PRINT "Tufting line: ",(lrcounter)," of ",(maxline+1)," lines"
SIGNAL 33
LAPPRO linestart,-needoff
BREAK
SIGNAL -33
TWAIT 1
OUTSPEED
SIGNAL 33
TWAIT 0.2
ACCEL 0.4
DECEL 0.4
LMOVE tuftend
BREAK
SIGNAL -33
OUTSPEED 0
CALL sp_needledown
BREAK
PRINT "Line done."
IF lcounter==maxline THEN
GOTO 360
END
LDEPART needoff
BREAK
lcounter = lcounter+1
IF counter==0 THEN
patcorr = pat*stitchspace/2
POINT linestart = TRANS(t[1]-patcorr,s[2]-(lcounter*linespace)+linecorr,
s[3],0,180,0)
POINT tuftend = TRANS(s[1],s[2]-(lcounter*linespace)+linecorr,s[3]-needoff,
0,180,0)
ACCEL 1
DRAW ,,,,,-90
BREAK
ACCEL 1
DRAW ,,,,,-90
BREAK
LMOVE linestart
BREAK
counter = counter+1
GOTO 350
ELSE
POINT linestart = TRANS(s[1],s[2]-(lcounter*linespace),s[3],-180,180,0)
POINT tuftend = TRANS(s[1]+distx,s[2]-(lcounter*linespace),s[3]-needoff,-
180,180,0)
ACCEL 1
```

```
        DRAW ,,,,,90
        BREAK
        ACCEL 1
        DRAW ,,,,,90
        BREAK
        LMOVE linestart
        BREAK
        counter = counter-1
        GOTO 350
        END
360     BRAKE
        OUTSPEED
        SIGNAL -33,34,-35; servo lock, parking pos.
        OUTSPEED 0
        TWAIT 3
        CALL sp_threadcut
        CALL sp_needleup
        GOTO 370
370     PRINT " "
        PRINT "ATTENTION! Tufting head moves back to starting point."
        TWAIT 3
        SPEED 200 MM/S ALWAYS
        IF counter==0 THEN
        GOTO 380
        ELSE
        ACCEL 1
        DRAW ,,,,,90
        BREAK
        ACCEL 1
        DRAW ,,,,,90
        BREAK
        GOTO 380
        END
380     LMOVE starttuft
        BREAK
.END
```

Subrouting *sp_anglex*

```
.PROGRAM sp_anglex()
410     PRINT " "
        PRINT "_____________ Definition of Tufting Angle _____________ "
        PRINT " "
        PRINT "Enter the tufting angle, rotated positively around the x axis"
        PROMPT "(in degree, between -45 and +45°):",anglex
```

```
        IF anglex>45 OR anglex<-45 THEN
        PRINT "Angle above or below limits. Please enter again."
        GOTO 410
        END
        PRINT " "
        PRINT "...rotating the tufting head around x-axis..."
        PRINT " "
        TWAIT 2
        ACCEL 0.1
        DRAW ,,,anglex
        BREAK
        PRINT "Done."
.END
```

Subrouting *sp_tuftxangline*

```
.PROGRAM sp_tuftxangline()
420     PRINT " "
        PRINT "_____________ Definition of Tufting Pattern _____________ "
        PRINT " "
        PRINT "    ->| |<- tuft spacing"
        PRINT "       | |"
        PRINT "  .-.-.-.-.-.-.-.-.-< SP   <-- (+) x-axis"
        PRINT " |                   |"
        PRINT " |< row length >|"
        PRINT " "
        PRINT "Enter the tuft spacing between each tuft along"
        PROMPT "the x-axis (in mm, max.10).",stitchspace
        IF stitchspace>10 OR stitchspace<0 THEN
        PRINT "VALUE ABOVE or BELOW LIMITS. Please enter again."
        GOTO 420
        END
        maxrps = 500/60
        tuftspeed = maxrps*stitchspace
421     PRINT " "
        PRINT "Enter the total tuft row length"
        PROMPT " along the x-axis (in mm, max. 900mm).",distx
        IF distx>900 OR distx<0 THEN
        PRINT "Distance above or below limits. Please enter again."
        GOTO 421
        END
        tuftno = distx/stitchspace
        maxtuftno = INT(tuftno)+1
        PRINT " "
```

```
        PRINT "Tuft spacing: ",(stitchspace)," mm, total tuft row length: ",(distx)," mm."
        PRINT "--> Tufts per tuft row:",(maxtuftno)," "
        PRINT " "
        PROMPT "Do you want to keep these settings? (yes=1 no=0)?",decision1
        CASE decision1 OF
        VALUE 0:
        GOTO 420
        VALUE 1:
        GOTO 422
        any:
        GOTO 421
        END
422     PRINT " "
        PRINT "_____ Definition of Tufting Speed _____ "
        PRINT " "
        PRINT "Enter the tufting speed"
        PRINT "(as % value of the max. absolute tufting speed v= ",(tuftspeed)," mm/s, in general 80%)"
        PROMPT "(between 5 ... 100 %):",perctsp
        IF perctsp>100 OR perctsp<5 THEN
        PRINT "Speed above or below limits. Please enter again."
        GOTO 422
        END
        maxtuftspeed = tuftspeed*perctsp/100
        SPEED maxtuftspeed MM/S ALWAYS
        SETOUTSIG 3000,8,1
        SETOUTSPEED 0,tuftspeed,10,0
        OUTSPEED
        SIGNAL -33,-34,35
        OUTSPEED 0
        PRINT " "
        PRINT "...moving the needle to the lowest position..."
        CALL sp_needledown
        LMOVE posneed
        BREAK
424     CALL sp_check
        PRINT " "
        PRINT "_____ Tufting Start _____ "
        PRINT " "
        TIMER 1 = 0
        TWAIT 5
        SIGNAL 33
        LAPPRO starttuft,-needoff
        BREAK
        SIGNAL -33
```

```
        HERE startangtuft
        DECOMPOSE u[1] = startangtuft
        POINT tuftend = TRANS(u[1]+distx,u[2],u[3],u[4],u[5],u[6])
        TWAIT 2
        OUTSPEED
        SIGNAL 33
        TWAIT 0.2
        ACCEL 0.4
        DECEL 0.4
        LMOVE tuftend
        BREAK
        SIGNAL -33
        OUTSPEED 0
        CALL sp_needledown
        OUTSPEED
        SIGNAL -33,34,-35; servo lock, parking pos.
        OUTSPEED 0
        CALL sp_threadcut
        CALL sp_needleup
        GOTO 430
430     PRINT " "
        PRINT "ATTENTION! Tufting head moves back to starting point."
        TWAIT 3
        SPEED 200 MM/S ALWAYS
        LMOVE starttuft
        BREAK
440     PRINT " "
        PRINT "ATTENTION! Move tufting head manually away from specimen be-
        fore automatic approach of robot home"
.END
```

Appendix B - Single aramid tuft bridging behaviour

In the following, additional experimental results on the bridging behaviour of single aramid tufts in non-crimped fabric composite under mode I loading are presented. All specimens were manufactured and tested in pull-out according to the procedures of Chapter 9. Half of the aramid specimens were tested in frictional pull-out by grinding off the interlocking surface loop.

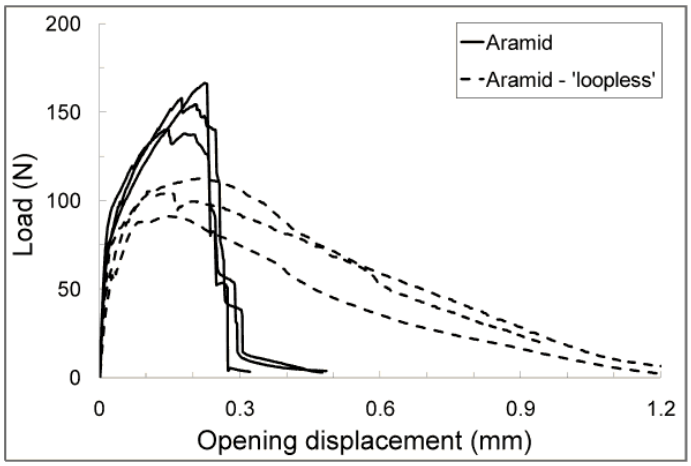

Figure B.1 – Pull-out: experimental bridging response of single aramid tufts with and without surface loop

Figure B.1 shows bridging traction to opening displacement for single aramid tuft specimens with and without surface loop. The maximum load at failure is lower than the measured values for carbon tufts as the aramid thread features a lower strength and compliance. In contrast, the maximum opening displacement is 40% higher than carbon tufts due to the higher maximum strain of aramid. The single aramid tufts exhibit a 52% lower maximum strength, derived from the load versus dry tuft cross-section area of 0.13 mm^2, compared to the impregnated strength of aramid thread rodstock (see Chapter 3). This agrees with observations on carbon and glass tufts, as differences in the straightness of the untensioned thread segments of each tuft cause the tuft to fail prematurely. The aramid tufts in all specimens failed in direct vicinity to the delamination plane as internal axial stresses are maximal at the delamination interface and reduce with distance to the crack plane due to opposing shear frictional along the debonded tuft.

Table B.1 summarises the measured results for single aramid tuft specimens in mode I pull-out.

Table B.1 - Pull-out: experimental bridging results for single aramid tuft specimens (Std.dev in brackets)

Thread	#	F_{max}	$u_{t,fail}$	$u_{t,max}$	U_{fail}	U_{max}	s_t	τ
	(-)	(N)	(mm)	(mm)	(Nmm)	(Nmm)	(mm)	(MPa)
Aramid	7	150 (15)	0.28 (0.05)	0.40 (0.08)	30 (4.1)	31 (4.3)	-	-
Aramid (loopl.)	6	107 (18)	-	1.19 (0.12)	-	61 (21)	2.4 (0.2)	34 (8)

By removing the interlocking surface loop, the total energy dissipation was enhanced by 50% due to frictional pull-out. By assuming a constant shear friction along the fully debonded tuft an average shear value of 33.9 MPa was calculated based on the shear lag theory by interpolating the load-displacement curve in the area of frictional pull-out between maximum bridging load and full pull-out. The measured friction stress is in close agreement with values determined in pull-out tests of loopless carbon tufts in NCF composite.

Appendix C - Design of single tuft shear fixture

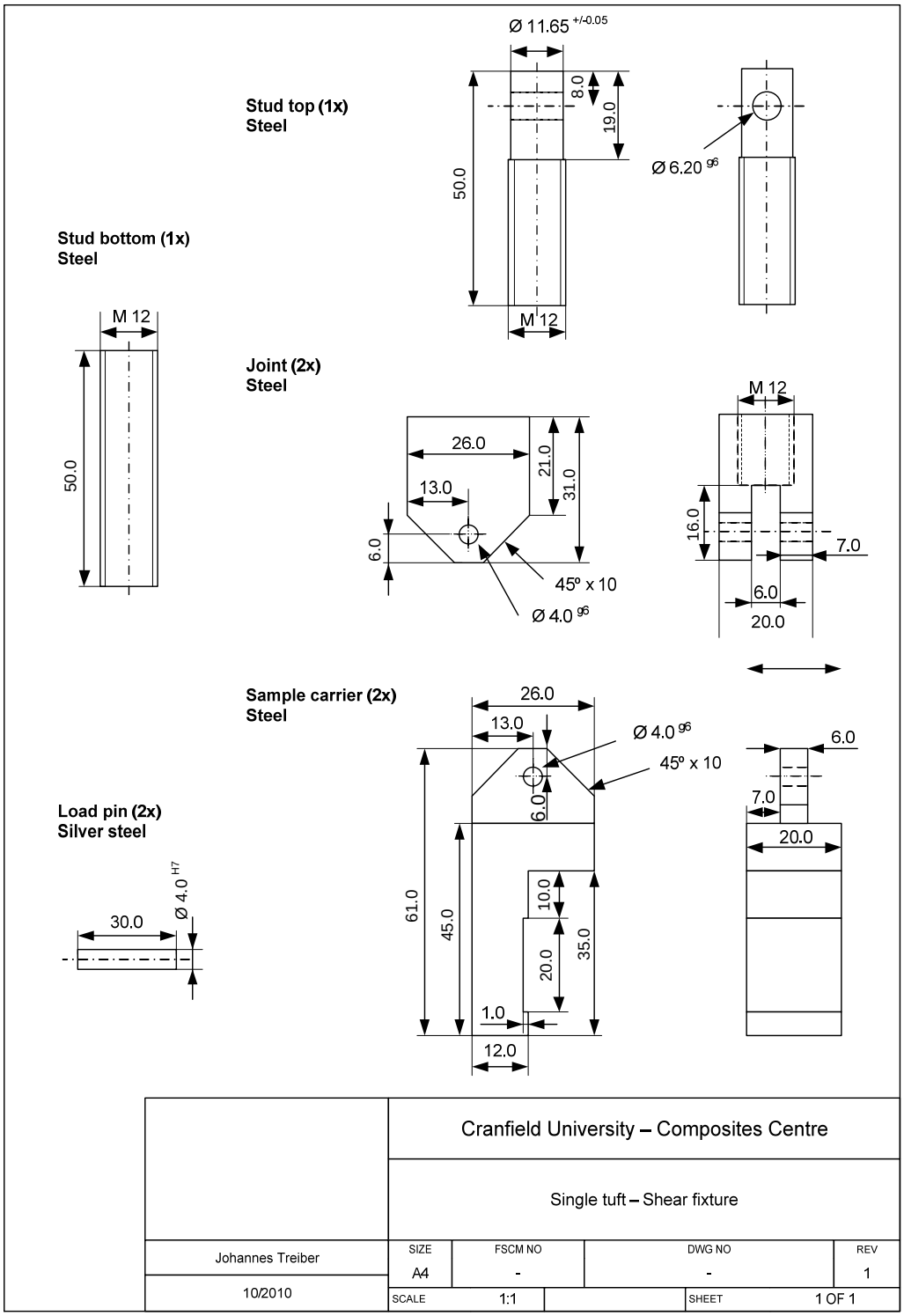

Appendix D - Analytical prediction model for single tuft bridging

The following appendix describes the analytical micro-mechanical model to predict the bridging law of a continuous Z-reinforcement in mode I pull-out and mixed mode shear loading, developed by Cox and colleagues [195; 212; 215].

In extension to the initially developed model, enhanced friction within the zone of lateral deflection of tufts under shear loading is implemented, which was originally observed and implemented only for discontinuous fibrous rods [197; 29].

For the case of continuous Z-reinforcements the model can only be solved by numerical iteration. Hence, the model was implemented into Matlab code allowing the general solution of resulting bridging tractions of a vertical Z-reinforcement for both given mode I and mixed mode crack displacement vectors, see appendix E.

Model definition

A continuous Z-reinforcement of uniform but general cross-section is assumed to bridge between the delamination surfaces (z = 0) of a laminate with half thickness h in the fixed x-z material coordinate system. Due to symmetric response only one half of the laminate and Z-reinforcement are modelled ($z \geq 0$). The normal cross-section of the Z-reinforcement has an area A_t, circumference s_t and width D_t (in y-direction, i.e. normal to the analysis plane). In generalised form the model allows for the Z-reinforcement to be inserted at an initial angle φ relative to the z-axis. Figure D.1 shows a schematic of the inclined Z-reinforcement and associated model parameters.

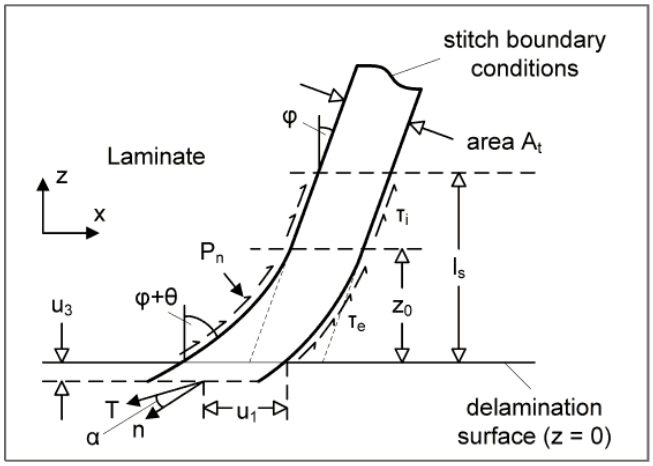

Figure D.1 – Schematic of single Z-reinforcement in mixed mode loading after initial debonding with definition of model parameters (adapted from [212]**)**

The bridging law *T[u]* of a single Z-reinforcement is defined as the relation between the traction $T=(T_1,T_3)$ and the total crack displacement *2u*, with $u=(u_1,u_3)$. Each vector can be separated into two components acting parallel (in x) and normal (in z) to the delamination plane, denoted by the subscripts *1* and *3*. As the traction vector is defined as force acting on the deformed cross-sectional area of the Z-reinforcement with the dimensional unit of stress, the absolute force vector components can be derived as follows:

$$F = \frac{A_t}{\cos(\varphi + \theta)} \cdot T \qquad \text{D-1}$$

Depending on the angle α between traction vector *T* and unit vector *n* defining the fibre direction of the Z-reinforcement at the delamination plane the entity is either loaded with (both α and φ >0 or <0) or against the nap (α>0,φ<0 or α<0,φ>0).

In out-of-plane loading the Z-reinforcement is assumed to debond from the surrounding composite and stretch elastically in axial direction, opposed by uniform friction τ_i acting along the increasing slip zone of lengths l_s. Initial elastic deformation of the fully bonded entity within the surrounding laminate is neglected.

Under shear loading the Z-reinforcement debonds and deflects at an angle $\theta(z)$ over a length z_0 by ploughing laterally into the surrounding laminate. Observed plastic deformation and formation of axial splitting between the filaments of the fibrous Z-reinforcement under shear allow the assumption of the entity to be a rigid/perfectly plas-

tic material which yields only after overcoming the shear flow stress τ_0. Hence, bending effects of the Z-reinforcement are ignored. Furthermore, ploughing is opposed by the resistance of the surrounding laminate which is modelled as uniform force P_n per unit length normal to the deflecting tow. P_n can be derived from the crushing strength (or yield compression strength) of the laminate which is idealised as perfectly plastic material [215]. Within the zone of ploughing locally enhancement of the friction stress τ_e is assumed (with the ratio $\mu_e=\tau_e/\tau_i$) which was observed experimentally in a recent experimental study on discontinuous rods [29]. Cartié et al applied a simple shear lag approach to estimate the friction enhancement factor from discrete Z-reinforcements during frictional pull-out after debonding in mode II loading. Necessary is a close quantification of the ploughing zone length in relation to the applied bridging load and remaining frictional length of the Z-reinforcement within the composite (see derivation for Z-pins in Chapter 9).

Equilibrium equations

From a slice of Z-reinforcement between z and $z + dz$ the first equations of equilibrium between local displacements $\xi(z)$ and $\zeta(z)$ in x- and z-direction and axial strain ε and angle of deflection θ in the entity can be derived as follows:

$$\varepsilon = \cos\varphi\left[\left(\frac{\partial\xi}{\partial z}+\tan\varphi\right)^2+\left(1+\frac{\partial\zeta}{\partial z}\right)^2\right]^{1/2}-1$$

$$\theta = \tan^{-1}\left[\left(\frac{\partial\xi}{\partial z}+\tan\varphi\right)\Big/\left(1+\frac{\partial\zeta}{\partial z}\right)\right]-\varphi \qquad \textbf{D-2}$$

Three stress components act within the local coordinates (x', z') of the deformed slice which are: axial stress $\sigma_t = \sigma'_{zz}$, axial shear stress σ'_{zx} and transverse compression $\sigma_n = \sigma'_{xx}$. The axial stress is assumed to be decoupled from shear and transversal deformation and can be derived from the elastic strain ε and Young's modulus E_t of the Z-reinforcement in fibre direction following the linear elastic law $\sigma_t = \varepsilon E_t$. Transverse compression acts only within the zone of deflection and is independent of the coordinate z. The axial shear stress satisfies the condition $|\sigma'_{zx}| \leq \tau_0$.

In order to balance the stress components, the earlier introduced laminate resistance P_n and surface friction stresses τ_i and τ_e in the slice between z and $z + dz$ the following equilibrium of forces (in x- and z-direction) is required:

$$\text{x:}-\sigma_{zx}(z)\frac{A_t}{\cos(\varphi+\theta)}+\sigma_{zx}(z+dz)\frac{A_t}{\cos(\varphi+\theta+d\theta)}+$$
$$+\eta_1 P_n\frac{dz}{\cos(\varphi)}\cos(\varphi+\theta)+s_t\tau_{i/e}\frac{dz}{\cos(\varphi)}\sin(\varphi+\theta)=0$$

D-3

$$\text{z:}-\sigma_z(z)\frac{A_t}{\cos(\varphi+\theta)}+\sigma_z(z+dz)\frac{A_t}{\cos(\varphi+\theta+d\theta)}-$$
$$-\eta_1 P_n\frac{dz}{\cos(\varphi)}\sin(\varphi+\theta)+s_t\tau_{i/e}\frac{dz}{\cos(\varphi)}\cos(\varphi+\theta)=0$$

with $\eta_1=\pm 1$ in order for P_n to be always a positive quantity.

Boundary conditions for tuft

- *Fracture plane (z=0):*

Figure D.2 a) illustrates the free-body diagram for a wedge of Z-reinforcement at the delamination plane *z=0* with the equilibrium between the stress components σ_t, σ'_{zx} and σ_n and the external bridging tractions T_1 and T_3.

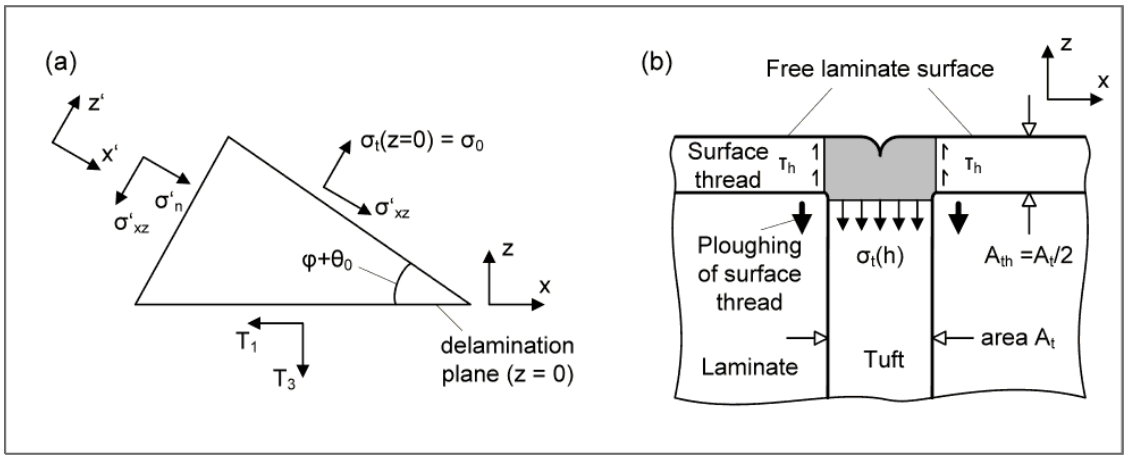

Figure D.2 – Boundary conditions: a) free-body diagram of Z-reinforcement with equilibrium between applied stresses and bridging traction on delamination plane (z=0) [212]**, b) force balance between Z-reinforcement and interlocking threads on laminate surface (z=h) (adapted from** [215]**)**

With the boundary values of $\sigma_0=\sigma_t(z=0)$ and $\theta_0=\theta(z=0)$ and the substitution of σ'_{zx} with τ_0, following the assumption of start of yielding at very small displacements, the traction vector components can be derived as follows:

$$T_1=\frac{1}{2}(\sigma_0-\sigma_n)\sin\big(2(\varphi+\theta_0)\big)+\tau_0\cos\big(2(\varphi+\theta_0)\big)$$

D-4

$$T_3 = \sigma_0 \cos^2(\varphi + \theta_0) + \sigma_n \sin^2(\varphi + \theta_0) - \tau_0 \sin\big(2(\varphi + \theta_0)\big)$$

The transversal compressive stress σ_n acts in reality only on the compressive side of the deflected Z-reinforcement within the limits of $0 \leq z \leq z_0$.and is related to the contact pressure P_n. However, for simplification an averaged value is derived of the original compressive force acting on the total circumference.

- *Zone of deflection ($z \leq z_0$):*

Only if the Z-reinforcement yields and deforms in plastic shear a zone of deflection exists with the limits of $0 \leq z \leq z_0$. Beyond the upper limit z_0 the deflection angle $\theta(z)$ is required to take the value $\theta(z)=0$ for $z \geq z_0$.

- *Slip zone ($z \leq l_s$ for $l_s < h$):*

At the fracture plane the axial stress is required to fulfil the following boundary condition which is derived by inverting equations D-4:

$$\sigma_0 = T_3 + \frac{{T_3}^2 - {\tau_0}^2}{T_3 - \sigma_n} \qquad \textbf{D-5}$$

The boundary conditions on the opposing end of the slip zone depend on the extension of the slip zone in relation to the laminate surface. In the initial phase of debonding, as long as the slip zone is not reaching the laminate surface ($l_s \leq h$), the axial stress within the Z-reinforcement has to take the value $\sigma_t(z=l_s)=0$.

- *Slip zone beyond laminate surface ($l_s > h$):*

When the debonding zone reaches the laminate surface, the further bridging response depends on the type of Z-reinforcement. In contrary to discrete Z-pins the surface threads of the tuft restrict frictional pull-out of the Z-reinforcement. Instead, the interlocking surface threads are assumed to debond and plough into the surface analog to a tuft ploughing into the surrounding laminate under shear loading at the delamination plane. The axial stress $\sigma_t(z=h)$ within the vertical Z-reinforcement is transferred to the two surface threads as shear stress τ_h (see Figure D.2 b). Since each surface thread features half the cross-sectional area $A_{th} = A_t/2$ of the through-the-thickness segment of the

tuft the shear stress τ_h is equal to the axial stress σ_t. The axial stretching of the tuft on the laminate surface $\zeta(z=h)$ can be calculated by determining the ploughing deformation ξ^* of the surface segments within a rotated coordinate system with orientation of z^* along the fibre direction of the surface threads. Hence, the boundary condition for $z=h$ is:

$$\zeta(\mathrm{z} = \mathrm{h}) = \mathrm{u_1}^* = \xi^*(z^* = 0) \quad \text{with } \mathrm{T_1}^* = \sigma_t(z = h)\,, \mathrm{T_3}^* = 0 \qquad \textbf{D-6}$$

The superscript "*" indicates the analysis of the surface thread response in the rotate analysis coordinate system (x^*,z^*). Each surface thread has the circumference s_{th} and ploughing width D_{th}.

- *Tuft failure:*

In contrary to discontinuous rods the final failure of the tufts is not defined by frictional pull-out but rupture of the continuous thread. As frictional stress along the slip zone reduces the axial stress within the Z-reinforcement with increasing distance to the de-lamination plane failure of the tuft appears at the failure plane $z=0$ with:

$$\sigma_0 = 0 \quad \text{for} \quad \sigma_t(z = 0) \geq \sigma_{0,max} \qquad \textbf{D-7}$$

where $\sigma_{0,max}$ is the axial strength of the tuft. As failure appears at the delamination plane frictional pull-out of tuft segments, which was observed for part of the single tuft specimens in experiments of Chapter 9, is neglected.

General solution

With the assumptions of perfect plasticity within the Z-reinforcement ($\partial\sigma'_{zx}/\partial z=0$) and of small stress ratio σ'_{zx}/σ_t the following simplified model equations can be derived from equations D-3:

$$\frac{\partial\sigma_t}{\partial z} = -\frac{s_t\tau_e}{A_t\cos\varphi} \qquad \text{for } (0 \leq z \leq z_0) \qquad \textbf{D-8}$$

$$\frac{\partial\sigma_t}{\partial z} = -\frac{s_t\tau_i}{A_t\cos\varphi} \qquad \text{for } (z_0 \leq z \leq l_s) \qquad \textbf{D-9}$$

$$\sigma_t \frac{\partial \theta}{\partial z} = -\eta_1 \frac{P_n}{A_t \cos\varphi} \qquad \textbf{D-10}$$

Considering the introduced boundary conditions the following general solution for $\theta(z)$ results from equation D-10:

$$\theta(z) = \theta_0 + \eta_1 \frac{P_n}{s_t \cdot \tau_e} \ln\left[1 - \frac{\tau_e \cdot s_t \cdot z}{\sigma_0 \cdot A_t \cos\varphi}\right] \qquad \textbf{D-11}$$

With the condition of $\theta(z=z_0)=0$ at the end of the deflection zone ($z=z_0$) it follows:

$$z_0 = \frac{\sigma_0 \cdot A_t \cos\varphi}{\tau_e \cdot s_t}\left[1 - e^{-\frac{\theta_0 \cdot s_t \cdot \tau_e}{P_n}}\right] \qquad \textbf{D-12}$$

The displacements $\xi(z)$ and $\zeta(z)$ can be related to axial stress $\sigma_t(z)$ and rotation angle $\theta(z)$ with the boundary conditions as follows:

$$\xi(z) = \int_{z_0}^{z}\left[\frac{\sin\big(\varphi + \theta(z)\big)}{\cos\varphi} - \tan\varphi\right]dz \qquad \textbf{D-13}$$

$$\text{for } (0 \le z \le z_0)$$

$$\zeta(z) = \int_{l_s}^{z}\left[\underbrace{\frac{\cos\big(\varphi + \theta(z)\big)}{\cos\varphi}\frac{\sigma_t(z)}{E_t}}_{\text{elastic stretching}} + \underbrace{\frac{\cos\big(\varphi + \theta(z)\big)}{\cos\varphi} - 1}_{\text{contribution of deflected tow}}\right]dz \qquad \textbf{D-14}$$

$$\text{for } (l_s \le h)$$

$$\zeta(z) = \xi^*(z^* = 0) + \int_{h}^{z}\frac{\cos\big(\varphi + \theta(z)\big)}{\cos\varphi}\frac{\sigma_t(z)}{E_t} + \qquad \textbf{D-15}$$

$$+\frac{\cos\big(\varphi + \theta(z)\big)}{\cos\varphi} - 1\,dz \qquad \text{for } (l_s \ge h)$$

In equations D-14 and D-15 the first part of the integral presents the contribution of elastic stretching, integrated over the full frictional length $0 \leq z \leq l_s$ and $0 \leq z \leq h$ respectively. If the Z-reinforcement ploughs into the surrounding laminate an additional term for the contribution of the mode II displacement is present. In case of ploughing, also the elastic term has to be integrated in two steps between $0 \leq z \leq z_0$ and $z_0 \leq z \leq l_s$ as friction is enhanced within the ploughing zone and $\sigma_t(z)=f(\tau_i,\tau_e)$. The additional first term in equation D-15 is the contribution of surface deformation.

The displacements u_1 and u_3 in x- and z-direction at the fracture plan are given by:

$$u_1 = -\xi(\mathrm{z}=0) - \zeta(\mathrm{z}=0) \cdot \tan\big(\varphi + \theta(\mathrm{z}=0)\big) \cdot \eta_2 \qquad \textbf{D-16}$$

$$u_3 = -\zeta(\mathrm{z}=0) \qquad \textbf{D-17}$$

The second term in equation D-16 arises from the contribution to mode II displacement of the stretched tow segment within the crack wake when opening displacement is non-zero.

In mode I loading of a vertical tuft without inclination the transversal components of the bridging law parallel to the delamination plane are zero:

$$T_1 = 0$$
$$\frac{u_{1,tot}}{2} = -\xi(\mathrm{z}=0) = 0 \qquad \textbf{D-18}$$

From the integration of equation D-9 a closed form solution can be derived for the relation of bridging traction T_3 and total opening displacement $u_{3,tot}$ in the initial debonding phase for $l_s<h$ with the following boundary conditions:

$$T_3 = \sigma_0 = \frac{F_3}{A_t}$$
$$\frac{u_{3,tot}}{2} = u_3 = -\zeta(\mathrm{z}=0) = -\frac{1}{2}\frac{{\sigma_0}^2 A_t}{E_t s_t \tau_i} \qquad \text{for } (l_s \leq h) \qquad \textbf{D-19}$$

For the slip zone $l_s>h$ the system of non-linear equations of $u_1^*=f(\theta_0^*)$ and $\sigma_0^*=f(\theta_0^*)$ has to be solved under the condition of $\zeta(0)-u_3=0$ according to equations D-15 and D-10 to D-13. A detailed approach for solution is given in [197]. The contribution of axial stretching to the surface deflection displacement, i.e. the second term of equation D-16, becomes zero as the surface threads plough into the laminate only under transversal displacement. Furthermore, surface deformation is assumed to initiate only if the defined internal shear yield strength of the surface threads is overcome. Until then the approach according to equation D-19 is used. In the Matlab code of Appendix E the simple function *fsolve* was used for iterative solution of according system of equations requiring only an initial guess of the deflection angle θ_0^* at the laminate surface.

As for the mode I ploughing stage, a general explicit analytical solution can not be derived for the bridging relation of $F=F[u]$ pure mode II or mixed mode loading conditions, where the total displacement is a combination of lateral ploughing of the tuft into the surrounding composite at the delamination plane and at the specimen surface. An iterative search with adaptation of both deflection angles θ_0 and θ_0^* is necessary.

Appendix E - Implementation of single tuft bridging model in Matlab

Matlab code to predict the bridging law of a single tuft in mode I and mixed mode delamination. The presented model is based on given crack opening and shear displacement vectors and derives the corresponding crack closure forces which act parallel and orthogonal on the delamination plane.

Code for bridging response in mode I

```
%%%
```

```
%%%%%%%%%%%%%%%%%%%%

N1=30;                                  %No of discrete points in first section

u31=zeros(1,N1);
F31=zeros(1,N1);

u31=[0:(s*ti*h^2/(2*A*Et))/(N1-1):(s*ti*h^2/(2*A*Et))];     %Half crack displacement - [mm]
u31t=2*u31;                                                 %Total crack displacement - [mm]

for i=1:N1
   F31(1,i)=(u31(1,i)*2*Et*s*ti*A)^0.5;     %Crack bridging load - [N]
   sig01(1,i)=F31(1,i)/A;                   %Axial stress in tuft at crack interface - [MPa]
end

%%%%%%%%%%%%%%%%%%%%%%%%%%
%    Fully Debonded/Surface Deformation ls>h    %
%%%%%%%%%%%%%%%%%%%%%%%%%%

N2=100;                                 %No of discrete points in first section

u32=zeros(1,N2);
F32=zeros(1,N2);
theta0h=zeros(1,N2);                    %Deflection angle of single thread at laminate surface
theta0g=0.2;                            %Initial guess for deflection angle

u32=[u31(1,N1):(u32max-u31(1,N1))/(N2-1):u32max];
                                        %Chosen Crack bridging displacement increments

%%%   Iterative search for theta (so that function T1h - sigth = 0 for each sigth)   %%%

for i=1:N2
   theta0h(1,i)=fzero(@(x) solveu32(x,sign,tau0,ti,te,h,Et,s,A,mue,Ath,sth,Pnt,u32(1,i)),theta0g);
   theta0hdeg(1,i)=theta0h(1,i)*180/pi();  %Angle of deformation of surface thead
end

sig0h=zeros(1,N2);                      %Axial stress in surface thread
for i=1:N2
   sig0h(1,i)=sig0hf(theta0h(1,i),ti,te,Et,Pnt,sth,mue);
end

%%%   Determination of axial stress in tuft on laminate surface   %%%

for i=1:N2
   sigth(1,i)=(sig0h(1,i)-sign)*sin(theta0h(1,i))*cos(theta0h(1,i))+tau0*cos(2*theta0h(1,i));
end

%%%   Check for shear flow condition   %%%

for i=2:N2
   if sigth(1,i)<=sigth(1,i-1)
      theta0h(1,i-1)=0;
      sigth(1,i-1)=(u32(1,i-1)*2*Et*s*ti*A)^0.5/A-s*ti*h/A;
   end
end
```

```
%%%   Determination of axial stress in tuft and bridging load at crack interface   %%%

for i=1:N2
   sig02(1,i)=sigth(1,i)+s*ti*h/A;                    %Axial stress in tuft at crack interface
   if (sig02(1,i)>= sig0max)
      sig02(1,i)=0;
   end;
   F32(1,i)=sig02(1,i)*A;                             %Crack bridging load at crack interface
end

%%%   Deflection of laminate surface element   %%%

for i=1:N2
   u1h(1,i)=sig0h(1,i)*Ath/(sth*te)*1/(1+Pnt^2/(sth^2*te^2))*(sin(theta0h(1,i))-…
            Pnt/(sth*te)*(cos(theta0h(1,i))-exp(-theta0h(1,i)*sth*te/Pnt)));
end

%%%   Stretching of debonded straight tuft element u32h = u32 - u1h   %%%

for i=1:N2
   u32h(1,i)=sig02(1,i)*h/Et-s*ti*h^2/(2*Et*A);
end


%%%%%%%%%%%
%    Result vectors   %
%%%%%%%%%%%

%%%   Combined deformation and stretching of surface and tuft   %%%

u32t=2*u32;                                           %Total displacement of both crack surfaces

%%%   Total opening u3 for ls<h and ls>h   %%%

u3t=[u31,u32];                                        %Total displacement

%%%   Bridging force F3 for ls<h and ls>h   %%%

F3=[F31,F32];                                         %Total force

%%%%%%%%%%%%%%%%%%%%%%%%%%%%%%%%%%%%%%%%%%%%%%%%%%%%%%%%%%%%%%%%%%%%%%%%%%%%

%%%%%%%%%%%%%%%%%
% Required solution functions %
%%%%%%%%%%%%%%%%%

%%%%%%%%%%%%%%%%%%%%%%%%%%%%%%%%%%%%%%%%%%%%%%%%%%%%%%%%%%%%%%%%%%%%%%%%%%%%

function f = sig0hf(x,ti,te,Et,Pnt,sth,mue)

f = -2*ti*Et*(1/(1+Pnt^2/(sth^2*te^2))*(cos(x)-1+Pnt/(sth*te)*(sin(x)-Pnt/(sth*te)*(1-…
   exp(-x*sth*te/Pnt))))/(1+(mue-1)*exp(-x*te*sth/Pnt)));

%%%%%%%%%%%%%%%%%%%%%%%%%%%%%%%%%%%%%%%%%%%%%%%%%%%%%%%%%%%%%%%%%%%%%%%%%%%%
```

```
function f = solveu32(x,sign,tau0,ti,te,h,Et,s,A,mue,At,st,Pnt,u32)

sig0h=(-2*ti*Et*(1/(1+Pnt^2/(st^2*te^2))*(cos(x)-1+Pnt/(st*te)*(sin(x)-Pnt/(st*te)*(1-…
        exp(-x*st*te/Pnt))))/(1+(mue-1)*exp(-x*te*st/Pnt))));

f = (((sig0h-sign)*sin(x)*cos(x)+tau0*cos(2*x)+s*ti*h/A)*h/Et-…
    s*ti*h^2/(2*Et*A))+(At*sig0h/(st*te)*(1/(1+Pnt^2/(st^2*te^2)))*(sin(x)-Pnt/(st*te)*(cos(x)-…
    exp(-x*st*te/Pnt))))-u32;

%%%%%%%%%%%%%%%%%%%%%%%%%%%%%%%%%%%%%%%%%%%%%%%%%%%%%%%%%%%%%%%%%%%%%%%%%%%%
```

Code for bridging response in mixed mode

```
%%%%%%%%%%%%%%%%%%%%%%%%%%%%%%%%%%%%%%%%%%%%%%%%%%%%%%%%%%%%%%%%%%%%%%%%%%%%
%          Mixed Mode I/II Shear Model - Single Tuft                          %
%                                                                             %
% based on B.N Cox and  N. Sridhar 2002 / B.N. Cox 2005                       %
% created by:   Johannes Treiber                                             %
% control:      crack displacements given, bridging forces determined        %
%                                                                             %
%%%%%%%%%%%%%%%%%%%%%%%%%%%%%%%%%%%%%%%%%%%%%%%%%%%%%%%%%%%%%%%%%%%%%%%%%%%%

clear all

%%%%%%%%%%%%%%%%%%%
%%%   Parameter Definition   %%%
%%%%%%%%%%%%%%%%%%%

h=2;                                %Laminate half thickness - [mm]

%%% NCF %%%
Et=113458;                          %Tuft stiffness (Assumed carbon thread) - [MPa]
N_fil = 2000;                       %No. of filament in thread - [-]
Ath=N_fil*0.0035^2*pi()/0.5;        %Thread area (assumed carbon thread, Vf = 50%) - [mm^2]
rth=(Ath*2/pi())^0.5;               %Thread half width (assumed ellipse with a = 2b) - [mm]
sth=pi()*(3*(rth+rth/2)-((3*rth+rth/2)*(rth+3*rth/2))^0.5);
                                    %Thread circumference (Ramanujan) - [mm]
A=2*Ath;                            %Tuft area (two threads, Vf = 50%) - [mm2]
r=(A/pi())^0.5;                     %Tuft radius (assumed circular tuft shape) - [mm]
s=2*r*pi();                         %Tuft circumference - [mm]
sig0max=(3544*0.5)/2;               %Tuft strength (1/2 of infused thread strength)- [MPa]
u1max=0.2;                          %Max. shear crack displacement - [mm]

Rmod=0.1;                           %Ratio of mode I to II displacement - [-]

ti=10;                              %Friction in straight section - [MPa]
mue=3;                              %Friction ratio te/ti - []
te=ti.*mue;                         %Enhanced friction in deflected zone - [MPa]
Pnt=2.97*149*2*rth;                 %Hydrostatic pressure at deflected single thread - [N/mm]
Pn=2.97*320*2*r;                    %Hydrostatic pressure at deflected tuft - [N/mm]

sign=0;                             %Normal compressive force on deflected tuft - [MPa]
```

```
tau0=75;                            %Shear flow of tuft - [MPa]

%%%%%%%%%%%%%%%%%%%%%%%%%%%%%
%%%   Definition of crack displacement vector   %%%
%%%%%%%%%%%%%%%%%%%%%%%%%%%%%

N(1,1)=30;

u1=zeros(1,N(1,1));
u3=zeros(1,N(1,1));

u1=[0:(u1max/(N(1,1)-1)):u1max];                    %Half crack displacement in x - [mm]
u3=[0:(u1max*Rmod/(N(1,1)-1)):(u1max*Rmod)];        %Half crack displacement in z - [mm]

u1t=2*u1;                                           %Total crack displacement in x - [mm]
u3t=2*u3;                                           %Total crack displacement in z- [mm]

%%%%%%%%%%%%%%%%%%%%
%   Initial Debonding/Stretching ls<h   %
%%%%%%%%%%%%%%%%%%%%

%%%   Iterative search for theta (so that function f(u11) - u11  = 0 )   %%%

theta0g=0.05;                                       %Initial guess for deflection angle – [rad]

k=1

for i=1:N(k,1)
   X=fsolve(@(x) solveu1131(x,ti(1,k),te(1,k),h,Et,Pn(1,k),s,A,mue,u1(k,i),u3(k,i)),[theta0g]);
   theta0(k,i)=X;
   theta0deg(k,i)=theta0(k,i)*180/pi();
end

%%%   Axial stress in tuft at delamination plane   %%%

for i=1:N(k,1)
   sig0(k,i)=(s*te(1,k))/A*(1+Pn(1,k)^2/(s^2*te(1,k)^2))*(u1(k,i)+u3(k,i)*tan(theta0(k,i)))/…
             (sin(theta0(k,i))-Pn(1,k)/(s*te(1,k))*(cos(theta0(k,i))-…
             exp(-theta0(k,i)*s*te(1,k)/Pn(1,k))));
end

%%%   Total debonding length   %%%

for i=1:N(k,1)
   ls(k,i)=sig0(k,i)*A/(s*ti(1,k))-(mue-1)*(A*sig0(k,i)/(s*te(1,k))*(1-…
           exp(-theta0(k,i)*s*te(1,k)/Pn(1,k))));          %Debonding length - [mm]
end

%%%   Calculation of axial stress in surface thread - only relevant for ls>h   %%%

for i=1:N(k,1)
   sigth(k,i)=sig0(k,i)*exp(-theta0(k,i)*s*te(1,k)/Pn(1,k))*(1-1/mue)+1/mue*sig0(k,i)-s*ti(1,k)*h/A;
end

%%%   Derivation of relative crack bridging loads   %%%
```

```
for i=1:N(k,1)
   F1(k,i)=(sig0(k,i)*sin(theta0(k,i))*cos(theta0(k,i))+tau0*cos(2*theta0(k,i)))*A/cos(theta0(k,i));
                                          %Crack bridging load in x - [N]
   F3(k,i)=(sig0(k,i)*cos(theta0(k,i))-tau0*sin(2*theta0(k,i)))*A/cos(theta0(k,i));
                                          %Crack bridging load in z - [N]
end

%%%%%%%%%%%%%%%%%%%%
%   Initial Debonding/Stretching ls<h   %
%%%%%%%%%%%%%%%%%%%%

thetag=0.2;                               %Initial guess for tuft deflection angle – [rad]

for i=1:N(k,1)
   if ls(k,i)>=h

      %%%   Iterative search for theta   %%%
       sig0hg=300;                        %Initial guess for axial stress – [MPa]
       thetahg=0.2;                       %Initial guess for thread deflection angle – [rad]


         X=fsolve(@(x) solveu1232(x,sign,tau0,ti(1,k),te(1,k),h,Et,Pn(1,k),s,A,mue,Ath,sth,…
                  Pnt(1,k),u1(k,i),u3(k,i)),[thetag;thetahg;sig0hg],…
                  optimset('MaxFunEvals',2000000,'MaxIter',10000));
         sig0h(k,i)=sig0f(abs(X(2)),ti(1,k),te(1,k),Et,Pnt(1,k),sth,mue);
         sigth(k,i)=(X(3)*exp(-abs(X(1))*s*te(1,k)/Pn(1,k))*(1-1/mue)+1/mue*abs(X(3))-…
                  s*ti(1,k)*h/A);
         sig0(k,i)=abs(X(3));
         theta0(k,i)=abs(X(1));
         theta0h(k,i)=abs(X(2));
         theta0deg(k,i)=abs(X(1))*180/pi();
         theta0hdeg(k,i)=abs(X(2))*180/pi();

         if (sig0(k,i)>=sig0max)
            sig0(k,i)=0;
         end

         thetag=theta0(k,i);

      %%%   Deflection of laminate surface element   %%%

         F1(k,i)=(sig0(k,i)*sin(theta0(k,i))*cos(theta0(k,i))+tau0*cos(2*theta0(k,i)))*…
                  A/cos(theta0(k,i));          %Crack bridging load in x - [N]
         F3(k,i)=(sig0(k,i)*cos(theta0(k,i))-tau0*sin(2*theta0(k,i)))*…
                  A/cos(theta0(k,i));          %Crack bridging load in z - [N]
   end

   z0(k,i)=A*sig0(k,i)/(te*s)*(1-exp(-theta0(k,i)*s*te/Pn));

end
%%%%%%%%%%%%%%%%%%%%%%%%%%%%%%%%%%%%%%%%%%%%%%%%%%%%%%%%%%%%%%%%%%%%%%%%%%%%
```

```
%%%%%%%%%%%%%%%%
% Required solution functions %
%%%%%%%%%%%%%%%%

%%%%%%%%%%%%%%%%%%%%%%%%%%%%%%%%%%%%%%%%%%%%%%%%%%%%%%%%%%%%%%%%%%%%%%%

function f = sig0f(x,ti,te,Et,Pn,s,mue)

f = -2*ti*Et*(1/(1+Pn^2/(s^2*te^2))*(cos(x)-1+Pn/(s*te)*(sin(x)-Pn/(s*te)*(1-…
    exp(-x*s*te/Pn))))/(1+(mue-1)*exp(-x*te*s/Pn)));

%%%%%%%%%%%%%%%%%%%%%%%%%%%%%%%%%%%%%%%%%%%%%%%%%%%%%%%%%%%%%%%%%%%%%%%

function f = solveu1131max(x,ti,te,h,Et,Pn,s,A,mue,u11,u31)
% x(1) - theta01, x(2) - sig01 %

sig0=(s*te)/A*(1+Pn^2/(s^2*te^2))*(u11+u31*tan(x(1)))/(sin(x(1))-Pn/(s*te)*(cos(x(1))-…
        exp(-x(1)*s*te/Pn)));
f = [(A*sig0/(s*te)*(1/(1+Pn^2/(s^2*te^2)))*(cos(x(1))-1+Pn/(s*te)*(sin(x(1))-Pn/(s*te)*(1-…
    exp(-x(1)*s*te/Pn)))))+(A*sig0^2/(2*s*te*ti*Et)*(1+(mue-1)*exp(-x(1)*s*te/Pn)))-u31];

%%%%%%%%%%%%%%%%%%%%%%%%%%%%%%%%%%%%%%%%%%%%%%%%%%%%%%%%%%%%%%%%%%%%%%%

function f = solveu1232(x,sign,tau0,ti,te,h,Et,Pn,s,A,mue,At,st,Pnt,u12,u32)
% x(1) - theta02, x(2) - theta02h, x(3) - sig0 %

sig0h=-2*ti*Et*(1/(1+Pnt^2/(st^2*te^2))*(cos(x(2))-1+Pnt/(st*te)*(sin(x(2))-Pnt/(st*te)*(1-…
         exp(-x(2)*st*te/Pnt))))/(1+(mue-1)*exp(-x(2)*te*st/Pnt)));
u1h=At*sig0h/(st*te)*(1/(1+Pnt^2/(st^2*te^2)))*(sin(x(2))-Pnt/(st*te)*(cos(x(2))-…
       exp(-x(2)*st*te/Pnt)));
z0=A*x(3)/(te*s)*(1-exp(-x(1)*s*te/Pn));

f = [(A*x(3)/(s*te)*(1/(1+Pn^2/(s^2*te^2)))*(cos(x(1))-1+Pn/(s*te)*(sin(x(1))-Pn/(s*te)*(1-…
     exp(-x(1)*s*te/Pn)))))+(x(3)*z0/Et-s*te*z0^2/(2*A*Et)-s*ti*h*z0/(A*Et)+s*ti*z0^2/(2*A*Et)+…
     s*ti*h^2/(A*Et*2))+u1h-u32;
    A*x(3)/(s*te)*(1/(1+Pn^2/(s^2*te^2)))*(sin(x(1))-Pn/(s*te)*(cos(x(1))-exp(-x(1)*s*te/Pn)))+…
    u32*tan(x(1))-u12;
   ((sig0h-sign)*sin(x(2))*cos(x(2))+tau0*cos(2*x(2)))-(x(3)*exp(-x(1)*s*te/Pn)*(1-…
   1/mue)+1/mue*x(3)-s*ti*h/A)];
```

Appendix F - Additional publications

Johannes W.G. Treiber, Denis D.R. Cartié, Ivana K. Partridge, DETERMINATION OF CRACK BRIDGING LAWS IN TUFTED COMPOSITES, Oral presentation at 17th International Conference on Composite Materials, Edinburgh, UK, Jul. 2009

Johannes W.G. Treiber, Giuseppe Dell'Anno, Ivana K. Partridge, COMPARING CRACK BRIDGING LAWS FOR TUFTED AND Z-PINNED COMPOSITE, Accepted for oral presentation at 6th ESIS TC4 International Conference on the Fracture of Polymers, Composites and Adhesives, Les Diablerets, Switzerland, Sept. 2011

Johannes W.G. Treiber, Denis D.R. Cartié, Ivana K. Partridge, EFFECTS OF MESOSTRUCTURE ON THE IN-PLANE PROPERTIES OF TUFTED CARBON FABRIC COMPOSITES, Oral presentation at 5th International Conference on Composites Testing and Model Simulation, Lausanne, Switzerland, Feb. 2011

Ivana K. Partridge, Johannes W.G. Treiber, Mathieu Préau, DEFORMATION AND FAILURE IN A TUFTED CARBON FABRIC/EPOXY Ω – STIFFENER, Accepted for oral presentation at 11th Conference on Deformation and Fracture of Composites, Cambridge, UK, Apr. 2011

Determination of crack bridging laws in tufted composites

J.W.G. Treiber, D.D.R. Cartié, I.K. Partridge
Composites Centre, School of Applied Sciences, Cranfield University
Cranfield, Bedfordshire, MK43 0AL, UK
j.treiber@cranfield.ac.uk

SUMMARY

Crack bridging laws are determined for single tufts inserted into dry preforms (UD, woven and NCF), infused and cured by RTM. Pull-out and shear test fixtures apply Mode I and mixed mode delamination loading. Existing analytical models are tested against the obtained results. Tuft failure modes were identified for different material-loading combinations.

Keywords: Bridging law, traction, pull-out, tufting, RTM

INTRODUCTION

Tufting as modified single thread stitching process offers the advantage of an unstrained, truly vertical Z-reinforcement of composite structures which requires only single sided access. The selective insertion of tufts aims at the improvement of interlaminar failure properties (mode I and II delamination) of critical composite structures under impact or out-of-plane loading with minimal disruption of its in-plane properties [1]. In order to determine and to model the effect of a tuft on the delamination properties it is necessary to determine its closure traction for a defined crack surface displacement, also known as the tuft bridging law.

EXPERIMENT & ANALYSIS

This project focuses on the experimental determination of mode I and mixed mode bridging laws for glass and carbon tuft material based on pull-out and shear test of a single tuft inserted in various composite preforms (woven twill, non-crimp (NCF) and unidirectional carbon fabric).

Materials and methods

In order to simulate crack propagation into a tufted area, specimens were prepared with a release film at its centre plane which is only penetrated by a single tuft. The tuft was tested in a mode I and mixed mode configuration by bonding the specimen between two vertically loaded steel t-tabs or a specially designed shear jig, which allows shear and opening of the cracked specimen (see fig. 1.a) and 1.b)). A digital image correlation system (DIC) was used to record the 3-D displacements of the loaded specimens.

Analysis and results

At least ten specimens were tested for each variable (tuft material, laminate material, and loading case) and analysed post-mortem using SEM and micrographs.

The typical load-displacement behaviour and corresponding tuft failure (debonding, resin ploughing through laminate matrix, tuft rupture, frictional pull-out) were determined.

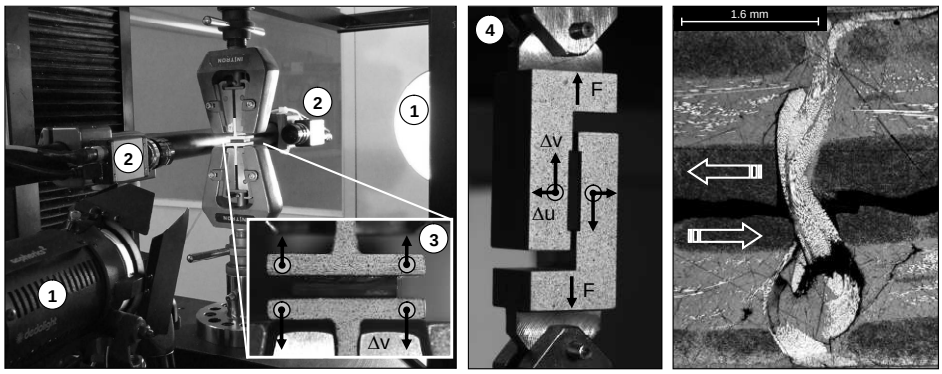

Figure 1 – Experimental setup (1+2) DIC recording system (3) pull-out setup (4) shear setup; micrograph of sheared carbon tuft in NCF laminate (90°)

The representative, apparent stress strain curves in figure 2 indicate that not only the tuft and laminate material, but also loading type and direction (with (0°) or against (90°) the laminate direction) at the crack interface influence the tuft bridging behaviour.

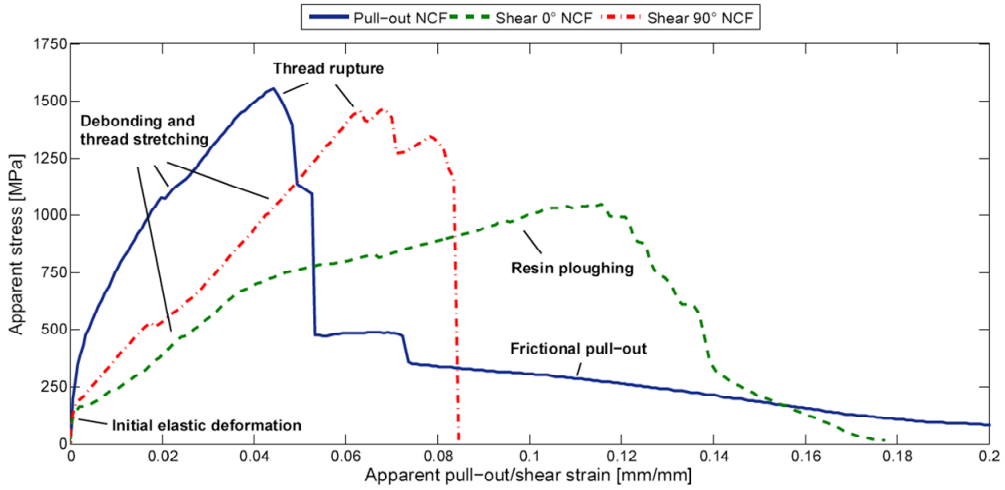

Figure 2 – Representative, apparent stress-strain curves for pull-out and shear (0° and 90° to interface laminate direction) of a carbon tuft in NCF laminate

Analytical models, presented by Cox [2], were adapted and validated to predict the tuft bridging behaviour for variable loading and material parameters which influence the tuft response.

ACKNOWLEDGEMENTS

The presented work is part of a project funded by the Engineering and Physical Science Research Council through grant EP/F037937.

References

1. Lowe, J., Carbon fibre sewing yarn for structural reinforcement of textile composite applications, International SAMPE Technical Conference, 2005

Comparing crack bridging laws for tufted and Z-pinned composite

J W G Treiber, G Dell'Anno , I K Partridge

Cranfield University, Composites Centre, Cranfield, Bedford MK43 0AL, UK

giuseppe.dellanno@cranfield.ac.uk

The paper reports experimentally determined mode I and mixed mode bridging laws for single glass and carbon tufts in bidirectional non-crimped (NCF) carbon fabric preforms, infused and cured with epoxy resin via RTM. For direct comparison purposes, the same single pin pull-out and shear tests were performed on equivalent samples containing carbon Z-pins.

Specimen containing a single tuft or Z-pin, bringing across a thin release film, was bonded between two vertically loaded steel T-tabs or within a specially designed shear jig which allows shear and opening of the specimen (see fig. 1 a). A DIC system was used to record the relative opening and shear displacements of the loaded specimens. The typical load-displacement behaviour and corresponding failure mechanisms (debonding, ploughing through laminate matrix, tuft rupture and frictional pull-out) are shown in figures 1 b) and c) respectively.

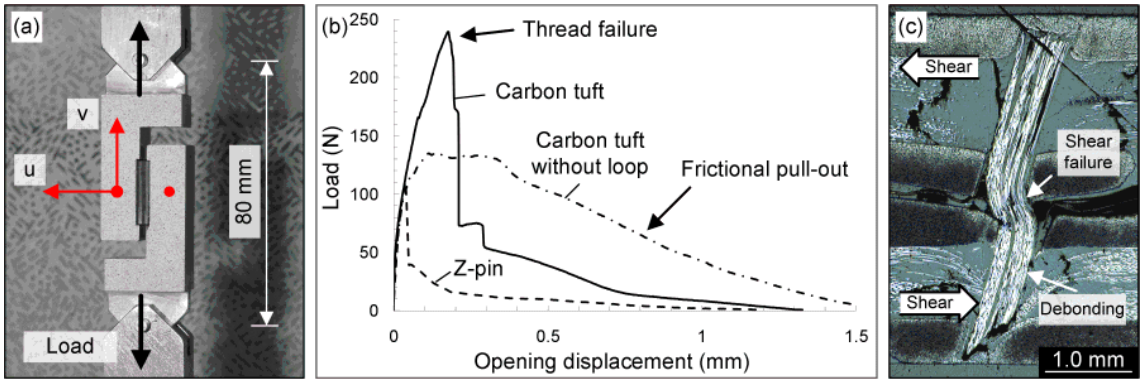

Figure 1 – Exp. mode II shear setup (a), mode I comparison between tuft, tuft without loop and Z-pin (b), micrograph of 90° sheared carbon Z-pin in NCF laminate (c)

The results show that the highest specific energy dissipation is achieved by frictional pull-out of the loop-less tufts. The loading mode and direction (with respect to the fabric fibre orientation at the crack interface) influence the crack bridging effectiveness of both reinforcement types. Furthermore, for shear loading the effect of crack opening in the presence of both Z-reinforcement types cannot be ignored and must be taken into consideration for modelling approaches.

EFFECTS OF MESOSTRUCTURE ON THE IN-PLANE PROPERTIES OF TUFTED CARBON FABRIC COMPOSITES

Johannes W.G. Treiber, Denis D.R. Cartié and Ivana K. Partridge

Cranfield University, Composites Centre
Cranfield, Bedford, MK43 0AL, United Kingdom
Email: j.treiber@cranfield.ac.uk, web page: http://www.cranfield.ac.uk/sas/composites

Keywords: Tufting, Carbon fabric/epoxy, In-plane properties, Mesostructure, Finite elements

ABSTRACT

A pseudo-UD fabric and a biaxial non-crimped carbon fibre fabric were layered and tufted with Tenax twisted carbon sewing thread (3x68 g/km), using tuft spacings of 2.8, 3.9 and 5.6 mm in a square and in a triangular pattern. The selected spacings correspond to areal densities of Z-direction reinforcement of 0.5%, 1% and 2% respectively. A full description of the tufting procedure can be found in [1]. The tufted preforms were infused with ACG's MVR444 resin in a resin transfer moulding (RTM) machine and cured in its rectangular closed mould with adjustable thickness. For a given fabric type the mould thickness determines the fibre volume fraction of the "equivalent" 2D (i.e.tuftless) laminate [2].

In- and out-of-plane 2D micrographs (Fig.1) were used to determine the size and distribution of resin-rich pockets around the perimeter of the (infused and cured) tufts, along with fabric fibre deviation and local fibre volume fraction.

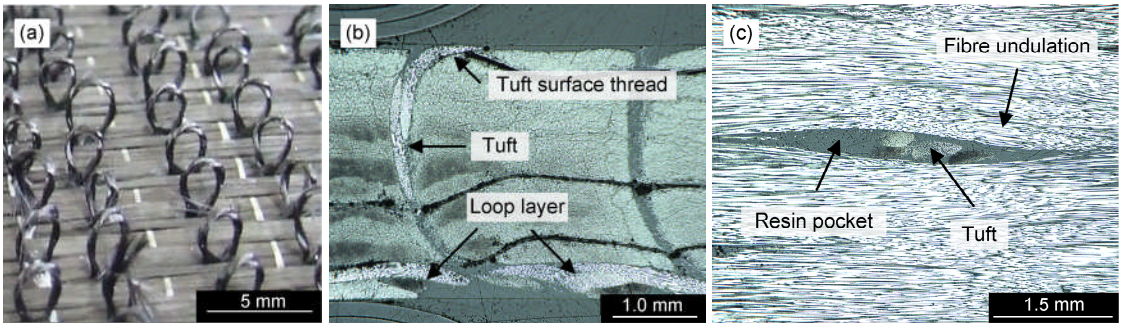

Figure 1: (a) Carbon tufted dry pseudo-UD fabric; Optical micrographs of polished section of cured tufted UD laminate, showing characteristic (b) out-of-plane and (c) in-plane fabric disruption and identifying major meso-structure features

A simplified representative volume element (RVE) was derived from the experimental observations as basis for a parametric 3D finite element model in MSC Patran. Each RVE contains a single tuft, a resin rich pocket, resin rich thread and loop layer, and individual fabric layers, simulated as uniform, transversely isotropic unidirectional layers. Quantified local fibre deviation and local increase in fibre volume fraction are incorporated around each resin-rich pocket. The procedures described by Lomov et al [3] were used for modelling and homogenisation. A non-linear strength analysis was performed on the RVE in tension, applying the Puck failure criterion to determine failure of the transversely isotropic UD layers and the tuft reinforcement, combined with a simple progressive damage algorithm, as available in the MSC Marc solver. The continuous change in local fibre volume fraction does not allow the experimental determination of the material properties for each volume element. To reduce the computational effort, an analytical set of equations is used to predict each element strength and stiffness [4]. The model correctly predicts the transverse splitting initiated at the edge of the resin rich pocket under tensile loading – see Fig.2.

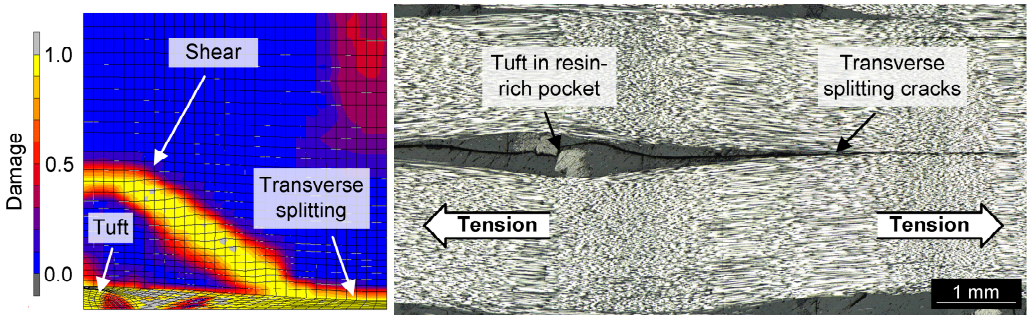

Figure 2: Damage in quarter RVE for 0.5% square tufted UD configuration and the equivalent micrograph of tufted pseudo-UD composite with damage under tensile load at 1.1% strain

	Experiment		RVE Model			
			Square pattern		Triangular pattern	
Tuft density [%]	Modulus E_t [GPa]	Strength X_t [MPa]	$E_t/E_{0,t}$ [-]	$X_t/X_{t,0}$ [-]	$E_t/E_{0,t}$ [-]	$X_t/X_{t,0}$ [-]
0.0	103.4 (2.5)	2160 (52)	1.000	1.00	1.000	1.00
0.5	104.7 (1.6)	1746 (61)	0.999	0.94	0.997	0.82
2.0	105.5 (1.0)	1775 (58)	1.003	0.95	0.984	0.57

Table 1: Measured and predicted tensile moduli and strengths of tufted pseudo-UD composites

Tensile tests on control, 0.5% and 2.0% tufted pseudo-UD samples showed no significant reduction of elastic modulus with increasing tuft density, but reduced tensile strength by up to 19%. Increase in local volume fraction around the tuft compensates for possible degradation of elastic modulus by fibre deviation around the resin-rich pocket. Integration of local fibre volume changes into the model is critical for the correct prediction of tensile modulus. The increasing local fabric fibre deviation for higher tuft density is the reason for the degradation in tensile strength. The combination of the Puck failure criterion with a simplified damage algorithm is sufficient to predict an 'upper and lower bound' for the drop in strength, dependent on the tuft spacing and tufting pattern.

In corresponding NCF samples the modulus also remains unaltered by the inclusion of tufts and the tensile strength drop in 2% tufted samples is only 11%. The mesostructural details for these differences have been identified and will be described in the presentation.

The work described here was funded through the UK's Engineering and Physical Sciences Research Council (EP/F037937).

REFERENCES

[1] G. Dell'Anno, D. D. Cartié, I. K. Partridge, A. Rezai, Exploring mechanical property balance in tufted carbon fabric/epoxy composites, *Composites Part A: Applied Science and Manufacturing*, 38 (11), 2007, pp. 2366 – 2373.

[2] A. P. Mouritz, B. N. Cox, A mechanistic interpretation of the comparative in-plane mechanical properties of 3D woven, stitched and pinned composites, *Composites Part A: Applied Science and Manufacturing*, 41 (6), 2010, pp. 709 – 728.

[3] S. V. Lomov, D. S. Ivanov, I. Verpoest, M. Zako, T. Kurashiki, H. Nakai, S. Hirosawa, Meso-FE modelling of textile composites: Road map, data flow and algorithms, *Composites Science and Technology*, 67 (9), 2007, pp. 1870 – 1891.

[4] C. C. Chamis, Simplified composite micromechanics equations for hygral, thermal and mechanical properties, *SAMPE quarterly*, 15 (3), 1984, pp. 14 - 23

Deformation and failure in a tufted carbon fabric/epoxy Ω – stiffener

I K Partridge, J W G Treiber and M Préau

Cranfield University, Composites Centre, Cranfield, Bedfordshire, MK43 0AL, UK

i.partridge@cranfield.ac.uk

Sample manufacture : - An omega-stiffener/skin joint configuration was selected as a suitable structural element to evaluate the effects of tufting on the damage resistance of carbon fibre/epoxy composites made via the resin-transfer-moulding route. Tufting is a form of one-sided stitching, whereby a single thread in a hollow needle is passed through a dry fibre preform, exiting through the same position as the insertion point but leaving a loop of the thread held either outside of or within the preform.

The dry preform was constructed from several layers of carbon non-crimped fabric, in a quasi-isotropic configuration, and shaped over a specially prepared metal tool to arrive at the so called Ω-stiffener configuration. Commercial twisted glass or carbon thread was used to tuft across the skin-stringer joint (see Fig.1a), using tuft-to-tuft spacing of 5.6 mm. The tufted preform was injected with ACG's MVR444 resin in metal resin-transfer-moulding tool and cured. The cured 300x800 mm structural panel was then cut into 30 mm wide individual structural coupons for testing.

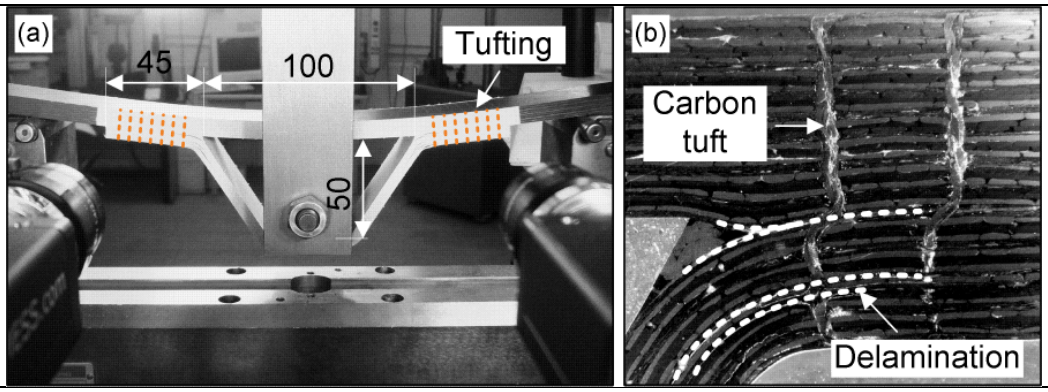

Fig.1 (a) Ω-stiffener pull-off configuration, with localised tufting and DIC and (b) detail of failure under pull-off loading

Testing: - The coupons were tested in pull-off and in (two different) 4-pt-bend configurations at constant cross-head speed of 0.5 and 1mm/min respectively. Failure under pull-off loading was identified by a sudden load drop, coinciding with complete skin-stringer delamination. The failure mode in 4pt-bending depends on the placement of the rollers relative to the position of the tufted region. The test configuration shown in Fig.2a produces peel forces on both ends of the tufted region, with mixed mode (MI/MII > 1) loading over the entire section. With increasing flexure, the traction exerted by the stretching tufts reduces the contribution of crack opening response to the overall failure. Digital image correlation (DIC) was used to quantify the degree of mode mixity in the samples under load. In all cases, the significant increase in the area under

the load-displacement curve indicates that the tufting leads to considerable additional energy absorption by the loaded sample. Catastrophic failure in pull-off occurs at nearly twice the critical load for the control sample and twice the displacement; in 4-pt-bending the localised tufting increases the energy absorbed by the sample by an order of magnitude.

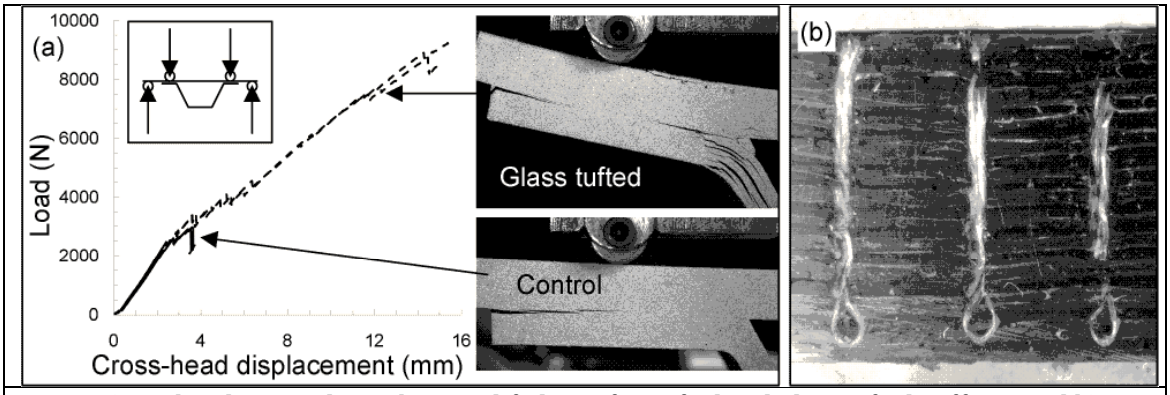

Fig. 2 a) 4pt bending results with typical failure of untufted and glass tufted stiffener and b) micrograph of partially through-the-thickness inserted glass tufts

Whilst the increased energy absorption is an expected outcome of the localised Z-direction reinforcement [1,2] it is important to note comparisons between the relative effectiveness of carbon and glass tufting threads, with the carbon thread being the more effective in any predominantly 'pull-out' deformation modes.

Sample morphology and 'partial tufting' : - A structural study of the untested and partially failed samples provides indication of the morphological reasons for the differences in effectiveness between glass and carbon tufts. This is found in the differences between the structures of the threads themselves, but also in their interaction with the structure of the preform. Newly explored technique of 'partial tufting', in which the tuft is contained fully within the preform (see Fig.2b), shows particular promise. The avoidance of resin rich layers on one side of the specimen makes analysis and modelling of mechanical response easier. A further benefit appears to be gained by the creation of additional energy absorbing micromechanisms from the complex resin-rich regions created within the composite at the head of the loop.

The work reported here has been funded by EPSRC (EP/F037937).

1. Cartié, D. D. R., Dell'Anno, G., Poulin, E. and Partridge, I. K. (2006), "3D reinforcement of stiffener-to-skin T-joints by Z-pinning and tufting", Engineering Fracture Mechanics, vol. 73, no. 16, pp. 2532-2540.

2. Stickler, P. B. and Ramulu, M. (2001), "Investigation of mechanical behavior of transverse stitched T-joints with PR520 resin in flexure and tension", Composite Structures, vol. 52, no. 3-4, pp. 307-314.